



UNIVERSITEIT ANTWERPEN

Faculteit Wetenschappen  
Departement Fysica

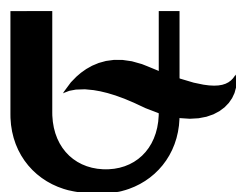
**Measurement of  $K^{*\pm}(892)$  Production in Deep Inelastic  
*ep* Scattering with the H1 Detector at HERA**

Proefschrift voorgelegd tot het behalen van de graad van  
Doctor in de Wetenschappen  
aan de Universiteit Antwerpen  
te verdedigen door

**Deniz SUNAR**

**Promotor:** Prof. dr. E. A. De Wolf

Antwerpen, 2009



UNIVERSITEIT ANTWERPEN

Faculteit Wetenschappen  
Departement Fysica

Measurement of  $K^{*\pm}(892)$  Production in Deep Inelastic  
*ep* Scattering with the H1 Detector at HERA

---

Meting van de  $K^{*\pm}(892)$  Productie in Diepe Inelastische  
*ep* Verstrooiingen met de H1 Detector bij HERA

Proefschrift voorgelegd tot het behalen van de graad van  
Doctor in de Wetenschappen  
aan de Universiteit Antwerpen  
te verdedigen door

Deniz SUNAR

## LEDEN VAN DE DOCTORAATSJURY

Prof. dr. E. Goovaerts (voorzitter), Universiteit Antwerpen  
Prof. dr. E. A. De Wolf (promotor), Universiteit Antwerpen  
Prof. dr. F. Peeters, Universiteit Antwerpen  
Prof. dr. P. Van Mechelen, Universiteit Antwerpen  
Prof. dr. L. Favart, Universite Libre de Bruxelles  
Prof. dr. H. Jung, Hamburg University

*To my dear parents Ayda and Züher,  
my brother Sertan,  
and Salim*



## Acknowledgements

The years I have spent for my PhD indeed brought me invaluable and memorable experiences, moments and especially “people” who I will always have a special place in my heart. I am grateful to all the people who touched my life and gave me the strength that I needed during this long path towards the PhD. This thesis would not have been possible without their remarkable patience and support.

First of all I am deeply indebted to my supervisor Professor Eddi De Wolf who offered me the possibility to work in the H1 Collaboration at DESY and who gave assistance and constant encouragement throughout this work.

I would like to acknowledge the honourable members of my thesis committee, Prof. Etienne Goovaerts, Prof. Francois Peeters, Prof. Pierre Van Mechelen, Prof. Laurent Favart and Prof. Hannes Jung.

I owe a debt of thanks to Karin Daum, whose continuous interest, effort and useful advice were of great help. I am especially grateful for her guidance during my analysis and her critical reading of the thesis.

I would also like to thank Joerg Gayler not only for his careful reading and important criticism of the thesis but also for creating time whenever I needed him to discuss my analysis.

Very very special thanks to one of my dearest friend, Krzysztof Nowak, for unforgettable memories, fun and joy, “coffee & chocolate” times. Furthermore, having such a great heart which is full of positiveness and lots of patience. Also for fruitful discussions regarding things related with Physics as well as life. *Thank you!*

I wish to thank to my dear friend and a second brother, Adil Aktas, for his introduction to the H1LT software, support, encouragement, very wise advice and especially his great friendship. Many thanks to Zuzana Rurikova for being a lovely person and a good friend. Shiraz Habib deserves also heartfelt thanks for philosophical discussions with “tea breaks” which made me learn a lot and for the very friendly atmosphere during past years. Boy, I will sure miss our conversations and discussions.

During my time at DESY I appreciated the time spent with my friends: Michel Sauter, Guillaume Leibengut, Tobias Zimmerman, Julie Delvax, Anna Falkiewicz and Tomas Hreus. Many thanks also goes to Jacek Turnau, for preparing delicious “Polish tea” with “Turkish cookies” and for fruitful discussions made on the history of Physics and of the Ottoman Empire.

I would like to thank the H1 collaboration for the professional and friendly atmosphere that I have enjoyed. Especially, Andre Schoening and Stefan Schmitt for various physics discussions and ideas. Many thanks to my friends Maxime Gouzevitch and Roman Kogler who found time to read the thesis and gave insightful suggestions in improving the manuscript. My special thanks go to Hans Van Haeevermaet for the Dutch translation.

I would also like to thank the department secretary Hilde Evans and coordinator of Antwerp Doctoral School Jetje De Groof for their help and assistance.

Although Antwerp does not offer so much sun, there were people who made my stay and life feel like a sunny day. Many thanks to my lovely friend Semahat Resmi for always being just next to me whenever I needed help and for sending positive energies in my direction with “reiki” from a distance. *Thank you my dear friend.* A very warm thank you to my friends Pervin and Özgür Çınar for the wonderful “family” time they provided me in Antwerp. I also wish to thank my friend Sabahat Dönmez and her children for accepting me as part of their family. Thanks to Yasemin Köroğlu for listening me and making me happy even when I was in deep moods. A lot of thanks go to my friend Ahmet Ekicibil for being such a great friend and advisor.

Finally, warm and special thanks to my parents Ayda and Züher and also to my brother Sertan for immeasurable love, inspiration, encouragement, understanding and support they have provided throughout my life. A deep thank you goes to Salim for his unending moral support and for being in my life!

**THANK YOU!**

## Abstract

A first measurement is presented of  $K^*(892)^\pm$  vector mesons, observed through the decay chain

$$K^*(892)^\pm \rightarrow K_S^0 \pi^\pm \rightarrow \pi^+ \pi^- \pi^\pm,$$

in neutral current deep-inelastic  $ep$  scattering. The data were taken at the HERA collider in the years 2005 – 2007 with centre of mass energy  $\sqrt{s} = 319$  GeV using the H1 detector and correspond to an integrated luminosity of approximately  $302 \text{ pb}^{-1}$ . The measurement of differential cross section was performed in the kinematic range which covers the photon virtuality  $5 < Q^2 < 100 \text{ GeV}^2$  and the inelasticity  $0.1 < y < 0.6$ . The visible range of  $K^{*\pm}$  vector meson is restricted in transverse momentum  $p_T(K^{*\pm}) > 1 \text{ GeV}$  and pseudorapidity  $-1.5 < \eta(K^{*\pm}) < 1.5$ . The results are compared to predictions of leading order Monte Carlo models matched with the parton showers.

## Persbericht

Deze dissertatie behandelt een eerste meting van  $K^{*\pm}$  vector mesonen, waargenomen via het vervalkanaal

$$K^*(892)^\pm \rightarrow K_S^0 \pi^\pm \rightarrow \pi^+ \pi^- \pi^\pm,$$

in diep inelastische elektron-proton verstrooiing via neutrale stromen. De gegevens werden vergaard met de H1 detector bij de HERA versneller gedurende de jaren 2005 – 2007 bij een massamiddelpuntsenergie van  $\sqrt{s} = 319$  GeV en een overeenkomstige geïntegreerde luminositeit van  $302 \text{ pb}^{-1}$ . De differentiële werkzame doorsnede is bepaald in het kinematische gebied met een bereik van  $5 < Q^2 < 100 \text{ GeV}^2$  in foton virtualiteit en  $0.1 < y < 0.6$  in inelasticiteit. De  $K^{*\pm}$  mesonen werden gereconstrueerd met een minimale transversale impuls  $p_T(K^{*\pm}) > 1 \text{ GeV}$  en pseudorapiditeit  $-1.5 < \eta(K^{*\pm}) < 1.5$ . De resultaten zijn vergeleken met voorspellingen van leading order Monte Carlo modellen en overeenkomende parton showers.

# Contents

<b>List of Figures</b>	<b>13</b>
<b>List of Tables</b>	<b>20</b>
<b>1 Introduction</b>	<b>22</b>
<b>2 Theoretical Overview</b>	<b>25</b>
2.1 The Standard Model . . . . .	25
2.2 Deep Inelastic Scattering . . . . .	27
2.2.1 Kinematic Description . . . . .	28
2.3 The Quark Parton Model . . . . .	30
2.4 Cross Section for Deep Inelastic $ep$ Scattering . . . . .	31
2.5 Quantum Chromodynamics . . . . .	33
2.6 Renormalisation . . . . .	33
2.7 Factorisation . . . . .	34
2.8 Evolution of Partons . . . . .	36
2.8.1 DGLAP Evolution Equations . . . . .	37
2.8.2 BFKL Evolution Equations . . . . .	38
2.8.3 CCFM Evolution Equations . . . . .	39
<b>3 Strangeness Physics</b>	<b>40</b>
3.1 Characteristics of Strange Particles . . . . .	40
3.2 Strange Hadrons . . . . .	42
3.2.1 $K_S^0$ Meson . . . . .	44
3.2.2 $K^*$ Meson . . . . .	45
3.2.3 $\Lambda$ Baryon . . . . .	46

---

3.3	Strangeness Production Mechanism . . . . .	47
3.4	Strangeness Suppression . . . . .	48
3.5	Experimental Results on Strangeness Production . . . . .	49
3.5.1	Strangeness Production in $e^+e^-$ Annihilation . . . . .	49
3.5.2	Strangeness Production in $pp$ , $p\bar{p}$ , $pA$ and $AA$ Collisions . . . . .	52
3.5.3	Strangeness Production at the $ep$ Collider . . . . .	55
3.5.4	Strangeness Production in Other Experiments . . . . .	57
3.5.5	Summary . . . . .	57
<b>4</b>	<b>HERA and the H1 Detector</b> . . . . .	<b>59</b>
4.1	The HERA Ring . . . . .	59
4.2	The H1 Detector . . . . .	62
4.3	Tracking System . . . . .	65
4.3.1	Central Tracking Detector . . . . .	65
4.3.2	Forward Tracking Detector . . . . .	67
4.3.3	Track Reconstruction . . . . .	67
4.4	Calorimetry . . . . .	68
4.4.1	The Liquid Argon Calorimeter . . . . .	70
4.4.2	The SPACAL Calorimeter . . . . .	71
4.5	Luminosity Measurement . . . . .	73
4.6	Time-of-Flight System . . . . .	74
4.7	Trigger and Data Acquisition . . . . .	75
<b>5</b>	<b>Monte Carlo Simulation</b> . . . . .	<b>78</b>
5.1	Monte Carlo Event Generators . . . . .	78
5.2	Parton Cascade Models . . . . .	80
5.2.1	Parton Showers . . . . .	80
5.2.2	Colour Dipole Model . . . . .	80
5.3	Hadronisation Models . . . . .	81
5.3.1	String Model . . . . .	81
5.3.2	Cluster Model . . . . .	81
5.4	Deep Inelastic Scattering Event Generators . . . . .	83
5.4.1	DJANGO . . . . .	83

---

5.4.2	RAPGAP	84
5.5	Detector Simulation	84
<b>6</b>	<b>Event Selection</b>	<b>86</b>
6.1	Online Selection	86
6.1.1	Trigger Selection	86
6.2	Offline Selection	88
6.2.1	Run Selection	89
6.2.2	Event Vertex Position	89
6.2.3	Selection of DIS Events	90
6.2.3.1	Scattered Electron Selection	90
6.2.3.2	Energy Balance	93
6.2.3.3	DIS Event Reconstruction	93
6.2.3.4	Electron Method	93
6.2.3.5	Hadron Method	94
6.2.3.6	$\Sigma$ Method	95
6.2.3.7	Electron- $\Sigma$ Method	95
6.2.4	DIS Kinematics	95
6.2.5	Track Selection	96
6.3	Summary of the Selection	98
<b>7</b>	<b>Reconstruction of <math>K^{*\pm}</math></b>	<b>100</b>
7.1	$K_S^0$ Reconstruction	100
7.1.1	Extraction of $K_S^0$ Signal	104
7.1.2	$K_S^0$ Lifetime	106
7.1.3	Decay Topologies of $K_S^0$	107
7.2	Primary $\pi^\pm$ Selection	108
7.3	$K^{*\pm}$ Reconstruction	108
7.3.1	Signal Extraction	111
<b>8</b>	<b>Determination of the <math>K^{*\pm}</math> Cross Sections</b>	<b>117</b>
8.1	Cross Section Definition	117
8.2	Bin Selection	118
8.3	Correcting Data with Monte Carlo Simulations	119

---

8.3.1	Acceptance . . . . .	119
8.3.2	Purity and Stability . . . . .	121
8.4	Trigger Efficiency . . . . .	124
8.5	Systematic Uncertainties . . . . .	126
<b>9</b>	<b>Results</b>	<b>132</b>
9.1	Total Inclusive Cross Section . . . . .	132
9.2	Differential Inclusive Cross Sections . . . . .	133
9.3	Contribution of Different Production Mechanisms . . . . .	138
9.4	Double Differential Inclusive Cross Sections . . . . .	140
9.5	$K^{*+}$ and $K^{*-}$ Production Asymmetry . . . . .	143
<b>10</b>	<b>Summary and Conclusion</b>	<b>148</b>
10.1	Outlook . . . . .	150
<b>11</b>	<b>Samenvatting en Besluit</b>	<b>151</b>
11.1	Vooruitzichten . . . . .	153
	<b>Appendices</b>	<b>155</b>
<b>A</b>	<b>Cross Section Tables</b>	<b>155</b>
<b>B</b>	<b>Double Differential Cross-Section Tables</b>	<b>158</b>
	<b>References</b>	<b>162</b>
	<b>Curriculum Vitae</b>	<b>172</b>

# List of Figures

2.1	Leading order Feynman diagrams of inelastic electron proton scattering. The electron interacts with the proton via the exchange of a $\gamma$ or $Z^0$ boson (NC interactions, left), or a charged $W^\pm$ boson (CC interactions, right). . . . .	28
2.2	The proton structure function $F_2$ shown for the data from the collider experiment H1 and the fixed target experiments BCDMS and NMC. The results are compared to the SM prediction determined from the H1 PDF 2000 fit. The measurements at different $x$ values are displaced vertically by a factor $2^i$ . The figure is taken from [25]. . . . .	32
2.3	The strong coupling constant $\alpha_s$ with scale $\mu = Q$ . The solid line shows two loop solution of the renormalisation group equation obtained by evolving the $\alpha_s(M_Z)$ extracted from a simultaneous fit of 54 measurements of the normalised inclusive jet cross section as a function of $Q^2$ and $P_T$ , the normalised 2-jet cross section as function of $Q^2$ and $\langle P_T \rangle$ and the normalised 3-jet cross section as function of $Q^2$ [29]. . . . .	35
2.4	A schematic overview of the <i>gluon ladder diagram</i> of the parton evolution in $ep$ scattering. A quark from the proton interacts with a virtual photon from the electron after radiating $n$ gluons. The transverse and longitudinal momenta of the each emitted gluons are labelled as $k_{T,i}$ and $x_i$ . . . . .	36
2.5	The splitting functions $P_{jk}$ used for the DGLAP approximation. From left to right, the processes $q \rightarrow qg$ , $q \rightarrow gq$ , $g \rightarrow q\bar{q}$ and $g \rightarrow gg$ are shown. . . . .	38
3.1	The parton densities for the valence quarks $u$ , $d$ , and the sea $S$ quarks and gluons inside the proton are extracted by the H1 and ZEUS collaborations at $Q^2 = 10 \text{ GeV}^2$ [49]. The bands represent estimates of the experimental and theoretical uncertainties. Sea quark $S$ and gluon densities are scaled down by a factor of 0.05. . . . .	41
3.2	The Eightfold Way for pseudoscalar mesons (left) and vector mesons (right). The various states are classified by their strangeness content $\mathbf{S}$ and the third component of their isospin $I_3$ . . . . .	43
3.3	The oscillation of $K^0$ mesons with its antiparticle $\bar{K}^0$ . . . . .	44
3.4	The dominant decay channel $K_S^0 \rightarrow \pi^+\pi^-$ . . . . .	45

3.5	The main decay of strange baryon $\Lambda^0 \rightarrow p\pi^-$ . . . . .	46
3.6	Various mechanisms contributing to the production of strange particles. Shown are hard scattering off a $s$ sea quark a), boson gluon fusion (BGF) b), parton fragmentation c) and heavy quark decay d). . . . .	47
3.7	The differential cross section for $K^{*\pm}$ production at the OPAL experiment. Here $\beta$ is the particle velocity, $p/E$ , where $p$ and $E$ are the momentum and energy of the particle, respectively. $\sigma_{had}$ represents the first order hadronic cross section. The parameter $\frac{V}{(V+P)_s}$ is the probability that a strange meson carries spin-1, where $V$ represents the vector mesons and $P$ represents the pseudoscalar mesons. . . . .	50
3.8	The differential cross section for $K^{*\pm}$ production as a function of the fractional energy $x = 2E/\sqrt{s}$ at the CELLO experiment [69]. Here $\sigma_h$ is the first order hadronic cross section. Solid line shows the Lund model prediction. . . . .	51
3.9	Measurements of the total $K^*$ production cross section in $pp$ collisions as a function of centre of mass energy $\sqrt{s}$ [86]. . . . .	52
3.10	The yield ratios of $K^*/K$ (upper panel) and $\phi/K$ (lower panel) as a function of centre of mass system. The results from Au+Au and $p + p$ interactions are compared with various measurements [87]. . . . .	53
3.11	The ratio of the differential production cross section for $\Lambda$ baryons and $K_S^0$ mesons in the laboratory frame as a function of $p_T$ (left panel) and $\eta$ (right panel) [101]. Theory/Data ratios are shown for different MC predictions. For comparison, the data points are put to one and only uncorrelated errors are shown; the correlated systematic errors are indicated by the grey band. . . . .	55
3.12	The inclusive differential non-diffractive cross sections for $\rho^0$ , $K^{*0}$ and $\phi$ as a function of transverse momentum $p_T$ <b>a</b> ), and rapidity in laboratory frame <b>b</b> ). The curves correspond to power law, given in the legend with $f(E_T^{kin}) = \frac{A}{(E_{T0} + E_T^{kin})^n}$ where $E_T^{kin} = \sqrt{m_0^2 + p_T^2} - m_0$ is the transverse kinetic energy, $m_0$ is the nominal resonance mass, $A$ is a normalisation constant and $E_{T0}$ is a free parameter [102]. . . . .	56
3.13	The strangeness suppression factor measured by the different experiments. . . . .	58
4.1	Layout of HERA collider, and its injection and its pre-accelerators. . . . .	59
4.2	Luminosity produced by HERA (left) and accumulated by H1 (right) in individual years [115]. . . . .	61
4.3	An illustration of the H1 coordinate system. . . . .	62
4.4	The H1 detector with its major components [117]. . . . .	64
4.5	A longitudinal view of the H1 tracking system including the central and forward tracking detectors. . . . .	65
4.6	A radial view of the central tracking. . . . .	66

4.7	The definition of the helix trajectory parameters $\kappa$ , $d_{ca}$ , $z_0$ , $\theta$ and $\phi$ in $xy$ plane a), and in $rz$ plane b) [?]. . . . .	69
4.8	The LAr Calorimeter. a) the structure of wheels, b) the octant structure of wheels. . . . .	72
4.9	The location of SPACAL in the H1 detector. . . . .	73
4.10	The luminosity system. The ET is placed at -5.4 m, PD is at -101.8 m for HERA II. . . . .	74
4.11	The Time-of-Flight system. . . . .	75
4.12	An illustration of the data flow through the H1 trigger system. . . . .	76
5.1	A schematic view of the $ep$ scattering process in a MC event generator. The figure is taken from [130]. . . . .	79
5.2	An illustrative picture of a string between a quark and an anti-quark (left) and the Lund string hadronisation model (right). The quarks in $q\bar{q}$ pair move away from each other, the string breaks up and a $q\bar{q}$ pair is produced. This procedure continues till the energy is too low to produce a new $q\bar{q}$ pair. . . . .	82
5.3	A schematic picture of cluster model. . . . .	82
6.1	The $z_{vtx}$ distributions for data and simulated DJANGO and RAPGAP events before a), after b) the reweighting procedure. The data are shown as points, the DJANGO and RAPGAP simulations are shown as solid and dashed lines, respectively. The distributions are normalised to the number of events. . . . .	90
6.2	Scattered electron quantities energy $E_e$ a), polar angle $\theta_e$ b), and minimum radial distance of the cluster from the beam pipe $R_\theta$ c). Shown are data (full points) together with the simulations using DJANGO (solid line) and RAPGAP (dashed line). The distributions are normalised to the total number of events. . . . .	91
6.3	The distributions of $E - p_z$ for data compared with simulated DJANGO and RAPGAP events. The data are shown as points, the predictions of the DJANGO and RAPGAP simulation are shown as solid and dashed lines, respectively. The distributions are normalised to number of events. . . . .	94
6.4	The distributions of DIS event kinematics: $Q^2$ a), and $y$ b). Data are shown as full points. The histogram shows the predictions of DJANGO (solid line) and RAPGAP (dashed line). The distributions are normalised to number of events. . . . .	96
6.5	Angular ranges of the various track types: central ( $20^\circ < \theta < 160^\circ$ ), forward ( $6^\circ < \theta < 25^\circ$ ) and combined ( $0^\circ < \theta < 40^\circ$ ). . . . .	97

- 
- 6.6 The radial length (left panel) and polar angle  $\theta$  (right panel) of tracks are shown for data (full points) and DJANGO (solid line) and RAPGAP (dashed line) Monte Carlo simulations. . . . . 98
- 6.7 Event yield for the selection of DIS events with  $K^{*\pm}$  candidates is shown in different run periods. Each point corresponds to an integrated luminosity of  $50 \text{ nb}^{-1}$ . . . . . 99
- 7.1 A schematic view of an event with a  $K_S^0$  decay. The  $K_S^0$  is produced at the point represented *primary vertex* and travels some distance before it decays at which the point represented as *secondary vertex*. The  $K_S^0$  decays in two pions which can be detectable. The dashed line from primary to secondary vertex shows the undetectable trajectory of the  $K_S^0$ . . . . . 101
- 7.2 A schematic illustration of a decay  $V^0 \rightarrow D1 + D2$ , where  $V^0$  represents the mother particle  $K_S^0$ ,  $D1$  and  $D2$  are the first and second daughter particles, e.g.  $\pi^+$  and  $\pi^-$ . . . . . 102
- 7.3 Armenteros-Podolanski plot shown in idealised form (left panel), and as measured in the present analysis (right panel). . . . . 103
- 7.4 Control distributions of reconstructed  $K_S^0$  particles. Following quantities are shown: a) the pseudorapidity  $\eta_{(K_S^0)}$ , b) the transverse momentum  $p_{T(K_S^0)}$ , c) the polar angle  $\theta_{(K_S^0)}$  and d) the decay length  $L_{(K_S^0)}$ . The data (black points) are reasonably well described by the DJANGO (solid line) simulation. The distributions are normalised to the number of events. . . . 105
- 7.5 Invariant mass spectrum of the  $K_S^0 \rightarrow \pi^+\pi^-$  candidates. The points correspond to the observed data events. The distribution is fitted with a student's t function and a first order polynomial background function. The background is represented by the dashed line. . . . . 106
- 7.6 The lifetime of  $K_S^0$  candidates: a) uncorrected data, b) the ratio of simulated to reconstructed DJANGO events, c) corrected lifetime which is the resultant of application of ratio to the uncorrected data. The solid line represents the result of an exponential fit. . . . . 107
- 7.7 Decay topologies of  $K_S^0$ : Seagull (left) and Sailor (right) decay topology. . . 108
- 7.8 Invariant mass spectrum of  $K_S^0$  for different decay topologies: Seagull (top) and Sailor (bottom). . . . . 109
- 7.9 Control distributions for primary pions  $\pi^\pm$ . The following quantities are shown: a) the transverse momentum  $p_{T(\pi)}$ , b) the pseudorapidity  $\eta_{(\pi)}$ , c) the polar angle  $\theta_{(\pi)}$ , d) the distance of closest approach to the primary vertex  $dca'_{(\pi)}$ . Shown are data (full points) compared with DJANGO Monte Carlo simulation (solid line). . . . . 110

- 7.10 Control distributions of reconstructed  $K^{*\pm}$  mesons. The full dots indicate the data and the line indicates the DJANGO MC simulation. Following quantities are shown: a) the pseudorapidity  $\eta_{(K^*)}$ , b) the polar angle  $\theta_{(K^*)}$ , c) the azimuthal angle  $\phi_{(K^*)}$  and d) the transverse momentum  $p_{T(K^*)}$ . . . . . 111
- 7.11 Invariant mass spectra of  $K_S^0\pi^\pm$  combinations after application of the all cuts mentioned in details in the text. The distribution is fitted with a relativistic Breit-Wigner function (solid line) and a background function (dashed line). The signal is shown with dash-dotted lines. . . . . 113
- 7.12 Invariant mass spectra of  $K_S^0\pi^\pm$  combinations in intervals of transverse momentum  $p_T$ ; a)  $1 < p_T < 1.5$ , b)  $1.5 < p_T < 2$ , c)  $2 < p_T < 2.5$ , d)  $2.5 < p_T < 3.5$ , e)  $3.5 < p_T < 5$  and f)  $5 < p_T < 10$  GeV. The distribution is fitted with a relativistic Breit-Wigner function (black line) and a background function (red line). On the bottom of each figure the ratio distribution,  $\text{Ratio} = (N^{DATA} - N^{FIT})/\sqrt{N^{DATA}}$ , is shown. . . . . 114
- 7.13 The  $K_S^0\pi^\pm$  invariant mass distribution for DJANGO Monte Carlo simulation in intervals of transverse momentum  $p_T$ ; (a)  $1 < p_T < 1.5$ , (b)  $1.5 < p_T < 2$ , (c)  $2 < p_T < 2.5$ , (d)  $2.5 < p_T < 3.5$ , (e)  $3.5 < p_T < 5$  GeV and (f)  $5 < p_T < 10$  GeV. The distribution is fitted with a relativistic Breit-Wigner function (black line) and a background function (red line). The signal is shown with dashed lines. . . . . 115
- 7.14 Invariant mass spectra of  $K_S^0\pi^\pm$  combinations in intervals of scaled longitudinal momentum  $x_F$ ; a)  $0. < x_F < 0.1$ , b)  $0.1 < x_F < 0.25$ , c)  $0.25 < x_F < 0.4$ , d)  $0.4 < x_F < 0.6$  and e)  $0.6 < x_F < 1$ . The distribution is fitted with a relativistic Breit-Wigner function (black line) and a background function (red line). On the bottom of each figure the ratio distribution,  $\text{Ratio} = (N^{DATA} - N^{FIT})/\sqrt{N^{DATA}}$ , is shown. . . . . 116
- 8.1 A schematic view of the migrations. The *path* of an event from GEN level to REC level is shown by arrows. The thick squares are bins inside the measured phase space, dotted squares bins outside of the measured phase space. a) is an illustration of the situation where an event has the same GEN and REC bin, b) illustrates an event smearing out of GEN bin  $i$  into REC bin  $j$ , c) shows an event smearing into a REC bin  $i$  from GEN bin  $j$  or from outside of the bins in the GEN phase space (broken line), d) shows a GEN event being lost from REC sample by being reconstructed outside of the measured phase space. . . . . 120
- 8.2 The acceptance correction factors  $\mathcal{A}$  of the H1 detector as a function of all measured quantities of the  $K^{*\pm}$  cross section: (a) the transverse momentum  $p_T$ , (b) the pseudorapidity  $\eta$ , (c) the four momentum squared  $Q^2$ , (d) the centre-of-mass energy of the hadronic final state  $W_{\gamma p}$ , (e) the Feynman variable  $x_F$ , and (f) the squared transverse momentum of the  $K^{*\pm}$  meson in the photon proton rest frame,  $P_T^{*2}$ . . . . . 122

- 8.3 The purity  $\mathcal{P}$  (downward triangle) and stability  $\mathcal{S}$  (upward triangle) for the bins in which cross section measurements are performed: (a)  $p_T$ , (b)  $\eta$ , (c)  $Q^2$ , (d)  $W_{\gamma p}$ , (e)  $x_F$  and (f)  $P_T^{*2}$ . . . . . 123
- 8.4 The efficiency of the SPACAL trigger elements,  $\varepsilon_{SPACAL}$ , included in ST61 is shown as a function of: a) the scattered electron energy  $E_{e'}$ , b) the scattered electron angle  $\theta_{e'}$ , c) the energy and longitudinal momentum balance of events  $E - p_z$ , d) the squared four-momentum transfer  $Q^2$ , e) the inelasticity  $y_{e\Sigma}$ , and f) the maximum transverse momentum observed in all CJC tracks,  $p_T^{Max}$ . The data (full points) are compared with the DJANGO Monte Carlo simulation (solid line). . . . . 125
- 8.5 The efficiency  $\varepsilon_{TRACK}$  of the TRACK trigger elements included in ST61 shown as a function of: a) the scattered electron energy  $E_{e'}$ , b) the scattered electron angle  $\theta_{e'}$ , c) the energy and longitudinal momentum balance of events  $E - p_z$ , d) the squared four-momentum transfer  $Q^2$ , e) the inelasticity  $y_{e\Sigma}$ , and f) the maximum transverse momentum observed in all CJC tracks,  $p_T^{Max}$ . Data (full points) are compared with the DJANGO Monte Carlo simulation (solid line). . . . . 127
- 8.6 The terms which are used for the calculation of the ratio  $R = \frac{p}{t_1+p+t_2}$ . . . . 130
- 9.1 The measured inclusive differential cross section as a function of the transverse momentum  $p_T$ . The cross sections is measured in the visible range defined by  $p_{T(K^*)} > 1 \text{ GeV}$ ,  $|\eta_{(K^*)}| < 1.5$ ,  $5 < Q^2 < 100 \text{ GeV}^2$  and  $0.1 < y_{e\Sigma} < 0.6$ . The inner error in the figure represents the statistical error, while the outer is the statistical and the systematic errors added in quadrature. The measured cross section is compared to the DJANGO 1.4 (continuous red line) and RAPGAP 3.1 (dashed blue line) calculations. The corresponding ratios of the MC DJANGO and RAPGAP to the data,  $R$ , are shown at the bottom of the figure. . . . . 134
- 9.2 The measured inclusive differential cross section as a function of the pseudo-rapidity  $\eta$ . For details see the caption of Fig. 9.1. . . . . 135
- 9.3 The measured inclusive differential cross section as a function of the four momentum squared  $Q^2$ . For details see the caption of Fig. 9.1. . . . . 136
- 9.4 An illustration of the hadronic centre-of-mass system, i.e.  $\gamma^*p$  frame. . . . 137
- 9.5 The measured inclusive differential cross section as a function of the Feynman- $x$ ,  $x_F$ . For details see the caption of Fig. 9.1. . . . . 138
- 9.6 The measured inclusive differential cross sections as a function of: (a) the centre-of-mass energy of the hadronic final state  $W_{\gamma p}$ , and (b) the transverse momentum squared in the hadronic final state  $P_T^{*2}$ . For details see the caption of Fig. 9.1. . . . . 139

- 9.7 The relative fractions of the different quarks (up (full line), down (dash-dotted line), strange (dash line), charm (dotted line) and bottom (dash-double-dotted line)) are shown. contributing in the hard interaction to the production of  $K^{*\pm}$  in the visible range. The fractions are shown as a function of  $Q^2$ ,  $\eta$ ,  $p_T$  and  $x_F$ . . . . . 140
- 9.8 The measured inclusive differential cross sections as a function of the transverse momentum  $p_T$ ,  $\eta$ ,  $Q^2$ ,  $W_{\gamma p}$ ,  $x_F$  and  $P_T^{*2}$ . The cross sections are measured in visible range defined by  $p_{T(K^*)} > 1 \text{ GeV}$ ,  $|\eta_{(K^*)}| < 1.5$ ,  $5 < Q^2 < 100 \text{ GeV}^2$  and  $0.1 < y_{e\Sigma} < 0.6$ . The inner error in the figure represents the statistical error, while the outer is the statistical and the systematic errors added in quadrature. The quark contributions (ud (dotted lines), cb (dashed lines), and s (dash-dotted lines)) are shown. . . . . 141
- 9.9 The double differential cross section of inclusive  $K^{*\pm}$  mesons, presented as functions of  $P_T^{*2}$  in bins of  $x_F$ . The cross sections are measured in visible range defined by  $p_{T(K^*)} > 1 \text{ GeV}$ ,  $|\eta_{(K^*)}| < 1.5$ ,  $5 < Q^2 < 100 \text{ GeV}^2$  and  $0.1 < y_{e\Sigma} < 0.6$  and compared with the LO DJANGO MC predictions (solid line). The inner error in the figure represents the statistical error, while the outer is the statistical and the systematic errors added in quadrature. The quark contributions (ud (dotted lines), cb (dash-dotted lines), and s (dashed lines)) are shown. . . . . 142
- 9.10 The double differential cross section of inclusive  $K^{*\pm}$  mesons, presented as functions of  $Q^2$  in bins of  $x_F$ . For details see the caption of Fig. 9.9. . . . 144
- 9.11 The double differential cross section of inclusive  $K^{*\pm}$  mesons, presented as functions of  $P_T^{*2}$  in bins of  $Q^2$ . For details see the caption of Fig. 9.9. . . . 145
- 9.12 The differential cross section of inclusive  $K^{*+}$  mesons (upper plots) and  $K^{*-}$  mesons (lower plots) are presented as functions of  $Q^2$ ,  $p_T$  and  $\eta$ . . . . 146

# List of Tables

2.1	The properties of the fundamental fermions (quarks and leptons, $spin = \frac{1}{2}$ ) of the SM. The anti-particle partners of these fermions (not included in the table) have the same mass (M), but with the opposite electric charge (Q). Q is given in units of the proton charge [4]. . . . .	26
2.2	The fundamental forces and force carriers, i.e. <i>gauge bosons</i> . Three kinds of fundamental forces are combined in the SM. The fourth fundamental interaction, gravity, is shown separately as it is not yet included in the SM [4]. . . . .	27
3.1	The two families of hadrons: baryons and mesons with their quark contents.	42
3.2	The resonances with their most dominant decay channels, branching ratios, widths, lifetimes and masses [4]. The unit of lifetimes is given in femtometer ( $1 \text{ fm} = 10^{-15} \text{ m}$ ). . . . .	43
3.3	The isospin doublets of the kaons. . . . .	44
3.4	The characteristics of $K_L^0$ and $K_S^0$ particles [4]. . . . .	45
3.5	The isospin doublets of the vector mesons $K^*$ . . . . .	46
4.1	The rates of the main background and some physics processes. . . . .	77
6.1	The trigger elements of subtrigger ST61. The symbols $\wedge$ and $\vee$ stand for logical <b>AND</b> and <b>OR</b> , respectively. . . . .	87
6.2	The average prescale factors for each period. . . . .	88
6.3	The data samples used in the analysis and integrated luminosities for the used run selection. . . . .	89
6.4	Summary of the track selection criteria. . . . .	97
6.5	Summary of all applied event selection cuts. . . . .	98
8.1	The overall trigger efficiencies for data and DJANGO MC simulation. . . . .	126
8.2	Summary of the systematic uncertainties. . . . .	131

---

9.1	Summary of the total inclusive $K^{*\pm}$ cross sections in the visible range. . .	133
A.1	The single differential $K^{*\pm}$ meson production cross section as a function of the transverse momentum, $p_T$ . . . . .	155
A.2	The single differential $K^{*\pm}$ meson production cross section as a function of the pseudorapidity, $\eta$ . . . . .	155
A.3	The single differential $K^{*\pm}$ meson production cross section as a function of the four momentum squared, $Q^2$ . . . . .	156
A.4	The single differential $K^{*\pm}$ meson production cross section as a function of the centre-of-mass energy of the hadronic final state, $W_{\gamma p}$ . . . . .	156
A.5	The single differential $K^{*\pm}$ meson production cross section as a function of the Feynman variable, $x_F$ . . . . .	156
A.6	The single differential $K^{*\pm}$ meson production cross section as a function of the squared transverse momentum $P_T^{*2}$ of the $K^{*\pm}$ meson in the photon proton rest frame . . . . .	157
B.1	The double differential cross section of inclusive $K^{*\pm}$ mesons, presented as functions of $P_T^{*2}$ in intervals of $x_F$ . . . . .	159
B.2	The double differential cross section of inclusive $K^{*\pm}$ mesons, presented as functions of $Q^2$ in interval of $x_F$ . . . . .	160
B.3	The double differential cross section of inclusive $K^{*\pm}$ mesons, presented as functions of $P_T^{*2}$ in interval of $Q^2$ . . . . .	161

# Chapter 1

## Introduction

Elementary particle physics studies the structure of matter and its main building blocks at its most fundamental level. The Standard Model (SM) of particle physics is a successful theory which describes the basic constituents of matter and their interactions. Within the SM, the fundamental particles are classified into two types of fermions, the leptons and the quarks which each exist in three families. Experimentally six different types of quarks, known as *flavors*, have been observed: up ( $u$ ), down ( $d$ ), charm ( $c$ ), strange ( $s$ ), top ( $t$ ) and bottom ( $b$ ). The interactions among the particles are mediated by gauge bosons, called photon ( $\gamma$ ) for the electromagnetic interaction;  $Z$  and  $W^\pm$  for the electroweak and gluons for the strong interaction. The gravitational force is not included within the SM. According to the theory of strong interactions, quantum chromodynamics (QCD), the strong force is mediated by gluons which couple to colour charge. The values of the coupling constant of QCD,  $\alpha_s$ , depends on the energy scale of the interaction.

In the late 1960's, the experiments at the Stanford Linear Accelerator (SLAC) accelerated electrons up to energies of 20 GeV. The electrons were scattered against a liquid hydrogen ( $H_2$ ) target. At such high energies, far beyond what had been previously possible, the electrons can probe deep into the inner structure of the proton, a process called Deep Inelastic Scattering (DIS). The experiments at SLAC shed light on the identification of point-like quarks as the constituents of the proton (Quark Parton Model, QPM).

The worldwide only electron<sup>1</sup> proton collider HERA<sup>2</sup> at DESY<sup>3</sup> (Hamburg) opened up a large kinematic domain in order to perform DIS studies. At HERA, both 27 GeV electrons and 920 GeV protons were accelerated and collided at a centre-of-mass energy  $\sqrt{s} = 319$  GeV allowing to resolve the structure function of the proton down to distances  $\sim 10^{-18}$  m. After running for almost 10 years, the HERA collider was upgraded during 2000-2001 in order to increase the instantaneous luminosity and to provide longitudinally polarised electron beams ( "HERA II"). The upgrade made it possible to look into the proton structure with a better precision and, even more, to have improved possibilities to test the SM using the DIS interactions. HERA provided a higher centre-of-mass energy than

---

<sup>1</sup>Hereafter, both electron and positron are referred to as electrons, unless explicitly stated otherwise.

<sup>2</sup>Hadron Elektron Ring Anlage

<sup>3</sup>Deutsches Elektronen Synchrotron

previously obtained which improved the resolution of the measurements and extended the kinematic range. HERA data taking stopped in 2007 after 15 years of successful operation. The two collider experiments H1 and ZEUS contributed with many measurements to the understanding of QCD and its dynamics and the electroweak theory.

This thesis is based on data collected by the H1 detector at HERA during the running period from 2005 to 2007. The results are obtained by using approximately  $14.1 \times 10^6$  DIS  $e^-p$  and  $e^+p$  events, corresponding to integrated luminosities of  $167 \text{ pb}^{-1}$  and  $135 \text{ pb}^{-1}$ , respectively.

The production of strange hadrons in high energy particle collisions provide an opportunity to investigate the strong interactions both in the perturbative and non-perturbative regimes. Strange quarks can be produced via various subprocesses such as directly in the hard scattering off a strange sea quark inside the proton, boson gluon fusion and decays of heavier quarks. The dominant production mechanism of strange quarks is found to be the string fragmentation.

The resulting cross sections of this analysis represent the first measurement of strange vector meson  $K^{*\pm}$  (892) production in DIS at HERA. Such a measurement provides an opportunity to study the strange content of the proton as well as the processes involved in the production of strange hadrons. For example, a difference in the  $K^{*+}$  and  $K^{*-}$  cross sections would indicate an asymmetric distribution of the sea quarks in the proton. The measurement gives direct information about the strangeness suppression factor ( $\lambda_s = P(s)/P(u)$ ) which sets the probability of strange ( $s$ ) quark production  $P(s)$  relative to the probability of up ( $u$ ) and down ( $d$ ) quark production  $P(u) = P(d)$ .

The  $K^{*\pm}$  mesons are reconstructed using the decay channel

$$K^{*\pm} \rightarrow K_s^0 \pi^\pm,$$

with the subsequent decay  $K_s^0 \rightarrow \pi^+ \pi^-$ . A clean  $K_s^0$  signal was obtained by the reconstruction of  $K_s^0$  decaying at a secondary vertex which can be well separated from the interaction point.

The large sample of approximately 80000 reconstructed  $K^{*\pm}$  mesons permits the high accuracy measurement. This allows comparisons to be made with other experiments which study similar processes.

In the present analysis, inclusive cross sections  $\sigma(ep \rightarrow eK^{*\pm}X)$  are presented differentially as a function of various kinematic variables in the laboratory and photon proton frames. The measured cross sections are compared to leading order Monte Carlo predictions obtained from the DJANGO and RAPGAP generators.

\*\*\*

*The results of the analysis presented here have been presented at the XVII International Workshop on Deep-Inelastic Scattering and Related Subjects, Madrid, Spain by the author [1]. They have been published by the H1 Collaboration as a contributed paper to the 34th International Conference on High Energy Physics, Philadelphia, USA [2]. Furthermore, they have been presented at the XXXVIII International Symposium on Multiparticle Dynamics (ISMD 2008), Hamburg, Germany [3].*

\*\*\*

The structure of this dissertation is as follows:

**Chapter 2** gives an overview of the Standard Model followed by the phenomenology of deep inelastic  $ep$  scattering and its basic concepts.

In **Chapter 3** the strange particles and some of their characteristic properties and a summary of different production mechanisms of strange particles are introduced. This chapter ends with a section where an overview of existing measurements is presented.

**Chapter 4** introduces the HERA collider which made possible to observation of deep inelastic scattering events of electron on protons and in more detail the H1 detector, with particular emphasis on the detector components directly used in this analysis.

**Chapter 5** describes the basic principles of Monte Carlo event generators and models which are the computer programs used for simulating the complete quantum mechanical final state of DIS events.

**Chapter 6** outlines the event selection procedure and explains the online trigger conditions and offline applied selection criteria.

**Chapter 7** introduces the strategy followed in this analysis to extract the  $K^{*\pm}$  signal and describes the reconstruction of the invariant mass of the  $K^{*\pm}$  candidates.

**Chapter 8** describes the determination of the inclusive  $K^{*\pm}$  cross sections. The procedure of extracting the inclusive  $K^{*\pm}$  cross sections is explained, including the correction for the detector effects and the trigger efficiency. A description of possible systematic error sources is given.

**Chapter 9** presents the measured inclusive  $K^{*\pm}$  meson differential cross sections with a comparison of data from the leading order Monte Carlo models.

**Chapter 10** summarises the conclusions drawn from the measurement.

### A note on units

In this work, a system of natural units will be used, whereby  $\hbar = c = 1$ .

This work has been carried out in the frame of the H1 Collaboration through the High Energy Physics Group of the University of Antwerpen. The author was financially supported by the *Fonds voor Wetenschappelijk Onderzoek Vlaanderen* (FWO, Research Foundation - Flanders).

# Chapter 2

## Theoretical Overview

In this chapter, the basic theoretical and phenomenological concepts related to the present analysis are summarised. First, an overview of the Standard Model (SM) of particles and forces is given. The phenomenology of deep inelastic  $ep$  scattering is introduced in the second section and the basic concepts of deep inelastic scattering (DIS) theory, i.e. the quark parton model (QPM), and the theory of strong interactions (QCD) are introduced. The parton evolution equations are given in the last section.

### 2.1 The Standard Model

The Standard Model (SM) is the experimentally well-tested theory of particle physics based on fundamental particles and their interactions. Within this model, fundamental particles can be classified according to three basic types: **quarks, leptons and carriers of force (the gauge bosons)**. The quarks and leptons, which are divided into three generations, are members of a family of particles called *fermions* (particles with spin- $\frac{1}{2}$ ). The properties of these fundamental fermions are summarised in Table 2.1. Experimentally six different types of quarks, known as *flavors*, have been observed: up ( $u$ ), down ( $d$ ), charm ( $c$ ), strange ( $s$ ), top ( $t$ ) and bottom ( $b$ ) are grouped into 3 generations. The *left handed* (L) quarks, which have spin aligned opposite to the direction of motion, are grouped into doublets. The *right handed* (R) quarks, where the spin is aligned along the direction of motion, are grouped into singlets.

$$\begin{pmatrix} u \\ d \end{pmatrix}_L, \begin{pmatrix} c \\ s \end{pmatrix}_L, \begin{pmatrix} t \\ b \end{pmatrix}_L, u_R, d_R, c_R, s_R, t_R, b_R \quad (2.1)$$

All visible matter is composed of the first generation particles, e.g. protons and neutrons are made up of  $u$  and  $d$  quarks. Quarks have never been observed as free isolated particles but exist only in bound states, e.g. baryons represent the bound states of three quarks ( $qqq$ ), and mesons are quark-antiquark ( $q\bar{q}$ ) pairs.

Leptons are spin- $\frac{1}{2}$  particles which can be observed as free particles. Analogous to the quarks, there are 3 known generations which differ from each other only in mass and

Generation	Flavour	Quarks		Leptons		
		Q	M (GeV)	Flavour	Q	M (GeV)
1 <sup>st</sup>	<i>u</i> (up)	2/3	$2.55_{-1.05}^{+0.75} \times 10^{-3}$	<i>e</i> (electron)	-1	$5.1 \times 10^{-4}$
	<i>d</i> (down)	-1/3	$5.04_{-1.54}^{+0.96} \times 10^{-3}$	$\nu_e$ ( <i>e</i> -neutrino)	0	$< 1.10^{-8}$
2 <sup>nd</sup>	<i>c</i> (charm)	2/3	$1.27_{-0.11}^{+0.07}$	$\mu$ (muon)	-1	0.105
	<i>s</i> (strange)	-1/3	$104_{-34}^{+26} \times 10^{-3}$	$\nu_\mu$ ( $\mu$ -neutrino)	0	$< 2.10^{-4}$
3 <sup>rd</sup>	<i>t</i> (top)	2/3	$171.2 \pm 2.1$	$\tau$ (tau)	-1	1.776
	<i>b</i> (bottom)	-1/3	$4.20_{-0.07}^{+0.17}$	$\nu_\tau$ ( $\tau$ -neutrino)	0	$< 2.10^{-2}$

**Table 2.1:** The properties of the fundamental fermions (quarks and leptons,  $spin = \frac{1}{2}$ ) of the SM. The anti-particle partners of these fermions (not included in the table) have the same mass (M), but with the opposite electric charge (Q). Q is given in units of the proton charge [4].

flavor. The electron ( $e$ ), muon ( $\mu$ ) and tau ( $\tau$ ) particles each have an associated low mass, chargeless neutrino. Leptons are also grouped into singlets and doublets:

$$\begin{pmatrix} e \\ \nu_e \end{pmatrix}_L, \begin{pmatrix} \mu \\ \nu_\mu \end{pmatrix}_L, \begin{pmatrix} \tau \\ \nu_\tau \end{pmatrix}_L, e_R, \mu_R, \tau_R. \quad (2.2)$$

The neutrinos, neutral leptons, are considered to be massless within the SM, however, it has been shown that the neutrinos cannot be massless [5, 6, 7, 8, 9, 10]. The electron, like the proton, is a stable particle and is present in almost all matter. The  $\mu$  and  $\tau$  particles are unstable and are found primarily in cosmic rays.

Important ingredients of the SM are the intermediate gauge bosons, or the carriers of force. Table 2.2 lists the fundamental forces and their carriers. The gauge bosons transmit three of the four fundamental forces through which matter interacts. The gluon ( $g$ ) is responsible for the strong force, which binds together quarks inside protons and neutrons, and holds together protons and neutrons inside atomic nuclei. The photon ( $\gamma$ ) is the electromagnetic force carrier that governs electron orbits and chemical processes. Photon couples to all electric charge. Lastly, the weak force is mediated by  $W^\pm$  and  $Z^0$  bosons responsible for radioactive decays. The weak force couples to quarks as well as leptons. Neutrinos, in fact, are coupled only via weak force. Due to the lack of electric charge, neutrinos do not interact via the strong or the electromagnetic force, and therefore interact with matter only via the weak interactions. Within the SM, theories of electromagnetic and of weak interactions are unified to the Electroweak theory by Glashow, Salam and Weinberg [11, 12, 13].

The SM includes the strong, electromagnetic and weak forces and all their carrier particles, and describes how these forces act on all the matter particles. However, the fourth force, gravity, is not part of the SM. In fact, attempts have been made to describe gravity as a quantum field theory, with the interaction mediated by a spin-2 boson, the *graviton*, associated to the gravitational field. Such extensions of the SM, however, need also an adapted description of the SM itself, because of problems such as non-renormalizability.

Force	Force Carriers	Coupling	Relative Strength	Mass (GeV)	Spin
Strong	$g$ (gluon)	quarks and gluons	1	0	1
Electromagnetic	$\gamma$ (photon)	quarks, $W^\pm$ and charged leptons	$1.4 \times 10^{-2}$	$< 3 \times 10^{-36}$	1
Weak	$W^\pm, Z^0$	quarks and leptons	$2.2 \times 10^{-6}$	80, 91	1
Gravitational	graviton	massive particles	$10^{-38}$	0	2

**Table 2.2:** The fundamental forces and force carriers, i.e. *gauge bosons*. Three kinds of fundamental forces are combined in the SM. The fourth fundamental interaction, gravity, is shown separately as it is not yet included in the SM [4].

The gravitational force does not play a significant role in atomic and subatomic processes because of its weakness compared to the SM scales.

Although the SM explains the interactions among quarks, leptons, and bosons, the theory does not include an important property of elementary particles, their mass. In 1964 Francois Englert and Robert Brout [14], in October of the same year Peter W. Higgs [15], and independently Gerald Guralnik, Carl R. Hagen, and Tom Kibble [16], proposed a mechanism that provided a way to explain how the fundamental particles could acquire mass. The theory states that the whole of space is permeated by a scalar field, now called the Higgs field, similar to the electromagnetic field. As particles move through space they travel through this field, and by coupling to it they acquire mass. The particle associated with the Higgs field is the Higgs boson, a particle with no intrinsic spin or electrical charge. The Higgs boson does not mediate a force as do the other gauge bosons. It has not been observed yet. Finding it is the key to discover whether the Higgs field exists, and whether the Higgs mechanism for the origin of mass is indeed correct. Detectors at Fermilab and eventually at the LHC<sup>1</sup> at CERN<sup>2</sup> are looking for the elusive Higgs particle.

## 2.2 Deep Inelastic Scattering

One of the most useful experimental techniques to study the internal structure of hadrons is the scattering of leptons on a hadronic target, typically a proton or a heavier nucleus. The process is called *elastic* when only the electron and the target particle (e.g. proton) appear in the final state, i.e.  $ep \rightarrow ep$ . In *inelastic* processes more hadronic particles are produced in the final state. When the momentum transfers are very large, an inelastic process is called *deep inelastic scattering* (DIS). In this case the target particle loses its identity completely and the resulting final state is a multiparticle state. The study of such states allows to gain insight into the internal structure of the hadron in the initial

<sup>1</sup>Large Hadron Collider

<sup>2</sup>Conseil Européen pour la Recherche Nucléaire

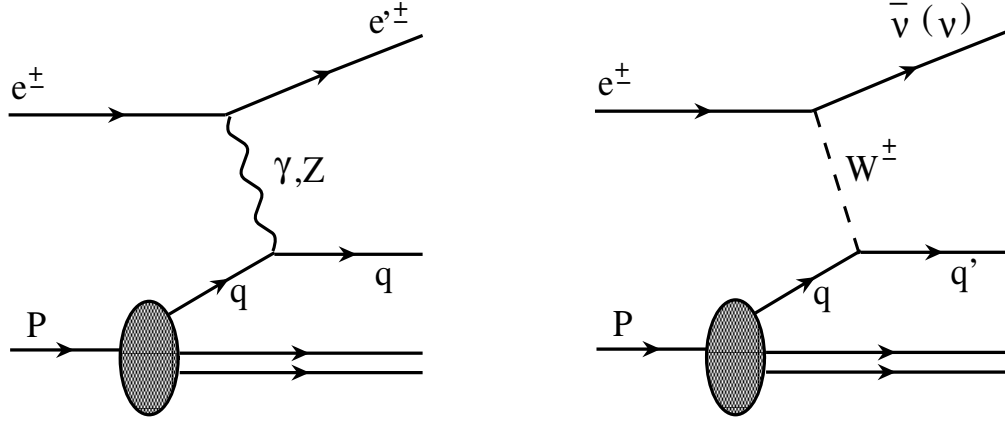


**Figure 2.1:** Leading order Feynman diagrams of inelastic electron proton scattering. The electron interacts with the proton via the exchange of a  $\gamma$  or  $Z^0$  boson (NC interactions, left), or a charged  $W^\pm$  boson (CC interactions, right).

state which is the proton in the case of HERA physics.

The interaction between an electron and a proton can be described via neutral current (NC) or charged current (CC) interactions which are the two contributing processes to DIS at HERA. Fig. 2.1 illustrates NC and CC processes in  $ep$  scattering in the form of Feynman diagrams. In NC interactions,

$$e^\pm p \rightarrow e^\pm X, \quad (2.3)$$

the interaction between the electron and the proton is mediated by a  $\gamma$  or a  $Z^0$ . In CC interactions,

$$e^\pm p \rightarrow \nu X, \quad (2.4)$$

a charged  $W^\pm$  boson is exchanged. In both interactions,  $X$  represents the hadronic final state. Both DIS processes are directly observed at HERA.

### 2.2.1 Kinematic Description

The kinematics of DIS are defined by Lorentz invariant event variables. Let  $\mathbf{k}$ ,  $\mathbf{k}'$ ,  $\mathbf{q}$  and  $\mathbf{P}$  denote the four momenta of the incoming lepton, the outgoing lepton, the four momenta of the exchanged boson and the momentum of the proton, respectively. Then the following kinematical variables can be defined :

- the virtuality of the exchanged boson,

$$Q^2 = -q^2 = -(\mathbf{k} - \mathbf{k}')^2, \quad (2.5)$$

- the fraction of the incoming proton momentum taking part in the scattering is called Bjorken scaling variable,

$$x = \frac{Q^2}{2\mathbf{P} \cdot \mathbf{q}}, \quad (2.6)$$

- the inelasticity which is the relative energy transfer from the lepton to the proton,

$$y = \frac{\mathbf{P} \cdot \mathbf{q}}{\mathbf{P} \cdot \mathbf{k}}. \quad (2.7)$$

In the proton rest frame, the inelasticity  $y$  can be expressed as:

$$y \approx 1 - \frac{E'_e}{E_e} \sin^2 \frac{\theta_e}{2}, \quad (2.8)$$

where  $E_e$  is the energy of incoming electron,  $E'_e$  is the energy of outgoing electron and  $\theta_e$  is the angle between the incoming and outgoing electron.

- the centre of mass energy  $s$  of the  $ep$  system,

$$s = (\mathbf{P} + \mathbf{k})^2 \approx 4E_e E_p + m_e^2 + m_p^2 \approx 4E_e E_p \approx \frac{Q^2}{xy}, \quad (2.9)$$

where  $E_p$  is the energy of incoming proton,  $m_e$  is the mass of the electron, and  $m_p$  is the mass of the proton.

- the centre of mass energy of the  $\gamma p$  system, or the invariant mass of the hadronic system recoiling against the scattered lepton,

$$W^2 = (P + q)^2 = P^2 + q^2 + 2P \cdot q \approx sy - Q^2. \quad (2.10)$$

The variables  $x$  and  $y$  are dimensionless and have values in the interval  $[0, 1]$ . In the quark-lepton centre of mass frame, the scattered electron and the quark are deflected by angle  $\theta_e$ . In this frame an event with  $y = 1$  corresponds to one in which the electron has scattered with  $\theta_e = \pi$ . In the rest frame of the proton, inelasticity  $y$  is a measure for the energy fraction of the scattered electron lost after interacting with the proton.

Experimentally the inelastic scattering processes are classified in two kinematical regimes. *Photoproduction* ( $Q^2 \approx 0$ ) processes where a quasi-real photon is exchanged and DIS ( $Q^2 \geq 1 \text{ GeV}^2$ ) where a virtual photon (or a  $Z^0$ ) is exchanged. The classification is done experimentally via the detection of the scattered electron in the detector.

## 2.3 The Quark Parton Model

In the Quark Parton Model (QPM) [17], the proton is assumed to be composed of point-like, non-interacting, spin-1/2 constituents (*partons*) that can be associated to the quarks. The inelastic scattering of the lepton off the proton is then viewed as the elastic scattering of the lepton off a parton within the proton. The cross section of  $ep$  scattering is given by the incoherent sum of the  $e$ -parton scattering processes. In the *infinite momentum frame*, ( $P^2 \gg m_p^2$ ), the transverse momenta of the quarks can be neglected and the proton is considered as a parallel stream of quasi-free partons. In Bjorken's picture, in the limit of high energies and  $Q^2 \rightarrow \infty$  but  $x$  finite, the structure function  $F_2$  depends only on  $x$

$$F_2(x, Q^2) \rightarrow F_2(x). \quad (2.11)$$

Thus, according to QPM the structure function  $F_2$  must be scale invariant, i.e., it does not depend on  $Q^2$  but only on  $x$ . This effect is referred to as *Bjorken scaling* [18]. The predictions of Bjorken scaling were confirmed by DIS experiments taking place at SLAC<sup>3</sup> [19, 20]. Let the probability of finding a parton of species  $i$  carrying a momentum fraction of the proton  $x$  be  $f_i$ , then the QPM predicts that

$$\sum_i \int x f_i(x) dx = 1, \quad (2.12)$$

where the summation runs over all parton flavours. The structure functions can then be written as

$$F_2(x) = \sum_i e_i^2 x q_i(x), \quad (2.13)$$

$$F_L(x) = 0, \quad (2.14)$$

where  $e_i$  is the charge of a parton  $i$  and  $F_L$  is the longitudinal structure function which is related to the exchange of longitudinally polarised photons. Experimental results have shown that the value of summing over all the charged partons is  $\sim 0.5$  which indicates that the rest of the proton momentum is carried by electrically neutral but strongly interacting partons, the *gluons* which are not part of the QPM. In 1979, the observation of 3-jet events in  $e^+e^-$  annihilation at DESY provided first direct evidence for the existence of gluons [21]. In addition, the QPM does not explain other experimental results like logarithmic violation of the scaling behaviour, non-zero longitudinal structure function, quark confinement, etc. These effects were successfully explained within the framework of Quantum Chromodynamics.

---

<sup>3</sup>Stanford Linear Accelerator Centre

## 2.4 Cross Section for Deep Inelastic $ep$ Scattering

In terms of Lorentz invariant variables the differential cross section for inelastic electron-proton scattering can be written as [22]:

$$\frac{d\sigma_{NC}^{\pm}}{dx dQ^2} = \frac{2\pi\alpha^2}{xQ^4} \left[ xy^2 F_1(x, Q^2) + (1-y)F_2(x, Q^2) \pm y \left(1 - \frac{y}{2}\right) xF_3(x, Q^2) \right]. \quad (2.15)$$

Using the helicity dependence of the electroweak interaction

$$Y_{\pm} = 1 \pm (1-y^2), \quad (2.16)$$

and the relation

$$F_L(x, Q^2) = F_2(x, Q^2) - 2xF_1(x, Q^2), \quad (2.17)$$

equation 2.15 can be rewritten as:

$$\frac{d\sigma_{NC}^{\pm}}{dx dQ^2} = \frac{2\pi\alpha^2}{xyQ^2} [Y_+ F_2(x, Q^2) \pm Y_- F_3(x, Q^2) - y^2 F_L(x, Q^2)]. \quad (2.18)$$

For spin 1/2 particles Eq. 2.17, known as the Callan-Gross relation [23], is equal to zero as long as the quark masses and the intrinsic transverse momenta are neglected [24]. The factors  $F_1(x, Q^2)$ ,  $F_2(x, Q^2)$ ,  $F_3(x, Q^2)$ , and  $F_L(x, Q^2)$  are the *proton structure functions* which have to be determined by measurements.  $F_2$  is the generalised structure function of the  $\gamma$  and  $Z^0$  exchange,  $F_L$  is the longitudinal structure function and  $F_3$  arises from  $Z^0$  exchange. The  $F_3$  structure function has only a small effect at  $Q^2 \ll M_{Z^0}^2$  and hence can be neglected here. The structure functions are related to the cross sections ( $\sigma_T$ ,  $\sigma_L$ ) for transversely and longitudinally polarised exchanged bosons according to

$$F_2(x, Q^2) = \frac{Q^2}{4\pi\alpha^2} [\sigma_T(x, Q^2) + \sigma_L(x, Q^2)], \quad (2.19)$$

$$F_L(x, Q^2) = \frac{Q^2}{4\pi\alpha^2} \sigma_L(x, Q^2). \quad (2.20)$$

Since the cross sections  $\sigma_L$  and  $\sigma_T$  have to be positive, these two relations imply that:

$$0 \leq F_L \leq F_2. \quad (2.21)$$

From Eq. 2.21 and the fact that the  $F_L$  term is proportional to  $y^2$  in Eq. 2.18, it can be seen that the  $F_2$  term is dominant in regions of low  $y$ , whereas the  $F_L$  term becomes more important as  $y$  increases. Therefore,  $F_L$  needs only to be taken into account at very high values of  $y$ . The  $F_L$  contribution will be neglected in the following discussions, since the

majority of the HERA data resides at low  $y$ . The structure function  $F_2$  has been measured in a wide range of the photon virtuality  $Q^2$  and  $x$ . Fig. 2.2 presents a compilation of the measurements of  $F_2$  (H1, BCDMS and NMC) as a function of  $Q^2$  for different values of  $x$  [25]. The scaling behaviour of  $F_2$ , i.e. independence of  $Q^2$ , can be seen in the region for values of  $x$  about 0.13. In all other  $x$ -regions  $F_2$  depends logarithmically on  $Q^2$ .

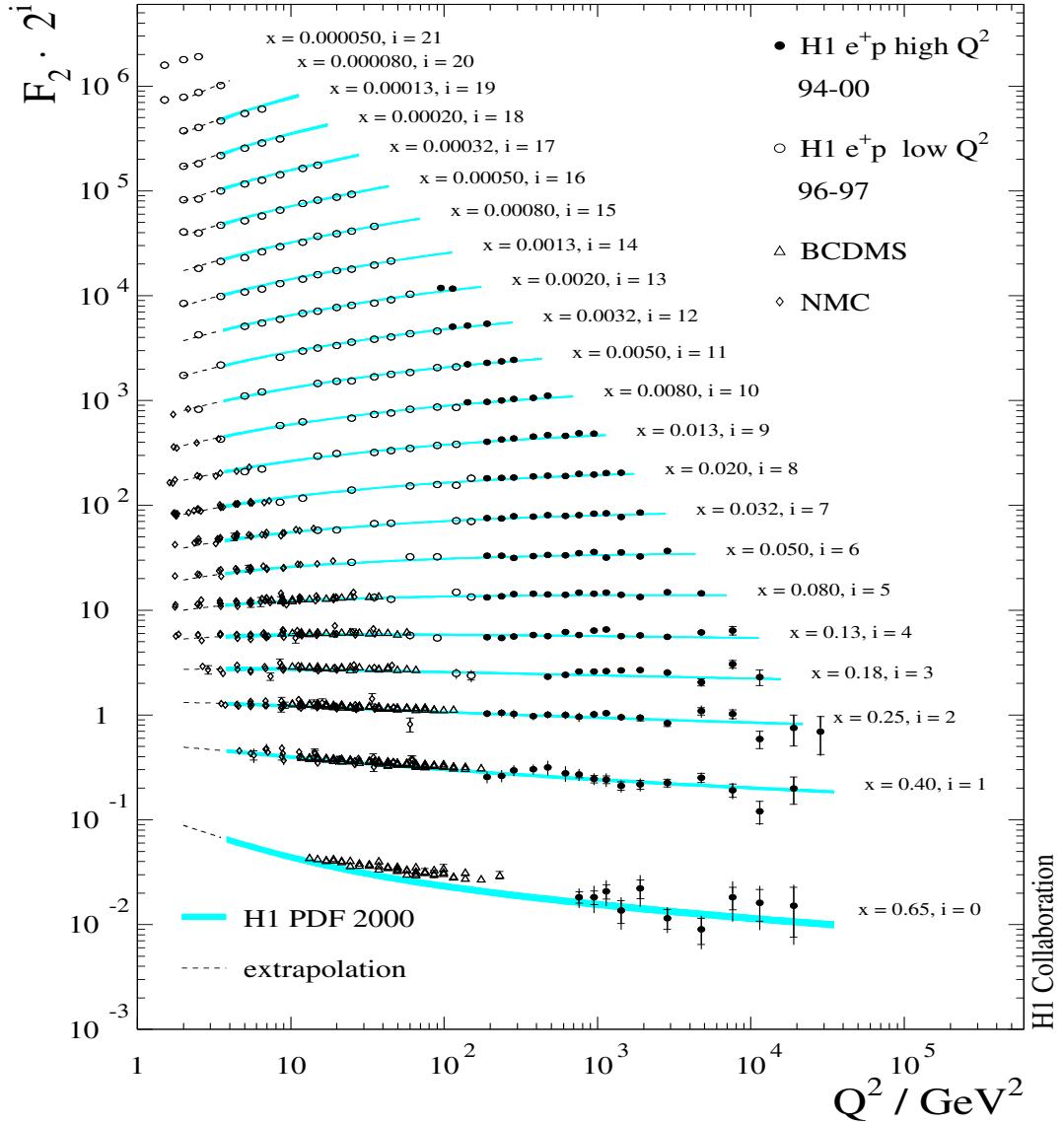


**Figure 2.2:** The proton structure function  $F_2$  shown for the data from the collider experiment H1 and the fixed target experiments BCDMS and NMC. The results are compared to the SM prediction determined from the H1 PDF 2000 fit. The measurements at different  $x$  values are displaced vertically by a factor  $2^i$ . The figure is taken from [25].

## 2.5 Quantum Chromodynamics

Quantum Chromodynamics (QCD) is the field theory of strong interactions which are one of the fundamental forces in nature and occur either between quarks and gluons or between gluons and gluons. The strong force involves a new quantum number called *colour charge*. Quarks carry one of three possible colour (or anti-colour) charges: e.g. red ( $r$ ), green ( $g$ ) and blue ( $b$ ). Gluons also carry color charge but in the combinations of one colour and one anti-colour (e.g.  $r\bar{g}$ ). Two important features arising from the QCD are asymptotic freedom and confinement.

- **Asymptotic freedom** : The mediators of strong interaction, gluons, unlike the photons of QED, can couple to each other with a coupling constant  $\alpha_s$ . Asymptotic freedom states that the strength of the interaction, or magnitude of the coupling, decreases at short distances and increases at large distances. In the *short distance* limit, quarks and gluons can be treated as *free* particles since their coupling is small, and the applicability of perturbation theory is restored [22]. This property of QCD, asymptotic freedom, was discovered by Wilczek, Gross and Politzer in 1973 [26, 27]. They showed that every non-Abelian SU(3) gauge theory exhibits asymptotic freedom, i.e. a decrease of the coupling constant with increasing energies, thus making QCD a realistic candidate for describing strong interactions.
- **Confinement (Infrared slavery)** : Conversely, the strong coupling  $\alpha_s$  becomes stronger as the separation between  $q$  and  $\bar{q}$  increases and perturbation theory breaks down at low  $Q^2$ . Because of the gluon self-coupling, the exchanged gluons will attract each other (unlike photons) and so the colour lines of force get constrained to a tube-like region (called *flux tube*) between the quarks. If this tube has a constant energy density per unit length, then the potential energy of the interaction will increase with the separation, so the quarks and gluons can never escape the hadron. This is the origin of the *confinement* (i.e. *infrared slavery*) and explains why free quarks are not observed [28].

## 2.6 Renormalisation

In order to calculate QCD cross sections, integrations have to be performed over the entire phase space of real and virtual quarks and gluons. These integrals lead to divergent expressions. A scheme called *regularisation* is therefore defined to leave out the divergent parts of the integrals. As a result, the calculated cross-sections then depend on the renormalisation energy scale  $\mu_r^2$ . Since  $\mu_r^2$  is not a prediction of the theory, it has to be chosen. The dependency on  $\mu_r^2$  is compensated by defining an effective coupling constant  $\alpha_s$ . This leads to a dependence of the renormalised  $\alpha_s$  on  $\mu_r^2$ . When all orders of  $\alpha_s$  are taken into account, any physical observable  $R$  must be independent of the choice for  $\mu_r^2$ . For any truncated calculation, the dependence of  $R$  on  $\mu_r^2$  must be canceled by the dependence of  $\alpha_s$  on  $\mu_r^2$ .

This is expressed by the *renormalisation group equation* (RGE)

$$\mu_r^2 \frac{dR}{d\mu_r^2} = \left( \mu_r^2 \frac{\partial}{\partial \mu_r^2} + \mu_r^2 \frac{\partial \alpha_s}{\partial \mu_r^2} \frac{\partial}{\partial \alpha_s} \right) R = 0. \quad (2.22)$$

The partial derivative  $\partial \alpha_s / \partial \mu_r^2$  in Eq. 2.22 can be used to compute the dependence of the strong coupling constant  $\alpha_s$  on  $\mu_r^2$

$$Q^2 \frac{\partial \alpha_s}{\partial Q^2} = \beta(\alpha_s) = -\alpha_s \sum_{n=0}^{\infty} \beta_n \left( \frac{\alpha_s}{4\pi} \right)^{n+1} = -\frac{\beta_0}{4\pi} \alpha_s^2(Q^2) - \frac{\beta_1}{16\pi^2} \alpha_s^3 + O(\alpha_s^4), \quad (2.23)$$

where the coefficients  $\beta_0$  and  $\beta_1$  depend on the number of active quark flavours  $n_f$  (i.e. the quark flavours with masses smaller than  $\mu_r^2$ ) and scale  $Q^2$  as

$$\beta_0 = 11 - \frac{2}{3}n_f, \quad (2.24)$$

$$\beta_1 = 102 - \frac{38}{3}n_f. \quad (2.25)$$

The running constant  $\alpha_s$  can be written in terms of the renormalisation scale in the one-loop approximation as

$$\alpha_s(\mu_r^2) = \frac{4\pi}{\beta_0 \log(\mu_r^2 / \Lambda_{QCD}^2)}, \quad (2.26)$$

where  $\Lambda_{QCD}^2$  is a fundamental parameter of QCD which cannot be calculated. Fig. 2.3 shows the running of the coupling constant  $\alpha_s$  with scale  $\mu_r = Q$  [29]. The depicted experimental results show that  $\alpha_s$  indeed decreases with increasing  $\mu_r$  which is also seen in more recent data from HERA [30,31]. The coupling constant  $\alpha_s$  diverges in the limit of  $\mu_r^2 \rightarrow \Lambda_{QCD}^2$  and perturbative QCD theory breaks down. Thus,  $\Lambda_{QCD}^2$  provides an approximate boundary energy scale between perturbative and non-perturbative QCD.

## 2.7 Factorisation

The *factorisation theorem* in QCD [32] states that for the hard scattering process the interaction can be factorised into two processes, a *soft* and a *hard* one. The hard process (i.e. *short-range*) describes the interaction of high energy partons and can be calculated within perturbative QCD. For the soft process (i.e. *long-range*) perturbative calculations are not applicable. Within this framework, the proton structure function  $F_2$  can be

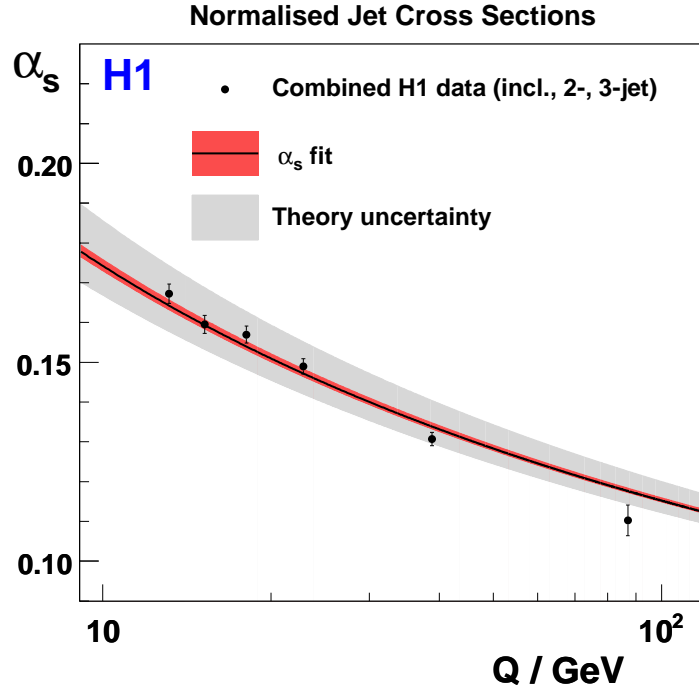


**Figure 2.3:** The strong coupling constant  $\alpha_s$  with scale  $\mu = Q$ . The solid line shows two loop solution of the renormalisation group equation obtained by evolving the  $\alpha_s(M_Z)$  extracted from a simultaneous fit of 54 measurements of the normalised inclusive jet cross section as a function of  $Q^2$  and  $P_T$ , the normalised 2-jet cross section as function of  $Q^2$  and  $\langle P_T \rangle$  and the normalised 3-jet cross section as function of  $Q^2$  [29].

written as a convolution of the parton density functions (PDF)  $f_{i/p}(\xi)$ , which can be interpreted as the probability of finding a parton of type  $i$  carrying a fraction  $\xi$  of the proton's longitudinal momentum, and perturbatively calculable coefficient functions  $C_i$ ,

$$F_2(x, Q^2) = x \sum_{i=q, \bar{q}, g} \int_x^1 d\xi f_{i/p}(\xi, \mu_r^2, \mu_f^2) \cdot C_i \left( \frac{x}{\xi}, \frac{Q^2}{\mu_r^2}, \frac{\mu_f^2}{\mu_r^2}, \alpha_s \right). \quad (2.27)$$

Here,  $\mu_f$  is the factorisation scale which defines the separation between soft (non-perturbative) and hard (perturbative) processes. Processes with  $Q > \mu_f$  are perturbatively calculable and absorbed in the hard scattering coefficients  $C_i$ , while processes with  $Q < \mu_f$  lie outside the perturbative regime and contained in the PDF  $f_{i/p}$ . The coefficient functions  $C_i$  do not depend on the type of hadron but on the parton flavour  $i$  and on the exchanged boson, and therefore are process independent. Because the coefficient functions have been calculated only up to  $O(\alpha_s^2)$  for the inclusive  $ep$  cross section, the calculated cross sections as well as the parton distribution functions exhibit dependences on the choices of the renormalisation and factorisation scales [33].

## 2.8 Evolution of Partons

A calculation from first-principles of the parton distributions  $f_{i/p}$  is beyond the scope of perturbative QCD and  $f_{i/p}$  should be extracted from the experimental measurements. Nevertheless, the dependence of  $f_{i/p}$  on  $\mu_f$  can be studied within the framework of perturbative QCD since the cross section must not depend on the parameter  $\mu_f$ . This leads to the *parton evolution equations* which are used to evolve parton density functions, which have been assumed at a certain starting scale  $\mu$ , up to the factorisation scale  $\mu_f$ . In order to solve the parton evolution equations some QCD approximations are commonly used which are expected to be valid only in certain regions of phase space. In the context of perturbative QCD, the evolution equations contain terms of order  $(\alpha_s \log Q^2)$  and  $(\alpha_s \log \frac{1}{x})$ . The parton evolution equations can be obtained by gluon splitting and gluon radiation processes which lead to the *gluon ladder*. The *ladder diagram* of gluon emissions is shown in Fig. 2.4. In the following the two main approximations are described.

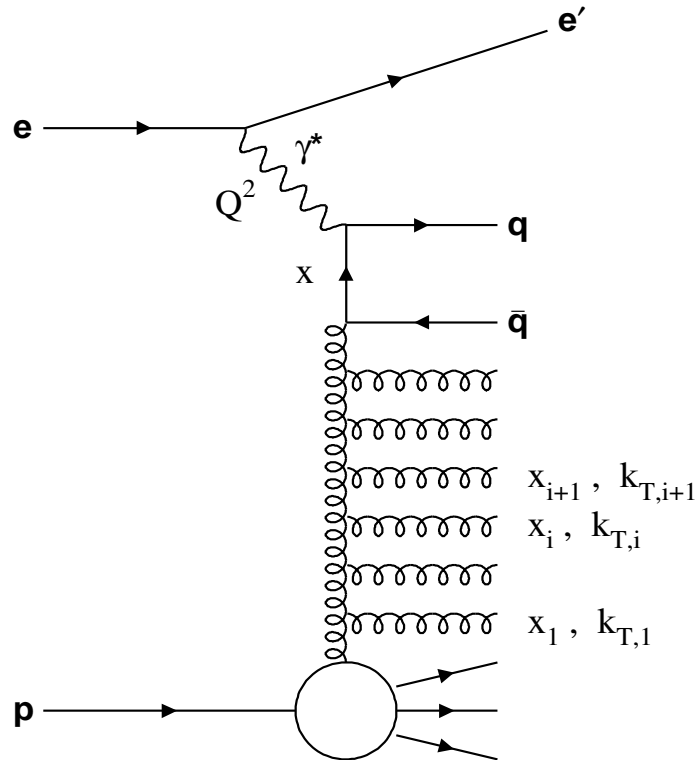


**Figure 2.4:** A schematic overview of the *gluon ladder diagram* of the parton evolution in *ep* scattering. A quark from the proton interacts with a virtual photon from the electron after radiating  $n$  gluons. The transverse and longitudinal momenta of the each emitted gluons are labelled as  $k_{T,i}$  and  $x_i$ .

### 2.8.1 DGLAP Evolution Equations

The Dokshitzer-Gribov-Lipatov-Altarelli-Parisi (DGLAP) evolution equations [34, 35, 36, 37, 38] define the way in which gluon and quark momentum distributions in the hadron evolve with the scale of the interaction  $Q^2$ . Within the DGLAP approach, a strong ordering of the transverse momenta  $k_{T,i}^2$

$$Q^2 \gg k_{T,i}^2 \gg k_{T,i-1}^2 \gg k_{T,i-2}^2 \dots \gg k_{T,1}^2 \gg Q_0^2, \quad (2.28)$$

and a soft ordering of the fractional longitudinal momenta  $x_i$

$$x_i < x_{i-1} < x_{i-2} < \dots < x_1, \quad (2.29)$$

are assumed. Here  $Q_0^2$  is the virtuality of the parton at the start of the emission cascade and  $Q^2$  the virtuality of the exchanged photon.

The DGLAP evolution equations which are typically written in the form of integro-differential equations are given by,

$$\frac{dq_i(x, Q^2)}{d \log Q^2} = \frac{\alpha_s(Q^2)}{2\pi} \int_x^1 \frac{dy}{y} \left[ \sum_i q_i(y, Q^2) P_{qq} \left( \frac{x}{y} \right) + g(y, Q^2) P_{qg} \left( \frac{x}{y} \right) \right], \quad (2.30)$$

$$\frac{dg(x, Q^2)}{d \log Q^2} = \frac{\alpha_s(Q^2)}{2\pi} \int_x^1 \frac{dy}{y} \left[ \sum_i q_i(y, Q^2) P_{gq} \left( \frac{x}{y} \right) + g(y, Q^2) P_{gg} \left( \frac{x}{y} \right) \right], \quad (2.31)$$

where  $q_i$  and  $g$  denote the quark density function of the flavour  $i$  and gluon density function, respectively and  $P_{ij}$  are the *splitting functions* of a parton  $i$  to parton  $j$  with the momentum fraction  $\left(\frac{x}{y}\right)$ , depicted in Fig. 2.5. These splitting functions give the probabilities of a parton  $j$  of momentum fraction  $y$  emitting a parton  $i$  of momentum fraction  $x$  in the interval of virtualities  $Q^2 \rightarrow Q^2 + d \log Q^2$ . Eq. 2.30 describes the change of the quark densities with  $Q^2$  due to gluon radiation and gluon splitting whereas Eq. 2.31 describes the change of the gluon density with  $Q^2$  due to gluon radiation off quarks and gluons. Both equations assume massless partons and are hence only valid for gluons and light quarks ( $u, d$  and  $s$ ). The splitting functions for each of these processes are given at the leading order by

$$P_{qq}(z) = \frac{4}{3} \left( \frac{1+z^2}{1-z} \right), \quad (2.32)$$

$$P_{gq}(z) = \frac{4}{3} \left( \frac{1+(1-z)^2}{z} \right), \quad (2.33)$$

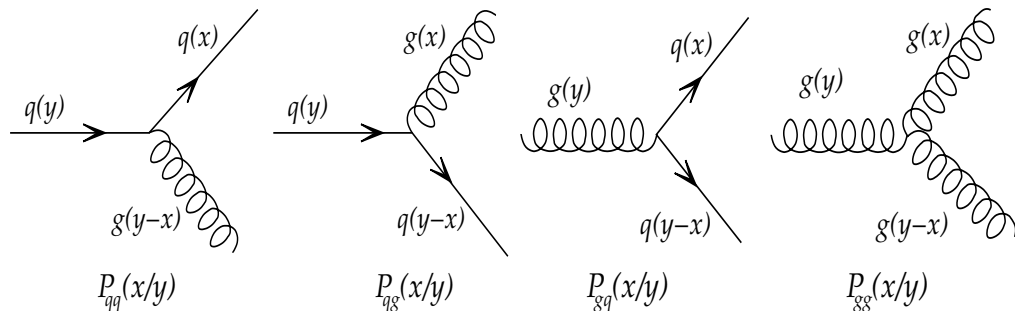


**Figure 2.5:** The splitting functions  $P_{jk}$  used for the DGLAP approximation. From left to right, the processes  $q \rightarrow qq$ ,  $q \rightarrow gq$ ,  $g \rightarrow q\bar{q}$  and  $g \rightarrow gg$  are shown.

$$P_{qg}(z) = \frac{1}{2}(z^2 + (1 - z^2)^2), \quad (2.34)$$

$$P_{gg}(z) = 6 \left( \frac{z}{1-z} + \frac{1-z}{z} + z(1+z) \right), \quad (2.35)$$

where the terms  $1/(1-z)$  and  $1/z$  are called singular terms since they give infinite contributions as  $z \rightarrow 1$  and  $z \rightarrow 0$ , respectively.

The DGLAP equations only describe strongly  $k_T$  ordered ladder diagrams and may therefore become inaccurate at very low  $x$ . But no strong experimental evidence of a breakdown of the DGLAP approximation at low  $x$  has been observed so far, although some data on the hadronic final state are not well described by calculations based on the DGLAP equations.

### 2.8.2 BFKL Evolution Equations

The DGLAP equations neglect terms of the form  $\log(1/x)$  which may become large as  $x$  becomes small. Summation of such contributions leads to unintegrated gluon distributions (dependent of the transverse momentum  $k_T$ ), which obey the Balitsky-Fadin-Kuraev-Lipatov (BFKL) [39, 40] approximation. In the framework of the unintegrated gluon distribution, predictions for the measured cross sections are calculated using the  $k_T$ -factorisation theorem [41]. Cross sections are factorised into an off-shell ( $k_T$  dependent) partonic cross section and a  $k_T$ -unintegrated parton distribution. The BFKL approximation allows the summation of terms with leading powers of  $\alpha_s \log \frac{1}{x}$  in the regime of very low  $x$  and moderate  $Q^2$ . In this approach, a strong ordering of the fractional longitudinal momentum  $x_i$

$$x_i \ll x_{i-1} \ll x_{i-2} \ll \dots \ll x_1, \quad (2.36)$$

and no ordering on the transverse momenta  $k_T$  along the ladder are assumed. The result-

ing BFKL evolution equation is given by

$$\frac{\partial f_{g/p}(x, k_T^2)}{\partial \log(1/x)} = \frac{3\alpha_s}{\pi} k_T^2 \int_0^\infty \frac{dk_T'^2}{k_T'^2} \left[ \frac{f_{g/p}(x, k_T'^2) - f_{g/p}(x, k_T^2)}{|k_T'^2 - k_T^2|} + \frac{f_{g/p}(x, k_T^2)}{\sqrt{4k_T'^4 + k_T^4}} \right]. \quad (2.37)$$

The terms within the brackets of Eq. 2.37 correspond to the real gluon emissions and virtual corrections, respectively. The BFKL equation gives the evolution of  $f_{g/p}(x, k_T^2)$  with respect to small  $x$ . It can be solved for any small  $x$  and  $k_T^2$  once  $f_{g/p}(x, k_T^2)$  is known for some starting value  $x_0$ . For fixed  $\alpha_s$ , the equation 2.37 can be solved and the result is

$$f(x, k_T^2) = F(x, k_T^2) \left( \frac{x}{x_0} \right)^{-\lambda}, \quad (2.38)$$

where  $\lambda = \frac{3\alpha_s}{\pi} 4 \log 2$  and  $F(x, k_T^2)$  is an unintegrated gluon distribution. Hence, this approximation predicts that the gluon density increases proportional to  $(1/x)^{-\lambda}$  as  $x$  decreases.

### 2.8.3 CCFM Evolution Equations

Both the DGLAP and the BFKL methods only sum over one particular leading behaviour of the evolution to obtain results. A complete (infinite order) calculation should take into account both, the terms in  $\log(Q^2)$  and  $\log(\frac{1}{x})$  and sum over them. To accomplish this, Ciafaloni [42] and Catani, Fiorani and Marchesini [43] introduced angular ordering for the emitted gluons. The maximum allowed angle is defined by the hard scattering, where the quark pair is produced (see Fig. 2.4). This is combined with unintegrated gluon densities and off-shell partons, like in the BFKL approach. This method seems very promising, as it can (approximately) reproduce the DGLAP and BFKL equations within the appropriate limits. However, this approach is incomplete. Currently, it does not include the quark contribution in the evolution.

# Chapter 3

## Strangeness Physics

Perturbative QCD (pQCD) can be applied in an energy regime where  $\alpha_s$  is small. It is very successful in describing the hard scattering and hard QCD radiation processes in which large momentum transfers are involved. However, it breaks down in processes where  $\alpha_s \sim 1$  and low momentum transfers, for instance in the hadronisation process where the final state hadrons are formed from quarks.

At HERA, the direct production from the hard interaction of photons and gluons dominates the production of heavy quarks i.e. charm, beauty and top. Therefore pQCD can be applied in this case. On the other hand, the production of the *strange quark* can either come from hard interactions or from pure fragmentation processes. Therefore the fragmentation process becomes important for strangeness production. In this chapter, the strange particles which are the subject of this thesis and some of their characteristic properties are introduced. The different production mechanisms by which strange particles are produced will be summarised. Finally an overview of existing measurements will be presented.

### 3.1 Characteristics of Strange Particles

The first strange particle, the  $K$ -meson, was discovered in cosmic rays in 1947 [44]. Although strange particles interact through the strong force, the strange ( $s$ ) quark itself can decay only by conversion to a quark of different type (such as  $u$  or  $d$ ) through weak interactions. For this reason, the lightest strange particles have very long lifetimes, of the order of  $10^{-10}$  s, compared to the lifetimes of the order of  $10^{-23}$  s for particles which decay via the strong interactions. In 1952, Abraham Pais hypothesised that the strange particles are always produced in pairs [45]. The prediction was confirmed one year later at the BNL<sup>1</sup> [46]. The observed long lifetime was the origin of the term *strange* particles. This stability was an important clue for the presence of quarks inside strongly interacting particles, and was one motivation for the development of the quark model in 1964 [47, 48].

---

<sup>1</sup>Brookhaven National Laboratory

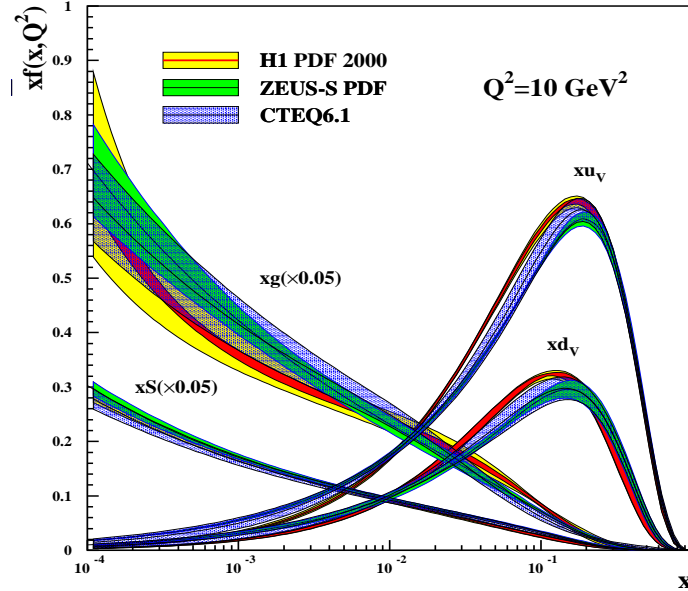


**Figure 3.1:** The parton densities for the valence quarks  $u$ ,  $d$ , and the sea  $S$  quarks and gluons inside the proton are extracted by the H1 and ZEUS collaborations at  $Q^2 = 10 \text{ GeV}^2$  [49]. The bands represent estimates of the experimental and theoretical uncertainties. Sea quark  $S$  and gluon densities are scaled down by a factor of 0.05.

Within the quark model such long lifetimes were explained by introducing a new quantum number, *strangeness* which is conserved in strong and electromagnetic interactions, denoted as  $\mathbf{S}$ . Strangeness is a property of particles, expressed as a quantum number for the description of particle decays in strong and electromagnetic reactions. The strangeness of a particle is defined as

$$S = N_{\bar{s}} - N_s, \quad (3.1)$$

where  $N_{\bar{s}}$  represents the number of strange anti-quarks ( $\bar{s}$ ) and  $N_s$  the number of strange quarks contained in the particle. Strange quarks have the strangeness quantum number  $S = -1$  while strange anti-quarks get  $S = +1$ .

Bound states of quarks, in which at least one of the constituents is of the strange type, are called *strange hadrons*. The  $s$ -quark is heavier than the up ( $u$ ) and down ( $d$ ) quarks. However, the  $s$ -quark is certainly not heavy enough to provide a new hard scale as do the masses of the charm and beauty quarks. Owing to its low mass ( $104_{-35}^{+26} \text{ MeV}$  [50]), it is produced in abundance, in a variety of ways in the  $ep$  collisions at HERA. As was illustrated in Fig. 3.1 the proton itself contains significant amounts of sea quarks, from the splitting of gluons to quark-antiquark pairs. Of these,  $\sim 30\%$  will be strange quarks [25]. The splitting of the interacting photon into a strange-antistrange quark pair is another possible source of strange quarks.

## 3.2 Strange Hadrons

According to the quark model, hadrons are colourless composites of two families called *mesons* and *baryons*. Some of the hadrons and their quark contents are listed in Table 3.1. The objects investigated in this thesis are *strange hadrons*, containing one strange quark ( $s$ ) or anti-quark ( $\bar{s}$ ). Mesons can be classified by their quark contents  $q\bar{q}$  and their total angular momentum

$$J = L + S, \quad (3.2)$$

where  $L$  is the orbital angular momentum of the meson with integer values  $L = 0, 1, 2, \dots$  and  $S$  is the meson spin  $S = 0, 1$ . The wave function of the  $q\bar{q}$  state has an important property called parity  $P = (-1)^{L+1}$ . The mesons with  $L = 0$  are classified as *pseudoscalar* and *vector mesons*. Pseudoscalar mesons have total spin 0 and odd parity ( $J^P = 0^-$ ) whereas vector mesons have total spin 1 and odd parity ( $J^P = 1^-$ ).

Baryons		Mesons	
Symbol	Quark Content	Symbol	Quark Content
$p$	$uud$	$\pi^+$	$u\bar{d}$
$n$	$udd$	$\pi^0$	$\frac{1}{\sqrt{2}}(d\bar{d} - u\bar{u})$
$\Lambda$	$uds$	$\pi^-$	$d\bar{u}$
$\Sigma^+$	$uus$	$\rho^+$	$u\bar{d}$
$\Sigma^0$	$uds$	$\rho^0$	$\frac{1}{\sqrt{2}}(u\bar{u} - d\bar{d})$
$\Sigma^-$	$dds$	$\rho^-$	$\bar{u}d$
$\Delta^+$	$uud$	$K^-$	$\bar{u}s$
$\Delta^0$	$udd$	$K^0$	$d\bar{s}$
$\Delta^-$	$ddd$	$K^+$	$u\bar{s}$
$\Xi^+$	$dds$	$K^{*+}$	$u\bar{s}$
$\Xi^0$	$uss$	$K^{*0}$	$d\bar{s}$
$\Xi^-$	$dss$	$K^{*-}$	$s\bar{u}$
$\Omega$	$sss$	$\Phi$	$s\bar{s}$

**Table 3.1:** The two families of hadrons: baryons and mesons with their quark contents.

The possible  $q\bar{q}$  combinations of light  $u$ ,  $d$ , and  $s$  quarks group are shown in Fig. 3.2. The states are classified by their strangeness content,  $\mathbf{S}$ , and the third component of their isospin,  $I_3$ , which differentiates the particles belonging to the same isospin family. These representations are called *Eightfold Way* and independently proposed by Ne'eman and Gell-Mann [51, 52]. The Eightfold Way consists of a classification scheme to group the observed baryons and mesons with the same spin according to their third isospin component (related to charge) and hypercharge (related to strangeness) using the SU(3) group symmetry. Some hadrons were not yet discovered when the Eightfold Way was

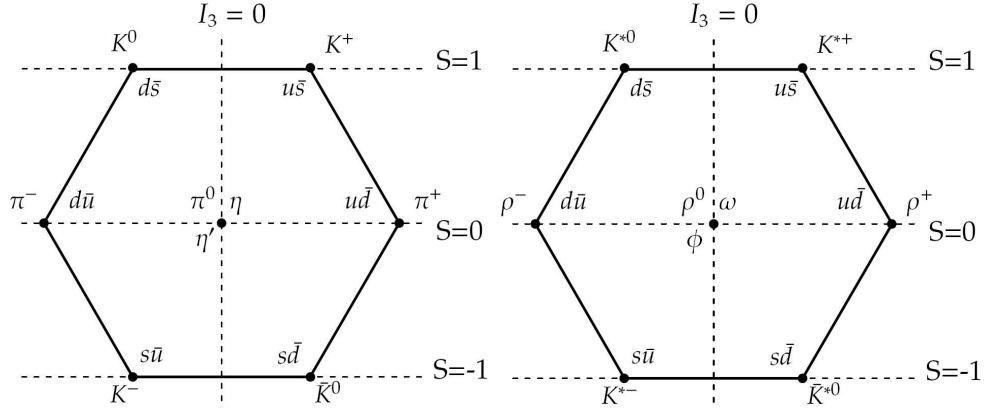


**Figure 3.2:** The Eightfold Way for pseudoscalar mesons (left) and vector mesons (right). The various states are classified by their strangeness content  $\mathbf{S}$  and the third component of their isospin  $I_3$ .

Resonance	Decay Channel	Branching Ratio(%)	Width (MeV)	Lifetime (fm)	Mass (MeV)
$\rho^0(770)$	$\pi\pi$	$\sim 100$	$150.2 \pm 2.4$	1.3	$775.49 \pm 0.34$
$f^0(980)$	$\pi\pi$	dominant	40 to 100	2.6	$980 \pm 10$
$K^*(892)$	$K\pi$	$\sim 100$	$50.8 \pm 0.9$	4	$891.66 \pm 0.26$
$\Sigma(1385)$	$\Lambda\pi$	$87 \pm 1.5$	$39.4 \pm 2.1$	5.7	$1383.7 \pm 1.0$
$\Lambda(1520)$	$N\bar{K}$	$45 \pm 1$	$15.6 \pm 1.0$	13	$1519.5 \pm 1.0$
$\omega(783)$	$\pi^+\pi^-\pi^0$	$89.2 \pm 0.7$	$8.49 \pm 0.08$	23	$782.65 \pm 0.12$
$\Phi(1020)$	$K^+K^-$	$49.2 \pm 0.6$	$4.26 \pm 0.04$	45	$1019.455 \pm 0.020$

**Table 3.2:** The resonances with their most dominant decay channels, branching ratios, widths, lifetimes and masses [4]. The unit of lifetimes is given in femtometer (1 fm =  $10^{-15}$  m).

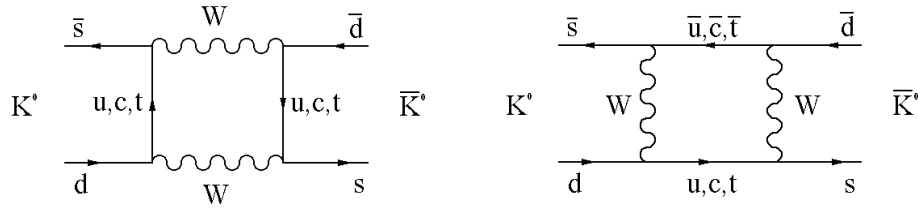


**Figure 3.3:** The oscillation of  $K^0$  mesons with its antiparticle  $\bar{K}^0$ .

proposed. The discovery of a predicted particle  $\Omega$  with  $Q = -1$  and  $S = -3$  in 1964 led to wide acceptance of the Eightfold Way. Table 3.2 lists some of the resonances with their most dominant decay channels, branching ratios, widths, lifetimes and masses. In the following the hadrons which are relevant to this analysis are briefly discussed.

### 3.2.1 $K_S^0$ Meson

The lightest mesons, that contain one  $s$  or  $\bar{s}$  quark and therefore have strangeness  $S = 1$  or  $S = -1$ , are called *kaons* ( $K$ ). Kaons are pseudoscalar mesons and have the following quark content:  $K^+ = |u\bar{s}\rangle$ ,  $K^- = |\bar{u}s\rangle$ ,  $K^0 = |d\bar{s}\rangle$  and  $\bar{K}^0 = |\bar{d}s\rangle$ . The kaons can be arranged in isospin doublets as shown in Table 3.3. The  $K^0$  is not an antiparticle to itself, unlike  $\pi^0$  and  $\phi$ ; its antiparticle is  $\bar{K}^0$ . The symmetry operator  $CP^2$  can be used to explain this  $CP(K^0) = \bar{K}^0$ .

	$S = + 1$	$S = - 1$
$I_3 = -\frac{1}{2}$	$K^0$	$K^-$
$I_3 = +\frac{1}{2}$	$K^+$	$\bar{K}^0$

**Table 3.3:** The isospin doublets of the kaons.

The two particles differ by two units of strangeness, but the strangeness is not conserved in the weak interactions and the neutral kaons can decay as  $\bar{K}^0 \rightarrow \pi^+\pi^-$ , and also its antiparticle has the same decay mode  $K^0 \rightarrow \pi^+\pi^-$ . Since the two states can not be distinguished by the decay products the two states can oscillate  $K^0 \rightarrow \pi^+\pi^- \rightarrow \bar{K}^0$ , see Fig. 3.3.

If the  $CP$  symmetry holds, the kaons observed in the laboratory are  $CP$  eigenstates of  $K^0$  and  $\bar{K}^0$ . Two eigenstates are created:

$$K_1 = \frac{1}{\sqrt{2}}(K^0 + \bar{K}^0), \quad CP = +1, \quad (3.3)$$

<sup>2</sup> $CP$  is the product of two symmetry operation:  $C$  for charge conjugation, which transforms a particle into its antiparticle, and  $P$  for parity, which creates the mirror image of a physical system. The strong interaction and electromagnetic interaction are invariant under the combined  $CP$  transformation operation, but this symmetry is violated in certain types of weak decay.

$$K_2 = \frac{1}{\sqrt{2}}(K^0 - \bar{K}^0), \quad CP = -1. \quad (3.4)$$

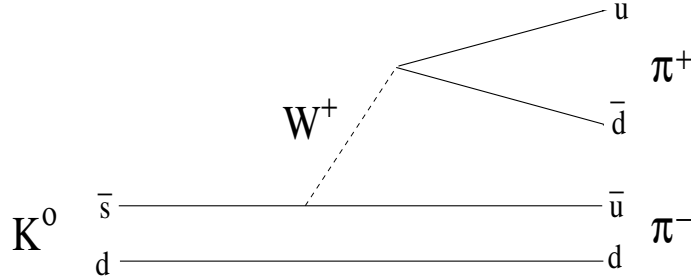


**Figure 3.4:** The dominant decay channel  $K_S^0 \rightarrow \pi^+\pi^-$ .

The eigenstate  $K_1$  corresponds to the *short-lived* component  $K_S^0$  ( $c\tau = 2.6842$  cm) and the eigenstate  $K_2$  corresponds to the *long-lived* component  $K_L^0$  ( $c\tau = 15.51$  m) [4]. 50% of both  $K^0$  and  $\bar{K}^0$  decay as  $K_L^0$  and the other half as  $K_S^0$ . The characteristics of  $K_L^0$  and  $K_S^0$  particles are given in Table 3.4. Only the  $K_S^0$  meson, which dominantly decays into two pions, is accessible in this analysis. The dominant decay mode  $K_S^0 \rightarrow \pi^+\pi^-$  which proceeds via an intermediate  $W^+$  emission, is depicted in Fig. 3.4.

Particle	Mass (MeV)	Decay	Branching Ratio (%)	Lifetime ( $10^{-10}$ s)
$K_S^0$	$497.648 \pm 0.022$	$\pi^+\pi^-$ $\pi^0\pi^0$ $\pi^+\pi^-\pi^0$	$69.20 \pm 0.05$ $30.69 \pm 0.05$ $(3.5 \pm 1.0) \times 10^{-7}$	$0.8953 \pm 0.0005$
$K_L^0$	$497.648 \pm 0.022$	$\pi^\pm l^\mp \nu_l$ $\pi^0\pi^0\pi^0$ $\pi^+\pi^-\pi^0$	$67.55 \pm 0.22$ $19.56 \pm 0.14$ $12.56 \pm 0.05$	$511.4 \pm 2.1$

**Table 3.4:** The characteristics of  $K_L^0$  and  $K_S^0$  particles [4].

### 3.2.2 $K^*$ Meson

The  $K^*$  mesons are the vector mesons and can be interpreted as being the excited states of their corresponding pseudoscalar mesons with the same quark content. The  $K^*$  vector meson resonances are the excited states of the Kaon pseudoscalar mesons. The arrangement of the  $K^{*\pm}$  mesons within an isospin doublet is analogous to the kaons (see Table 3.5).

The vector mesons  $K^{*\pm}$  decay nearly exclusively via the strong interaction into a kaon and a pion

$$K^{*+} \rightarrow \begin{cases} K^0\pi^+ & (66.6)\% \\ K^+\pi^0 & (33.3)\% \end{cases}$$

	$S = + 1$	$S = - 1$
$I_3 = -\frac{1}{2}$	$K^{*0}$	$K^{*-}$
$I_3 = +\frac{1}{2}$	$K^{*+}$	$\bar{K}^{*0}$

**Table 3.5:** The isospin doublets of the vector mesons  $K^*$ .

$$K^{*-} \rightarrow \begin{cases} K^0\pi^- & (66.6)\% \\ K^-\pi^0 & (33.3)\% \end{cases}$$

with the width of  $50.8 \pm 0.9$  MeV and mass of  $891.66 \pm 0.26$  MeV [4]. Due to the strong decay, the  $K^{*\pm}$  vector mesons have very short lifetimes. The mean lifetime of  $K^{*\pm}$ ,  $\tau$ , is  $\approx 1.3 \cdot 10^{-23}$  s, or correspondingly,  $c\tau \approx 4$  fm. In this thesis, in order to select the  $K^{*\pm}$  mesons the following decay channel is used

$$K^{*\pm} \rightarrow K_s^0\pi^\pm \rightarrow \pi^+\pi^-\pi^\pm \quad (\text{BR} = 50 \times 66.6 \times 69)\%, \quad (3.5)$$

where the  $K_s^0$  is identified by its decay into two charged pions and form a  $K^{*\pm}$  candidate by adding a third pion coming from the primary vertex (see Chapter 7).

### 3.2.3 $\Lambda$ Baryon

The lightest baryon carrying strangeness is the  $\Lambda$  baryon.  $\Lambda$  ( $uds$ ) is a neutral particle of mass 1.116 GeV that decays weakly with a decay length  $c\tau = 7.891 \pm 0.006$  cm [4]. The dominant decay is  $\Lambda \rightarrow p + \pi^-$  ( $63.9 \pm 0.5\%$ ), shown in Fig. 3.5. The other important weak decay  $\Lambda \rightarrow n + \pi^0$  ( $35.8 \pm 0.5\%$ ), has only neutral particles in the final state and is difficult to identify. The  $\Lambda$  baryon is the member of the baryon-octet with positive parity, spin  $1/2$ ;  $J^P = \frac{1}{2}^+$ .

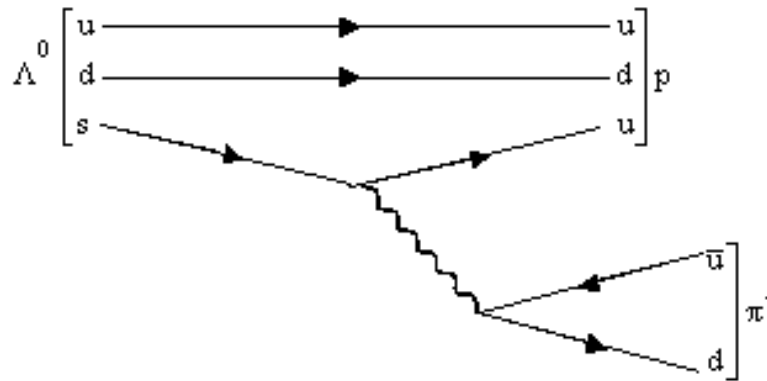


**Figure 3.5:** The main decay of strange baryon  $\Lambda^0 \rightarrow p\pi^-$ .

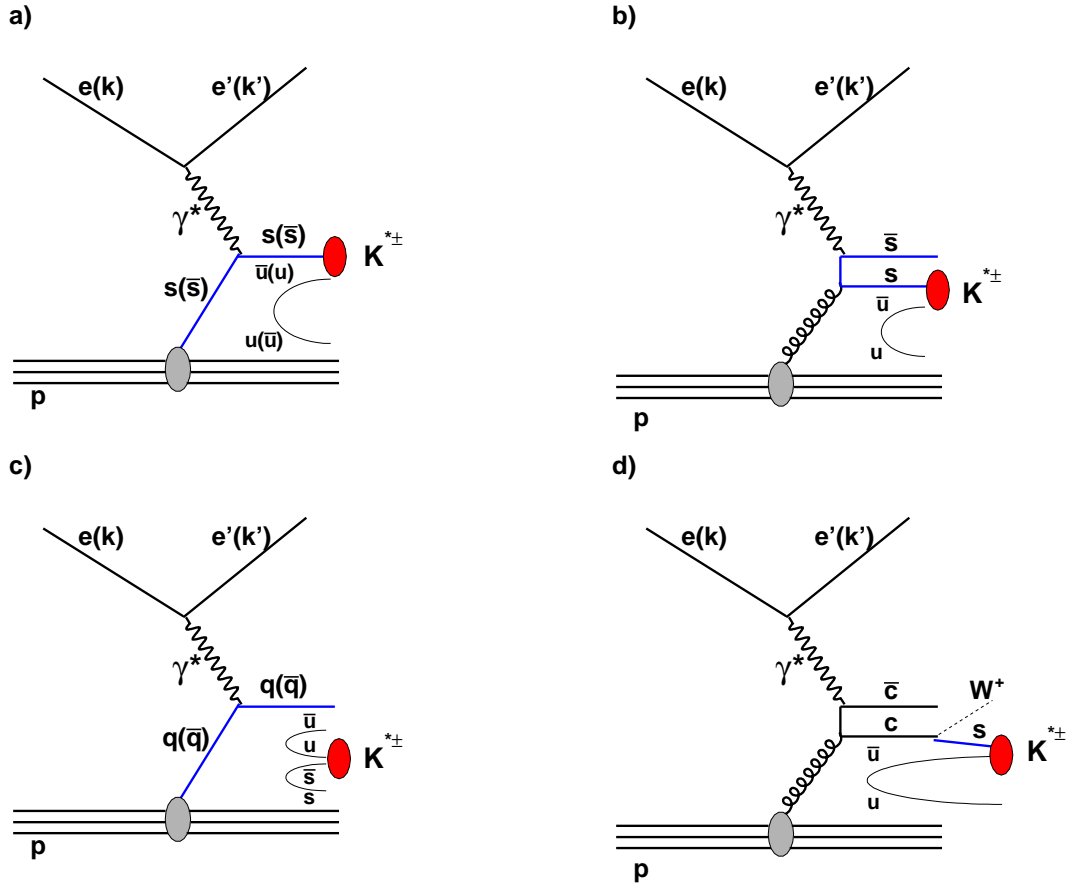


**Figure 3.6:** Various mechanisms contributing to the production of strange particles. Shown are hard scattering off a  $s$  sea quark a), boson gluon fusion (BGF) b), parton fragmentation c) and heavy quark decay d).

### 3.3 Strangeness Production Mechanism

The production of strange particles in  $ep$  collisions can proceed via various subprocesses as illustrated by diagrams in Fig. 3.6. In the following, the different production mechanisms accessible at HERA are described.

#### 1. Strangeness in hard subprocess

- **Direct production:** Strange quarks can be produced directly in the hard scattering off a strange sea quark inside the proton (see Fig. 3.6a). Even though there is no strange valence quark among the proton constituents, as  $Q^2$  increases, the  $s(\bar{s})$  sea quarks can be resolved by the virtual photon and can be knocked out to form a final strange hadron. This production mechanism is expected to become important at higher  $Q^2$  and lower  $x$  values since the gluon and sea quark content increases rapidly as  $x$  decreases (see Fig. 3.1).

- **Boson gluon fusion:** BGF is a production mechanism in which the virtual photon couples with a gluon of the proton via a virtual  $s - \bar{s}$  quark pair (Fig. 3.6b). Due to the lighter mass of the strange quark, BGF process does not play an outstanding role as for the production of heavy flavors  $c$  and  $b$ , for which this is the main source of production. The available measurements show the rise of both gluon and sea-quark distributions for low  $Q^2$  and small Bjorken- $x$ . Particularly within the range of small  $x$  one expects a dominance of BGF processes also for the strange quark production.

## 2. Strangeness in soft subprocess

- **Fragmentation:** It has been experimentally shown that the production of strangeness occurs dominantly through the hadronisation process where universal fragmentation is considered to take place [53, 54, 55]. In order to understand this kind of mechanism phenomenological models must be used. A parton from the hard scattering process is followed by a parton shower in which  $s\bar{s}$  pair can be created by gluon splitting (Fig. 3.6c).
- **Decays of heavier quarks:** Strange quarks in the final state can result from decays of heavy flavors, i.e. charm and beauty quarks as shown in Fig. 3.6d.

## 3.4 Strangeness Suppression

In order to conserve the quantum numbers like charge, colour and flavor, the strange  $q\bar{q}$  pairs should be produced at the same space-time point. If the quarks have mass  $m$  and/or transverse momentum  $p_T$  then the quark and antiquark must be produced with a finite separation in order to transform the field energy between them into the sum of the quarks transverse masses  $m_T$ . This is (classically) forbidden and can only be achieved by a quantum mechanical tunnel effect. The tunnelling probability is given by

$$\exp\left(\frac{-\pi m_T^2}{\kappa}\right) = \exp\left(\frac{-\pi m^2}{\kappa}\right) \exp\left(\frac{-\pi p_T^2}{\kappa}\right), \quad (3.6)$$

where  $m_T$  is the transverse mass,  $m$  is the quark mass,  $p_T$  is the transverse momentum and  $\kappa$  is the constant. This leads to a suppression of heavier quarks like charm with different quark flavours into a ratio

$$u : d : s : c \approx 1 : 1 : 0.3 : 10^{-11}.$$

In the fragmentation process, different flavors are produced with different probabilities, which leads to a suppression of strange hadrons with respect to non-strange particles. The ratio of strange quark pairs with respect to the non-strange quark pairs can be expressed as a *strangeness suppression factor*,  $\lambda_s$ , with

$$\lambda_s = \frac{P(s\bar{s})}{P(u\bar{u})} \approx \frac{P(s\bar{s})}{P(d\bar{d})}, \quad (3.7)$$

where  $P(s\bar{s})$ ,  $P(u\bar{u})$  and  $P(d\bar{d})$  are probabilities for the production of  $s\bar{s}$ ,  $u\bar{u}$  or  $d\bar{d}$ , respectively. The strangeness suppression factor  $\lambda_s$  is related to the mass difference between  $s$ ,  $u$  and  $d$  quarks. Since the quark masses are not precisely known, the parameter  $\lambda_s$  needs to be adjusted according to experimental results. A value  $\lambda_s = 0.3$  was found to be appropriate in the  $e^+e^-$  experiments at LEP<sup>3</sup> [56, 57, 58], early results from  $p\bar{p}$  collider experiments suggest even a value of about 0.5 [59].

## 3.5 Experimental Results on Strangeness Production

Within this section a brief summary of the experimental results obtained so far on strangeness production with different experiments are presented. Although this analysis concentrates on the production of  $K^{*\pm}(892)$ , the results on the other strange particles are also mentioned.

### 3.5.1 Strangeness Production in $e^+e^-$ Annihilation

A large number of studies of inclusive vector meson production have so far concentrated on the measurement of fragmentation functions and total inclusive rates (see for example [60]). The rôle of the meson spin in the production dynamics has also been investigated. The DELPHI detector at the  $e^+e^-$  storage ring LEP has reported measurements for  $\rho^0(770)$ ,  $K^*(892)^0$  and  $\phi(1020)$  confirming the OPAL observations of vector meson spin alignment<sup>4</sup> at large scaled momentum,  $x_p$ <sup>5</sup>, [61]. A comprehensive compilation of experimental data on inclusive particle production in  $e^+e^-$  interactions is presented in [62]. Measurements of inclusive distributions of  $K^*(892)^\pm$ ,  $\Lambda$  and  $\Xi^-$  have been made in the DELPHI experiment at the  $Z^0$ . The following average multiplicities per event for strange particles have been measured:

$$\begin{aligned} \langle N_{K^0} \rangle + \langle N_{\bar{K}^0} \rangle &= 2.12 \pm 0.07, \\ \langle N_{K^{*+}} \rangle + \langle N_{K^{*-}} \rangle &= 1.33 \pm 0.26, \\ \langle N_{\Lambda} \rangle + \langle N_{\bar{\Lambda}} \rangle &= 0.36 \pm 0.07, \\ \langle N_{\Xi^-} \rangle + \langle N_{\bar{\Xi}^+} \rangle &= 0.020 \pm 0.005, \end{aligned}$$

where statistical and systematic errors have been summed in quadrature [63].

The OPAL experiment at LEP has presented the inclusive cross-section for  $K^*(892)^\pm$  production in hadronic decays of the  $Z^0$ . A mean rate of  $0.72 \pm 0.002 \pm 0.08$   $K^{*\pm}$  mesons per hadronic event was found [64]. In the same measurement, the mass ( $M$ ) and width

<sup>3</sup>Large Electron Positron

<sup>4</sup>The spin alignment can be described in terms of the spin density matrix  $\rho_{\lambda,\lambda'}$ , which is a  $3 \times 3$  Hermitian matrix with unit trace usually defined in the helicity basis. Its diagonal elements,  $\rho_{11}$ ,  $\rho_{-1-1}$ , and  $\rho_{00}$  represent the relative intensities of the helicity  $\lambda = +1$ ,  $\lambda = -1$  and  $\lambda = 0$  states. Because vector mesons decay strongly, the diagonal elements  $\rho_{11}$  and  $\rho_{-1-1}$  are degenerate and  $\rho_{00}$  is the only independent observable.

<sup>5</sup>The definition of scaled momentum is  $x_p = p/p_{beam}$ , where  $p$  is the momentum of hadronic final state particles and  $p_{beam}$  is the momentum of initial state particles.

( $\Gamma$ ) of the  $K^{*\pm}$  mesons have measured as  $889.2 \pm 2$  MeV and  $60 \pm 5$  MeV, respectively. The differential cross section for  $K^{*\pm}$  production as a function of the scaled  $K^{*\pm}$  energy,  $x_E$ , is shown in Fig. 3.7.

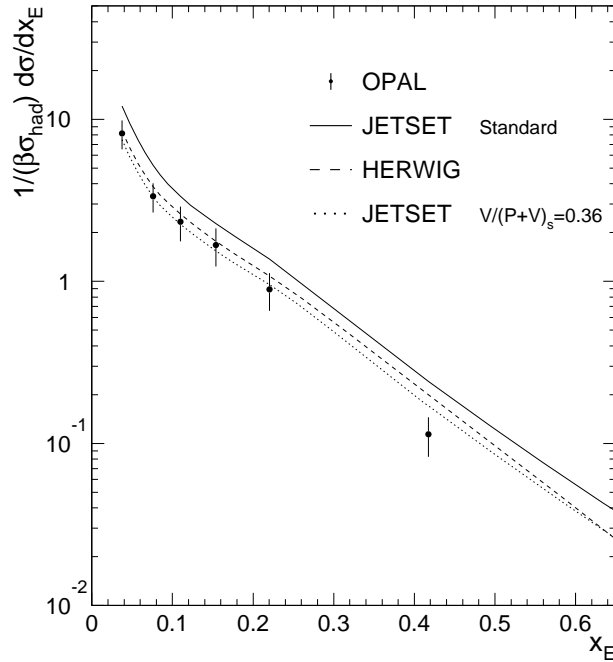


**Figure 3.7:** The differential cross section for  $K^{*\pm}$  production at the OPAL experiment. Here  $\beta$  is the particle velocity,  $p/E$ , where  $p$  and  $E$  are the momentum and energy of the particle, respectively.  $\sigma_{had}$  represents the first order hadronic cross section. The parameter  $\frac{V}{(V+P)_s}$  is the probability that a strange meson carries spin-1, where  $V$  represents the vector mesons and  $P$  represents the pseudoscalar mesons.

The production of neutral  $K^*$  mesons was also studied at  $\sqrt{s} = 29$  GeV using the High Resolution Spectrometer at PEP. Differential cross sections for  $K^{*0}$  were presented as a function of the scaled energy variable<sup>6</sup>  $z$  and compared to  $\pi^0$  and  $K^0$  production [65]. The total cross section was measured to be  $\sigma(K^{*0}) = 252 \pm 40$  pb. The data have shown that the vector and pseudoscalar meson partners have fragmentation functions that differ significantly.

Inclusive distributions of  $K_S^0$  [66],  $K^{*\pm}(892)$ ,  $\Lambda$ ,  $\Xi^-$  [63],  $K^*(892)^0$ ,  $\phi$  [56],  $\rho^0$ ,  $f_0(975)$ ,  $f(1270)$  [67], and  $\Lambda$ ,  $\Xi^-$ ,  $\Sigma^\pm(1385)$ ,  $\Xi^0(1530)$ , and  $\Omega^-$  [68] (and the corresponding antiparticles) have been measured by OPAL at the  $Z^0$ . These particles are identified via their decays over essentially the entire momentum range and allow measurements of the differential and integrated yields with very good accuracy.

In a study of strange particles produced inclusively in  $e^+e^-$  annihilation, the CELLO col-

<sup>6</sup>The definition of scaled energy variable is  $z = x_E = 2E/\sqrt{s}$ , where  $E$  is the energy of the measured particle and  $\sqrt{s}$  the centre of mass energy  $\sqrt{s} = 29$  GeV.

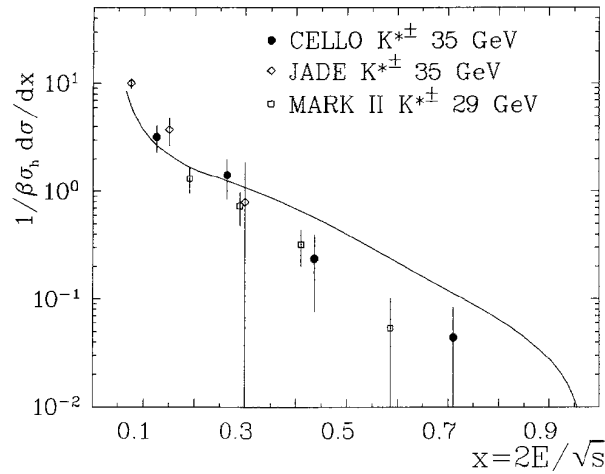


**Figure 3.8:** The differential cross section for  $K^{*\pm}$  production as a function of the fractional energy  $x = 2E/\sqrt{s}$  at the CELLO experiment [69]. Here  $\sigma_h$  is the first order hadronic cross section. Solid line shows the Lund model prediction.

laboration has measured the production rates for  $K^0$ ,  $\bar{K}^0$ ,  $K^{*\pm}$ ,  $\Lambda$  and  $\bar{\Lambda}$  at  $\sqrt{s} = 35$  GeV and found consistency with results reported by other PETRA and PEP experiments [69]. The resulting cross sections for  $K^{*\pm}$  are displayed in Fig. 3.8 together with the Lund model prediction. The agreement is reasonable, but as is visible in Fig. 3.8, the combined data from PEP and PETRA indicate a somewhat steeper drop of the cross section with increasing  $x$  than suggested by the Lund model. The integrated cross section is  $186 \pm 40$  (stat.)  $\pm 33$  (syst.) pb for the  $x$  range covered by the analysis. The Lund model was used to correct the unobserved  $x$  region. A total cross section of  $214 \pm 46$  (stat.)  $\pm 39$  (syst.) pb was obtained. The ratio of primary pseudoscalar to vector meson production rates was determined from  $K$  and  $K^{*\pm}$  production and indicates a suppression of the vector mesons ( $V/(V+P)_s = 0.59^{+0.20+0.10}_{-0.10-0.05}$ ) in the fragmentation process. This behaviour is also suggested by theoretical ideas of quark fragmentation. The strange baryon yield is significantly lower than the strange meson yield, a result also expected from phenomenological fragmentation models.

Since the perturbation theory is not applicable for the process of hadronisation, whereby coloured partons are confined inside colourless hadrons, one has to rely on phenomenological models. PETRA and PEP experiments have extensively tested the successful models of string and cluster fragmentation. The JADE collaboration at PETRA studied the multiplicity of  $K_S^0$  production at the centre of mass energy  $\sqrt{s} = 12$  and  $\sqrt{s} = 35$  GeV. The value of  $\lambda_s$  was found to be  $\lambda_s = 0.27 \pm 0.03$  (stat.)  $\pm 0.05$  (syst.) [70]. The TASSO collaboration at PETRA which has measured the production of  $K_S^0$  and  $\Lambda$  at  $\sqrt{s} = 14, 22$  and  $34$  GeV [71] was found a consistent result with [70]. A value  $\lambda_s = 0.35 \pm 0.02$  (stat.)  $\pm 0.05$  (syst.) was extracted [71]. The production of strange particles ( $K^0$ ,  $\bar{K}^0$ ,  $K^{*\pm}$ ,  $\Lambda$ ,  $\bar{\Lambda}$ , and  $\Xi^-$ ) has also been extensively studied by the TASSO collaboration in [72, 73, 74].

The ALEPH, OPAL, DELPHI and L3 [75, 76, 77, 78, 79] experiments have used hadronic  $Z^0$  decays to study strangeness production in the hadronisation process and suggest a

strangeness suppression factor of  $\lambda_s \approx 0.3$  consistent with the PETRA results. However, a more recent measurement of the OPAL collaboration determined the suppression of strange quarks to be  $\lambda_s = 0.422 \pm 0.049$  (stat.)  $\pm 0.059$  (syst.) [80].

### 3.5.2 Strangeness Production in $pp$ , $p\bar{p}$ , $pA$ and $AA$ Collisions

A compilation of cross sections for inclusive  $K^*$  production in  $pp$  collisions as a function of the centre of mass energy  $\sqrt{s}$  is shown in Fig. 3.9. It can be seen from Fig. 3.9 that all cross sections rise with  $\sqrt{s}$  and seem to saturate at higher energies. It is also noticeable that particles  $K^{*+}$  and  $K^{*0}$  (with strangeness  $S = 1$ ) are more frequently produced than the particles  $K^{*-}$  and  $\bar{K}^{*0}$  (with strangeness  $S = -1$ ). This difference tends to decrease towards higher values of  $\sqrt{s}$ . The measurements are available for an energy range of  $7.5 \leq \sqrt{s} \leq 53$  GeV. The measurements up to  $\sqrt{s} = 26$  GeV focus on the charged  $K^*$  only, while total cross sections of neutral  $K^*$  production are available for  $\sqrt{s} = 27.5$  GeV and  $\sqrt{s} = 52.5$  GeV [81, 82, 83, 84, 85].

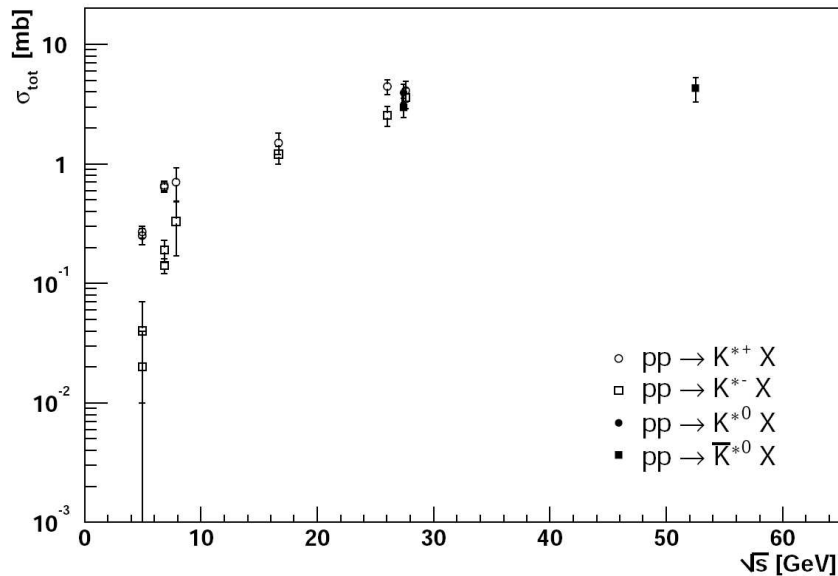


**Figure 3.9:** Measurements of the total  $K^*$  production cross section in  $pp$  collisions as a function of centre of mass energy  $\sqrt{s}$  [86].

In recent years, experiments using relativistic heavy ion collisions have provided opportunities for the use of resonances to study various properties of the hot and dense nuclear matter under extreme conditions. The main facilities for studying heavy ion collisions are localised at BNL and at CERN. The accelerators at the two laboratories provide different energy regimes, from the AGS<sup>7</sup> at BNL ( $\sqrt{s} = 22$  GeV), via the SPS<sup>8</sup> at CERN

<sup>7</sup>Alternating Gradient Synchrotron

<sup>8</sup>Super Proton Synchrotron

( $\sqrt{s} = 400$  GeV), to RHIC<sup>9</sup> at BNL ( $\sqrt{s} = 200$  GeV).

Production at mid-rapidity ( $|y| < 0.5$ ) of  $K^{*0}(892) \rightarrow K\pi$  and  $K^{*\pm}(892) \rightarrow K_S^0\pi^\pm$  measurements in Au+Au and  $pp$  collisions at  $\sqrt{s_{NN}} = 200$  GeV were studied by the STAR Collaboration [87]. In this measurement, the  $K^{*0}(892)$  mass has been studied as a function of  $p_T$  in minimum bias  $pp$  and central Au+Au collisions. The  $K^*/K$  yield ratios as a function of the centre of mass system energies  $\sqrt{s_{NN}}$ , shown in the upper panel of the Fig. 3.10, were compared to measurements in A+A,  $pp$ ,  $p\bar{p}$ ,  $e^+e^-$  collisions at various colliding energies. The  $K^*/K$  yield ratios do not show a strong dependence on the colliding system or the centre of mass energy. The  $K^*/K$  yield ratios in Au+Au collisions were observed to be smaller than the ratio in  $p + p$  interactions. Recently, the same collaboration presented the first spin alignment measurements for both  $K^*(892)$  and  $\phi(1020)$  at mid-rapidity with transverse momenta up to 5 GeV. The data were consistent with the expectations from unpolarised strange quark production and thus no evidence was found for the transfer of the orbital angular momentum of the colliding system to the vector meson spins [88].

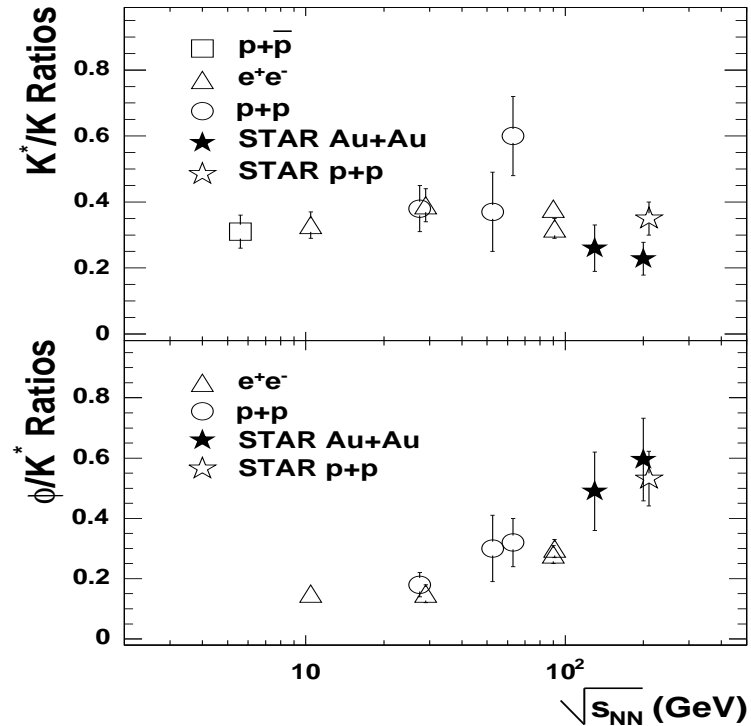


**Figure 3.10:** The yield ratios of  $K^*/K$  (upper panel) and  $\phi^*/K$  (lower panel) as a function of centre of mass system. The results from Au+Au and  $p + p$  interactions are compared with various measurements [87].

<sup>9</sup>Relativistic Heavy Ion Collider

The production of baryons relative to mesons is another topic that has been intensively studied by the data from RHIC. It is of interest to check this ratio to understand the hadron formation. The baryon to meson ratio becomes quite large and could be greater than 1 in various regions of the heavy ion collision phase space which cannot be explained by the standard mechanism of fragmentation approach (where each parton produced is convoluted with its probability of becoming a particular hadron) [89]. Therefore alternative models exist to explain the large ratio of baryons.

A similar study from the BRAHMS collaboration showed that baryon to meson ratio is enhanced (factor of  $\sim 2$ ) in nucleus-nucleus collisions compared to  $pp$  collisions [90].

An overview of recent results on resonance production at RHIC in different collisions ( $A + A$ ,  $d + Au$ , and  $p + p$ ) and energies can be found in [91].

The inclusive production cross sections of the strange vector mesons  $K^{*0}$ ,  $\bar{K}^{*0}$  and  $\phi$  mesons have been measured for the first time in interactions of 920 GeV protons with C, Ti and W targets with the HERA-B detector at HERA [92]. It was observed that the cross section shows a power law dependence  $\sigma \propto A^\alpha$ , where  $A$  is the atomic mass of the target material, with an exponent of  $\alpha \approx 0.8 - 1.1$  depending on both the type of vector meson and the transverse momentum. It has also been noted that the  $K^*$  and  $\bar{K}^{*0}$  production is smaller than that of  $K^+$  and  $K^-$  mesons [92]. Results on inclusive doubly differential cross sections as a function of Feynman- $x$  ( $x_F$ ) and transverse momentum ( $p_T$ ) for the production of  $K_S^0$ ,  $\Lambda$  and  $\bar{\Lambda}$  were reported in [93].

The HERMES collaboration at HERA, also studied the strange particle production [94]. A measurement of the positive  $\Lambda$  and negative  $\bar{\Lambda}$  polarisations was presented [95]. The interpretation from the photoproduction data is that the  $s$  quarks in the  $\Lambda$  and  $\bar{\Lambda}$  originate predominantly from  $\gamma \rightarrow s\bar{s}$ . Hence, the fast  $s$  quarks are decelerated when they combine to the hadron, leading to opposite sign polarisation of approximately equal magnitude.

A measurement of the  $K_S^0$  yield in central PbAu collisions at SPS energies was performed by the CERES collaboration. The rapidity spectrum was found to agree with the measurements of charged kaons by NA49 and of  $K_S^0$  by NA57. The yield at mid-rapidity was found to be  $dN/dy = 21.2 \pm 0.9 \pm 1.7$  [96].

The FOPI Collaboration performed a study of strangeness production in Al+Al collisions at  $\sqrt{s_{NN}} = 2.65$  GeV. For the first time the production of  $\Sigma(1385)$  and  $K^*(892)$  resonances below threshold was reported. These measurements constrain the parameters of a statistical model [97] and provide information on cross sections in the nuclear medium for the different processes involved in strangeness production close to or below their thresholds. The production of strange particles has been also studied in  $p\bar{p}$  collisions from 200 GeV to 900 GeV centre mass of energies by the UA5 Collaboration [98, 99, 100].

### 3.5.3 Strangeness Production at the $ep$ Collider

The production of  $K_S^0$  and  $\Lambda$  in DIS ( $10 < Q^2 < 70\text{GeV}^2$ ) [53] and in photoproduction ( $Q^2 \approx 0$ ) [54] has been measured by the H1 Collaboration. The analysed data were taken in 1994 with an integrated luminosity of  $1.32\text{ pb}^{-1}$ .

A recent analysis of DIS events using  $17.8\text{ pb}^{-1}$  and a visible kinematic range of  $2 < Q^2 < 100\text{ GeV}^2$  is presented in [101]. The production cross sections and ratios of the production of  $K_S^0$ ,  $\Lambda$  and charged hadrons  $h^\pm$  are measured inclusively and also differentially as a function of the DIS variables,  $Q^2$  and  $x$ . The ratio of the differential cross section for  $\Lambda$  baryons and  $K_S^0$  mesons is shown in the Fig. 3.11. The CDM (see section 5.2.2 for details) implementation provides a reasonably good description of the data in the laboratory frame, although systematic deviations are seen at high  $Q^2$  and in the shape of the distribution not shown in here, whereas the MEPS (see section 5.2.1 for details) predictions somewhat underestimate the data. The model predictions are not sensitive to  $\lambda_s$ , as expected. Like the previous measurements of H1, a somewhat lower strangeness suppression factor than 0.3 is preferred. The data were best described with  $\lambda_s$  in the range  $0.23 - 0.25$ .

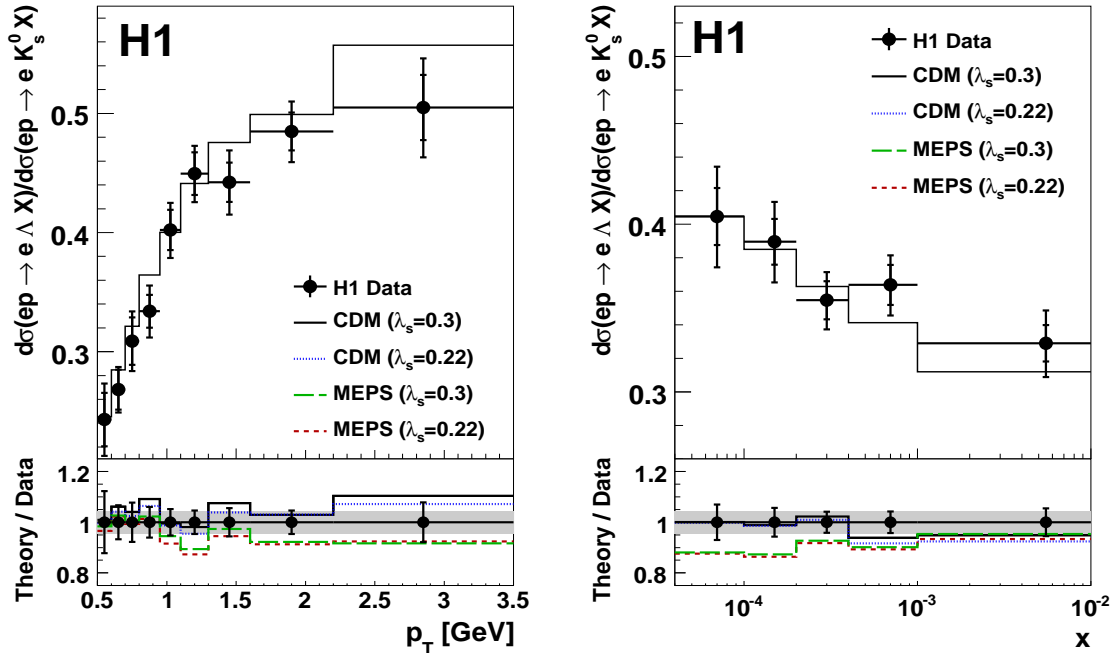


**Figure 3.11:** The ratio of the differential production cross section for  $\Lambda$  baryons and  $K_S^0$  mesons in the laboratory frame as a function of  $p_T$  (left panel) and  $\eta$  (right panel) [101]. Theory/Data ratios are shown for different MC predictions. For comparison, the data points are put to one and only uncorrelated errors are shown; the correlated systematic errors are indicated by the grey band.

The H1 collaboration recently published a measurement of the inclusive non-diffractive photoproduction of resonances  $\rho(770)^0$ ,  $K^*(892)^0$  and  $\phi(1020)$  at HERA [102]. The data were recorded in the year 2000 with an integrated luminosity of  $36.5 \text{ pb}^{-1}$ . The transverse momentum spectra and the rapidity of  $\rho^0$ ,  $K^{*0}$  and  $\phi$  mesons are shown in Fig. 3.12. It was observed that the resonances with different masses, lifetimes and strangeness content are produced with about the same value of the transverse kinetic energy. It was argued that the observation supports the thermodynamic picture of hadronic interactions in which the primary hadrons are thermalised during the interaction. The cross-section ratios  $R(K^{*0}/\rho^0)$ ,  $R(\phi/\rho^0)$ , and  $R(\phi/K^{*0})$  were determined. The ratio  $R(\phi/K^{*0})$  was found in agreement with the  $pp$  results, while it is observed to be smaller than in heavy-ion collisions.

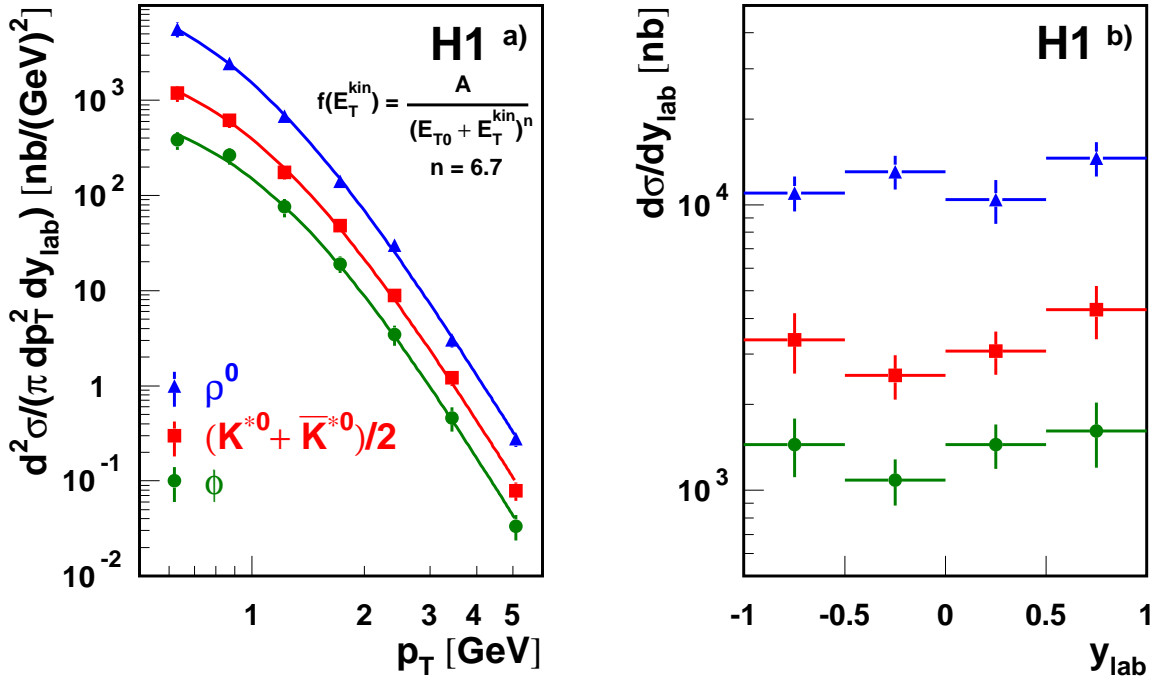


**Figure 3.12:** The inclusive differential non-diffractive cross sections for  $\rho^0$ ,  $K^{*0}$  and  $\phi$  as a function of transverse momentum  $p_T$  **a**), and rapidity in laboratory frame **b**). The curves correspond to power law, given in the legend with  $f(E_T^{\text{kin}}) = \frac{A}{(E_{T0} + E_T^{\text{kin}})^n}$  where  $E_T^{\text{kin}} = \sqrt{m_0^2 + p_T^2} - m_0$  is the transverse kinetic energy,  $m_0$  is the nominal resonance mass,  $A$  is a normalisation constant and  $E_{T0}$  is a free parameter [102].

The ZEUS collaboration also performed a detailed analysis of strangeness production. The first measurement was performed with an integrated luminosity of  $0.55 \text{ pb}^{-1}$  for DIS data in the range of  $10 < Q^2 < 640 \text{ GeV}^2$  [103]. In a more recent work  $121 \text{ pb}^{-1}$  of  $ep$  scattering data were analysed [104]. The following conclusions were obtained for strangeness production in DIS and photoproduction.

1. In DIS  $\lambda_s = 0.3$  is preferred compared to  $\lambda_s = 0.22$ ,
2. The numbers of produced  $\Lambda$  and  $\bar{\Lambda}$  are found to be equal i.e. no baryon asymmetry was observed,
3. The ratio of baryons to mesons varies from 0.2 to 0.5, similar to measurements at  $e^+e^-$  colliders. However, in photoproduction the ratio is found to be larger than in  $e^+e^-$  interactions.

### 3.5.4 Strangeness Production in Other Experiments

The NOMAD experiment, having the main goal to search for  $\nu_\mu \rightarrow \nu_\tau$  oscillations in a wide band neutrino beam from the CERN SPS, has also studied the production of strange particles [105, 106, 107, 108]. Yields of neutral strange particles ( $K_S^0$ ,  $\Lambda$ ,  $\bar{\Lambda}$ ) and clear signals corresponding to  $K^{*\pm}$ ,  $\Sigma^{*\pm}$ ,  $\Xi^*$  and  $\Sigma^0$  have been obtained [109]. A significant difference was observed between  $K^{*\pm}$  yields in the NOMAD data and the NOMAD Monte Carlo simulation (about a factor of 2). It is also observed that  $K^{*+}$  production is more abundant than  $K^{*-}$  production in  $\nu_\mu$  charged current DIS. This can be explained by the fact that the outgoing  $u$  quark can fragment directly into a  $K^{*+}$ , while both the  $\bar{u}$  and  $s$  quarks needed to produce a  $K^{*-}$  meson have to be created in the fragmentation process. Recently, first measurements of  $K^{*\pm}$  meson production properties and spin alignment in  $\nu_\mu$  charged current and neutral current interactions were reported by the NOMAD collaboration [110]. The yields of  $K^{*+}$  and  $K^{*-}$  mesons produced in  $\nu$  charged current interactions showed a monotonic rise with the kinematic variables  $E$ ,  $W^2$  and  $Q^2$ . The diagonal element  $\rho_{00}$  of spin density matrix was obtained both for  $K^{*+}$  and  $K^{*-}$  in neutral current and charged current interactions. No spin alignment was observed for the charged current, whereas an indication for preferential production in the helicity zero state was observed for  $K^{*+}$  produced in neutral current interactions. However, the statistical errors did not allow to reach a firm conclusion [110].

### 3.5.5 Summary

The hadronic final state of an interaction gets rather complex by the increasing beam energies. The composition of the hadronic final state depends on the structure of the incoming particles and on the mechanisms which determine the formation of hadron during the fragmentation. The fragmentation of quarks and gluons and furthermore the suppression of strange quarks relative to light quarks can be better understood by investigation of strangeness production.

A comprehensive compilation of strangeness suppression factors measured by the different experiments is given in Fig. 3.13. The strangeness suppression factor  $\lambda_s = 0.3$  was found to be appropriate for the  $e^+e^-$  annihilation. However, there are indications that different values may be needed for different experiments, i.e. a single  $\lambda_s$  value cannot accommodate the data in all kinematic regions in one experiment.

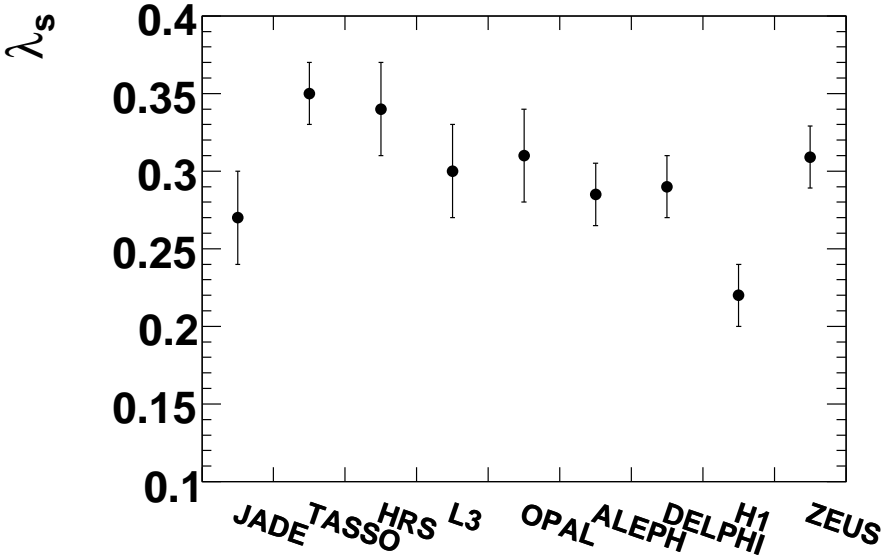


Figure 3.13: The strangeness suppression factor measured by the different experiments.

# Chapter 4

## HERA and the H1 Detector

In this chapter, the  $ep$  collider HERA at the DESY laboratory in Hamburg is introduced. The H1 detector at HERA, which was used to measure the data which are analysed in this thesis, is described.

### 4.1 The HERA Ring

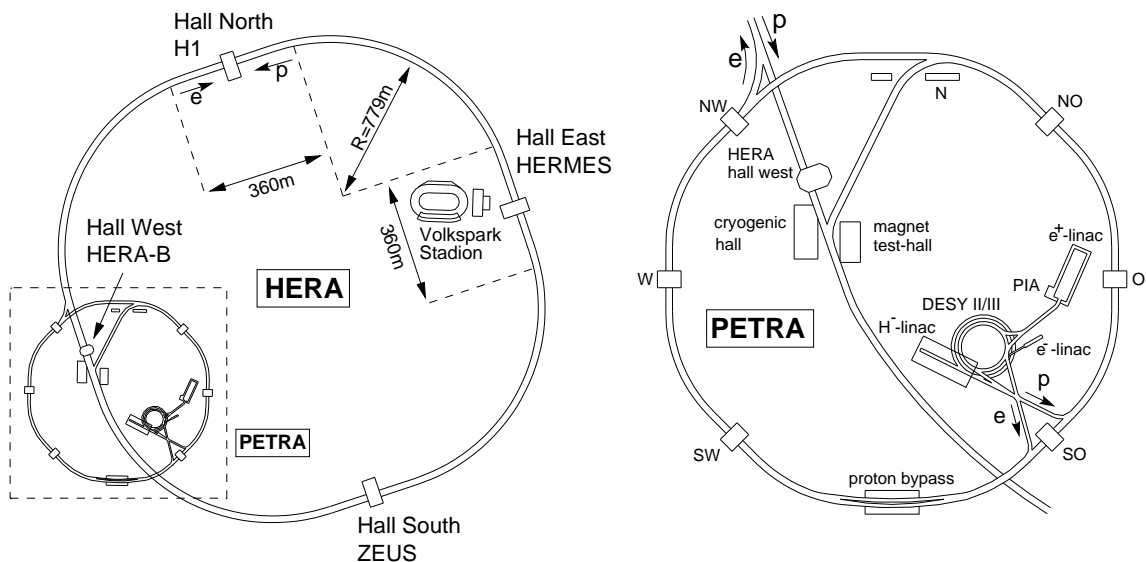


**Figure 4.1:** Layout of HERA collider, and its injection and its pre-accelerators.

The HERA [111], the first electron-proton collider, is a unique machine because of its asymmetry. Protons and electrons are circulated at high energies in opposite directions and brought to collision. Fig. 4.1 shows an overview of the HERA facility and its pre-accelerators system with the location of the different detector halls. Two independent rings, situated in a 6.3 km long tunnel, are used for acceleration and storage of the electrons and protons.

The proton injection into the ring starts with the acceleration of negatively charged hydrogen ions up to 50 MeV in the linear accelerator ( $H^-$ -linac). In order to obtain the protons, the electrons are stripped off the ions before injection into the DESY III ring. 11 bunches with a bunch crossing distance of 96 ns, identical to HERA, are filled into the DESY III ring and accelerated up to 7.5 GeV. After accumulating 70 bunches, the bunches are transferred to the PETRA<sup>1</sup> storage ring. The bunches are accelerated up to an energy of 40 GeV and then transferred to the HERA ring. The procedure is repeated until HERA is filled with 210 proton bunches. In the HERA ring, the protons are accelerated to their final energies of 920 GeV.

The lepton acceleration starts with the LINAC I or II for electrons or positrons, respectively. They are accelerated up to an energy of 450 MeV. A single bunch of electrons ( $\sim 60$  mA) is filled into the lepton intensity accumulator and is transferred to DESY II, where it is accelerated to 7 GeV. After accumulating 70 bunches, the bunch is injected into PETRA II with 96 ns spacing. 210 bunches are finally injected into HERA after the electrons were accelerated to 14 GeV. Every 96 ns the bunches cross each other, however, not all the bunches have a collision partner. The bunches with no colliding partner, so-called *pilot bunches*, are used to estimate beam induced background.

Altogether, there are four experiments located around the ring, the two collider experiments H1 and ZEUS [112] and the two fixed target experiments HERA-B [113] and HERMES<sup>2</sup> [114]. Protons and electrons are brought to head-on collisions in an interaction region in the centre of the H1 and ZEUS detectors. The third detector HERMES was added in 1995 and records the scattering of polarised electrons on polarised gas targets. The HERA-B detector, completely installed in 2000, was designed to measure the CP violations in  $B^0 - \bar{B}^0$  systems generated through collisions of beam protons with a stationary wire target.

The performance of an accelerator is characterised by the produced integrated luminosity, which is proportional to the number of events expected in  $ep$  collisions

$$N^{ep} = L \cdot \sigma^{ep}, \quad (4.1)$$

where  $\sigma^{ep}$  is the total  $ep$  cross section. The total produced luminosity is defined as the time-integrated instantaneous luminosity  $\mathcal{L}(L = \int \mathcal{L} \cdot dt)$ .  $\mathcal{L}$  depends on the bunch-crossing frequency, the number of particles per bunch and the collimation of the beams. Hence, the luminosity is strictly limited by the accelerator design. Fig. 4.2 shows the integrated luminosity produced by HERA and used for physics analyses by H1 in different years. The HERA running is divided into the HERA I period from 1994 to 2000 and the HERA II period from 2002 to 2007. The machine had an extended shutdown and upgrade in 2001. The main goal was to increase the delivered luminosity by a factor of 4 to 5 by inserting super-conducting quadrupole magnets close to the H1 and ZEUS interaction regions. Spin rotators were installed to provide the interaction regions with a longitudinally polarised electron beam.

In this thesis, the data taken in 2005-2007 with the integrated luminosity of  $\sim 302 \text{ pb}^{-1}$  are

<sup>1</sup>Positron Elektron Tandem Ring Anlage

<sup>2</sup>HERA MEasurement of Spin

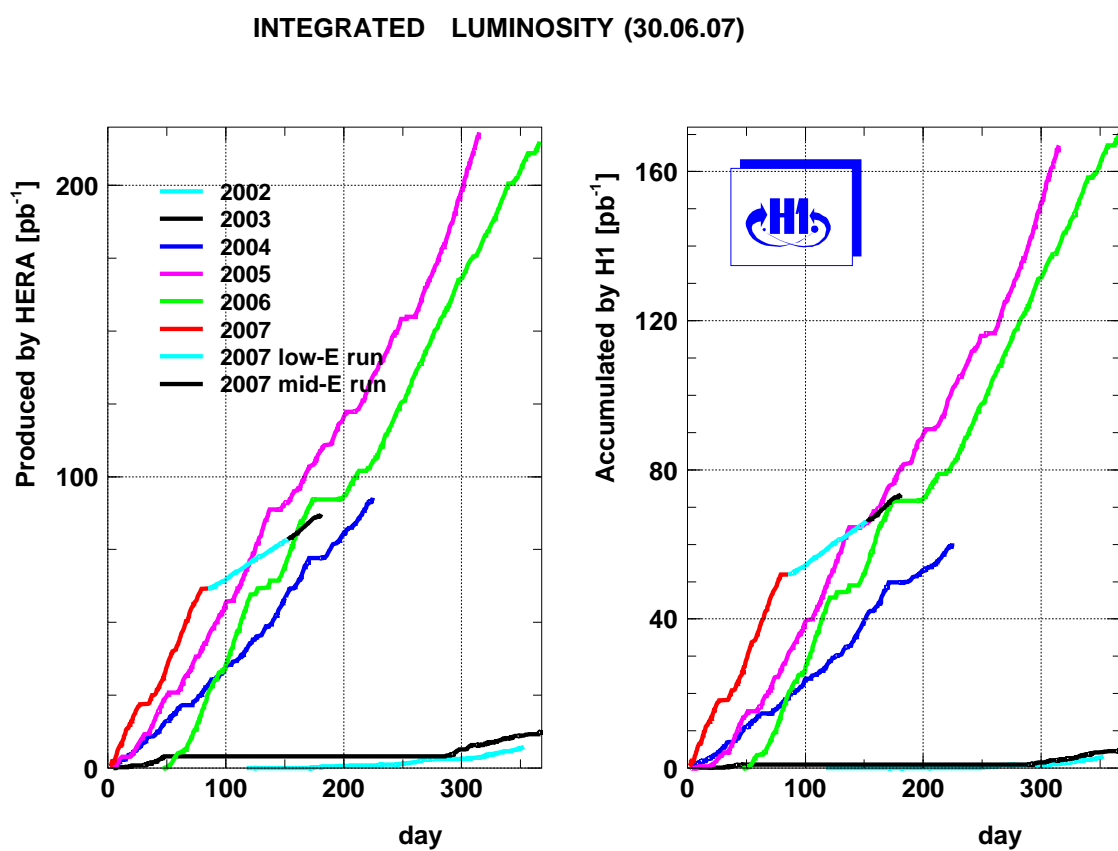


**Figure 4.2:** Luminosity produced by HERA (left) and accumulated by H1 (right) in individual years [115].

analysed. During this period, HERA operated with the beam energies 27.6 GeV for electrons and 920 GeV for protons, yielding a centre-of-mass energy  $\sqrt{s}= 319$  GeV.

## 4.2 The H1 Detector

The multi-purpose detector H1 [116] at the northern part of the HERA ring was designed to measure the direction, energy and charge of particles resulting from the  $ep$  interactions produced by the HERA machine. It provides nearly hermetic coverage of the interaction region, the main limitation coming from the space occupied by the beam pipe itself.

A right-handed Cartesian coordinate system, shown in Fig. 4.3, is used to describe the orientation of the detector, such that the  $z$ -axis follows the direction of the proton beam, the  $y$ -axis points vertically upwards with respect to the ground and the  $x$ -axis points to the centre of HERA ring. The origin of the coordinate system is the nominal interaction point within the detector.

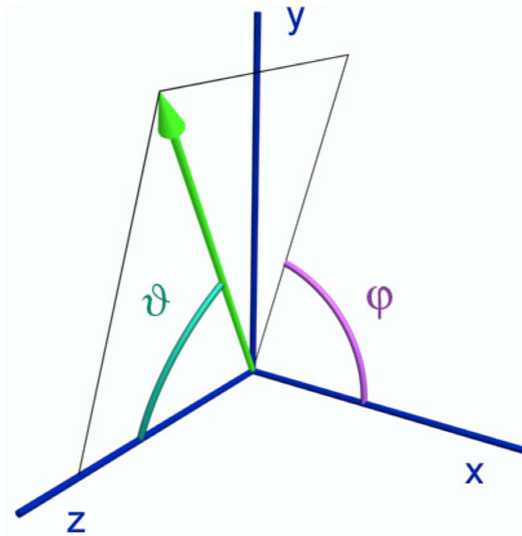


**Figure 4.3:** An illustration of the H1 coordinate system.

It is also convenient to use the cylindrical polar coordinates. In this system  $r$  lies perpendicular to the  $z$  coordinate, the polar angle is defined as  $\theta = 0^\circ$  for the proton direction and  $\theta = 180^\circ$  for the electron direction. The azimuthal angle  $\phi = 0^\circ$  points along the  $x$ -direction.

Another important variable which is often used for the ultra-relativistic particles is the pseudorapidity  $\eta$

$$\eta = -\ln \left[ \tan \frac{\theta}{2} \right]. \quad (4.2)$$

In the limit where the particle is travelling close to the speed of light, or in the approximation that the mass of the particle is nearly zero (massless particles),  $\eta$  corresponds to

the rapidity<sup>3</sup>,  $y$  :

$$y = \frac{1}{2} \ln \frac{E + p_z}{E - p_z}, \quad (4.3)$$

where  $p_z$  is the component of the momentum along the beam direction and  $E$  is the energy.

A useful feature of  $\eta$  and  $y$  is that they transform linearly under the Lorentz boosts along the  $z$  axis. The consequence is that (pseudo)rapidity differences  $\Delta y$  ( $\Delta\eta$ ) are invariant under such boosts. The proton has a larger momentum than the electron, hence the majority of the products of the  $ep$  interactions are produced with large positive values of the pseudorapidity ( $z > 0$ ,  $\eta > 0$ ,  $\theta < 90^\circ$ ), so-called *forward* region. The region having large negative values of pseudorapidity ( $z < 0$ ,  $\eta < 0$ ,  $\theta > 90^\circ$ ) is called the *backward* region.

In Fig. 4.4 the H1 detector is illustrated with its major detector components. In total, the H1 detector measures approximately  $12 \times 10 \times 15 \text{ m}^3$  (length  $\times$  width  $\times$  height) and weighs 2800 tons. Due to the different beam energies the H1 detector was instrumented asymmetrically. Electrons enter from the left, protons from the right side of the interaction region (see Fig. 4.4). The interaction point is surrounded by a tracking system in which the trajectories of charged particles, bent due to a magnetic field, are measured. The tracking system is surrounded by calorimeters. The calorimeters are contained within a  $B = 1.15 \text{ T}$  homogeneous magnetic field provided by a superconducting magnet. The field allows to determine the charge and momentum of charged particles. The iron return yoke of the superconducting magnet consists of ten iron plates which are instrumented with limited streamer tubes for muon detection. In the following, the focus will be on those detector components which are relevant for the analysis presented in this thesis.

---

<sup>3</sup>Note that the same term “ $y$ ” was already used to denote the inelasticity in section 2.2.1. Unless otherwise stated  $y$  will be used to refer to inelasticity.

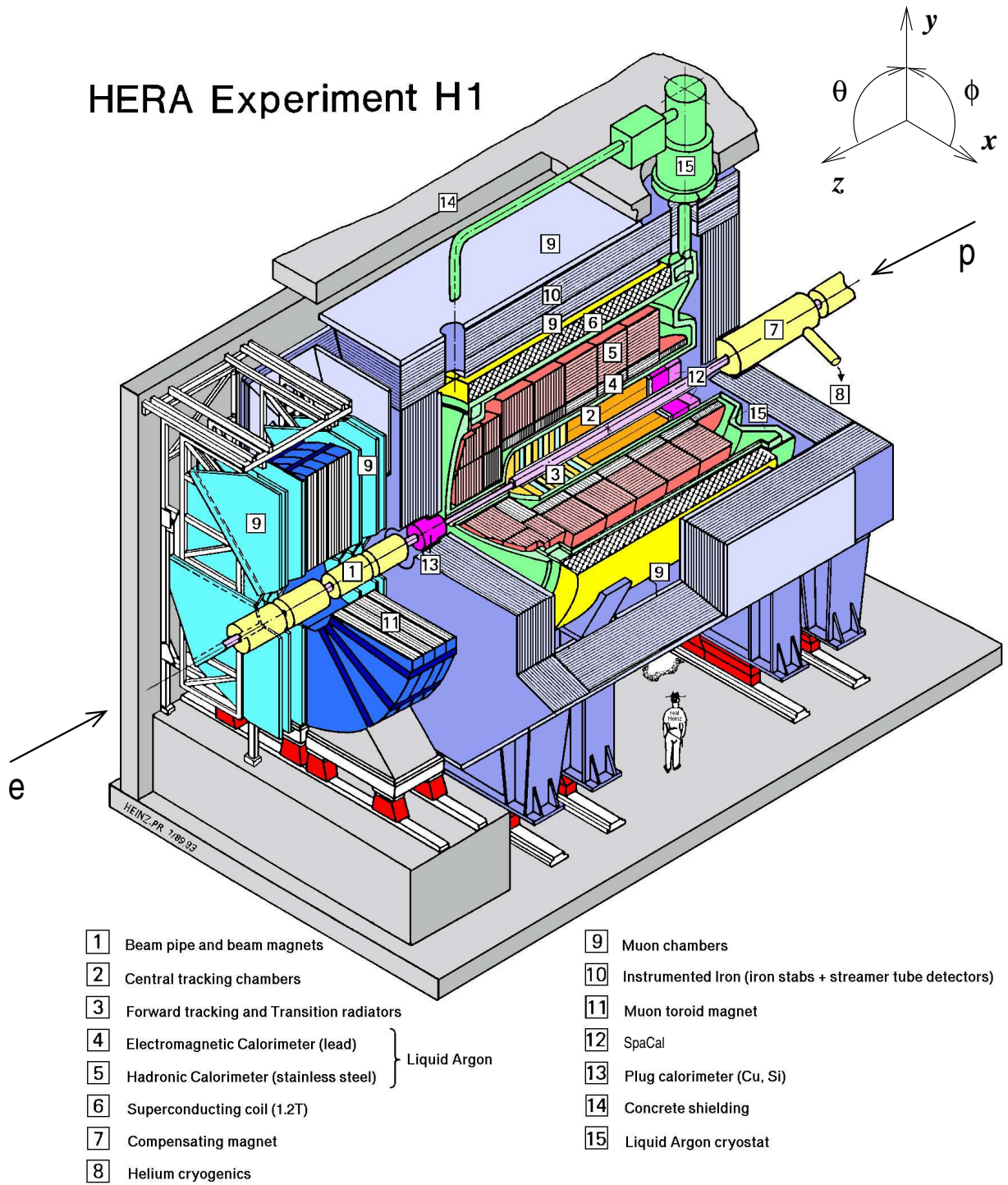
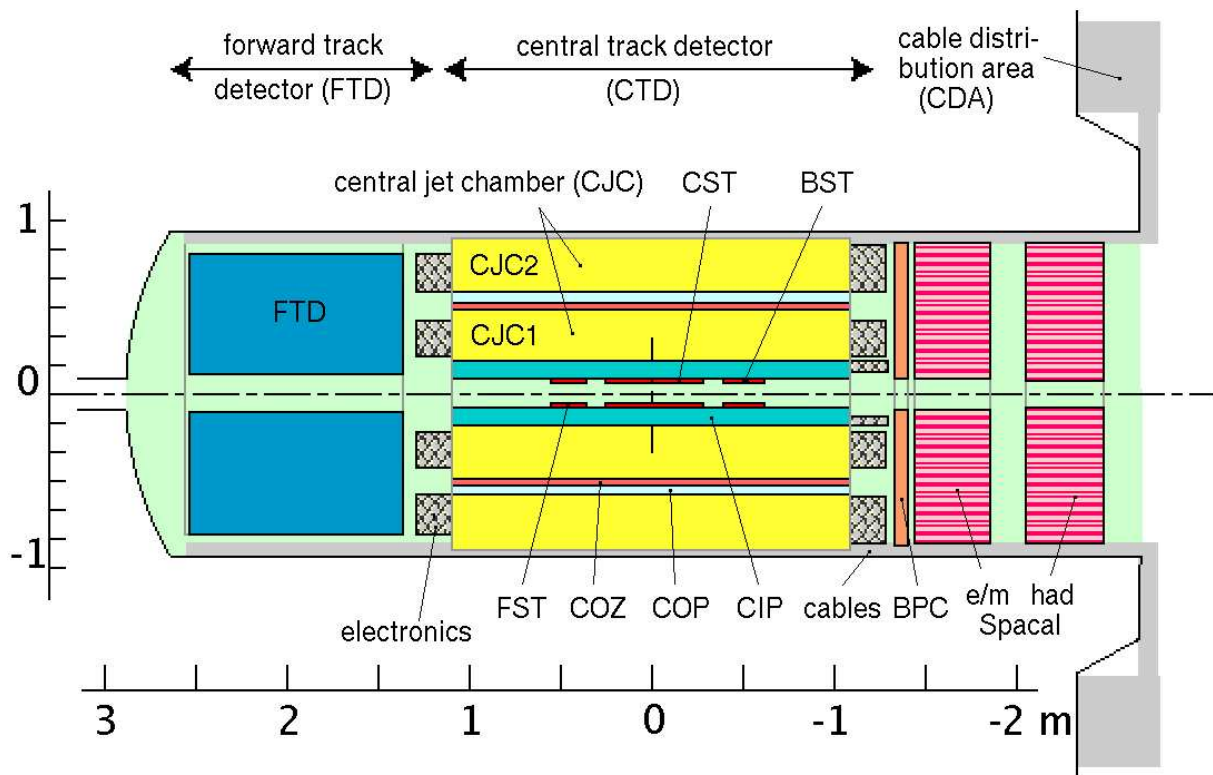


Figure 4.4: The H1 detector with its major components [117].

## 4.3 Tracking System

The tracking system of H1 is used for the track reconstruction, vertex determination, momentum measurement and particle identification. It is surrounding the interaction region and covers the angular range  $5^\circ < \theta < 178^\circ$  with full azimuthal coverage. Fig. 4.5 gives a longitudinal view of H1 tracking system with the central tracking detector (CTD) and forward tracking detector (FTD). In order to have high efficiency of the track reconstruction in the full angular range the tracking system is divided into two distinct components, the CTD and the FTD.



**Figure 4.5:** A longitudinal view of the H1 tracking system including the central and forward tracking detectors.

### 4.3.1 Central Tracking Detector

The CTD covers the region  $15^\circ < \theta < 165^\circ$  and consists of two large concentric drift and multiwire proportional chambers.

- Drift chambers consist of cells which are filled with gas and contain anode sense wires and a cathode plane. The high voltage applied to the anode wires and cathode wires creates a nearly uniform electric field. The charged particles pass through

the chamber, the electrons created by ionisation in the gas *drift* (hence the name drift chamber) towards the anode wires whereas the positive ions drift toward the cathode wires. As the electrons approach the wire, the increased field strength induces secondary collisions with the gas atoms. This *avalanche* of collisions around the anode induces a current and a resulting pulse along the wire. A precise spatial measurement is possible in the drift volume through the measurement of the electron drift time.

- Multiwire proportional chambers (MWPC) are similar to drift chambers except that they consist of many closely placed anode wires lying between cathode wires. Because the anode wires are placed closely, the electrons drift towards the closest anode wire and consequently secondary ionisations are produced due to the high field. The signal received is *proportional* to the initial ionisation, hence the term proportional. The signals are collected promptly enough for use in triggering and give a spatial precision of the wire spacing ( $\sim 10$  mm).

Fig. 4.6 shows a radial view of the CTD. The principal components of CTD are the central jet chambers (CJC). The CJC1 and CJC2 [?] are two large drift chambers in the CJC. CJC1 (CJC2) consists of 30 (60) with 24 (32) wires parallel to the  $z$  axis. The main purpose of the CJC1 and CJC2 is to provide an accurate measurement in the  $r - \phi$  plane, hence their sense wires run parallel to the beam pipe. The CJC has a spatial resolution of  $\sigma_{r\phi} = 170 \mu\text{m}$  and  $\sigma_z = 2.2$  cm.

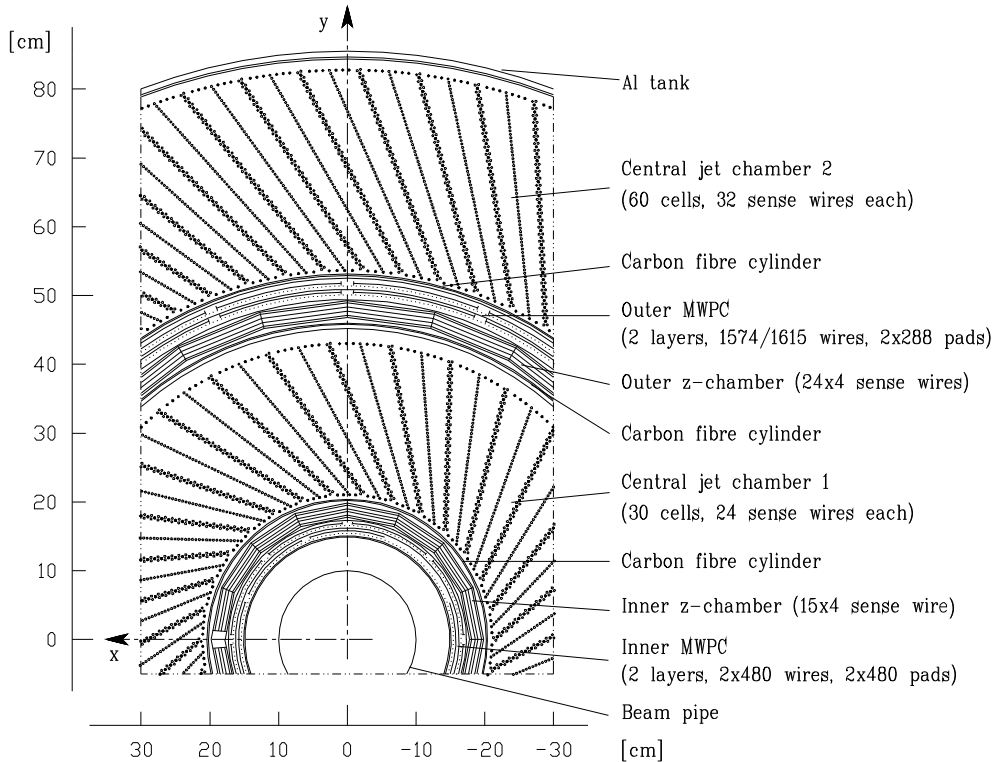


Figure 4.6: A radial view of the central tracking.

The resolution in  $z$  is significantly enhanced by two additional  $z$ -chambers: Central Inner  $z$ -Chamber (CIZ) [?] and Central Outer  $z$ -Chamber (COZ) [?]. These thin drift chambers are directly adjacent inside and outside of the CJC1. They have circular sense wires perpendicular to the beam axis. This allows for a measurement of the  $z$ -position with an accuracy of typically  $300 \mu\text{m}$ .

The central tracking system is completed by two MWPCs. The Central Inner Proportional Chamber (CIP) is located inside of the CIZ whereas the Central Outer Proportional Chamber (COP) placed between COZ and CJC2. The CIP and CIZ were replaced for the HERA II period by a five-layer proportional chamber with high granularity (CIP2k) [?] in order to overcome the increased non- $ep$  background.

### 4.3.2 Forward Tracking Detector

The Forward Tracking Detector (FTD) is a set of drift chambers designed to detect tracks in the polar angle range  $5^\circ < \theta < 25^\circ$  from the interaction point and was upgraded for the HERA II. It consists of three identical supermodules aligned along the  $z$ -axis. Each of super module contains a planar drift chamber and a proportional chamber.

### 4.3.3 Track Reconstruction

The tracks used in this analysis are reconstructed using the CTD and are used to determine the interaction vertex, the track of the scattered electron and of particles of the hadronic final state. The raw digitised detector information is used to reconstruct the tracks and the vertices from which they originate. The first step, *hit finding*, uses the raw detector data as an input and finds the corresponding space coordinate where a particle interacted with the medium of the detector, referred to as *space hit*. The next stage is either fitting parts of tracks (referred to as *track segments*) and then combining these segments to one track extending to the full acceptance of the detector or skipping segment finding and fitting directly a full track obeying an adequate track model. In both cases a fast, iterative pattern recognition fitting procedure is used in order to find from a significant number of hit combinations the ones coming most probably from physical particles and reject the rest of the combinations following a strict fit quality criterion. Finally based on the track information the most probable position of a *primary* and a set of *secondary* vertices is defined and each track is refitted to the corresponding vertex to which it is associated.

The charged particle which moves in a homogeneous magnetic field is forced to a circular trajectory in the plane perpendicular to the magnetic field. The whole helix trajectory is described by five parameters ( $\kappa$ ,  $d_{ca}$ ,  $z_0$ ,  $\theta$  and  $\phi$ ). The helix trajectory parameters are shown in Fig. 4.7.

- **Track curvature**,  $\kappa$ , is a measure of the transverse momentum of a track which

can be calculated from

$$p_T[\text{GeV}] = -Q[\text{C}] \cdot \frac{c\left[\frac{\text{m}}{\text{s}}\right] \cdot B_z[\text{T}]}{\kappa[\text{m}^{-1}]}, \quad (4.4)$$

where  $Q$  is the charge of the particle track,  $B_z$  is the  $z$ -component of the magnetic field. The track curvature  $\kappa$  is the signed inverse radius of the track,  $\kappa = \pm\frac{1}{r}$ . The sign of  $\kappa$  is defined by the direction of movement of the particle track. If the particle moves clockwise,  $\kappa$  is negative, otherwise  $\kappa$  is positive.

- **Distance of closest approach**,  $d_{ca}$ , is the smallest distance between the track and the origin of H1 coordinate system (Fig. 4.7a).
- **The coordinate**,  $z_0$ , is the distance measured in  $z$  from the origin of  $z$  axis to the point of closest approach  $d_{ca}$  (Fig. 4.7b).
- **Polar angle**,  $\theta$ , is the angle between the tangent to the circle in the point of  $d_{ca}$  and the  $z$  axis.
- **Azimuthal angle**,  $\phi$ , is the angle defined by the direction of  $x$  axis of the H1 coordinate system and the tangent to the track to the circle in the point of  $d_{ca}$ .

Since a particle track is a circle in the  $r\phi$  plane and a straight line in the  $rz$  plane, the trajectory parameters can be obtained with a circular fit in the  $r\phi$  plane or a linear fit in the  $rz$  plane [?]. In the  $r\phi$  plane the track fitting procedure uses the hit information from the CJs for determining the parameters  $\kappa$ ,  $\phi$  and  $d_{ca}$ . The fitting procedure is extended using the information coming from other tracking detectors. In the end of the track fitting procedure the event vertex in the  $r\phi$  plane is determined with these tracks. The fitting procedure in the  $r\phi$  plane and in the  $rz$  plane are iterated with the additional constraint of the event vertex for the tracks which do not come from secondary vertices. Since the vertex information is determined from many tracks, an accuracy of the vertex position is achieved. The procedure provides tracks and more precise vertex fitted tracks.

## 4.4 Calorimetry

Calorimeters provide an energy measurement for all particles except neutrinos and muons of energies above a few GeV, complementing the momentum measurements provided by the tracking detectors for charged particles. In particular, calorimeters allow the reconstruction of the energy and direction of neutral hadrons and photons, which cannot be detected by tracking detectors. In addition, calorimeters improve the reconstruction of highly energetic charged particles; the relative energy resolution of calorimeters typically improves as  $\sigma/E \sim 1/\sqrt{E}$  with the energy  $E$  of the incident particles, in contrast to the tracking detectors, whose momentum resolution decreases as  $\sigma_{p_T}/p_T \sim p_T$ .

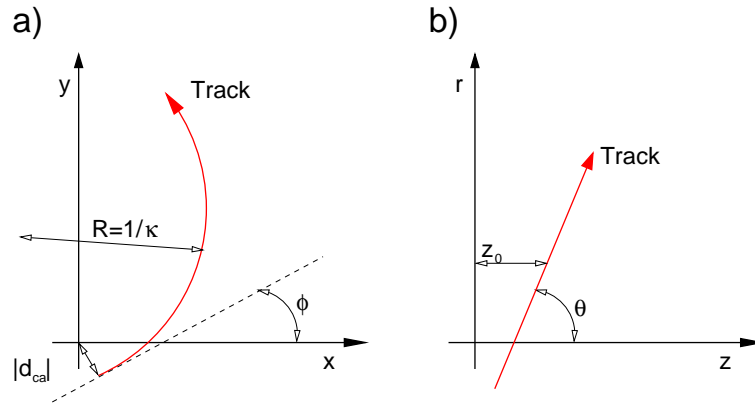


**Figure 4.7:** The definition of the helix trajectory parameters  $\kappa$ ,  $d_{ca}$ ,  $z_0$ ,  $\theta$  and  $\phi$  in  $xy$  plane a), and in  $rz$  plane b) [?].

For the energy reconstruction in calorimeters the total absorption method is mainly used. Due to the interactions between the incident particles and the calorimeter material, the incident particles are stopped and they finally lose all their energy. This energy is measured in the calorimeters, hence the term *calorimeter* [?].

All of the calorimeters used within H1 rely on the same detection principle. Each calorimeter consists of two main components: a series of absorbing (passive) layers and sampling (active) layers.

The passive layers absorb most of the energy of the incident particles. For this purpose the layers are designed of dense materials which have a small mean path length between subsequent interactions of incident particles. Dense materials which have high atomic charge number  $Z$  are used for the electromagnetic section of the calorimeter whereas large absorbing masses are needed for the hadronic section of the calorimeter. Electrons and photons lose energy in a calorimeter via electromagnetic interactions with the atomic nuclei in the passive layers. This occurs rapidly via the bremsstrahlung and pair-production processes. The resulting shower consists of electrons, positrons and photons. Longitudinal progress of electromagnetic shower is characterised by the radiation length of the passive layer,  $X_0$ , which is the mean distance in which it loses all but  $1/e$  of its initial energy in that material.

Hadrons interact strongly with the nuclei of the passive layers, elastically and inelastically resulting in a shower which is determined by the interaction length of the passive layer,  $\lambda_i$ . The interaction length  $\lambda_i$  is much larger than  $X_0$  for the same material and hence hadronic showers will develop more slowly than electromagnetic ones. Since the hadronic showers tend to be more spread out laterally than the electromagnetic showers, hadronic showers are topologically distinguishable from electromagnetic showers.

The energy absorbed in the passive layers is measured in the active layers. Several methods can be applied in order to measure the absorbed energy. In the H1 detector, mainly the liquid-filled ionisation chambers are used to count the number of charged shower particles entering the active layers from the passive layers.

The calorimeter system of the H1 detector comprises four calorimeters. The Liquid Argon Calorimeter (LAr), which covers the central and forward regions. The “spaghetti” calorimeter SPACAL covers the backward region. The PLUG calorimeter covers the very forward region closest to the beam pipe ( $0.6^\circ < \theta < 3.5^\circ$ ) closing the gap between the forward part of LAr and the beam pipe. The energy leakage through the LAr is detected by the Tail Catcher (TC). TC is only important for jets with very high energies (above 120 GeV).

#### 4.4.1 The Liquid Argon Calorimeter

The LAr [?] calorimeter covers a large part of the solid angle around the interaction point of  $ep$  collisions with an angular coverage  $4^\circ < \theta < 154^\circ$ . The main advantages of LAr are ease of calibration, high stability, possibility of fine granularity and homogeneity of the response. The LAr is located in a cryostat inside the solenoid coil to minimise the amount of the dead material in front of the calorimeter. The total thickness of the LAr varies between 4 to 8 interaction lengths ( $\lambda$ ). It is composed of two sections, an *electromagnetic calorimeter* (ECAL) with lead absorbers and a *hadronic calorimeter* (HCAL) with steel absorbers. The ECAL and HCAL are segmented into about 45000 cells. These cells consist of high voltage planes and read out pads.

For easier handling, the LAr calorimeter is divided into 8 wheels that are shown in Fig. 4.8.

- Backward Barrel Electromagnetic calorimeter (BBE),
- Central Barrel calorimeter modules (CB1, CB2, CB3),
- Forward Barrel calorimeter (FB1, FB2),
- Outer and Inner Forward calorimeters (OF, IF).

In the radial direction, all wheels except the BBE and OF are composed of an ECAL and a HCAL, respectively. The OF consists of two HCAL and the BBE of one ECAL. The wheels are divided into eight octants in the azimuthal angle  $\phi$ . The shape of the BBE octants is made such that the BBE has a 16-fold symmetry. The regions between modules are problematic for the measurement due to energy losses and inactive materials. These gaps between the wheels are called  $z$  – *cracks*, between the octants  $\phi$  – *cracks*.

With the test beam measurements [?, ?] an electromagnetic energy resolution of

$$\frac{\delta_{el}(E)}{E} = \frac{0.12}{\sqrt{E [GeV]}} \oplus 0.01 \quad (\text{for electron}), \quad (4.5)$$

and a hadronic energy resolution of

$$\frac{\delta_{had}(E)}{E} = \frac{0.50}{\sqrt{E [GeV]}} \oplus 0.02 \quad (\text{for pion}), \quad (4.6)$$

were determined.

### 4.4.2 The SPACAL Calorimeter

In the backward region, the LAr is complemented by the SPACAL [?] which covers the polar angle range  $153^\circ < \theta < 177.5^\circ$  that implies a coverage in photon virtuality of  $1 < Q^2 < 100 \text{ GeV}^2$ . The SPACAL was installed in the 1994/1995 shutdown, replacing the previous backward calorimeter (BEMC [?]). The purpose of SPACAL is the detection of electrons scattered at small angles (large polar angles  $\theta$ ). In addition, it allows the measurement of backward jets. Fig. 4.9 shows the location of the SPACAL in the H1 detector.

The SPACAL, like LAr, is a non-compensating<sup>4</sup> sampling calorimeter with an electromagnetic and a hadronic section. Both parts are fabricated using grooved lead plates and long scintillating fibres (hence so-called “spaghetti”). The incident particles cause electromagnetic and hadronic showers in the lead. The detection of those particles is done by the excitation of the molecules in scintillator material. The collection of scintillation light is done at the backward end of the fibres. The scintillation light is collected by photomultiplier tubes where the light is converted into electrical signals.

The electromagnetic energy scale calibration is done by comparing the energy deposit of reconstructed electrons with the expectation determined by the *double angle method* [118] in neutral current DIS events. The neutral current DIS events are also used to calibrate the hadronic energy scale by requiring the transverse momentum of the hadronic final state to balance that of the calibrated scattered electron [119]. The electromagnetic part is composed of 1192 cells of size  $4.05 \times 4.05 \text{ cm}^2$ . This ensures a good spatial resolution. The depth corresponds to 27.5 radiation lengths. The fine granularity allows for a good  $e/\pi$  separation. In the test beam measurements, an energy resolution of the SPACAL for electrons [120]

$$\frac{\delta_{el}(E)}{E} = \frac{0.07}{\sqrt{E [\text{GeV}]}} \oplus 0.01, \quad (4.7)$$

and for single charged pions [121]

$$\frac{\delta_{had}(E)}{E} = \frac{0.50}{\sqrt{E [\text{GeV}]}} \oplus 0.02, \quad (4.8)$$

was determined. In the same test beam setup the time resolution of SPACAL was determined to be  $\delta_{cal} = 0.38 \pm 0.03 \text{ ns}$  [122]. As a consequence, the SPACAL provides a precise *time-of-flight* measurement, that can allow the rejection of non- $ep$  background, which is asynchronous to the nominal bunch crossings of 96 ns.

As mentioned earlier, with the installation of the new magnets, the SPACAL had to be

---

<sup>4</sup>Non-compensating term means that the energy response of the calorimeter is different for electrons and pions entering the calorimeter with same energy.

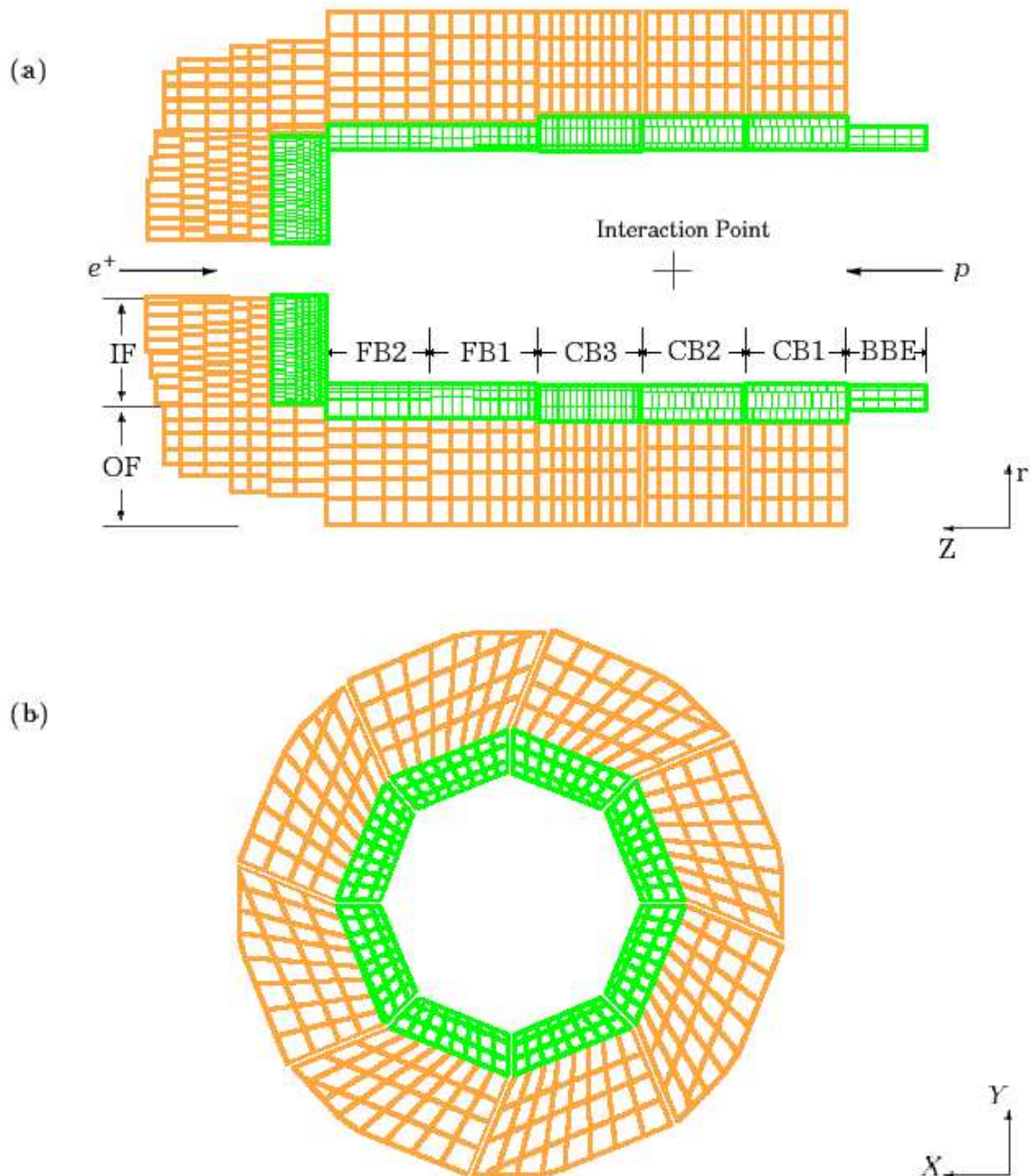


**Figure 4.8:** The LAr Calorimeter. a) the structure of wheels, b) the octant structure of wheels.

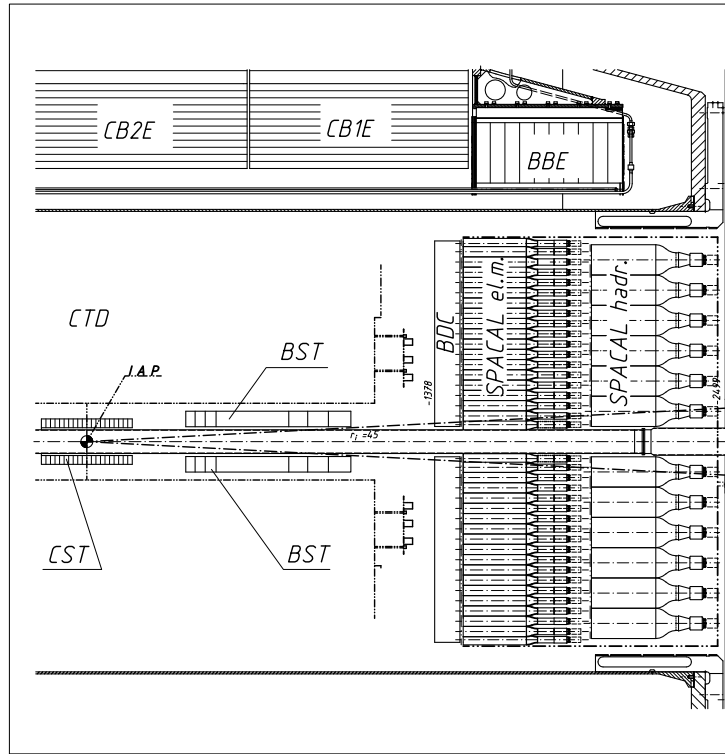


**Figure 4.9:** The location of SPACAL in the H1 detector.

modified during the HERA II running period. In particular, some modules of the hadronic part were removed by lowering the range to  $153^\circ < \theta < 174^\circ$  [123].

## 4.5 Luminosity Measurement

An essential part of a cross section measurement is the accurate determination of the integrated luminosity which corresponds to the amount of collected data. Integrated luminosity  $\mathcal{L}$  is the integral over the instantaneous luminosity  $L$ , which connects the cross section  $\sigma$  and event rate  $dN/dt$ :

$$\frac{dN}{dt} = L \cdot \sigma. \quad (4.9)$$

Integration over the whole measurement yields  $N = \mathcal{L} \cdot \sigma$ . Hence this equation shows how the luminosity can be measured. If the cross section of a process is well known from theory, the event rate of the process can be used to obtain the luminosity.

The luminosity in H1 is measured by counting the rates of the Bethe-Heitler (BH) bremsstrahlung process ( $ep \rightarrow ep\gamma$ ) [124]. This process is a reference process with a theoretically well known cross section and an experimentally clean signal. The main background source to BH process is bremsstrahlung from the beam pipe residual gas;  $eA \rightarrow e\gamma A$ . In order to exclude the background processes, the electron pilot bunches are

used. The H1 luminosity system serves for several purposes:

- Online and offline luminosity measurement,
- Energy measurement of scattered electrons at small angles and tagging of photo-production events,
- Initial state radiation measurement,
- Electron beam monitoring for HERA.

The layout of the luminosity system is shown in Fig. 4.10. The electron tagger (ET) and photon detector (PD) are the two principal components of the system. The ET was installed at  $z = -5.4$  m, where scattered electrons are directed into its acceptance by the beam optics. The PD was placed next to the proton beam pipe at  $z = -101.8$  m for HERA II. Determination of the luminosity is done with two different methods. Online luminosity measurement is done with the coincidence method where the simultaneous detection of outgoing photons and scattered electrons is required. In the single-photon method, used for the offline luminosity measurement, the number of BH events with a certain photon energy above the threshold is counted.

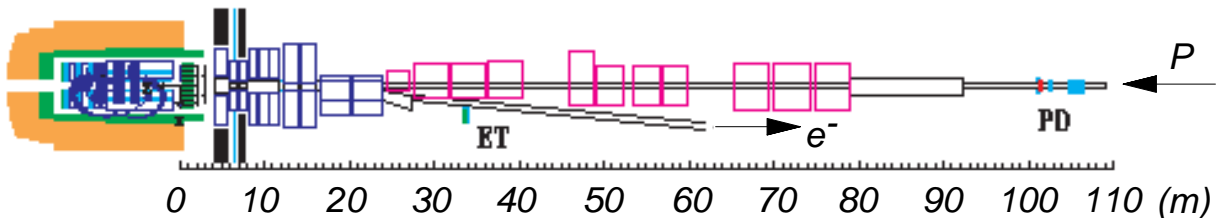


**Figure 4.10:** The luminosity system. The ET is placed at  $-5.4$  m, PD is at  $-101.8$  m for HERA II.

## 4.6 Time-of-Flight System

The rejection of background originating mainly from non- $ep$  interactions is vital in order to record efficiently  $ep$  scattering events. The major source of such interactions is beam gas or beam wall collisions. The Time-of-Flight (ToF) system is used to reject such background interactions.

The ToF system shown in Fig. 4.11 consists of plastic scintillation detectors placed at various locations around the H1 detector: within the backward iron endcap (BToF), within the unused gaps of the Plug absorber (PToF) and close to the forward muon detector (FToF). The non- $ep$  interactions can produce significant signal in the central detectors,

but arrive at a time  $|z|/c$  before or after the desired  $ep$  interactions ( $z$  is the position of the ToF along the beam line).

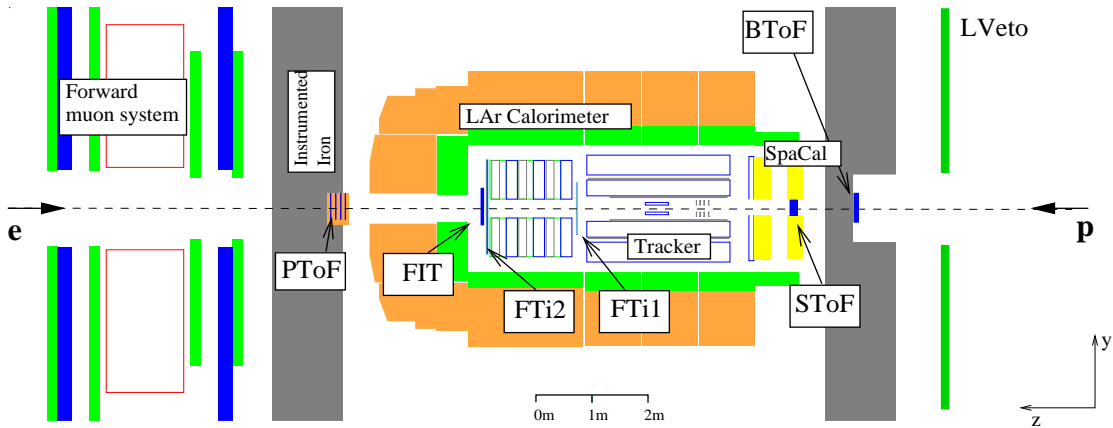


Figure 4.11: The Time-of-Flight system.

## 4.7 Trigger and Data Acquisition

Every bunch crossing of HERA can lead to  $ep$  interactions, i.e., a decision needs to be taken every 96 ns whether the detector information is to be recorded. The time of 96 ns corresponds to the very high beam crossing frequency 10.4 MHz. The detection of the interesting physics events from the genuine  $ep$  collisions is a challenge for the H1 detector since the background is orders of magnitude higher than the expected rate of  $ep$  collisions. Due to hardware and cost limitations the rate at which events can be permanently stored is about 20 Hz. Thus, the H1 trigger system [125, 116] which is used for the online selection of genuine  $ep$  collisions, consists of several levels, denoted L1 to L4. Only after an event has been accepted by all these four systems, it is written to tape and analysed by the offline reconstruction. An illustration of the data flow through the H1 trigger system is shown in Fig. 4.12.

The first level trigger, L1, consists of around 200 *trigger elements* providing information from different parts of the detector. These elements are combined into 128 *subtriggers*, the majority of which are designed to select a variety of different physics processes, although some are used to monitor background and trigger efficiencies. An event is kept if one of 128 *subtriggers* (S0-S127) has fired. The decision of L1 takes 22 bunch crossings ( $2.3 \mu\text{s}$ ), so all of the information from subsequent bunch crossings is kept in a pipeline, ensuring

new data can be constantly taken. This causes a free deadtime on L1 trigger. The trigger elements are linked logically and the L1 decides whether an event is rejected or accepted.

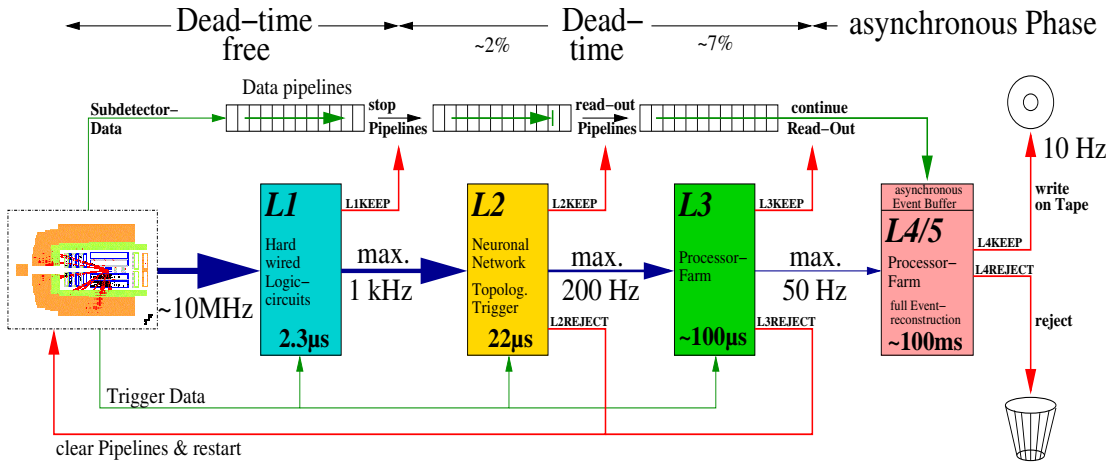


**Figure 4.12:** An illustration of the data flow through the H1 trigger system.

More complex decisions than possible in L1 can be taken at the second level trigger L2. The L2 is constructed of two different processor systems as topological triggers L2TT [126] and neural network triggers L2NN [127]. These systems confirm or falsify the decisions of L1 within  $20 \mu\text{s}$ . L2TT uses a grid in  $(\theta, \phi)$  on which signals are projected to discriminate against background events and to select events of interest. L2NN makes use of neural network algorithms applied to the information delivered by the detectors. When the L2 trigger accepts an event, the time consuming treatment of the information coming from the detectors starts.

The third level trigger L3 was designed to further select events within  $800 \mu\text{s}$  [128]. L3 may interrupt the time consuming detector readout and prematurely end the dead time. In the HERA I running period the L3 trigger was not used. Instead, the L2 was configured to meet the maximal L4/5 input rate. In the HERA II running period L3 was installed as a part of fast track trigger (FTT) [129] and was in operation since 2006 summer. The FTT is integrated in the H1 trigger system with the characteristic that the third level of the H1 trigger system is realised as the FTT L3 system. The task of the FTT system is to provide a high reduction factor to cope with the increased event rates at the upgraded HERA machine. The FTT utilises 12 wire layers out of the 56 wire layers of the H1 Central Jet Chambers. These 12 wire layers are organised in four trigger layers of three wire layers within which a search for track segments is performed.

After the completion of subsystem readout, all further steps for the data taking do not happen synchronously, whenever the relevant processors are available. The level four trigger L4 has access to all raw data and could hence be used to reconstruct the full online event with the full intrinsic detector resolution. Reject or accept decision is taken with 50 Hz. In case of a L4 accept signal, the raw data of the full event is stored permanently to disk. L4 is also used for monitoring purposes by filling online histograms that can be evaluated by the detector shift crews. Table 4.1 shows the rates of the main background processes and some physics interactions.

Process	Rate
Bunch crossing rate	10.4 MHz
Beam induced background	$\leq$ 50 kHz
<i>ep</i> interactions	$\sim$ 1 kHz
DIS $1 < Q^2 < 10 \text{ GeV}^2$	$\sim$ 40 Hz
DIS $Q^2 > 10 \text{ GeV}^2$	$\sim$ 4 Hz
Heavy quark production	$\sim$ 0.05 Hz
Charged current	$\sim$ 0.01 Hz

**Table 4.1:** The rates of the main background and some physics processes.

Events passing all precedent trigger levels are permanently written to tape in two different formats. If an event belongs at least to one class, it is stored on so called physics output tapes (POTs) or in a compressed way on disks named data summary tapes (DSTs). POTs contain the whole event data including raw and reconstructed information. DSTs only store a subset of predominantly reconstructed quantities. The data used in this thesis are stored on DSTs.

# Chapter 5

## Monte Carlo Simulation

One of the main goals of an experiment is to test theoretical models and possibly contribute to a better understanding of the physics involved. Theoretical calculations are complemented with phenomenological models where the calculations are too complicated to be solved analytically. In addition MC simulations are used to correct for limited geometrical acceptance of the detectors and to understand the effects of the detector resolution on kinematic variables. The first output of the MC simulation is a list of all particles that participated in the event during one or more of its phases, from the initial colliding particles and exchanged boson, to the final hadrons (so called *physics simulation*). The list of final state particles is then propagated through a *detector simulation* program which simulates the response of the detector components to individual particles.

In this chapter the basic principles of MC event generators and models are presented. The main MC generators which were used in this analysis are introduced.

### 5.1 Monte Carlo Event Generators

Monte Carlo event generators are used to model events as detailed as they could be observed by a perfect detector. Since the process of event generation is too complex to be performed in one go, it is subdivided into several steps. A schematic view of the stages to be followed by a MC event generator for  $ep$  scattering is shown in Fig. 5.1 and consists of the following stages:

**Parton density functions (PDFs):** represent the probability to find a parton in the proton at a particular value of  $Q^2$  and  $x$ . PDFs cannot be derived from the first principles and have to be determined from the data. This is done by adjusting a starting distribution such that after the parton evolution to large scales and a convolution with matrix elements (ME) data are described. In this thesis different sets of PDFs have been used depending on the MC program.

**Hard sub-process:** Lepton-parton or parton-parton interactions where substantial transverse momenta are involved are called the *hard sub-process*. The generation of the hard

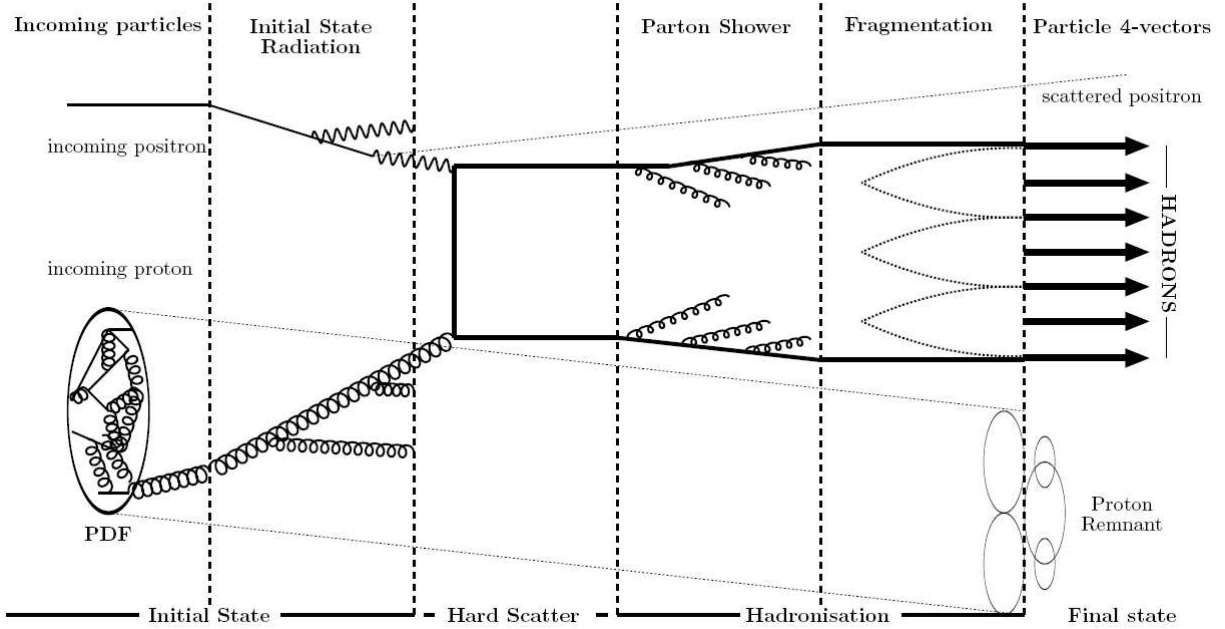


**Figure 5.1:** A schematic view of the  $ep$  scattering process in a MC event generator. The figure is taken from [130].

sub-process is calculated according to Feynman rules. This process determines the main characteristics of the event.

**Initial and final state radiation:** in processes involving charged and coloured objects, the topology of an event can be strongly influenced by the emission of gluons and photons in the initial or final state. These perturbative corrections are usually modelled by the so called *parton shower* method (see section 5.2.1), where the radiation is simulated by a random number of branchings of one to two partons, like:  $e \rightarrow e\gamma$ ,  $q \rightarrow qg$ ,  $q \rightarrow q\gamma$ ,  $g \rightarrow q\bar{q}$ . Two daughters may branch in turn, producing other partons, and so on. The shower stops at a fixed non perturbative scale typically of the order of 1 GeV below which the strong coupling constant  $\alpha_s$  becomes too large for a further calculation of the parton showering process in perturbative QCD.

**Hadronisation (fragmentation):** Hadronisation is the process in which the coloured partons are formed into the colourless hadrons after the parton shower. Due to its low momentum scale it is not colourless in perturbative QCD. Phenomenological models are available to generate the hadronic final state starting from the partons.

**Beam remnant:** The interacting partons carry only a fraction of the initial proton beam energy, the rest is taken by the beam remnant. If the shower initiator is coloured, so is the beam remnant, which is therefore connected to the rest of the event and has to be fragmented and reconstructed coherently.

The two Monte Carlo generators DJANGO [131] and RAPGAP [132], used in the context of this analysis, are explained briefly in the following. A DJANGO Monte Carlo sample

is used to determine acceptance and efficiencies in order to correct the number of signal events in this analysis.

## 5.2 Parton Cascade Models

In this section two different approaches for the description of hadronic final states in high energy processes will be described.

### 5.2.1 Parton Showers

The parton shower model (PS) describes the parton cascade process by splitting of a parent parton into two daughters. The splitting continues with the daughters going on to form parents. Possible transitions are  $q \rightarrow qg$ ,  $g \rightarrow q\bar{q}$ ,  $g \rightarrow gg$ . The evolution of the shower is based on the DGLAP equations introduced in section 2.8.1.

In the initial cascade, at each branching, one parton becomes more space-like ( $m^2 < 0$ ) which will go on to enter the hard interaction while the other becomes more time-like ( $m^2 > 0$ ). After the hard interaction the outgoing quark is off-shell in a time-like manner. The time-like quark's off-shell mass is reduced by further splitting into daughter partons. Any time-like partons from the initial state cascade will also undergo a similar development, until all partons are essentially on-shell ( $m \approx 0$ ). This model is implemented in the RAPGAP MC program [133].

### 5.2.2 Colour Dipole Model

An alternative to the parton shower model is given by colour dipole model (CDM) [130]. CDM was originally developed for  $e^+e^-$  reactions. The basic idea is that the quarks produced in an annihilation process represent a colour dipole which subsequently radiates gluons. The radiation leads to additional dipoles which again radiate partons resulting in a parton cascade.

In the case of  $ep$  scattering the colour dipole is initiated by a struck quark and the proton remnant. The amount of emissions is controlled by the extension of the proton and the photon. In  $e^+e^- \rightarrow q\bar{q}$  processes, the  $q$  and  $\bar{q}$  are point-like objects whereas in DIS the proton remnant is an extended object. Since both photon and proton remnant are considered to be extended objects the radiation is suppressed according to parameters which quantify this extension. The QCD Compton and higher order processes can be calculated in the frame of the CDM. The processes initiated by gluons like BGF ( $\gamma g \rightarrow q\bar{q}$ ) have to be realised by allowing the radiation of an anti-quark from the primary dipole. The generation of parton showers in the framework of the dipole model is not ordered in the  $k_T$  of the emitted partons. Hence, it follows the philosophy of the BFKL parton evolution. The CDM is implemented in the ARIADNE [134] MC program.

## 5.3 Hadronisation Models

The mechanism by which partons dress themselves and become hadrons is called *hadronisation*. The hadronisation process takes place at large distances, and therefore perturbative QCD cannot be applied. Instead, phenomenological approaches are used. In order to simulate the hadronisation process various models have been proposed. The idea of the hadronisation schemes is to apply it to different reactions from different colliders without need to tune it for each dataset individually. Two hadronisation models implemented in the MC generators are discussed below.

### 5.3.1 String Model

In the Lund string model [135], two colour charged objects are bound together by a colour field which is squeezed into a narrow tube (so called *string*). The colour field is described by a Coulomb potential which gives a linear increases with the distance between the objects plus a term which is a massless one dimensional string potential. The colour field potential thus has the form

$$V(r) = -\frac{4\alpha_s}{3r} + \kappa \cdot r, \quad (5.1)$$

where  $r$  is the distance between two coloured objects and  $\kappa$  is the energy density of the string with a value of  $\kappa \approx 1$  GeV/fm. The second term in Eq. 5.1 rapidly increases for rising separation of the two quarks. An illustrative picture of a string between a quark and an anti-quark is shown in Fig. 5.2 (left). As the two particles move apart, the potential energy in the string will increase. When enough energy is stored in the string, the string breaks up and new quarks are produced. An illustration of the break up of the strings is shown in Fig. 5.2 (right). In order to conserve quantum numbers like charge or colour the created particles must be either a quark-anti-quark pair or a diquark-anti diquark pair. Each of the newly created quarks connects to the old quarks with the remaining parts of the colour string. The break up process of strings is repeated until no sufficient energy to break further remains, and bound states (i.e. hadrons) are produced. The model is implemented in PYTHIA [136] MC program.

### 5.3.2 Cluster Model

Another often used hadronisation model is the cluster model. According to the idea of preconfinement, colour connected partons tend to be developing closely in phase space. The cluster model works by splitting all final state gluons into  $q\bar{q}$  pairs. Pairs of  $q$ 's and  $\bar{q}$ 's then form colourless clusters. The clusters will subsequently decay to create hadrons and resonances. These clusters are taken to be superpositions of meson and baryon resonances and decay into mesons or baryons according to the available phase space (see Fig. 5.3). Compared to the string model, the cluster model has less parameters to be tuned to describe hadron production, but has problems in several areas. Attempt to solve these

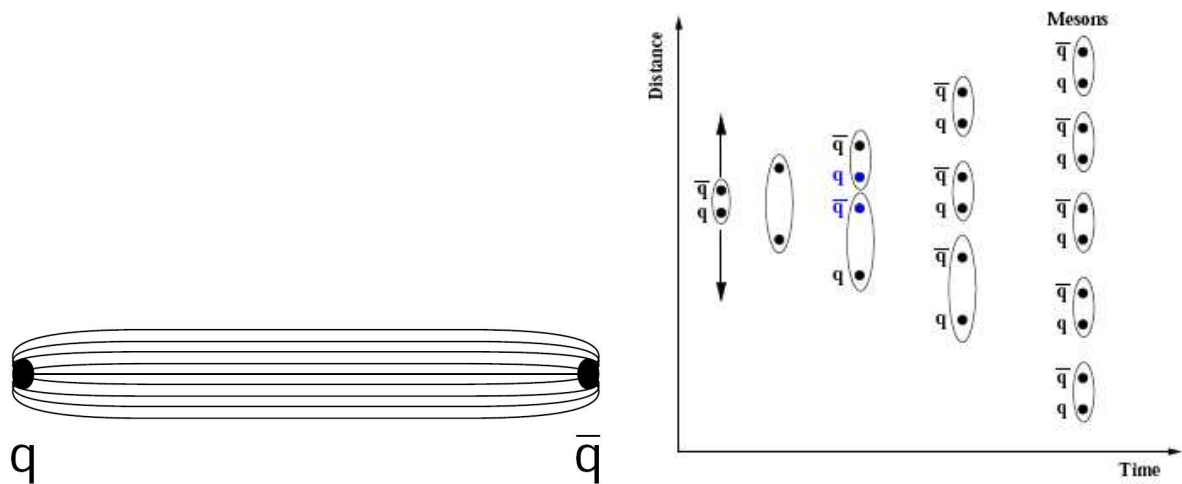


**Figure 5.2:** An illustrative picture of a string between a quark and an anti-quark (left) and the Lund string hadronisation model (right). The quarks in  $q\bar{q}$  pair move away from each other, the string breaks up and a  $q\bar{q}$  pair is produced. This procedure continues till the energy is too low to produce a new  $q\bar{q}$  pair.

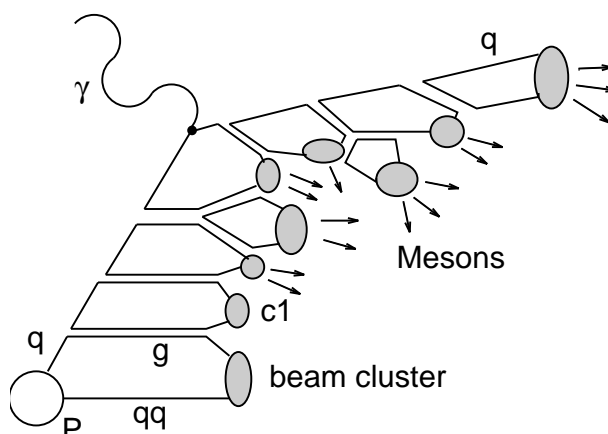


**Figure 5.3:** A schematic picture of cluster model.

problems involve adding extra adjustable parameters which produce a more string-like model. The cluster model is implemented in HERWIG [137] MC program. In this thesis, the cluster model was not used.

## 5.4 Deep Inelastic Scattering Event Generators

In this thesis, two different leading order MC generators DJANGO [131] and RAPGAP [132] are used to generate the neutral current DIS processes. They are used for physics analysis but also to determine the effects of the detector resolution and acceptance by detailed simulation of the detector response to the generated events (see section 5.5).

### 5.4.1 DJANGO

The MC generator DJANGO is used to describe the inclusive electron-proton DIS interaction at leading order. DJANGO generates the hard QCD  $2 \rightarrow 1$  or  $2 \rightarrow 2$  subprocesses like  $\gamma q \rightarrow q$ ,  $\gamma^* g \rightarrow q\bar{q}$ , convoluted with the proton PDF. In this thesis the PDFs are chosen to be CTEQ5L [138] or GRV94 LO [139]. The DJANGO program describes the higher order effects which produce further hard outgoing partons with two approaches. The first approach, the parton shower approach, is implemented in LEPTO whereas the second one is the CDM approach (discussed in section 5.2.2) implemented in ARIADNE [134]. The hadronic final state in DJANGO is modelled according to the Lund string model (see section 5.3.1). In this thesis the following ALEPH-tuned parameters [79] are used:

- PARJ(1) = 0.108. This parameter is  $P(qq)/P(q)$ . The probability of a light diquark-antidiquark pair production,  $P(qq)$ , is compared with a light quark-antiquark pair production,  $P(q)$ .
- PARJ(2) = 0.286. This parameter is  $P(s)/P(u)$ . The relative production probability of  $s$  quark,  $P(s)$ , compared with  $u$  or  $d$  production,  $P(u)$ .
- PARJ(3) = 0.699. This parameter is

$$\frac{P(us)}{P(ud)} / \frac{P(s)}{P(d)}.$$

The extra suppression of strange diquark production compared with the normal suppression of strange quarks.

A realistic simulation of the hadronic final states at low values of energy  $W$  was not implemented in DJANGO. In previous versions of DJANGO the simulation was restricted to  $W > 5$  GeV. In order to improve this situation, the SOPHIA [140] model was implemented in DJANGO to simulate the region  $W < 5$  GeV where the proton resonances need to be taken into account.

For this analysis  $15 \cdot 10^6$  events were generated with the DJANGO 1.4 version, corresponding to an integrated luminosity of  $\mathcal{L} \approx 86 \text{ pb}^{-1}$ . The phase space was restricted to  $Q^2 \geq 4 \text{ GeV}^2$  and  $0.05 < y < 0.7$ .

### 5.4.2 RAPGAP

The MC generator RAPGAP is a multi-purpose event generator also covering diffractive<sup>1</sup> and non-diffractive processes in  $ep$ -scattering both for photoproduction and for DIS. The latest version of RAPGAP includes leading order calculations of the cross sections for direct and resolved photon interactions together with initial and final state radiation obtained using the DGLAP evolution equations in the leading log approximation. The renormalisation scale has been chosen to be  $\mu_r^2 = Q^2$ . The hadronisation is performed using the Lund string model as given by the JETSET Monte Carlo program [141]. Full first order  $\alpha$  initial photon radiation on the electron side, usually called QED radiation, is simulated via an interface to the HERACLES [142] program. RAPGAP does not include any model for multiple parton interactions.

In this thesis  $25 \cdot 10^6$  events were generated with RAPGAP 3.1 version, corresponding to an integrated luminosity of  $\mathcal{L} \approx 136 \text{ pb}^{-1}$ . The phase space was restricted to  $Q^2 \geq 4 \text{ GeV}^2$  and  $y > 0.025$ .

## 5.5 Detector Simulation

In order to make comparisons between the measured data and the predictions of theoretical models, detector effects such as acceptance, resolution, dead material and inefficient detector components have to be considered. Therefore a full simulation of the detector performance is needed to be applied on the generated events on hadron level by the MC programs.

Corrections due to the influence of the detector can be obtained from the ratio of the detector simulated MC events and the generated hadron level MC data. These corrections are then applied to the experimental data to achieve the measured signal on hadron level. The detector response to the particles generated in an event is simulated in detail by the H1SIM-package [143] which is based on the GEANT-program [144]. The parameters used by this program were determined in test beam measurements and optimised during the  $ep$  data taking. In H1SIM, the details of the geometrical acceptance and intrinsic resolution of the detector components as well as the distribution of instrumented and uninstrumented material are implemented, so that the detector response to the generated particles can be calculated.

### Reconstruction

After the detector simulation both data and simulated events are used as input for the

---

<sup>1</sup>Diffractive events are characterised by a large rapidity gap which contains no final state hadrons.

---

same event reconstruction program, H1REC [145]. The reconstruction package H1REC provides a level of simulation which is directly comparable to the recorded DST data described in section 4.7. This final stage is called the *reconstructed level*. The differences between two levels of simulation also provide a method of correcting detector acceptances and resolution effects in data.

# Chapter 6

## Event Selection

The event selection procedure consists of two stages, *online* and *offline selection*. The cuts applied on data by the H1 trigger system constitute the first online selection. The events which passed the online selection have met certain trigger criteria which are designed to meet the bandwidth and storage limitations of the H1 data acquisition system, and to minimise the loss of events relevant to the measurement in the kinematic range of interest.

Next, the events which passed the trigger selection are subjected to further offline selection requirements where the specific events to be analysed are chosen. The offline requirements are designed to clean the real data as well as restrict the cross section measurements to a kinematic region that is well within the range of the H1 detector and trigger acceptance.

This chapter outlines the event selection procedure for the present analysis and explains the online trigger conditions and offline applied cuts.

### 6.1 Online Selection

As mentioned in section 4.7, H1 uses a multi-level trigger system for the online event selection. During the data taking not all interactions are recorded but only interesting physics events satisfying certain trigger conditions are kept. In this section, a description of the selection criteria used at the online trigger selection is given.

#### 6.1.1 Trigger Selection

In order to collect a well defined sample of events taken with the H1 detector, it is necessary to require a well defined trigger condition for every event. Since it is important to make maximum use of the available luminosity, one should choose a subtrigger which triggers on as much of the selected events as possible. In the present analysis the subtrigger ST61, which depends on L1 trigger elements, is used. The subtrigger ST61 is based on a logical combination of trigger elements of the electron trigger for the SPACAL, trigger elements provided by time of flight systems and the tracking chamber CJC. The description of the

Year	Run Number	Definition of Subtrigger ST61
2005	399629 – 401616	$(\text{SPCLe\_IET} > 2 \vee \text{SPCLe\_IET\_Cen\_3}) \wedge \text{DCRPh\_THig} \wedge \text{VETO}$
	401617 – 401626	$(\text{SPCLe\_IET} > 2 \vee \text{SPCLe\_IET\_Cen\_3}) \wedge \text{FTT\_mul\_Tc} > 2 \wedge \text{VETO}$
	401627 – 405719	$(\text{SPCLe\_IET} > 2 \vee \text{SPCLe\_IET\_Cen\_3}) \wedge \text{FTT\_mul\_Tc} > 1 \wedge \text{VETO}$
	405720 – 436893	$(\text{SPCLe\_IET} > 2 \vee \text{SPCLe\_IET\_Cen\_3}) \wedge \text{FTT\_mul\_Td} > 0 \wedge \text{VETO}$
2006 – 2007	444307 – 500611	$(\text{SPCLe\_IET} > 2 \vee \text{SPCLe\_IET\_Cen\_3}) \wedge \text{FTT\_mul\_Td} > 0$

**Table 6.1:** The trigger elements of subtrigger ST61. The symbols  $\wedge$  and  $\vee$  stand for logical **AND** and **OR**, respectively.

subtrigger system as well as the definition of the trigger elements necessary to build ST61 is given in the following (see Table 6.1).

- The **SPACAL Inclusive Electron Trigger (IET)** [146] subsystem is the trigger used to detect events with a scattered electron in the backward region of the H1 detector. The SPACAL IET fires, if a candidate for an electron is detected in the electromagnetic part of the calorimeter. The following trigger elements are relevant for this analysis:
  - **SPCLe\_IET > 2:** This trigger element is set, if the energy of the electron candidate, which is the sum of the energy of one trigger tower and its neighbours, is above a threshold of  $E_e > 6$  GeV. The inner part of the calorimeter close to the beam pipe, is excluded due to the high background.
  - **SPCLe\_IET\_Cen\_3:** This trigger element is similar to  $\text{SPCLe\_IET} > 2$  and requires an energy deposition of 6 GeV but for one of the central trigger towers.
- The **DCRPhi Trigger** [147] uses signals produced by the central tracking chambers CJC1 and CJC2. Since the L1 decision time is too short to completely reconstruct all the tracks coming from particles, the DCRPhi trigger estimates the number of particles with a transverse momentum above a certain threshold traversing through CJC1 and CJC2. The DCRPhi trigger differentiates tracks with high transverse momentum  $p_T > 800$  MeV from tracks with low transverse momentum  $400 < p_T < 800$  MeV and also distinguishes the charge sign of the particle. The only trigger element provided by the DCRPhi trigger entering the definition of the ST61 is:
  - **DCRPh\_THig:** This trigger element fires, when at least one track with a transverse momentum  $p_T > 800$  MeV was found.

In the beginning of 2005 the DCRPhi Trigger was replaced by a three level Fast Track Trigger (FTT).

- The **Fast Track Trigger (FTT)** has the purpose to reconstruct final states from tracks on trigger level and thus to select online interesting  $ep$  events. The ST61 trigger contains the following trigger elements:

- **FTT\_mul\_Tc**: The trigger element FTT\_mul\_Tc requires at least 2 (FTT\_mul\_Tc > 1) or 3 tracks (FTT\_mul\_Tc > 2) with transverse momentum greater than 400 MeV. This trigger element was not included after the run 405720.
  - **FTT\_mul\_Td**: The trigger element FTT\_mul\_Td fires when at least 1 track with transverse momentum greater than 900 MeV was found. This trigger element was included in the runs 405720 to 500611.
- **Veto Trigger Elements** Veto conditions from the time-of-flight system are applied to suppress background from non- $ep$  scattering events such as beam-gas and beam wall interactions. These veto conditions are common to most of the H1 subtriggers. The time-of-flight system consists of two detectors in the forward part of the H1 detector, providing information on whether a particle is found within (Forward Time of Flight Interaction (FToF\_IA)) or outside (Backward Time of Flight Background (BTOF\_BG)) the time window of a bunch crossing. Mid of 2006 an additional CIP veto was added to the subtrigger ST61 to suppress very high multiplicity events. The ST61 subtrigger does not use any conditions from the L2 or L3 system as the rate is comparably low, hence the events which passed the conditions of L1 are directed to L4.

The L1 trigger condition may not be sufficient to reduce the trigger rate to a tolerable level within the available band width. Thus the rate of subtrigger ST61 may be downscaled by applying so called *prescale factors*. A prescale factor of  $n$  means, that only each randomly chosen  $n^{\text{th}}$  event, when the subtrigger fires, is accepted and delivered further. Using the prescale factors does not have any impact on the shape of physical quantities but reduces the effective luminosity. The average prescale factors of the subtrigger ST61 used in the present analysis are listed in Table 6.2.

Year	Collision	Prescale Factor
2005	$e^-p$	1.02
2006	$e^-p$	1.0
2006	$e^+p$	1.01
2007	$e^+p$	1.0

**Table 6.2:** The average prescale factors for each period.

## 6.2 Offline Selection

In addition to the online selection discussed above, an additional set of selection criteria is applied to the data to optimise the rejection of non-interesting events in the sample. The various offline selection cuts are discussed in this section.

### 6.2.1 Run Selection

The data used in this analysis were collected between the years 2005 to 2007. During the H1 data taking, events were recorded in time intervals (about  $\sim 1$  hour) so called *runs* which contain data logged under stable accelerator and detector conditions. Depending on the overall detector performance, on the background situation, on readout inconsistencies of some of the detector components etc., the runs are classified as *good*, *medium* or *poor*. From the whole data sample, only runs which are of good or medium quality are used in this analysis. The minimal integrated luminosity per run has to be larger than  $0.1 \text{ nb}^{-1}$ . A very low luminosity collected in one run often is an indication of a technical problem. Only the runs where all detector systems essential for this analysis were fully operational (supplied by high voltage) and included in the readout, are accepted. The relevant detector components are the central jet chambers (CJC1 and CJC2), the proportional chamber (CIP), the LAr and SPACAL calorimeters, the time of flight, veto and luminosity systems. The resulting integrated luminosities of the analysed data sample within the mentioned requirements are given in Table 6.3. In total an integrated luminosity of  $\mathcal{L} = 301.9 \text{ pb}^{-1}$  is available.

Year	Collision	First Run	Last Run	$\mathcal{L} \text{ (pb}^{-1}\text{)}$
2005	$e^-p$	399629	436893	109.9
2006	$e^-p$	444307	466997	57.1
2006	$e^+p$	468531	492541	88.6
2007	$e^+p$	492559	500611	46.3
Total				301.96

**Table 6.3:** The data samples used in the analysis and integrated luminosities for the used run selection.

### 6.2.2 Event Vertex Position

A precise measurement of the kinematic variables and modelling of the detector acceptance requires an accurate determination of the primary interaction vertex. The collisions between the electrons and the protons are distributed in the  $z$ -direction of the primary vertex position especially due to the extension of the proton bunch ( $\sigma_z(p) = 13 \text{ cm}$ ). The electron bunches are much shorter ( $\sigma_z(e) = 2 \text{ cm}$ ). The longitudinal bunch structure of the protons can be described by a Gaussian distribution. The  $z$  position of the primary vertex along the beam line is required to be

$$-35 < z_{vtx} < 35 \text{ cm},$$

relative to the nominal  $ep$  interaction point. This cut is used to reject background events coming from interactions of the proton beam with the residual gas or with the beam pipe walls. Also interactions from satellite bunches are suppressed by this cut. After each

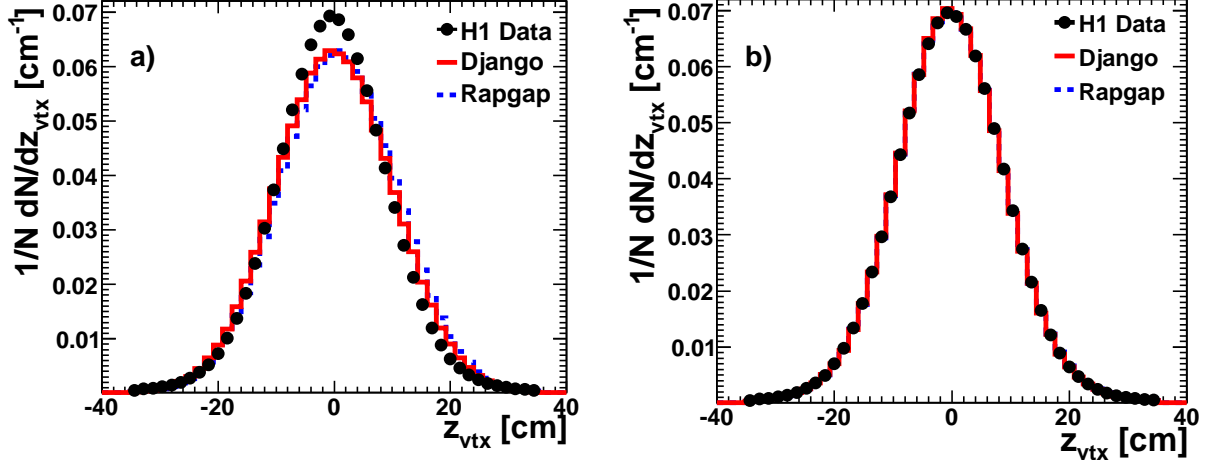


**Figure 6.1:** The  $z_{vtx}$  distributions for data and simulated DJANGO and RAPGAP events before a), after b) the reweighting procedure. The data are shown as points, the DJANGO and RAPGAP simulations are shown as solid and dashed lines, respectively. The distributions are normalised to the number of events.

new fill in HERA the beam orbits are optimised to give the highest possible luminosity which means that the true interaction region can vary from run to run. This variation is not only related to luminosity optimisation but also some other elements which influence beam conditions, magnetic field, shape of the bunches during the filling, radiation level. Unfortunately such variations are not easy to simulate within the MC, therefore the reconstructed Monte Carlo events have been reweighted according to the  $z_{vtx}$  distribution obtained from the data. Fig. 6.1 shows the  $z_{vtx}$  distribution for data and simulated DJANGO and RAPGAP events, before and after reweighting.

### 6.2.3 Selection of DIS Events

The selection of DIS events is almost completely based on a determination of the kinematics from the scattered electrons. However, other cuts also need to be applied in order to suppress background and exclude data from non-functioning parts of the detector.

In this section the selection criteria of DIS events are described.

#### 6.2.3.1 Scattered Electron Selection

The scattered electron is identified by a cluster in the electromagnetic part of the SPACAL, connected to a charged particle track. The energy measurement of the scattered electron is provided by the electromagnetic SPACAL calorimeter. In this analysis, the scattered electron is required to have an energy

$$E'_e > 11 \text{ GeV},$$

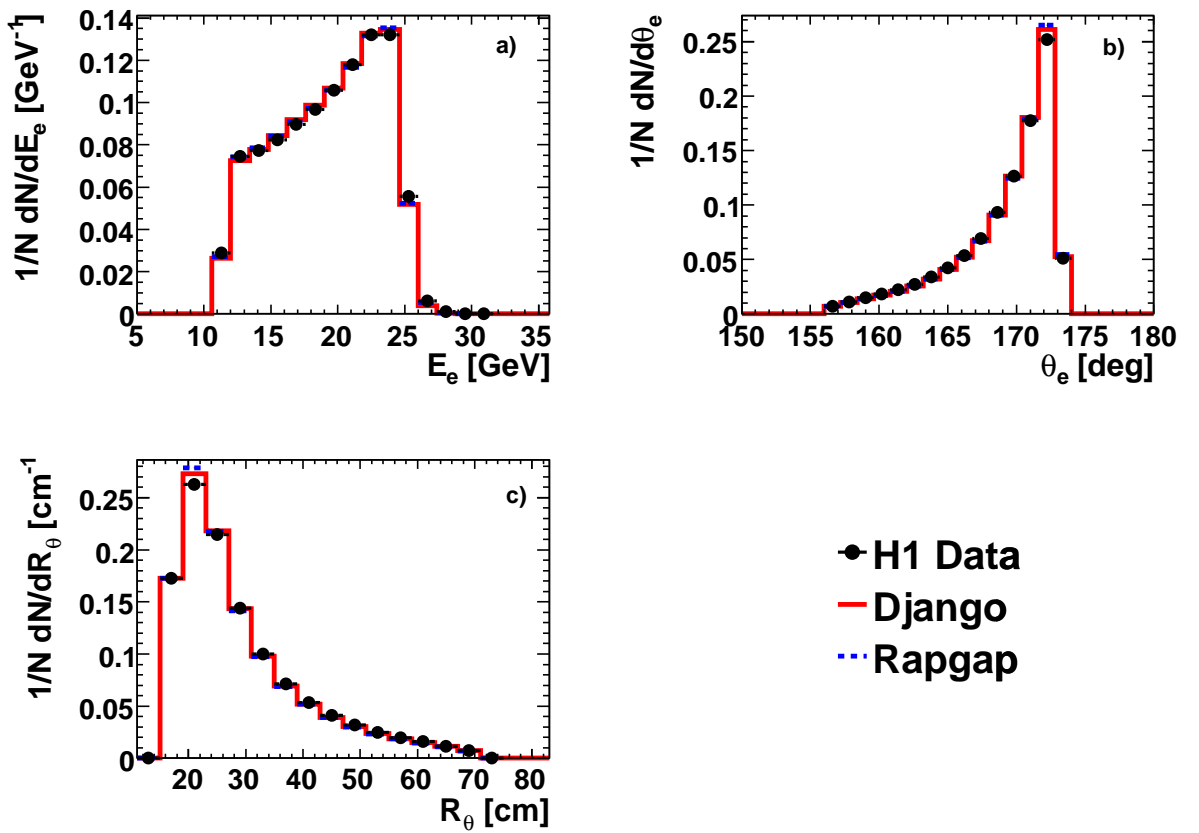


**Figure 6.2:** Scattered electron quantities energy  $E_e$  a), polar angle  $\theta_e$  b), and minimum radial distance of the cluster from the beam pipe  $R_\theta$  c). Shown are data (full points) together with the simulations using DJANGO (solid line) and RAPGAP (dashed line). The distributions are normalised to the total number of events.

and a polar angle

$$156 < \theta_e < 173^\circ.$$

The scattered electron energy  $E'_e$  and polar angle  $\theta_e$  distributions are shown in Fig. 6.2a and 6.2b, respectively. A good description of the data by the MC is achieved. The polar angle of the scattered electron,  $\theta_e$ , is calculated from the impact position in the BPC and the position of the energy cluster in the SPACAL together with the reconstructed interaction vertex. The cut on the scattered electron angle,  $\theta_e$ , is used to ensure that the scattered electron is within the acceptance of the SPACAL, while the cut on the energy,  $E'_e$ , is used to reduce background from photoproduction events. In standard DIS event analyses of H1, the scattered electron is associated to the electromagnetic cluster with the highest transverse momentum when a connected track is available.

Further requirements on the electromagnetic cluster of the electron are used to suppress background from photoproduction events, in which the electron escapes through the beam pipe and a hadron fakes the signature of an electron in the detector. The cluster is required to be compact, i.e. the radius of the cluster,  $R_{cluster}$ , is required to be small,

$$R_{cluster} < 4 \text{ cm},$$

since hadronic clusters are expected to be broader than electromagnetic clusters. The radius  $R_{cluster}$  is defined by

$$R_{cluster} = \frac{\sum_i E_i \sqrt{(x_{cluster} - x_i)^2 + (y_{cluster} - y_i)^2}}{E_{cluster}}, \quad (6.1)$$

where  $x_{cluster}$ ,  $y_{cluster}$  and  $E_{cluster}$  are the coordinates and energy of the cluster, respectively. The sum runs over all cells  $i$  (with coordinates  $x_i$ ,  $y_i$  and energy  $E_i$ ) belonging to that cluster. The energy in the hadronic part behind the electromagnetic cluster,  $E_{had}$ , is restricted to

$$E_{had} < 0.5 \text{ GeV}.$$

During the HERA II upgrade program the beampipe was modified and focusing magnets had to be inserted within the detector region. This implied modifications like a new elliptical shape of the beam pipe and a larger SPACAL hole, where the centre is shifted horizontally with respect to the nominal beam axis and the centre of the H1 coordinate system. At the SPACAL edge the electron energy and scattering angle cannot be measured correctly since the shower is only partly contained in the SPACAL. In order to avoid these problems, a minimal radial distance of the cluster from the beam pipe,  $R_\theta$ , is required

$$R_\theta > 12 \text{ cm}.$$

The low  $R_\theta$  region corresponds to low  $Q^2$  events. Hence, the cut is required to be as low as possible in order not to reject a large number of events. This innermost region however corresponds to a region of very high background rates. Fig. 6.2c shows the distribution of  $R_\theta$  which is well described by the MC simulations DJANGO and RAPGAP.

During the data taking period, some regions of the SPACAL suffered from high background radiation and dead cells. This was not included in the detector simulation, and

therefore the dead cells in SPACAL and cells with poor trigger efficiency are excluded from the analysis. An investigation for these problematic cells for different run periods was done in [148] and [149]. All these cells are excluded from the selection.

### 6.2.3.2 Energy Balance

The energy and longitudinal momentum balance of events is characterised by a quantity,  $E - p_z$ . Due to the energy momentum conservation before and after the interaction, the quantity  $E - p_z$  can be written as

$$\begin{aligned} E - p_z &= (E_p - p_{p,z}) + (E_e - p_{e,z}) \\ &= \sum_{i=\text{hadrons}} (E_i - p_{i,z}) + (E'_e - p'_{e,z}) \\ &\approx 2E_e \end{aligned} \quad (6.2)$$

where the sum runs over all measured hadronic final state objects. If the masses of the electron and proton are neglected,  $E - p_z$  should be equal to  $E - p_z \approx 2E_e \approx 55$  GeV. This quantity is very sensitive to particle losses in the backward direction, therefore well suited to suppress photoproduction background events ( $Q^2 \approx 0$ ), where the scattered electron escapes undetected through the beam pipe. In this analysis, it is required that

$$35 < E - p_z < 70 \text{ GeV}. \quad (6.3)$$

Fig. 6.3 shows the distribution of  $E - p_z$  for data compared with simulated DJANGO and RAPGAP events. The distribution of  $E - p_z$  has, because of energy and momentum conservation, a peak at  $2E_e = 55$  GeV.

### 6.2.3.3 DIS Event Reconstruction

The DIS variables can be fully reconstructed from two independent variables provided that the beam energies are known. In case of initial state radiation, a photon generally escapes undetected in the beam pipe. Consequently, the effective electron beam energy is unknown, and more than two variables are necessary for the kinematic reconstruction. Since both the electron and the hadronic final state can be measured with the H1 detector, several methods are available.

The kinematic reconstruction methods are described below.

### 6.2.3.4 Electron Method

In the electron method [150], the kinematics are reconstructed solely from the electron information as follows:

$$Q_e^2 = 4E_e E'_e \cos^2 \frac{\theta_e}{2}, \quad y_e = 1 - \frac{E'_e}{2E_e} (1 - \cos \frac{\theta_e}{2}), \quad x_e = \frac{Q_e^2}{y_e s}, \quad (6.4)$$

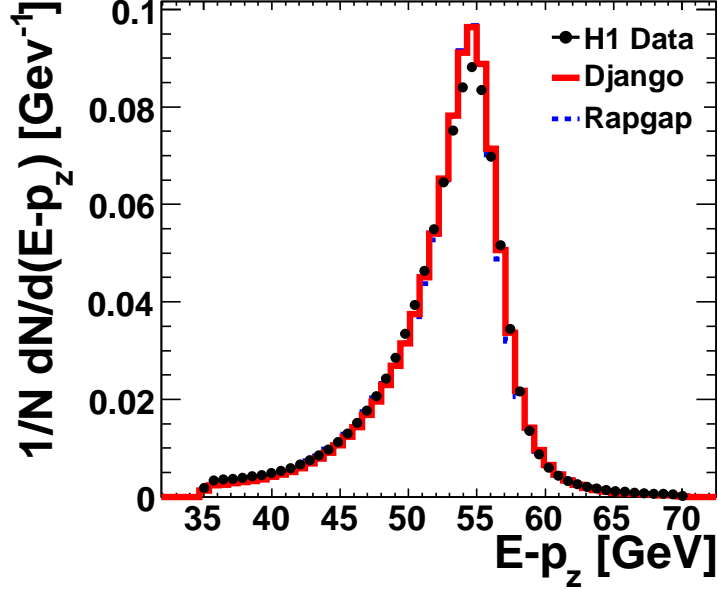


**Figure 6.3:** The distributions of  $E - p_z$  for data compared with simulated DJANGO and RAPGAP events. The data are shown as points, the predictions of the DJANGO and RAPGAP simulation are shown as solid and dashed lines, respectively. The distributions are normalised to number of events.

where  $E_e(E'_e)$  represents the energy of the initial (scattered) electron and  $\theta_e$  is the polar angle of the scattered electron. The electron method has a very good resolution at large  $y$  where the scattered electron can be well detected by CTD and SPACAL. However, this method has a poor  $x$  resolution at smaller  $y$ . The resolution  $\delta y/y$  rapidly degrades with  $1/y$  as  $E'_e$  approaches the electron beam energy  $E_e$ .

### 6.2.3.5 Hadron Method

The hadron method [151] also known as Jacquet-Blondel method is based on the measurement of the energy of the particles of the hadronic final state. The kinematic variables are determined (neglecting the particle masses) using four-momentum conservation. The hadronic final state is measured using the energy deposits in the calorimeters together with low momentum tracks. Summing over all particles in the hadronic final state, the squared four-momentum transfer  $Q^2$ , the inelasticity  $y$  and the Bjorken- $x$  are given by:

$$Q_h^2 = \frac{P_{T,h}^2}{1 - y_h}, \quad y_h = \frac{\sum_i (E_i - p_{z,i})}{2E_e}, \quad x_h = \frac{Q_h^2}{y_h s}, \quad (6.5)$$

where the variable  $P_{T,h} = \sqrt{(\sum p_{x,i})^2 + (\sum p_{y,i})^2}$ , is the total transverse momentum of the hadronic final state.

### 6.2.3.6 $\Sigma$ Method

The  $\Sigma$  method [152], makes use of both the electron and the hadronic final state variables and is less dependent on the initial state electron beam energy:

$$Q_{\Sigma}^2 = \frac{(E'_e \sin \theta_e)^2}{1 - y_{\Sigma}}, \quad y_{\Sigma} = \frac{\Sigma}{E - p_z}, \quad x_{\Sigma} = \frac{Q_{\Sigma}^2}{y_{\Sigma} s}. \quad (6.6)$$

Here  $E - p_z$  is the energy balance discussed in 6.2.3.2. This method is very important to determine the kinematic quantities because of its low sensitivity to radiative effects. This radiation reduces the effective energy of the incoming electron spoiling the measurement of  $y$  (see Eq. 6.4).

The  $y$  resolution of the  $\Sigma$ -method approaches the  $y$  resolution of the hadron method at low  $y$  and that of the electron method a high  $y$  and is therefore good in the whole kinematic range.

### 6.2.3.7 Electron- $\Sigma$ Method

The electron- $\Sigma$  method [153] is designed to combine the best features of the electron and the  $\Sigma$  method. Therefore, it combines the  $Q^2$  reconstruction from the electron method with the  $x$  reconstruction from the  $\Sigma$  method:

$$Q_{e\Sigma}^2 = Q_e^2, \quad x_{e\Sigma} = x_{\Sigma}, \quad y_{e\Sigma} = \frac{Q_{e\Sigma}^2}{x_{e\Sigma} s}. \quad (6.7)$$

Since the electron- $\Sigma$  method gives the best resolution in  $Q^2$  and  $x$  across the whole kinematic range at HERA, and since it is relatively insensitive to radiative corrections, the electron- $\Sigma$  method was chosen in the analysis described in this thesis.

## 6.2.4 DIS Kinematics

The DIS kinematic range covered by this analysis is defined in terms of cuts on the four momentum transfer squared,  $Q^2$ , and inelasticity,  $y$ :

$$5 < Q_{e\Sigma}^2 < 100 \text{ GeV}^2, \\ 0.1 < y_{e\Sigma} < 0.6.$$

The cuts on  $Q^2$  are motivated by the geometrical acceptance of the SPACAL calorimeter. In order to avoid the region of poor resolution in the event kinematics the lower limit on  $y$  was chosen as 0.1. The upper limit was chosen to suppress the events with large radiative effects. The control distributions of  $Q^2$  and  $y$  reconstructed with the electron- $\Sigma$  method as defined in Eq. 6.7 are shown in Fig. 6.4. Both distributions are nicely described by the MC (DJANGO and RAPGAP).

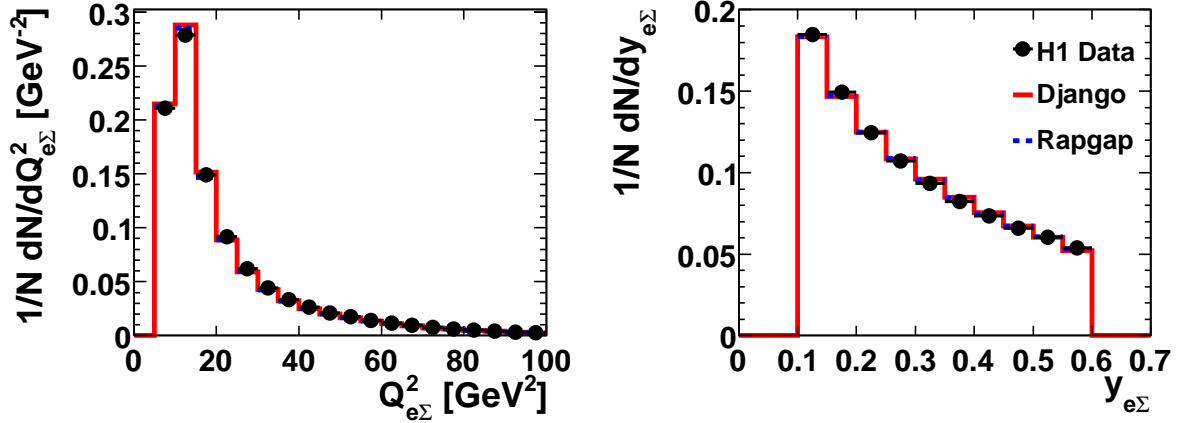


**Figure 6.4:** The distributions of DIS event kinematics:  $Q^2$  a), and  $y$  b). Data are shown as full points. The histogram shows the predictions of DJANGO (solid line) and RAPGAP (dashed line). The distributions are normalised to number of events.

### 6.2.5 Track Selection

The tracks of the hadronic final state, measured with the central and forward tracking detectors, are classified in three categories central ( $20^\circ < \theta < 160^\circ$ ), forward ( $6^\circ < \theta < 25^\circ$ ) and combined ( $0^\circ < \theta < 40^\circ$ ) as shown in Fig. 6.5. The central hadronic final state tracks are used by the present analysis. To ensure good track quality, only the vertex fitted tracks which fulfil the following selection criteria (so called *Lee West selection* [154]) are used for this analysis:

- The transverse momentum  $p_T$  of the tracks is required to be larger than 120 MeV. The lower cutoff in the  $p_T$  of the tracks is necessary since the H1 tracking system is not designed for tracks with a  $p_T < 120$  MeV. Tracks with such low momenta suffer from significant scattering on the dead material between the interaction point and CJC and their momenta cannot be reconstructed. In addition, the  $p_T$  cut is applied to be in the efficient region of the CJC which the track reaches the outer CJC which improves the reliability of the track reconstruction.
- The polar angle  $\theta$  of the tracks is restricted to  $20^\circ < \theta < 160^\circ$ .
- The track must be associated with a vertex such that the distance of closest approach of the track in the  $x - y$  plane to the  $z$ -axis,  $dca'$ , is less than 2 cm.
- The number of hits in the CJC,  $N_{hits}$ , is required to be greater than 10.
- The distance from the interaction point to the first CJC hit,  $R_{start}$  has to be less than 50 cm. This cut ensures that the reconstructed tracks start in the inner part of the CJC.

- The radial distance measured between the first and last measured hits of the track,  $R_{length}$ , should be at least 12 cm in the range of  $20^\circ < \theta < 150^\circ$ . In the backward region  $150^\circ < \theta < 160^\circ$  the requirement is reduced to 5 cm. The  $R_{length}$  cut protects against broken tracks (i.e. a single charge particle reconstructed as two separate tracks - typically one in CJC1 and the other in CJC2).

### track types

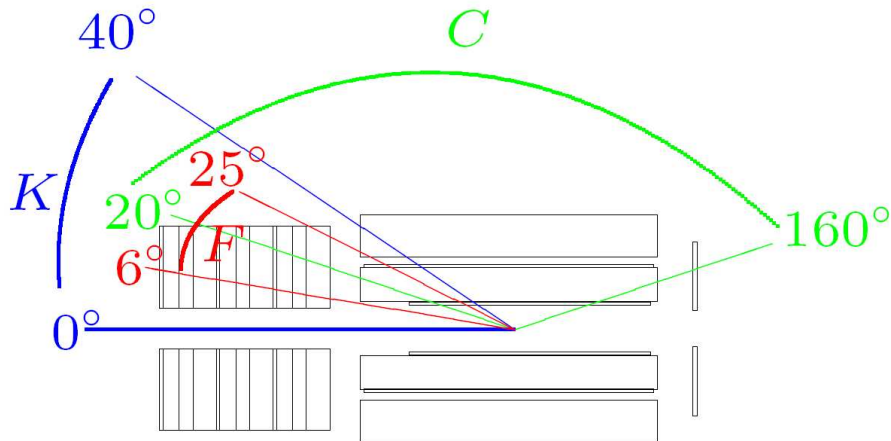


**Figure 6.5:** Angular ranges of the various track types: central ( $20^\circ < \theta < 160^\circ$ ), forward ( $6^\circ < \theta < 25^\circ$ ) and combined ( $0^\circ < \theta < 40^\circ$ ).

In addition to the Lee West track selection criteria mentioned above, a further cut is applied on the pseudorapidity of tracks ( $-1.5 < \eta < 1.5$ ). All the track selection criteria are summarised in Table 6.4.

Central Tracks
$p_T > 120$ MeV
$20^\circ < \theta < 160^\circ$
$ dca'  \leq 2$ cm
$N_{hits} > 10$
$R_{start} \leq 50$ cm
$R_{length} \geq 12$ cm for $20^\circ < \theta < 150^\circ$
$R_{length} \geq 5$ cm for $150^\circ < \theta < 160^\circ$
$-1.5 < \eta < 1.5$

**Table 6.4:** Summary of the track selection criteria.

The track selection efficiency is highly dependent on the radial length of tracks. The radial length and polar angle  $\theta$  of tracks are shown in Fig. 6.6. The distributions are in general well described by both DJANGO and RAPGAP. Due to the overall nice agreement between data and Monte Carlo down to 120 MeV for the tracks of the decay particles one may assume that the track reconstruction is well described by the Monte Carlos.

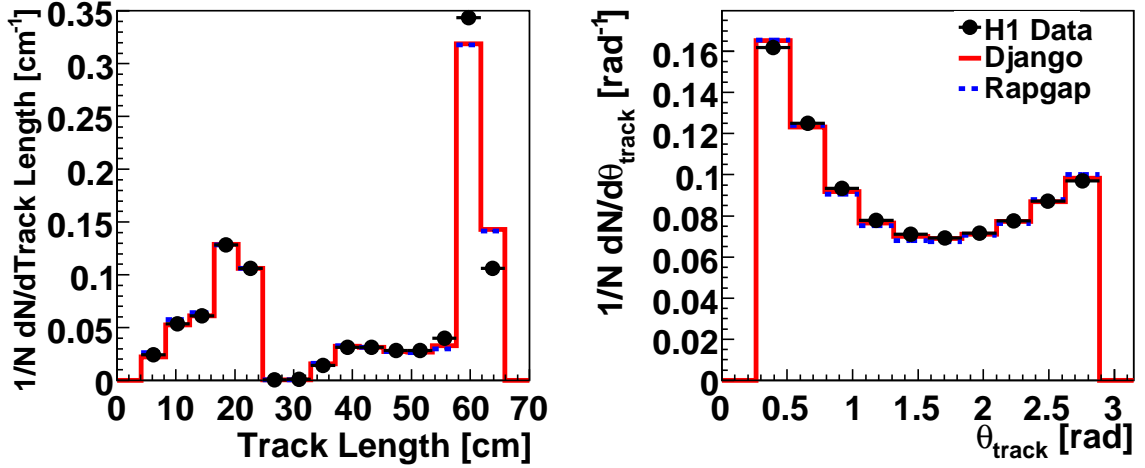


**Figure 6.6:** The radial length (left panel) and polar angle  $\theta$  (right panel) of tracks are shown for data (full points) and DJANGO (solid line) and RAPGAP (dashed line) Monte Carlo simulations.

### 6.3 Summary of the Selection

All the cuts discussed throughout this chapter are summarised in Table 6.5. The event yield for the different running periods is shown in Fig. 6.7 in bins of  $50 \text{ nb}^{-1}$ . No time dependence is observed, the event yield is stable. On average about 6 DIS events are selected per  $\text{nb}^{-1}$  of integrated luminosity.

DIS Event Selection		
Technical Cuts	Scattered $e^-$ Selection	Kinematic Cuts
ST61 subtrigger	$E'_e > 11 \text{ GeV}$	$5 < Q_{e\Sigma}^2 < 100 \text{ GeV}^2$
Run numbers (3399629-500611)	$156^\circ < \theta_e < 173^\circ$	$0.1 < y_{e\Sigma} < 0.6$
$-35 < z_{vtx} < 35 \text{ cm}$	$E_{had} < 0.5 \text{ GeV}$	
$35 < E - P_z < 70 \text{ GeV}$	$R_\theta > 12 \text{ cm}$	
Lee-West track selection	$R_{cluster} < 4 \text{ cm}$	
$-1.5 < \eta_{tracks} < 1.5$		

**Table 6.5:** Summary of all applied event selection cuts.

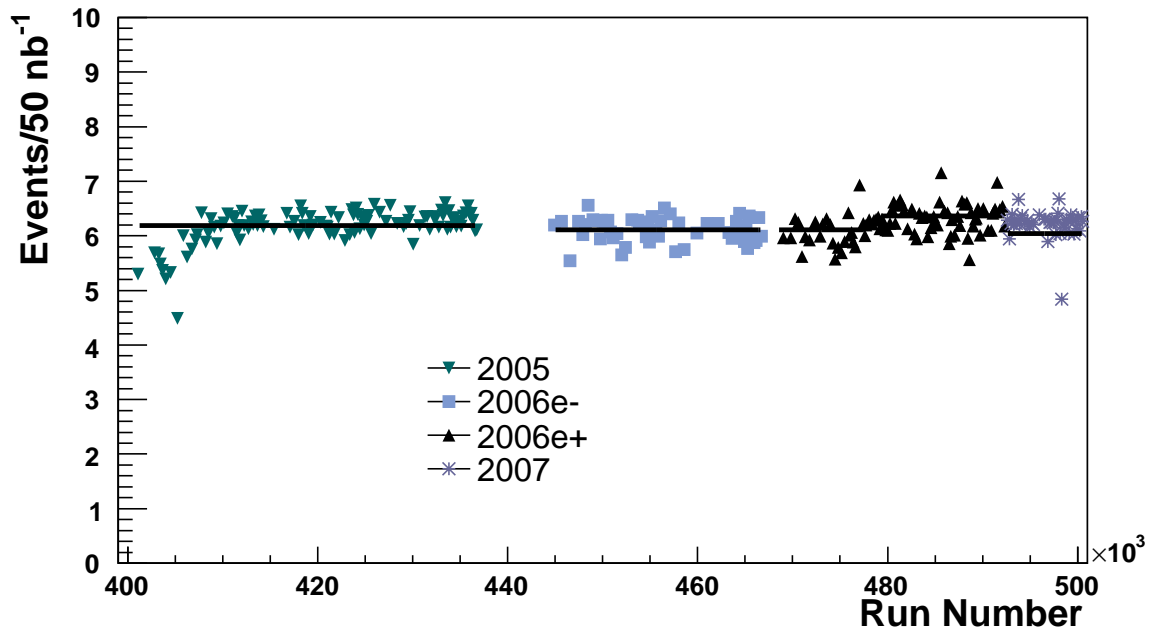


**Figure 6.7:** Event yield for the selection of DIS events with  $K^{*\pm}$  candidates is shown in different run periods. Each point corresponds to an integrated luminosity of  $50 \text{ nb}^{-1}$ .

# Chapter 7

## Reconstruction of $K^{*\pm}$ Mesons

The main subject of the present analysis is to select events from  $ep$  collisions with  $K^{*\pm}$  mesons. The  $K^{*\pm}$  mesons are identified using the decay channel

$$K^{*\pm} \rightarrow K_S^0 \pi^\pm,$$

with the subsequent decay  $K_S^0 \rightarrow \pi^+ \pi^-$ . The first stage in the  $K^{*\pm} \rightarrow K_S^0 \pi^\pm$  selection process is the identification of neutral kaons  $K_S^0$  mesons.

This chapter outlines the selection methods applied to extract the signal and describes the reconstruction of the invariant mass of the  $K^{*\pm}$  candidates.

### 7.1 $K_S^0$ Reconstruction

Events in which a neutral particle decays into two oppositely charged particles are generically called  $V^0$  events. The  $K_S^0$  meson studied here is an example of such particles.  $V^0$ 's are neutral particles and therefore cannot be observed directly. Experimentally, a  $V^0$ , here  $K_S^0$ , is characterised by its two oppositely charged daughter tracks. The reconstruction of  $K_S^0$  is performed by its decay into

$$K_S^0 \rightarrow \pi^+ \pi^-. \quad (7.1)$$

A schematic view of an event with a  $K_S^0$  decay is shown in Fig. 7.1. The angle  $\theta^*$  is defined as the angle between the  $K_S^0$  resultant momentum vector  $P_{K_s}$  and the vector defined by the secondary vertex and the primary vertex. The identity of a  $V^0$  or  $K_S^0$  candidate can be determined by calculating its invariant mass  $M$  which can be calculated from the measured properties of the two daughter particles with mass  $m_1$  and  $m_2$ , and momentum  $p_1$  and  $p_2$ . From the relation  $E_{1,2} = \sqrt{p_{1,2}^2 + m_{1,2}^2}$  it follows that

$$M = \sqrt{m_1^2 + m_2^2 + 2(E_1 E_2 - \vec{p}_1 \cdot \vec{p}_2)}, \quad (7.2)$$

where the momentum of the daughter particles can be obtained from their curvature in the magnetic field. A mass of value must be assumed for the daughter particles in

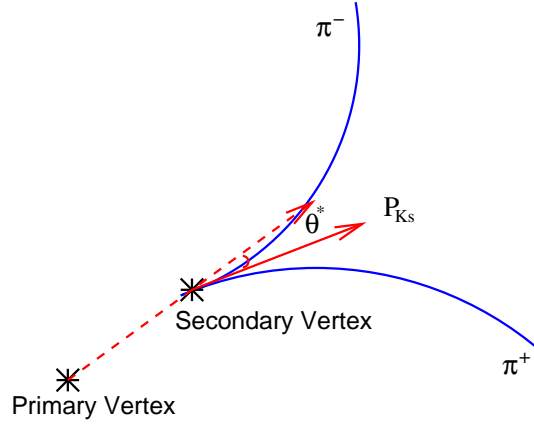


**Figure 7.1:** A schematic view of an event with a  $K_S^0$  decay. The  $K_S^0$  is produced at the point represented *primary vertex* and travels some distance before it decays at which the point represented as *secondary vertex*. The  $K_S^0$  decays in two pions which can be detectable. The dashed line from primary to secondary vertex shows the undetectable trajectory of the  $K_S^0$ .

order to calculate the invariant mass of the parent particle. For the reconstruction of  $K_S^0$  candidate, both daughter particles are assumed to be pions having a mass of  $m(\pi^\pm) = 139.57000 \pm 0.00035$  MeV [4].

In this thesis, two oppositely charged central tracks in the CTD which originate from a secondary vertex are considered as  $K_S^0$  decay products. The conditions, which each track has to fulfil, are given in the following.

- Each track is required to have a minimum transverse momentum  $p_T$  with respect to the beam direction  $p_T > 120$  MeV.
- In order to ensure that the track is well contained within the acceptance of the CTD the pseudorapidity of each track is restricted to  $-1.5 < \eta < 1.5$ .
- The angle in the  $xy$  plane between the vector linking the primary and secondary vertices and the charged track direction in the rest frame of the  $K_S^0$  candidate,  $\theta^*$ , is required to be  $|\cos(\theta^*)| < 0.95$ . This cut requires that the  $K_S^0$  can be traced back to primary vertex.
- The  $K_S^0$  candidates should have a radial decay length  $L > 2$  cm, where  $L$  is the distance between the primary and secondary vertex in the  $r - \phi$  plane.

### Background rejection

- In order to reject the photon conversions ( $\gamma \rightarrow e^+e^-$ ) both tracks of the  $K_S^0$  candidate are assigned the electron mass and considered to come from photon conversion if the invariant mass  $M(e^+e^-)$  of the pair is less than 50 MeV.

- The contamination from  $\Lambda \rightarrow p\pi^-$  and  $\bar{\Lambda} \rightarrow \bar{p}\pi^+$  decays is suppressed by requiring that the invariant mass of the track pair,  $m_{p\pi}$ , lies within a  $\pm 12$  MeV window around the nominal  $\Lambda$  mass, i.e.  $|M(p\pi) - M_\Lambda| > 12$  MeV. The higher momentum track is assumed to be that of a proton and the lower that of a pion.

### Armenteros-Podolanski parameter

$K_S^0$  candidates are classified and identified by a variable called Armenteros-Podolanski [155] parameter

$$\alpha = \frac{p_L^+ - p_L^-}{p_L^+ + p_L^-}, \quad (7.3)$$

where  $p_L$  is the longitudinal momentum component of the daughters ( $\pi^\pm$ ) with respect to the flight direction of the mother particle ( $K_S^0$ ), and sign indicates the electrical charge of the daughter. The momentum is measured in the laboratory frame. Only the Armenteros transverse momentum,  $p_T^{rel}$ , is used in the  $V^0$  finder and is defined as the absolute value of one daughter particle's momentum component transverse to the flight direction of the mother particle. Due to momentum conservation,  $p_T^{rel}$  is the same for both daughter particles,  $p_T^{rel}(D1) = p_T^{rel}(D2)$ . A schematic illustration of the  $V^0$  decay with  $p_T$  and  $p_L$  vectors is shown in Fig. 7.2.

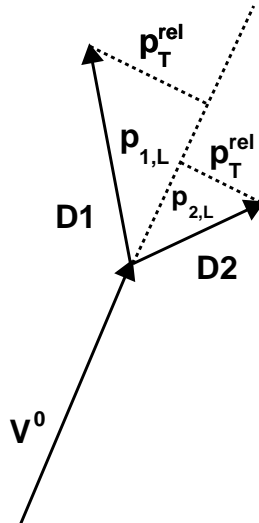


**Figure 7.2:** A schematic illustration of a decay  $V^0 \rightarrow D1 + D2$ , where  $V^0$  represents the mother particle  $K_S^0$ ,  $D1$  and  $D2$  are the first and second daughter particles, e.g.  $\pi^+$  and  $\pi^-$ .

The relative transverse momentum  $p_T^{rel}$  and the variable  $\alpha$  span the Armenteros-Podolanski plot as shown in Fig. 7.3. Possible decays of  $V^0$  particles form half ellipses. The centre

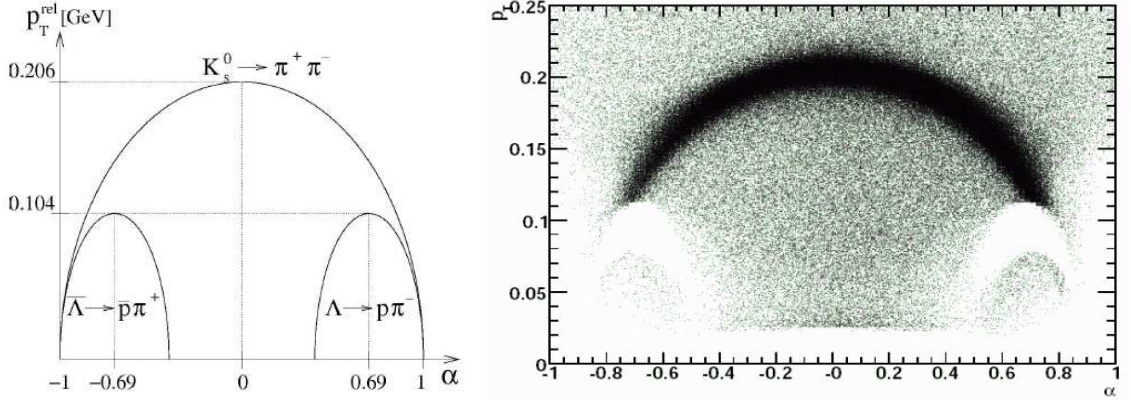


**Figure 7.3:** Armenteros-Podolanski plot shown in idealised form (left panel), and as measured in the present analysis (right panel).

of ellipses lie on the  $\alpha$ -axis, at a value defined by the mass difference of the daughter particles. The band structure is due to momentum conservation of the different  $V^0$  decays, while the band widths are determined by the widths of the  $V^0$ s combined with the detector resolution. The bands of  $\Lambda$  and  $\bar{\Lambda}$  are lower than the  $K_S^0$  band. The reason is that the  $\Lambda$  or  $\bar{\Lambda}$  decay has a smaller  $Q$  value<sup>1</sup> and therefore has less available phase-space since the sum of the pion and proton masses is only 38 MeV smaller than the  $\Lambda$  mass, while the sum of two pion masses is  $\sim 219$  MeV below the  $K_S^0$  mass. Due to the finite resolution the measured distributions are smeared out. However, the separation of  $K_S^0$  and  $\Lambda$  still can be seen. In this thesis the relative transverse momentum  $p_T^{rel}$  is required to satisfy  $p_T^{rel} > 0.11$  GeV. As it is expected, a small fraction ( $\leq 1$ ) of the  $K_S^0$  signal is rejected.

### Optimisation of $\chi^2$

The  $K_S^0$  has a decay length ( $c\tau$ ) in the order of a few centimetres and therefore decay at a secondary vertex which can be well separated from the primary vertex. After selecting good tracks, the secondary vertex is reconstructed. The vertices are determined by minimising the total  $\chi^2$  of a vertex fit which includes the primary and the secondary vertex. The statistical quantity  $\chi^2$  is an often used quantity for the quality of a fit. In this thesis,  $\chi^2 < 5.4$  is required.

### Cut on $\Delta(dca)$

It is required that the difference between the shortest distances of the charged tracks (or the parameterised circles) to the primary vertex,  $\Delta dca = |dca1 - dca2| > 0.5$  cm. Here the shortest distance  $dca1, 2$  gives us a sign, which is determined via the track curvature and the relative orientation to the primary vertex. In the case of combinatorial background,

<sup>1</sup>The  $Q$  value is equal to the mass difference between the mother particle and the sum of the daughter particles.

where both tracks originate from the primary vertex,  $\Delta dca$  has small values, whereas for secondary vertices it becomes maximal.

### Kinematic range

$K_S^0$  candidates are reconstructed in the visible phase space given by

$$0.5 < p_T(K_S^0) < 3.5 \text{ GeV} \quad \text{and} \quad -1.3 < \eta(K_S^0) < 1.3.$$

For further analysis, only  $K_S^0$  candidates reconstructed in the mass window

$$470 < M_{\pi^+\pi^-} < 520 \text{ MeV},$$

around the nominal mass of 497.61 MeV were retained. The control distributions of reconstructed  $K_S^0$  particles of the pseudorapidity  $\eta_{(K_S^0)}$ , the transverse momentum  $p_{T(K_S^0)}$ , the polar angle  $\theta_{(K_S^0)}$  and the decay length  $L_{(K_S^0)}$  are shown in Fig. 7.4, where good agreement between the data and DJANGO Monte Carlo simulation is seen.

#### 7.1.1 Extraction of $K_S^0$ Signal

The invariant mass distribution for  $\pi^+\pi^-$  pairs i.e.  $K_S^0$  candidates is shown in Fig. 7.5. The  $K_S^0$  mass spectrum is fitted to various functional forms, the best fit being given by

$$f(m_{\pi\pi}) = t(m_{\pi\pi}) + bg(m_{\pi\pi}), \quad (7.4)$$

where the student's t function  $t(m_{\pi\pi})$  is given by

$$t(m_{\pi\pi}) = \frac{\Gamma(\frac{v+1}{2})}{\sqrt{v\pi} \Gamma(\frac{v}{2})} \left(1 + \frac{m_{\pi\pi}^2}{v}\right)^{-\frac{(v+1)}{2}}, \quad (7.5)$$

where  $v$  is the number of degrees of freedom and  $\Gamma$  is the Gamma function. The background  $bg(m_{\pi\pi})$  is a linear first order polynomial function

$$bg(m_{\pi\pi}) = a + bm_{\pi\pi}, \quad (7.6)$$

where  $a$  and  $b$  are constants. The student's t function was chosen based on the fact that it provides a better description of signal than the other studied fit functions. The number of reconstructed  $K_S^0$  mesons determined from the fit is  $1319190 \pm 1139$ . The invariant mass of  $K_S^0$  obtained from the fit is  $497.630 \pm 0.010$  MeV which is consistent with the world average value<sup>2</sup> of  $497.614 \pm 0.024$  MeV [4].

---

<sup>2</sup>World average value is provided by Particle Data Group (PDG) which does a compilation or evaluation of particle properties. The properties of all particles are updated regularly. To obtain the world average value, the data which are based on the published results by various experiments all around the world are taken into account. World average value is commonly used by the Particle Physicists as the most precise and reliable value.

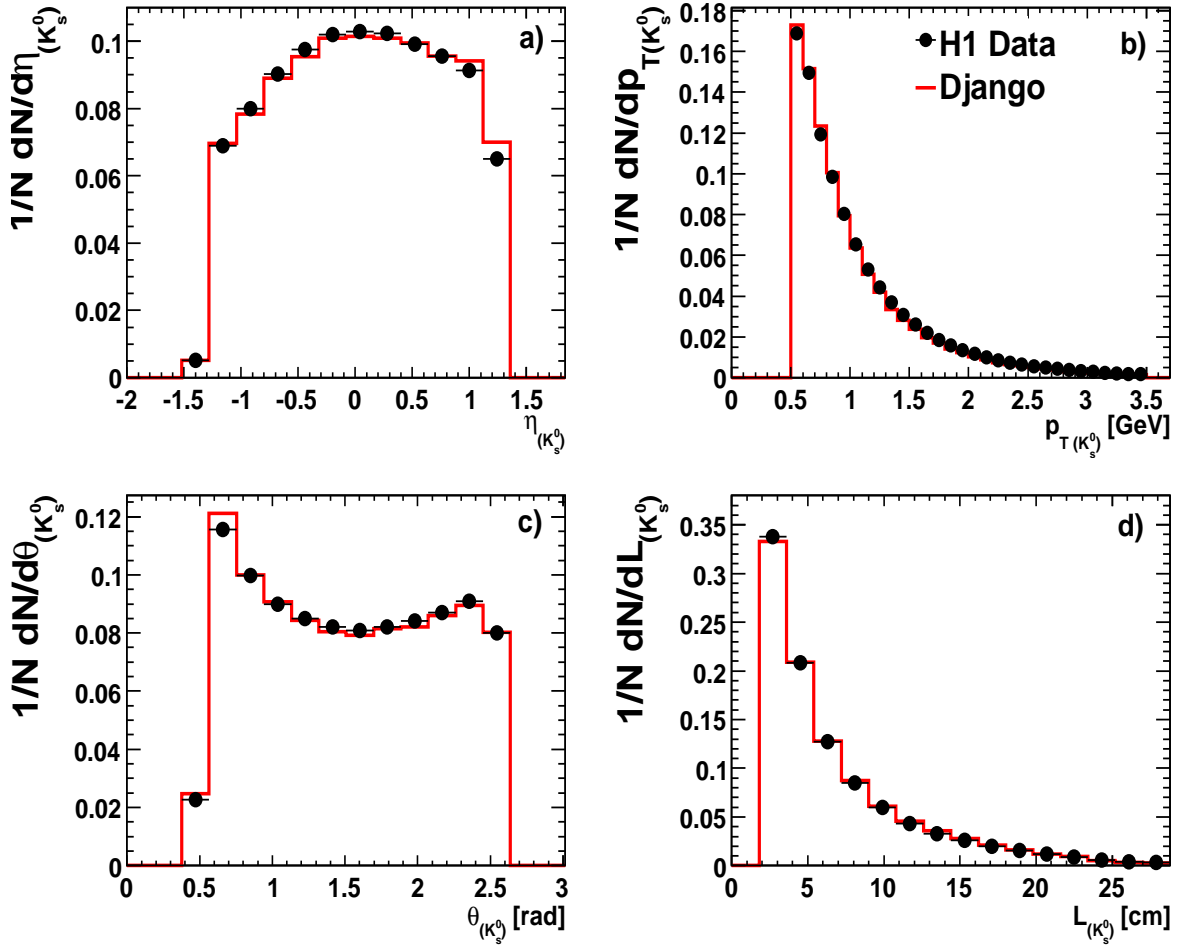


**Figure 7.4:** Control distributions of reconstructed  $K_S^0$  particles. Following quantities are shown: a) the pseudorapidity  $\eta_{(K_S^0)}$ , b) the transverse momentum  $p_{T(K_S^0)}$ , c) the polar angle  $\theta_{(K_S^0)}$  and d) the decay length  $L_{(K_S^0)}$ . The data (black points) are reasonably well described by the DJANGO (solid line) simulation. The distributions are normalised to the number of events.

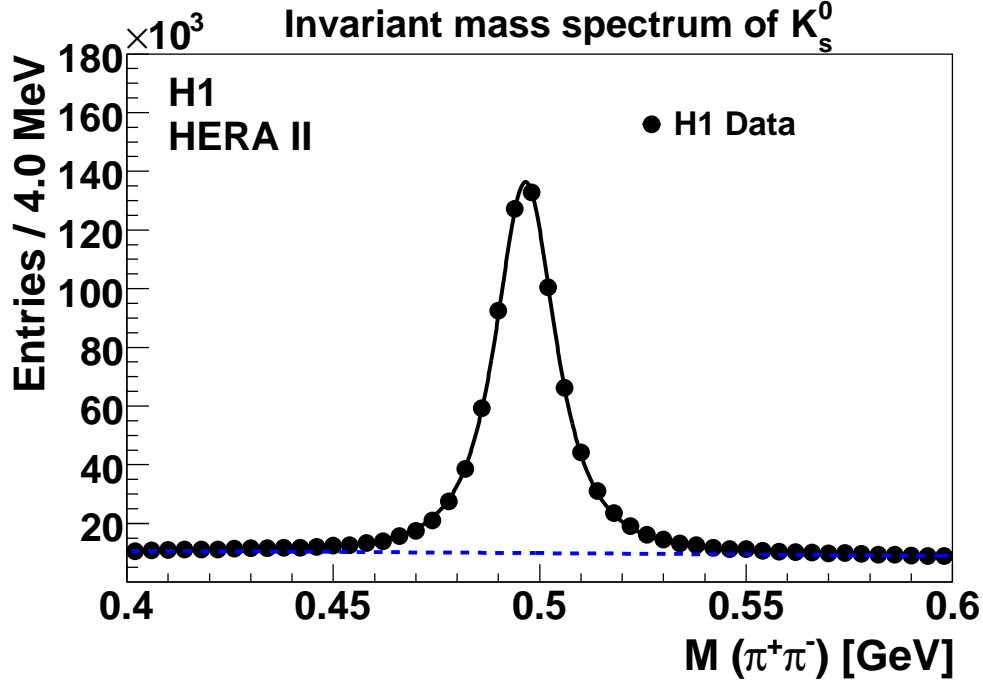


**Figure 7.5:** Invariant mass spectrum of the  $K_S^0 \rightarrow \pi^+\pi^-$  candidates. The points correspond to the observed data events. The distribution is fitted with a student's  $t$  function and a first order polynomial background function. The background is represented by the dashed line.

### 7.1.2 $K_S^0$ Lifetime

As an additional check of the  $K_S^0$  reconstruction, the lifetime of the selected  $K_S^0$  candidates is measured and compared with the MC. For the lifetime determination, the  $K_S^0$  candidates shown in Fig. 7.5 are divided into bins of  $c \cdot \tau$  and a fit to each of the resulting mass spectra is applied. The lifetime is determined by the equation

$$l = \beta\gamma \cdot c\tau = \frac{p}{m \cdot c} c \cdot \tau, \quad (7.7)$$

where  $l$  denotes 3-dimensional decay length,  $c$  is the speed of light,  $\beta$  is the ratio of the particle's velocity to speed of light  $c$ ,  $\beta = \frac{v}{c}$ ,  $\gamma$  is the relativistic relation,  $\gamma = \frac{1}{\sqrt{1-v^2/c^2}}$ ,  $\tau$  is the decay time,  $m$  is the mass and  $p = |\vec{p}|$  is the momentum of the  $K_S^0$  candidates. The lifetime of  $K_S^0$  candidates is shown for uncorrected data in Fig. 7.6a. The ratio of simulated to reconstructed DJANGO events (Fig. 7.6b) is applied to the data in order to have a corrected one. The corrected data is shown in Fig. 7.6c. The lifetime of  $K_S^0$  mesons is extracted by an exponential fit to this spectrum which yields

$$c\tau = 2.675 \pm 0.04 \text{ cm.}$$

The measured lifetime is in agreement with the world average value of  $c\tau = 2.678 \pm$

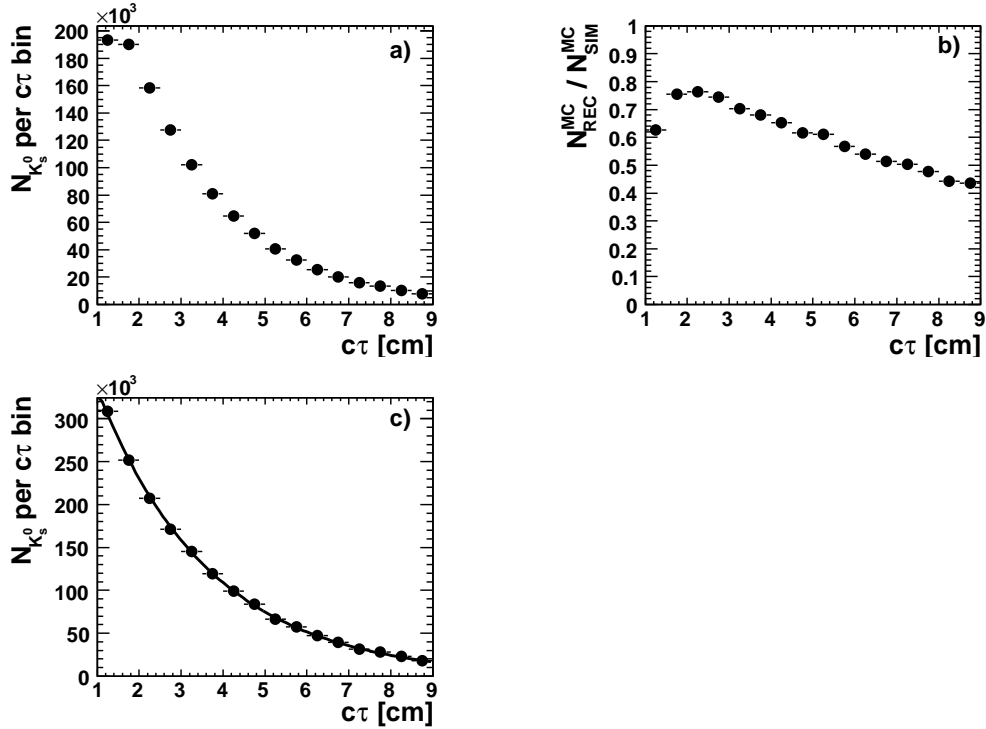


**Figure 7.6:** The lifetime of  $K_S^0$  candidates: a) uncorrected data, b) the ratio of simulated to reconstructed DJANGO events, c) corrected lifetime which is the resultant of application of ratio to the uncorrected data. The solid line represents the result of an exponential fit.

0.0015 cm [4]. This agreement gives further confidence that the selected  $K_S^0$  particles are indeed genuine  $K_S^0$  mesons produced at the interaction vertex.

### 7.1.3 Decay Topologies of $K_S^0$

The different topologies of the decay of  $K_S^0$  were examined for the signal. The  $K_S^0$  signal can be classified by the decay with inward or outward curved topology. Fig. 7.7 illustrates the two possible decay topologies which can be differentiated on the basis of the cross product of the momenta of two daughter particles.

The inward curved decay (so called *sailor decay topology*) is defined as

$$(\vec{p}_{\pi^+} \times \vec{p}_{\pi^-})_z < 0,$$

whereas the outward-curved (so called *seagull decay topology*) is

$$(\vec{p}_{\pi^+} \times \vec{p}_{\pi^-})_z > 0.$$

In Fig. 7.8,  $K_S^0$  signals are shown for seagull and sailor decay topologies. It can be seen that the seagull decays have a broader distribution than the sailor decays. The sailor decay topology is less sensitive to the track reconstruction resolution.



**Figure 7.7:** Decay topologies of  $K_S^0$ : Seagull (left) and Sailor (right) decay topology.

## 7.2 Primary $\pi^\pm$ Selection

Due to the short lifetime,  $K^{*\pm}$  mesons decay extremely close to the primary vertex and the daughters appear to originate from the interaction point. The charged pion candidates,  $\pi^\pm$ , are selected from central primary tracks whose measured distance of closest approach to the primary interaction vertex,  $dca'$ , is less than 0.25 cm. Each central primary track is required to have a minimum transverse momentum  $p_T$  with respect to the beam direction,  $p_T > 120$  MeV. The pseudorapidity is restricted to the range of  $|\eta(\pi^\pm)| < 1.5$ . The control distributions of primary pions  $\pi^\pm$  are shown in Fig. 7.9. In general the quantities of primary pions  $\pi^\pm$  are well described by DJANGO Monte Carlo simulation.

## 7.3 $K^{*\pm}$ Reconstruction

After applying the selection cuts, described above in detail, on both  $K_S^0$  and primary  $\pi^\pm$  candidates, tracks are combined to reconstruct  $K^{*\pm}$  candidates. For that purpose the mass of  $K_S^0$  candidate was fixed to the world average value of 497.61 MeV [4]. When pairing the  $K_S^0$  candidates with primary pions  $\pi^\pm$  to reconstruct the  $K^{*\pm}$  signal, track ID's (identification numbers assigned to each track in the event reconstruction stage) were checked in order to avoid using the same track as primary  $\pi^\pm$  and daughter pion of  $K_S^0$ .

Once the  $K^{*\pm}$  candidates are reconstructed, the cuts which determine the kinematic region can be applied. The kinematic region of the  $K^{*\pm}$  meson is restricted by the geometric acceptance and reconstruction efficiency of CTD as the follows:

- The pseudorapidity of the  $K^{*\pm}$  meson,  $\eta_{(K^*)}$ , is required to be in the range  $-1.5 < \eta_{(K^*)} < 1.5$  such that the reconstructed  $K^{*\pm}$  meson and its decay products lie within the acceptance of CTD.
- The transverse momentum of the  $K^{*\pm}$ ,  $p_{T(K^*)}$ , must be larger than 1 GeV. This cut suppresses combinatorial background from low  $p_T$  tracks, and the daughter particles are restricted to a momentum range where the CTD has high, well understood, reconstruction efficiency.

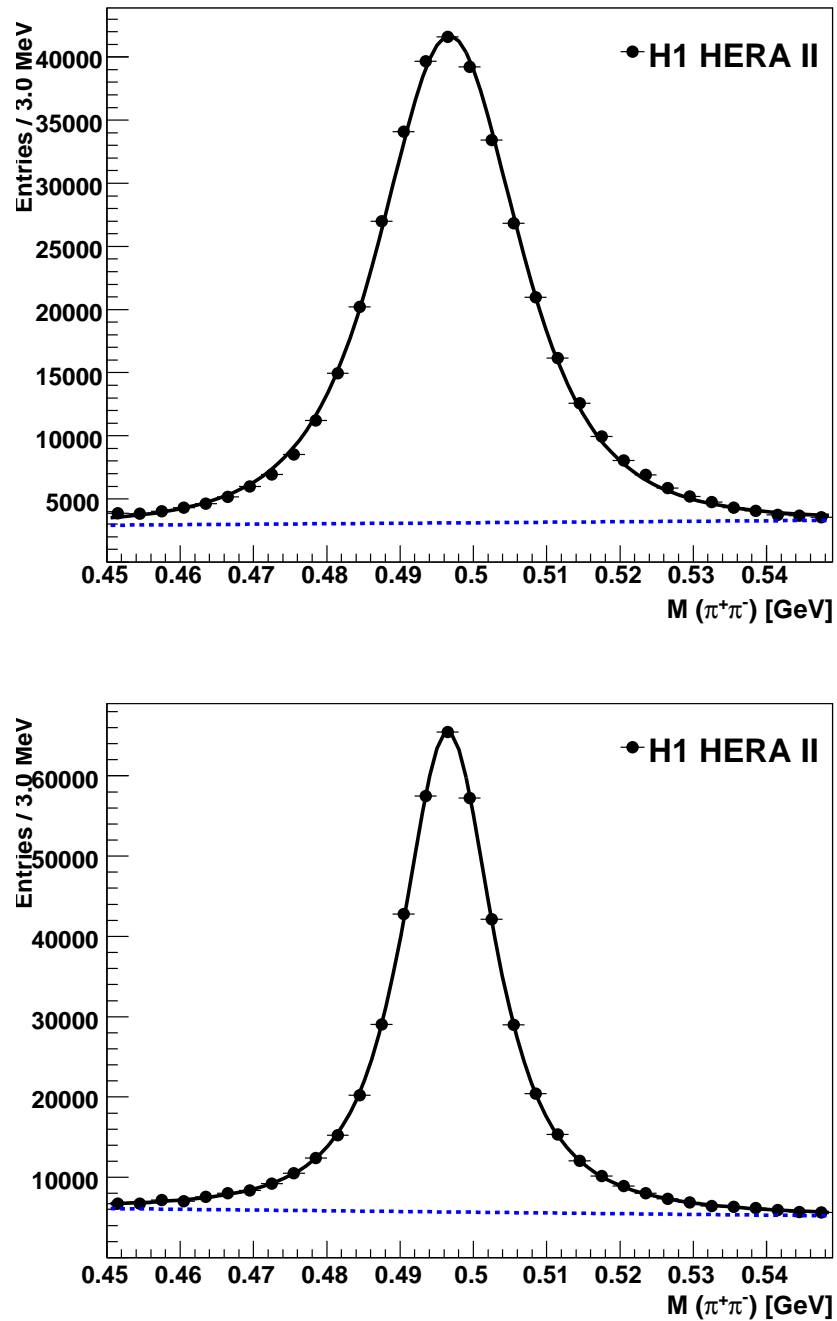
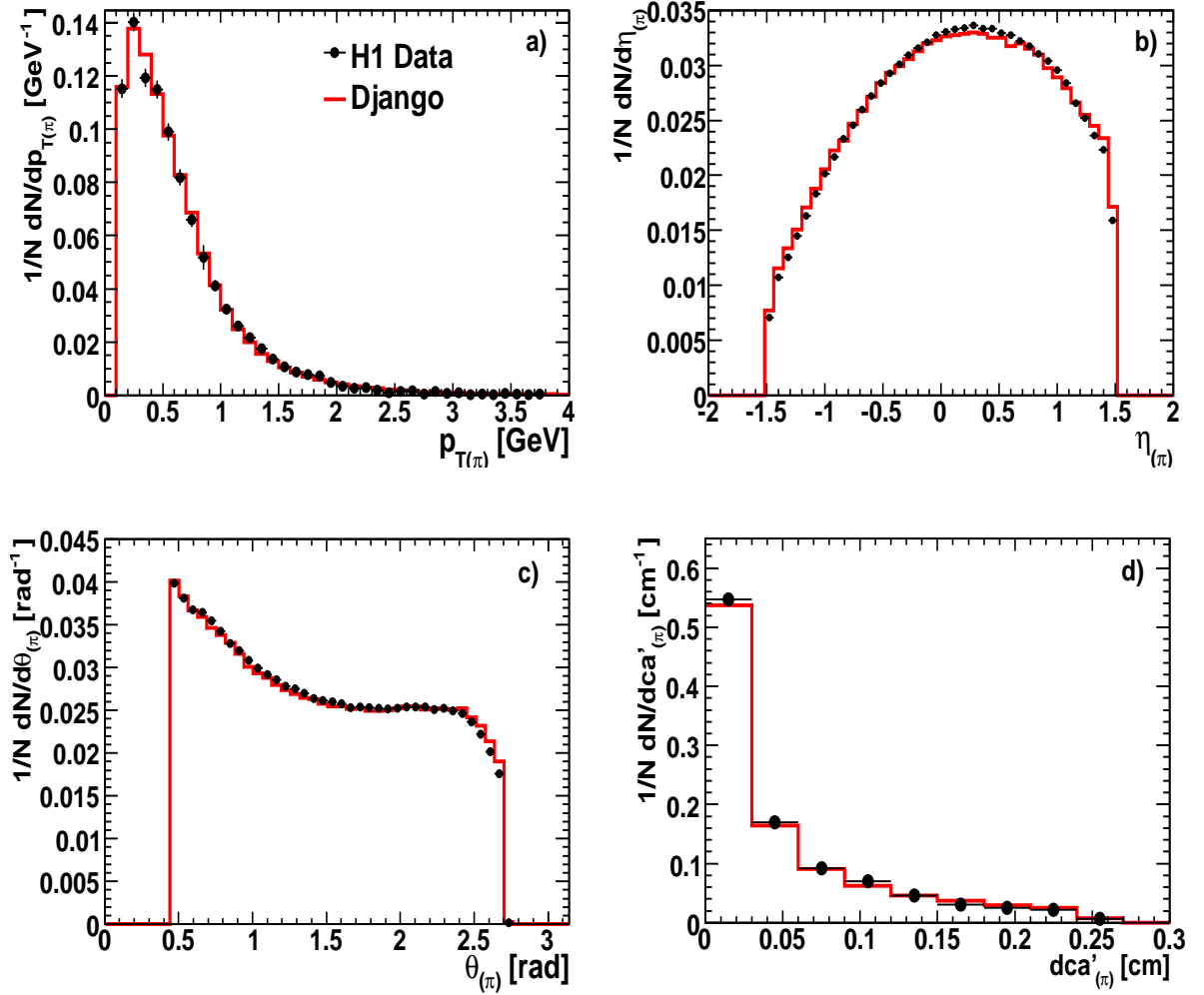


Figure 7.8: Invariant mass spectrum of  $K_S^0$  for different decay topologies: Seagull (top) and Sailor (bottom).



**Figure 7.9:** Control distributions for primary pions  $\pi^\pm$ . The following quantities are shown: a) the transverse momentum  $p_{T(\pi)}$ , b) the pseudorapidity  $\eta(\pi)$ , c) the polar angle  $\theta(\pi)$ , d) the distance of closest approach to the primary vertex  $dca'_{(\pi)}$ . Shown are data (full points) compared with DJANGO Monte Carlo simulation (solid line).

The control distributions of reconstructed  $K^{*\pm}$  particles of the pseudorapidity  $\eta_{(K^*)}$ , the polar angle  $\theta_{(K^*)}$ , the azimuthal angle  $\phi_{(K^*)}$  and the transverse momentum  $p_{T(K^*)}$  are shown in Fig. 7.10. The distributions are in general rather well described by the DJANGO Monte Carlo.

After having applied all selection cuts, the  $K^{*\pm}$  signal is still governed by a large combinatorial background. The fit to obtain a correct number of  $K^{*\pm}$  from the invariant mass distribution plays an important role in this analysis. The number of  $K^{*\pm}$  mesons is given by subtracting the background candidates from the candidates of the  $K^{*\pm}$  meson signal.

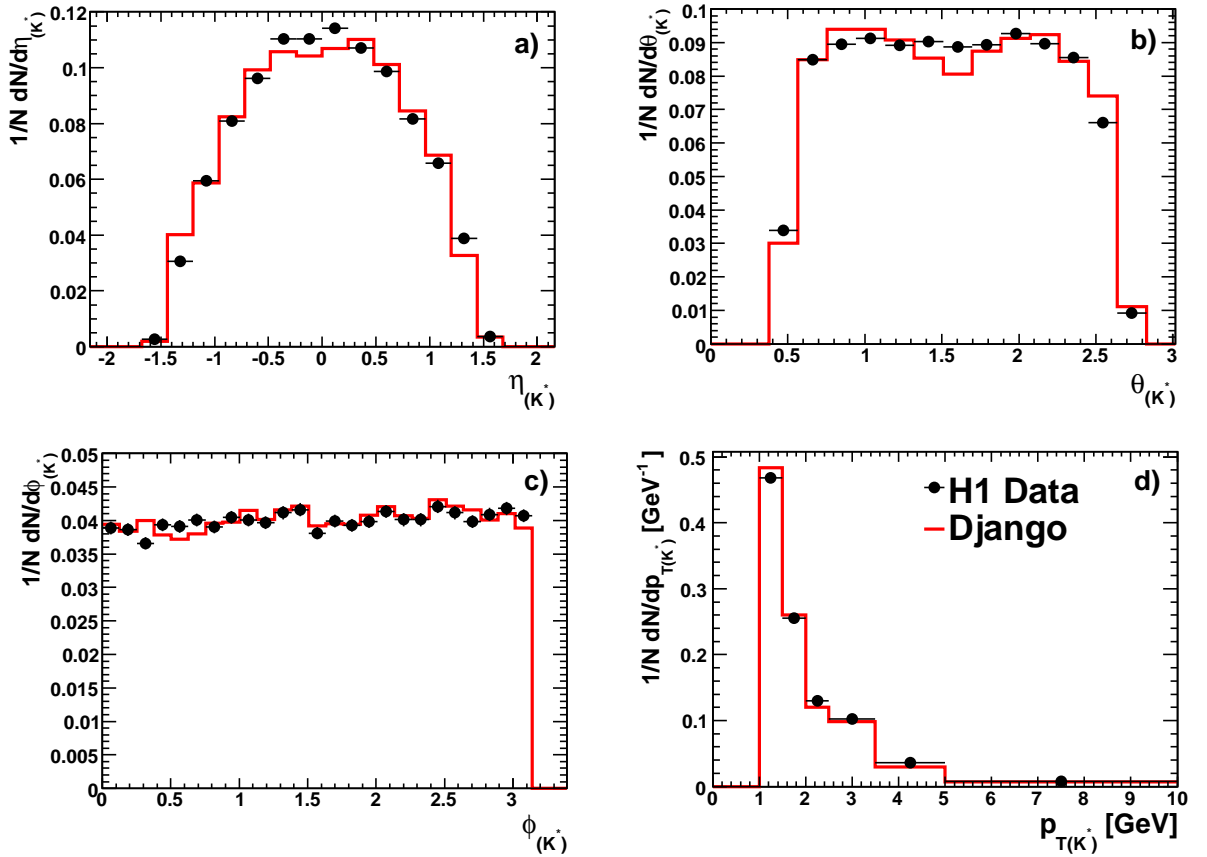


**Figure 7.10:** Control distributions of reconstructed  $K^{*\pm}$  mesons. The full dots indicate the data and the line indicates the DJANGO MC simulation. Following quantities are shown: a) the pseudorapidity  $\eta_{(K^*)}$ , b) the polar angle  $\theta_{(K^*)}$ , c) the azimuthal angle  $\phi_{(K^*)}$  and d) the transverse momentum  $p_{T(K^*)}$ .

### 7.3.1 Signal Extraction

The mass distribution of the  $K^{*\pm}$  signal is described with the relativistic Breit-Wigner function

$$BW(m) = \frac{m}{q} \cdot \frac{\Gamma'_K}{(m^2 - m_K^2)^2 + (m_K \cdot \Gamma_K'^2)}, \quad (7.8)$$

where  $m$  is the mass of  $K^*$ ,  $m_K$  is the central mass of the  $K^*$  mass distribution, and  $\Gamma'_K$  is defined as

$$\Gamma'_K(m) = \Gamma_K \cdot \left( \frac{q(m)}{q(m_K)} \right)^{2l+1} \cdot \frac{m_K}{m}, \quad (7.9)$$

where  $\Gamma_K$  is the natural width of the  $K^{*\pm}$ ,  $q$  is the momentum transfer to each decay particle in the centre of mass system and  $l$  is the relative angular momentum of the decay products. Since the  $K^{*\pm}$  are vector mesons decaying into two pseudoscalar mesons,  $l = 1$ .

The natural width  $\Gamma_K$  of  $K^{*\pm}$  is fixed to its PDG value of 50.8 MeV [4]. The mass position  $m_K$  is a free parameter of the fit function.

In the MC simulation the  $K^*$  signal is described by a so-called non-relativistic Breit-Wigner function:

$$BW(m) = \frac{\Gamma_K}{(m_0 - m)^2 + \frac{\Gamma_K^2}{4}}. \quad (7.10)$$

The background function parametrisation is chosen as

$$BG(m) = P_1 \cdot (m_0 - (m_{K^0} + m_\pi)^{P_2}) \cdot \exp(P_3 m + P_4 m^2 + P_5 m^3). \quad (7.11)$$

Here,  $P_1$ ,  $P_2$ ,  $P_3$ ,  $P_4$  and  $P_5$  are free parameters. The background function is used for both data and MC. The  $K_S^0 \pi^\pm$  tracks which do not come from the same  $K^{*\pm}$  are the dominant background source in the invariant mass distribution. The wrong combinations of  $K_S^0$  and  $\pi^\pm$  lead to a significant background under the signal. Another potential source of background is caused by tracks which do not come from a  $K^{*\pm}$  but from another resonance decay. The higher resonances like  $K^*(1430)$ ,  $K_2^*(1430)$  and  $K^*(1680)$  are the only known contributions to such backgrounds. Since these strange resonances contribute outside of the  $K^{*\pm}$  signal region and have smaller production cross sections than the  $K^{*\pm}$ , they can be safely neglected. To use the invariant mass for identification is most effective for two body decays as in the present analysis. The more particles are involved the higher is the combinatorial background. The invariant mass spectrum of  $K_S^0 \pi^\pm$  combinations is shown in Fig. 7.11. The number of  $K^{*\pm}$  mesons after background subtraction obtained from the fit is 78819. The fitted invariant mass,  $m_{K^{*\pm}}$ , for the data is measured as  $m_{K^{*\pm}} = 890.32 \pm 0.38$  MeV which is reasonably well in agreement with the world average value of  $891.66 \pm 0.26$  MeV [4].

Fig. 7.12 shows the invariant mass spectra of  $K_S^0 \pi^\pm$  combinations in six  $p_T$  bins in the range 1 to 10 GeV. At the bottom of each plot a ratio is shown and is defined as:

$$\text{Ratio} = \frac{N^{DATA} - N^{FIT}}{\sqrt{N^{DATA}}}, \quad (7.12)$$

where  $N^{DATA}$  and  $N^{FIT}$  are the number of entries obtained by data and fit function, respectively. Due to the limited statistics, there has been no  $K^{*\pm}$  signal obtained above

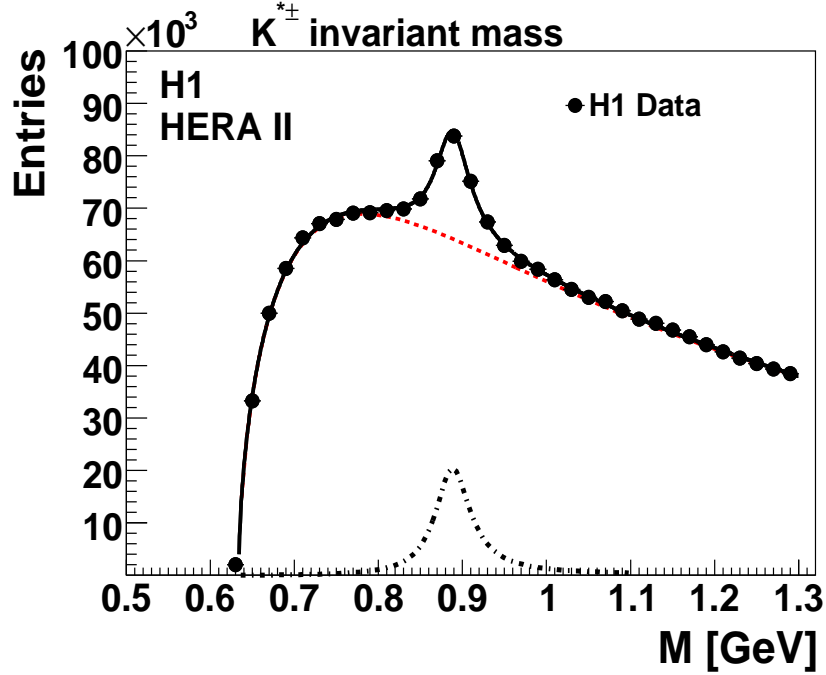


**Figure 7.11:** Invariant mass spectra of  $K_S^0\pi^\pm$  combinations after application of the all cuts mentioned in details in the text. The distribution is fitted with a relativistic Breit-Wigner function (solid line) and a background function (dashed line). The signal is shown with dash-dotted lines.

$p_T > 10$  GeV. The  $K_S^0\pi^\pm$  invariant mass distribution is also obtained for the DJANGO Monte Carlo simulation in intervals of transverse momentum  $p_T$ , see Fig. 7.13.

Furthermore, the invariant mass spectra of  $K_S^0\pi^\pm$  combinations are shown in five bins of scaled longitudinal momentum, Feynman  $x$  ( $x_F$ ), in Fig. 7.14. The Feynman variable  $x_F$  is defined as

$$x_F = \frac{2 \cdot p_L}{W}, \quad (7.13)$$

where  $p_L$  being the momentum of  $K^{*\pm}$  meson along the direction of exchanged boson  $\gamma$  and  $W$  the hadronic energy, both calculated in the hadronic centre of mass system<sup>3</sup> (i.e.  $\gamma p$  rest frame). In each plot shown in Figs. 7.12 - 7.14, a prominent  $K^{*\pm}$  signal peak appears above the large combinatorial background. The fit has also been performed for the other measured quantities of the cross section; pseudorapidity  $\eta$ , the four momentum squared  $Q^2$ , the centre-of-mass energy of the hadronic final state  $W_{\gamma p}$  and the transverse momentum squared in the hadronic final state  $P_T^{*2}$ ; which will be presented in chapter 8.

<sup>3</sup>The hadronic centre of mass system (CMS) is the rest frame of the beam proton and the exchanged boson. Both particles collide in the hadronic CMS head on along the  $z$ -axis, giving rise to a scattered quark and a proton remnant flying apart in opposite directions. Obviously, the transformation to this frame requires knowledge of the vector of the exchanged boson. The boson is defined as the 4-vector difference between the outgoing and incoming electron.

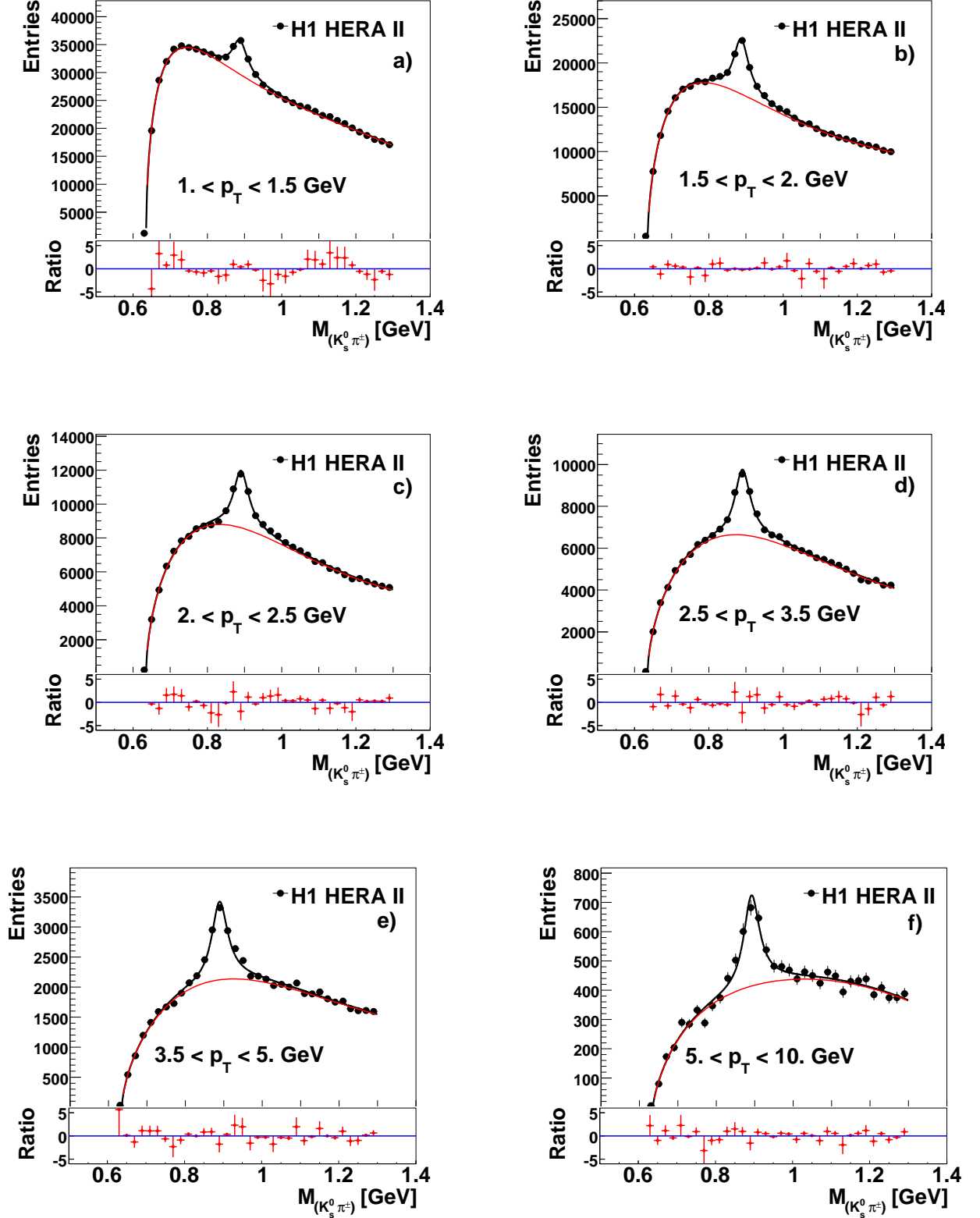
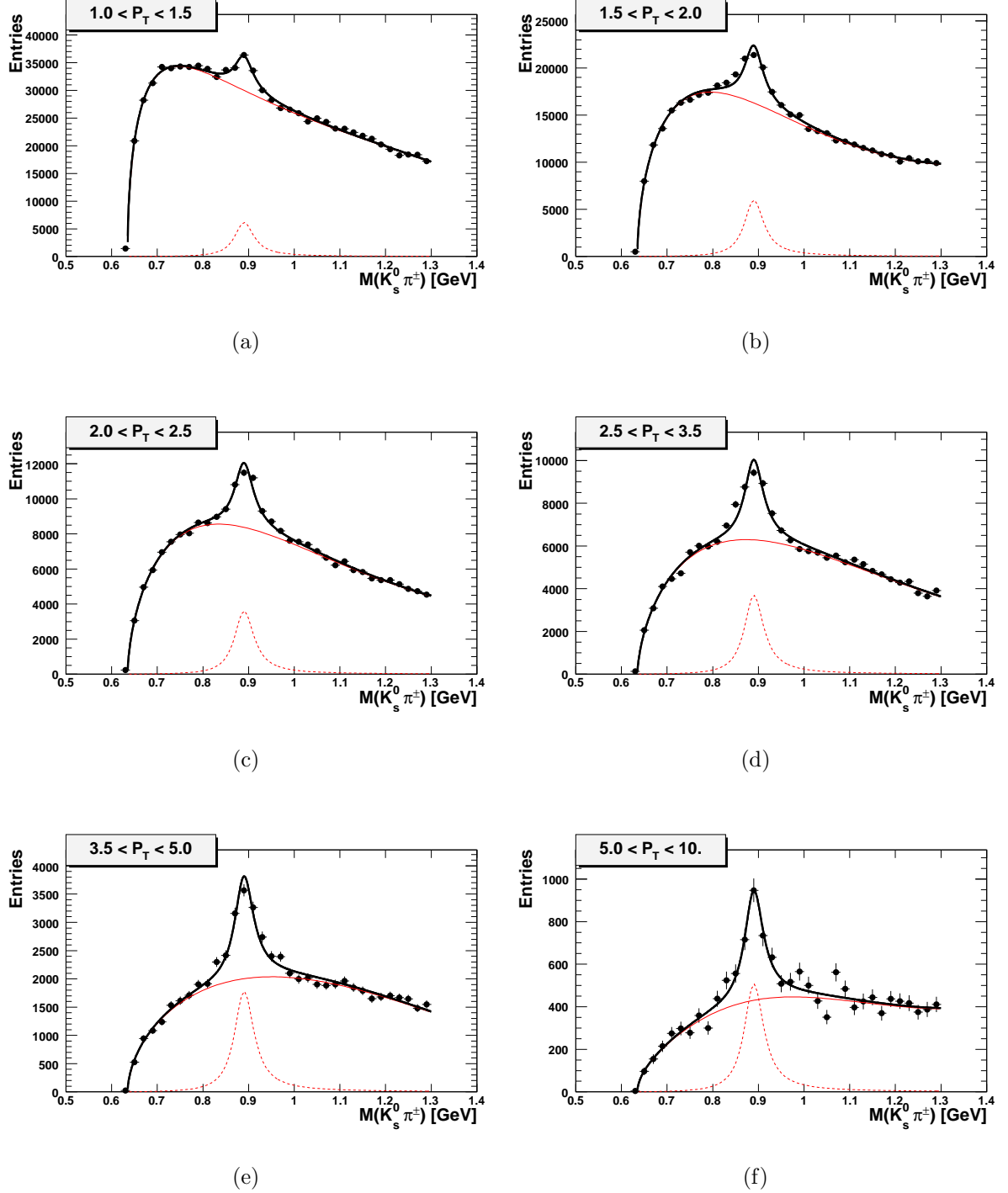
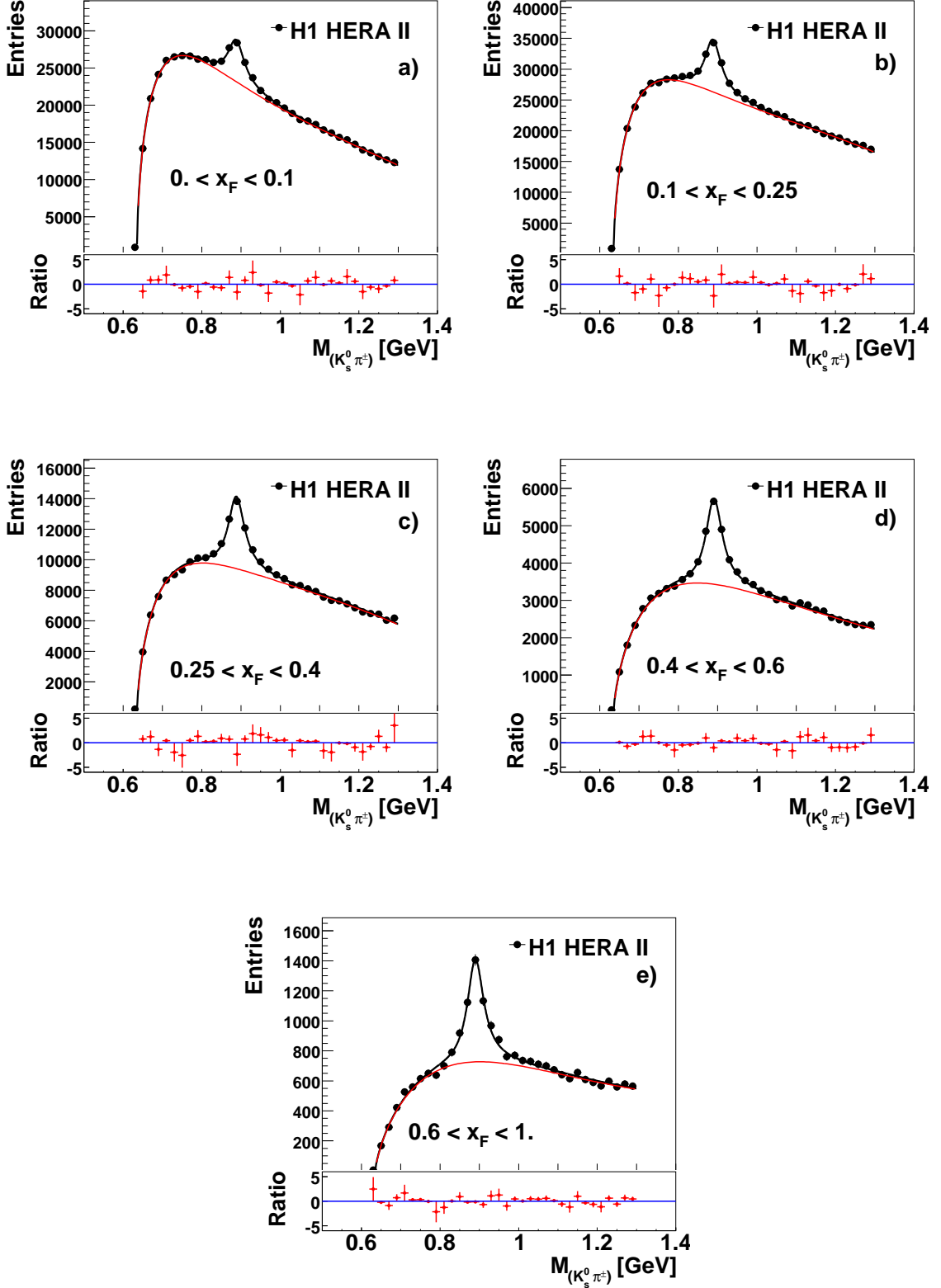


Figure 7.12: Invariant mass spectra of  $K_S^0 \pi^\pm$  combinations in intervals of transverse momentum  $p_T$ ; a)  $1 < p_T < 1.5$ , b)  $1.5 < p_T < 2$ , c)  $2 < p_T < 2.5$ , d)  $2.5 < p_T < 3.5$ , e)  $3.5 < p_T < 5$  and f)  $5 < p_T < 10$  GeV. The distribution is fitted with a relativistic Breit-Wigner function (black line) and a background function (red line). On the bottom of each figure the ratio distribution,  $\text{Ratio} = (N^{\text{DATA}} - N^{\text{FIT}})/\sqrt{N^{\text{DATA}}}$ , is shown.



**Figure 7.13:** The  $K_s^0 \pi^\pm$  invariant mass distribution for DJANGO Monte Carlo simulation in intervals of transverse momentum  $p_T$ ; (a)  $1 < p_T < 1.5$ , (b)  $1.5 < p_T < 2$ , (c)  $2 < p_T < 2.5$ , (d)  $2.5 < p_T < 3.5$ , (e)  $3.5 < p_T < 5$  GeV and (f)  $5 < p_T < 10$  GeV. The distribution is fitted with a relativistic Breit-Wigner function (black line) and a background function (red line). The signal is shown with dashed lines.



**Figure 7.14:** Invariant mass spectra of  $K_S^0\pi^\pm$  combinations in intervals of scaled longitudinal momentum  $x_F$ ; a)  $0. < x_F < 0.1$ , b)  $0.1 < x_F < 0.25$ , c)  $0.25 < x_F < 0.4$ , d)  $0.4 < x_F < 0.6$  and e)  $0.6 < x_F < 1$ . The distribution is fitted with a relativistic Breit-Wigner function (black line) and a background function (red line). On the bottom of each figure the ratio distribution,  $\text{Ratio} = (N^{\text{DATA}} - N^{\text{FIT}})/\sqrt{N^{\text{DATA}}}$ , is shown.

# Chapter 8

## Determination of the $K^{*\pm}$ Cross Section

This chapter describes the determination of the inclusive  $K^{*\pm}$  differential cross sections obtained from the analysis of the  $K^{*\pm} \rightarrow K_S^0 \pi^\pm$  decay chain. The cross sections are measured in the kinematic region

$$5 < Q^2 < 100 \text{ GeV}^2 \quad \text{and} \quad 0.1 < y_{e\Sigma} < 0.6,$$

and in the accessible range for the  $K^{*\pm}$  analysis

$$-1.5 < \eta_{(K^*)} < 1.5 \quad \text{and} \quad p_{T(K^*)} > 1 \text{ GeV}.$$

In the following sections, the procedure of extracting the cross sections from the measured  $K^{*\pm}$  signal is explained, including the corrections for the detector effects and the trigger efficiency. The different systematics sources and uncertainties are given in the last part of the chapter.

### 8.1 Cross Section Definition

The cross section,  $\sigma$ , is a Lorentz-invariant quantity and is a measure of the probability of interactions. It can be visualised as the geometrical overlap of the target and the projectile or the effective area presented by the target particle, which should be hit by the point-like projectile for an interaction to occur. Cross sections are useful as they can be directly compared to other experiments, whereas the number of  $K^{*\pm}$  candidates are different because each experiment has different luminosities, acceptances, etc.

The  $ep$  cross section ( $ep \rightarrow e'K^{*\pm}X$ ) is defined as

$$\sigma(ep \rightarrow e'K^{*\pm}X) = \frac{N_{K^*}}{\mathcal{L}}, \quad (8.1)$$

where  $N_{K^*}$  is the number of measured  $K^{*\pm}$  mesons in the given kinematic range for this process and  $\mathcal{L}$  is the luminosity.

The total cross section for  $K^{*\pm}$  mesons is given by the following equation:

$$\sigma_{tot}^{vis}(ep \rightarrow e'K^{*\pm}X) = \frac{N_{K^*}}{\mathcal{L} \cdot \mathcal{BR}(K^{*\pm} \rightarrow K_S^0\pi^\pm \rightarrow \pi^+\pi^-\pi^\pm) \cdot \mathcal{A} \cdot \epsilon_{rec} \cdot \epsilon_{trig}}, \quad (8.2)$$

where  $N_{K^*}$  is the total number of  $K^{*\pm}$  mesons obtained in the given visible range,  $\mathcal{L}$  is the total integrated luminosity,  $\mathcal{A}$  is the detector acceptance,  $\epsilon_{rec}$  and  $\epsilon_{trig}$  are the reconstruction and trigger efficiencies, respectively. These efficiencies will be described in the following sections.  $\mathcal{BR}(K^{*\pm} \rightarrow K_S^0\pi^\pm \rightarrow \pi^+\pi^-\pi^\pm)$  is the branching ratio of the analysed  $K^{*\pm}$  decay chain and amounts to 0.227 [4].

The differential cross section is defined like in Eq. 8.2, but with the difference that the number of  $K^{*\pm}$  mesons and the detector correction factors are obtained for each interval  $\Delta\xi$  of the interest quantity  $\xi$ . Hence, the differential cross section as a function of any given quantity  $\xi$ , can be written as:

$$\frac{d\sigma^{vis}(ep \rightarrow e'K^{*\pm}X)}{d\xi} = \frac{N_{K^*}}{\Delta\xi \cdot \mathcal{L} \cdot \mathcal{BR}(K^{*\pm} \rightarrow K_S^0\pi^\pm \rightarrow \pi^+\pi^-\pi^\pm) \cdot \mathcal{A} \cdot \epsilon_{rec} \cdot \epsilon_{trig}}, \quad (8.3)$$

where  $N_{K^*}$  is the number of  $K^{*\pm}$  mesons in a bin of width  $\Delta\xi$ .

## 8.2 Bin Selection

The inclusive differential  $K^{*\pm}$  cross section measurements were performed as functions of the transverse momentum  $p_T$ , the pseudorapidity  $\eta$ , the four momentum squared  $Q^2$ , the centre-of-mass energy of the hadronic final state  $W_{\gamma p}$ , the Feynman variable  $x_F$  and the squared transverse momentum of the  $K^{*\pm}$  meson in the photon proton rest frame  $P_T^{*2}$  with the following bin boundaries:

$$\begin{aligned} p_T &: 1, 1.5, 2, 2.5, 3.5, 5, 10 \text{ [GeV]} \\ \eta &: -1.5, -1.125, -0.750, -0.375, 0, 0.375, 0.750, 1.125, 1.5 \\ Q^2 &: 5, 10, 20, 40, 80, 100 \text{ [GeV}^2\text{]} \\ W_{\gamma p} &: 100, 125, 150, 175, 200, 250 \text{ [GeV]} \\ x_F &: 0, 0.1, 0.25, 0.4, 0.6, 1 \\ P_T^{*2} &: 0, 5, 10, 20, 40, 100 \text{ [GeV}^2\text{]}. \end{aligned}$$

The interval width of the bins is limited by the amount of statistics in data and also significance of  $K^{*\pm}$  mesons in the parametrisation, used to fit the invariant mass distribution. The approach is to achieve a binning which is as fine as feasible in order to obtain as much information about the  $K^{*\pm}$  mesons kinematics as possible, within the experimental resolution.

## 8.3 Correcting Data with Monte Carlo Simulations

The limitations of the detector performance give rise to errors on reconstructed quantities, which leads to distributions at the detector level which are smeared and shifted with respect to the true values. To obtain a precise measurement from the data, different effects of the detector need to be corrected for, i.e. the finite detector resolutions, efficiencies and geometric acceptances. For this purpose, in this analysis, events from the DJANGO Monte Carlo generator are compared before and after passing through the detector simulation, labelled *generator* (GEN) level and *reconstructed* (REC) level, respectively. If the REC level events describe the data in every detail, then it is possible to correct the data for the detector effects. If deficiencies are found in the simulation, for instance the resolution of a particular detector is not modelled correctly, then the simulated resolution is tuned to the data in order to acquire a better description.

The relation between GEN level and REC level events are used to study the detector effects. The same cuts are applied to both GEN and REC level events. This results in four different cases which can be characterised by four independent variables, illustrated in Fig. 8.1. The four independent variables are defined as following:

- $N_{\text{STAY}}^i$  : The number of events which are generated and reconstructed in the same bin ( $i$ ), (see Fig. 8.1a),
- $N_{\text{SMEAROUT}}^i$  : The number of events which smeared out of a generated bin ( $i$ ) but selected in bin ( $j$ ) with  $j \neq i$ , (see Fig. 8.1b),
- $N_{\text{SMEARIN}}^i$  : The number of events which smeared into a reconstructed bin ( $i$ ) but not originated from the same generated bin ( $i$ ), (see Fig. 8.1c),
- $N_{\text{LOST}}^i$  : The number of events with a generated bin ( $i$ ) but not selected at the reconstructed level, (see Fig. 8.1d).

The total number of GEN and REC events are then defined as:

- $N_{\text{GEN}}^i = N_{\text{STAY}}^i + N_{\text{SMEAROUT}}^i + N_{\text{LOST}}^i$ ,
- $N_{\text{REC}}^i = N_{\text{STAY}}^i + N_{\text{SMEARIN}}^i$ .

Using the definitions above, the following sections detail the quantities of acceptance ( $\mathcal{A}$ ), purity ( $\mathcal{P}$ ), and stability ( $\mathcal{S}$ ) which are relevant for the cross section determination.

### 8.3.1 Acceptance

Since the H1 detector does not cover a  $4\pi$  solid angle nor the full momentum range, there are areas where the final particles are not or only partially detected. In order to take account of such areas an acceptance correction is necessary. The acceptance,  $\mathcal{A}$ ,

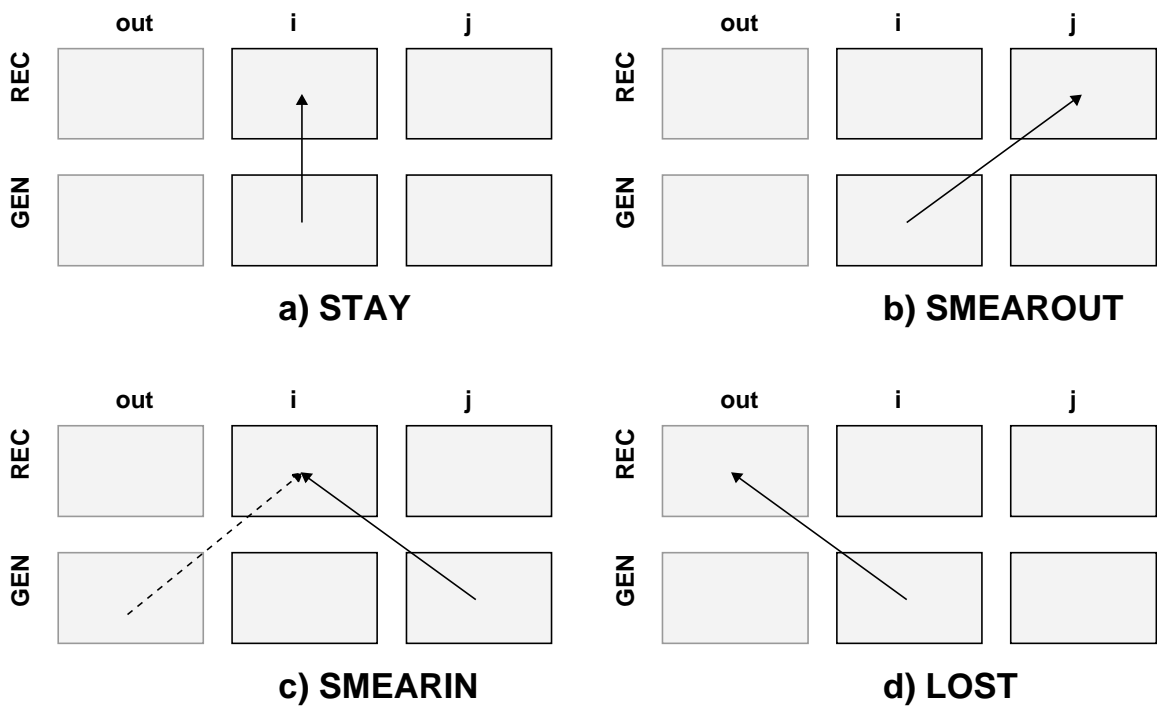


**Figure 8.1:** A schematic view of the migrations. The *path* of an event from GEN level to REC level is shown by arrows. The thick squares are bins inside the measured phase space, dotted squares bins outside of the measured phase space. a) is an illustration of the situation where an event has the same GEN and REC bin, b) illustrates an event smearing out of GEN bin  $i$  into REC bin  $j$ , c) shows an event smearing into a REC bin  $i$  from GEN bin  $j$  or from outside of the bins in the GEN phase space (broken line), d) shows a GEN event being lost from REC sample by being reconstructed outside of the measured phase space.

compares the number of reconstructed events to generated events. Hence, the acceptance of a bin  $i$  is defined as:

$$\mathcal{A} = \frac{N_{REC}^i}{N_{GEN}^i}, \quad (8.4)$$

where  $N_{REC}^i$  and  $N_{GEN}^i$  are described in the preceding section. Fig. 8.2 shows the acceptance as a function of  $p_T$ ,  $\eta$ ,  $Q^2$ ,  $W_{\gamma p}$ ,  $x_F$  and  $P_T^{*2}$ . These acceptances are determined with the DJANGO Monte Carlo simulation. The acceptance is around 17% on average. However, exceptions can be seen for the small values of momenta of the  $K^{*\pm}$  mesons  $p_T$  which are caused by the acceptance cut on the transverse momentum of the pion track. In addition, the most forward and backward bins of the pseudorapidity of  $K^{*\pm}$  mesons,  $\eta$ , are affected because of the acceptance cut applied on the polar angle  $\theta$  of tracks. The acceptance as a function of  $W_{\gamma p}$  is, as expected, approximately flat. In the present analysis in order to understand the source of having such a low acceptance a detailed investigation was performed. All selection criteria that are required to have a clean sample of  $K^{*\pm}$  has been checked one by one. Since the analysis of extracting the  $K^{*\pm}$  signal requires to identify a clean sample of  $K_S^0$  such a requirement results as 35% of efficiency drop down. The second big drop down around 50% has been observed for the requirement of primary pion tracks.

### 8.3.2 Purity and Stability

The purity is determined as the ratio of events reconstructed in a bin to those generated and reconstructed in that bin. The purity  $\mathcal{P}$  of bin  $i$  is defined as:

$$\mathcal{P} = \frac{N_{STAY}^i}{N_{REC}^i}, \quad (8.5)$$

where  $N_{STAY}^i$  and  $N_{REC}^i$  are described in section 8.3.

In order to describe how stable the distribution is with respect to migrations between the bins the stability,  $\mathcal{S}$ , is defined:

$$\mathcal{S} = \frac{N_{STAY}^i}{N_{GEN}^i - N_{LOST}^i}. \quad (8.6)$$

The stability gives the fraction of selected events which are reconstructed in the same bin they were generated in. In other words, the stability and purity quantify the fraction of events migrating out of and into the bin, respectively. These quantities are a measure of correlations between generated, true variables and their reconstructed values.

In the ideal case the purity would be equal to one which it is not reached in reality. Nevertheless, a large fraction of events should come from the bin which they are measured in. In Fig. 8.3, both purity  $\mathcal{P}$  and stability  $\mathcal{S}$  are shown for all bins for which the cross

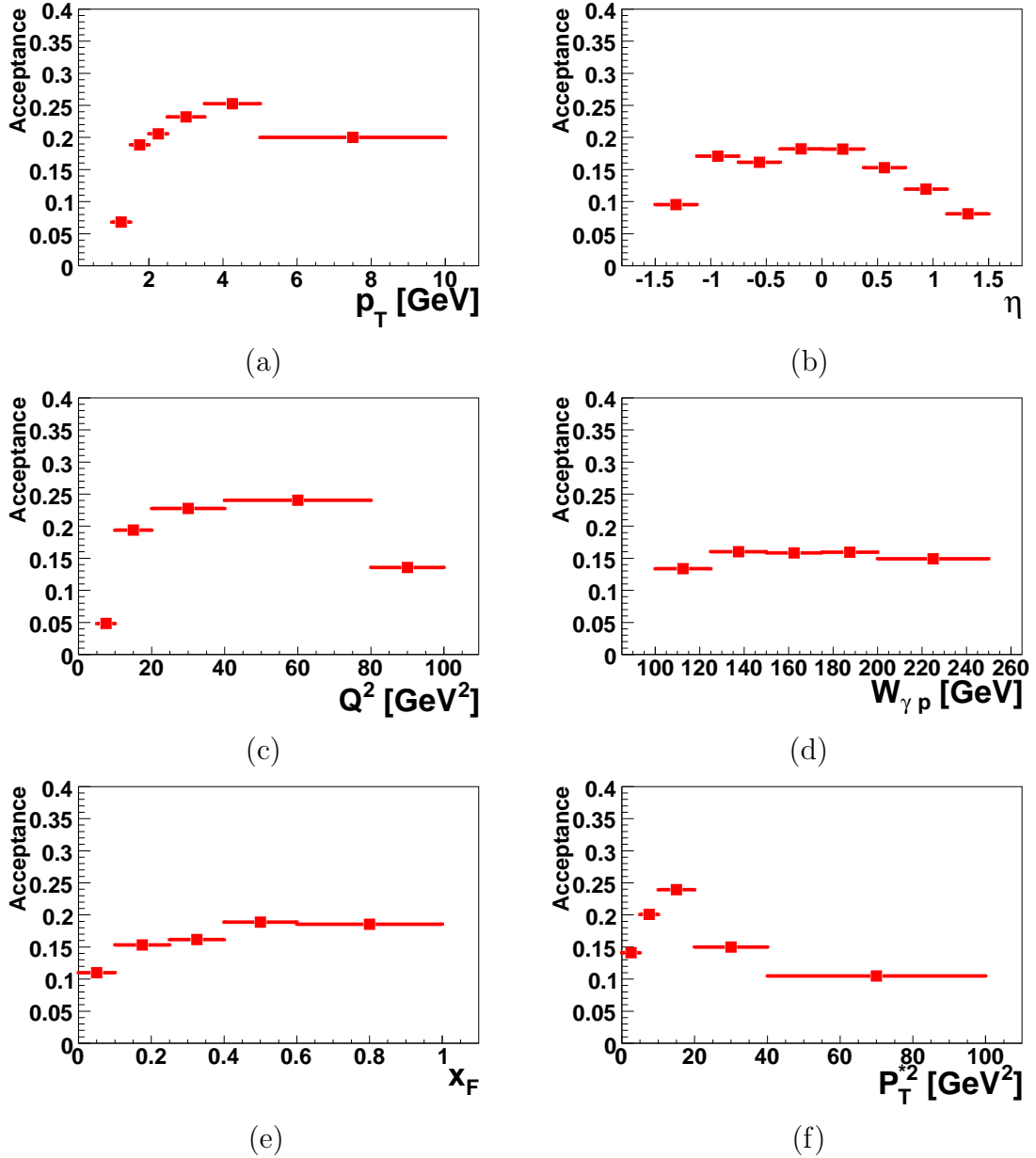
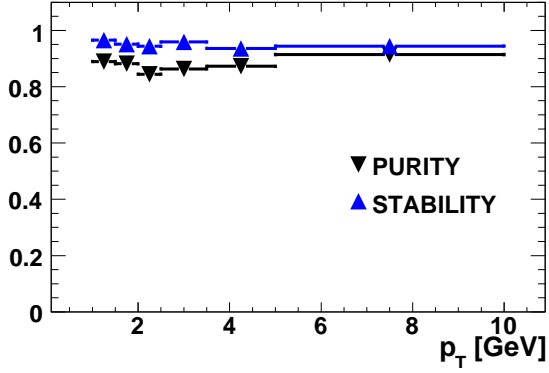
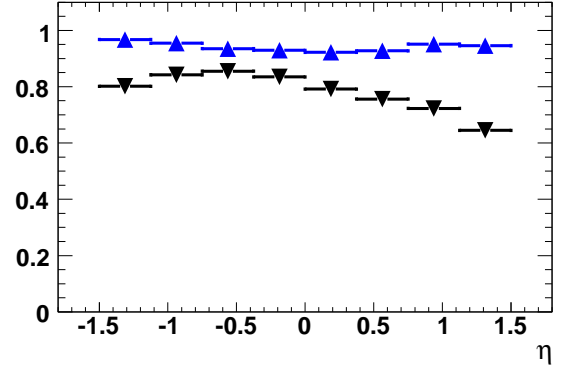


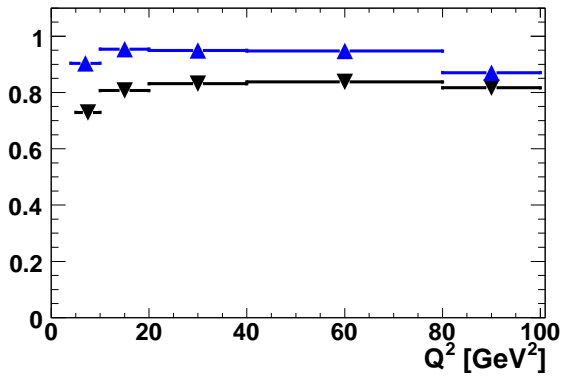
**Figure 8.2:** The acceptance correction factors  $\mathcal{A}$  of the H1 detector as a function of all measured quantities of the  $K^{*\pm}$  cross section: (a) the transverse momentum  $p_T$ , (b) the pseudorapidity  $\eta$ , (c) the four momentum squared  $Q^2$ , (d) the centre-of-mass energy of the hadronic final state  $W_{\gamma p}$ , (e) the Feynman variable  $x_F$ , and (f) the squared transverse momentum of the  $K^{*\pm}$  meson in the photon proton rest frame,  $P_T^{*2}$ .



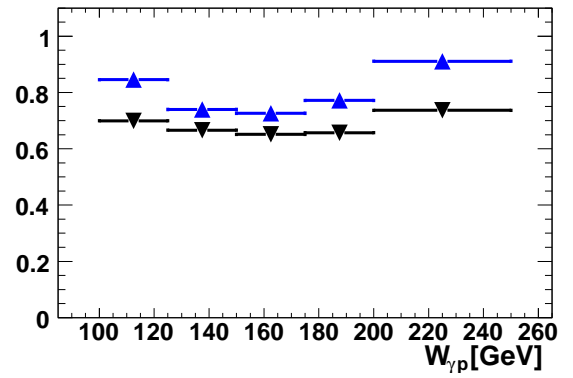
(a)



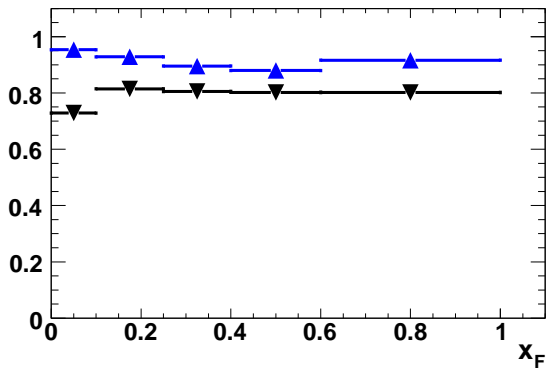
(b)



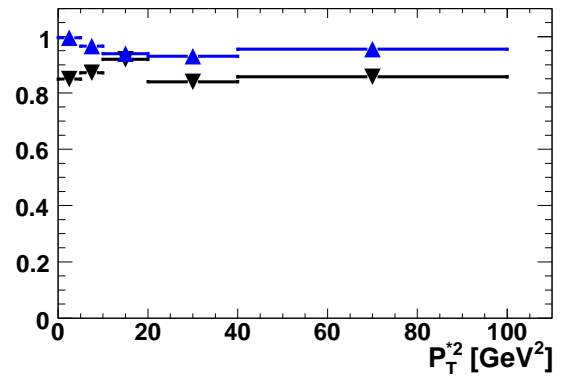
(c)



(d)



(e)



(f)

**Figure 8.3:** The purity  $\mathcal{P}$  (downward triangle) and stability  $\mathcal{S}$  (upward triangle) for the bins in which cross section measurements are performed: (a)  $p_T$ , (b)  $\eta$ , (c)  $Q^2$ , (d)  $W_{\gamma p}$ , (e)  $x_F$  and (f)  $P_T^{*2}$ .

section measurements are performed. In general the purity  $\mathcal{P}$  is around 80% with the some exceptions for instance at low  $Q^2$  and low  $x_F$  values the purity drops to 75%. Due to the worse resolution, the purity as a function of the quantity  $W_{\gamma p}$  is as expected lower than the other quantities. It can be seen that the stability  $\mathcal{S}$  is above 95% in all quantities.

## 8.4 Trigger Efficiency

In order to measure the cross section, any inefficiencies in the subtrigger used for this analysis must be well understood and corrected for. In this section the efficiency of the subtrigger ST61 will be determined.

The efficiency of a subtrigger ST is the probability that a signal event is detected by the subtrigger. The crucial point in the determination of a subtrigger ST is the definition of a *monitor trigger* (MT) sample. A suitable MT sample is composed of a large amount of events which have been triggered by one or several triggers which are independent of the subtrigger ST. The efficiency of the subtrigger ST is then defined as follows:

$$\varepsilon_{trig} = \frac{N_{ST \wedge MT}}{N_{MT}}, \quad (8.7)$$

where  $N_{ST \wedge MT}$  is the number of DIS events, passing all analysis cuts, triggered by subtrigger ST and monitor trigger MT, and  $N_{MT}$  is the number of DIS events triggered by the monitor trigger MT. In order to have enough statistics the subtrigger ST and the monitor trigger MT should have a large phase space overlap.

The subtrigger ST61 (see section 6.1.1) contains conditions based on the scattered electron candidate in the backward SPACAL calorimeter and general track conditions. Unfortunately, there is no subtrigger which collects enough statistics and which is completely independent of ST61. Therefore, the trigger efficiency of ST61 has to be determined with the efficiencies of its trigger elements. For the monitoring of the SPACAL part, the subtrigger ST71 which uses the LAr and the track trigger is taken. The track trigger is monitored by using the monitor triggers ST3, ST4, ST5, ST6, ST7 or ST9 which all are the SPACAL triggers. Hence the total trigger efficiency  $\varepsilon_{trig}$  is evaluated separately from the track trigger efficiency ( $\varepsilon_{TRACK}$ ) and the SPACAL trigger efficiency ( $\varepsilon_{SPACAL}$ ):

$$\varepsilon_{trig} = \varepsilon_{TRACK} \cdot \varepsilon_{SPACAL}. \quad (8.8)$$

The SPACAL trigger efficiency,  $\varepsilon_{SPACAL}$ , as a function of variables of the scattered electron and the event kinematics is displayed in Fig. 8.4. The efficiency is approximately 99.5% except in some bins of the scattered electron energy  $E_{e'}$  and the quantity  $E - p_z$  and is in agreement with the DJANGO MC simulation within 0.5%.

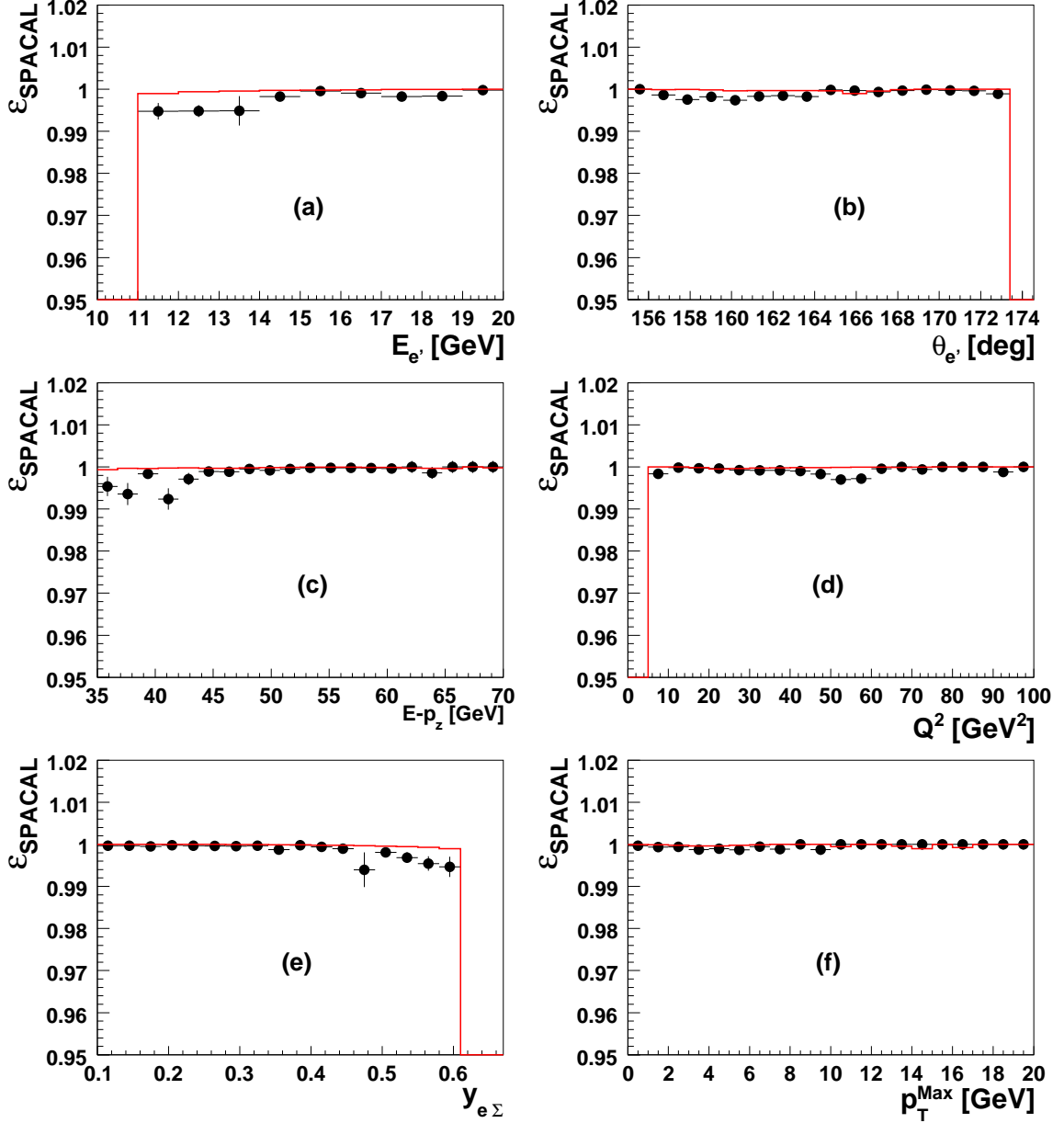


**Figure 8.4:** The efficiency of the SPACAL trigger elements,  $\varepsilon_{SPACAL}$ , included in ST61 is shown as a function of: a) the scattered electron energy  $E_{e'}$ , b) the scattered electron angle  $\theta_{e'}$ , c) the energy and longitudinal momentum balance of events  $E-p_z$ , d) the squared four-momentum transfer  $Q^2$ , e) the inelasticity  $y_{e\Sigma}$ , and f) the maximum transverse momentum observed in all CJC tracks,  $p_T^{Max}$ . The data (full points) are compared with the DJANGO Monte Carlo simulation (solid line).

The track condition which requires at least one track with a certain  $p_T$  threshold of 900 MeV is obtained from the FTT trigger (discussed in section 4.7). The track trigger efficiency,  $\varepsilon_{TRACK}$ , is shown in Fig. 8.5 as a function of the variables,  $E_{e'}$ ,  $\theta_{e'}$ ,  $E - p_z$ ,  $Q^2$ ,  $y_{e\Sigma}$ , and  $p_T^{Max}$ . The overall track trigger efficiency is above 97.8% and agrees with DJANGO within 0.5%.

The overall ST61 trigger efficiencies for data and MC are listed in Table 8.1. In data, the total trigger efficiency for DIS events with a  $K^{*\pm}$  candidate averaged over the entire data taking period amounts to 98%. Thus one can conclude that the trigger efficiency does not have a big impact on the data correction of the present analysis.

Trigger Element	Data	DJANGO
SPACAL	99.5%	100.0%
TRACK	97.8%	98.2%
ST61	97.3%	98.2%

**Table 8.1:** The overall trigger efficiencies for data and DJANGO MC simulation.

## 8.5 Systematic Uncertainties

The cross section measurement includes the determination of the accuracy of the measurement. Several sources can spoil the accuracy such as the uncertainty on the position determination of the detector, the uncertainty on the energy of the scattered electron etc. In order to estimate the influence of different sources, each source is varied separately by one standard deviation upwards and downwards and then the selection criteria are applied.

Corresponding to the two separate stages in the Monte Carlo production, the event generation and detector simulation, the sources of systematic uncertainties on the cross section measurement are divided in two categories. The experimental systematic uncertainties arise from the incomplete knowledge of detector effects and are related to the  $K^{*\pm}$  rate determination. The theoretical uncertainties represent the effect of uncertainties in the modelling of the  $ep$  interaction process.

The following systematic uncertainties are considered:

### Scattered Electron Energy and Polar Angle

The energy and polar angle of the scattered electron are not only used for evaluating the event kinematics of the four momentum transfer  $Q^2$ , the inelasticity  $y$  and the hadronic final state energy  $W$  but are used also for the boosting of particles from laboratory frame to  $\gamma^*p$  frame. Hence, the uncertainties on the scattered electron energy  $E_{e'}$  and the polar angle  $\theta_{e'}$  can indirectly influence the  $K^{*\pm}$  measurement.

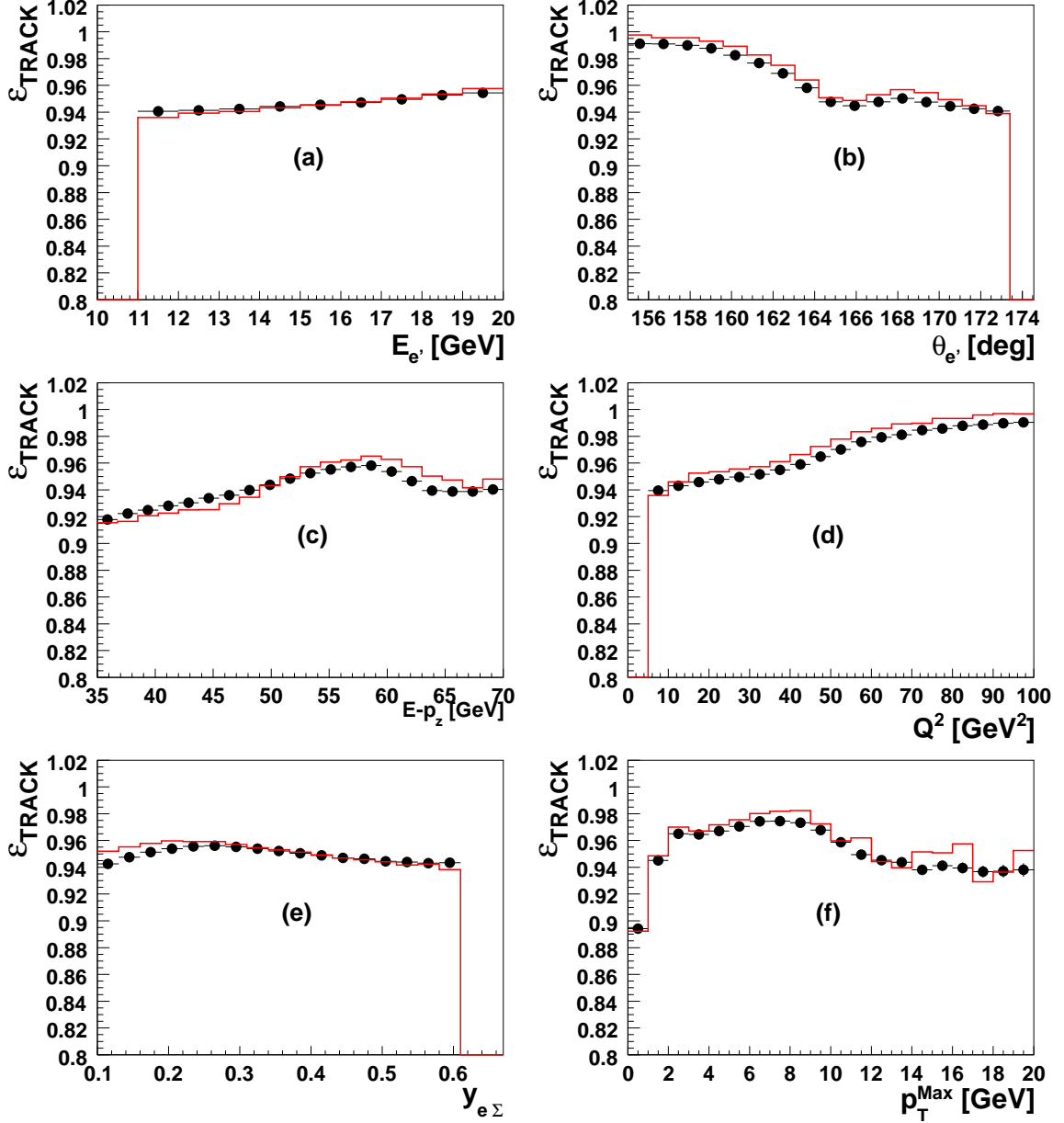


**Figure 8.5:** The efficiency  $\varepsilon_{TRACK}$  of the TRACK trigger elements included in ST61 shown as a function of: a) the scattered electron energy  $E_{e'}$ , b) the scattered electron angle  $\theta_{e'}$ , c) the energy and longitudinal momentum balance of events  $E-p_z$ , d) the squared four-momentum transfer  $Q^2$ , e) the inelasticity  $y_{e\Sigma}$ , and f) the maximum transverse momentum observed in all CJC tracks,  $p_T^{Max}$ . Data (full points) are compared with the DJANGO Monte Carlo simulation (solid line).

- The uncertainty in the polar angle of the scattered electron  $\theta_{e'}$  is varied within  $\pm 1$  mrad [?]. This contributes an uncertainty of  $\sim 2\%$  to the cross section.
- The energy of the scattered electron  $E_{e'}$  is known to within  $\pm 1\%$ . The variation of  $E_{e'}$  by  $\pm 1\%$  translates into a  $3.4\%$  uncertainty on the cross section.

### Luminosity

The determination of integrated luminosity leads to one of the important systematic uncertainty sources of the present analysis. In the end of the year 2006 a significant increase was observed in the yield (events/luminosity) around run 477000 in this and other analyses (see section 6.3). The origin of this increase has been identified as an acceptance problem of the detector, which has been used for the measurement of luminosity [156]. For the data taken before the increase an uncertainty of  $\delta L/L = 2.5\%$  was assigned to the luminosity measurement and  $\delta L/L = 5\%$  afterwards. The systematic uncertainty of the combined luminosity measurement for the present analysis is estimated to  $3.62\%$  where the errors are weighted, based on the amount of luminosity taken in the two run periods of different uncertainty.

### Track Efficiency

The dominant systematic error of this analysis is the uncertainty due to the charged track reconstruction efficiency. Since there is no other detector component available to test the tracking system, the determination of the tracking efficiency especially at low momentum values is a difficult task. This number is determined in H1 by looking at tracks that curl up within the CJC where the track is reconstructed after passing through some dead material. The resulting systematic error due to the uncertainty of the track efficiency is  $2\%$  per track, hence this analysis, where 3 tracks have to be measured, has a total track efficiency error of  $6\%$ .

### Trigger Efficiency

The determination of the trigger efficiency has already discussed in detail in section 8.4. The average difference of  $1\%$  between the trigger efficiency as extracted from the Monte Carlo simulation and the data is taken as the uncertainty on the trigger efficiency.

### Signal Extraction

The uncertainty of the overall number of reconstructed  $K^{*\pm}$  particles is determined from the data by comparing the numbers obtained from the fit of invariant mass spectra with the number obtained by simply counting the events after the subtraction of expected background. The systematic error of the reconstruction of the number of  $K^*$  has been determined as  $1\%$ .

### Photoproduction Background

Due to the higher cross section,  $\gamma p$  interactions ( $Q^2 \approx 0 \text{ GeV}^2$ ) usually cause a significant background in DIS samples, with particles from the hadronic final state faking electrons in SPACAL. The photoproduction background is significantly suppressed by the cuts on the electron. The photoproduction background has been estimated to be 0.15% [?].

### Primary Vertex Fit

The primary vertex is determined by fitting the tracks from CJC to their origin. Hence the primary vertex efficiency is defined as the probability to find a primary vertex and to fit the tracks of  $K^{*\pm}$  decay particles to this origin. The primary vertex fit efficiency can be obtained by the fraction  $N(K^*)_{vertex}/N(K^*)_{non-vertex}$  for both data and MC.  $N(K^*)_{vertex}$  and  $N(K^*)_{non-vertex}$  represent the number of primary and non primary vertex fitted tracks. The systematic uncertainty on the primary vertex fit is taken as 2.5% per  $K^*$ .

### Background Fit Function

A systematic uncertainty on the background distribution is performed by using a different function parametrisation, such as a Chebyshev polynomial:

$$BG(m) = a \cdot (\Delta m)^b \exp(\sum_{i=0}^3 a_i T_i(\Delta m)), \quad (8.9)$$

where  $T_i$  is the first kind of Chebyshev polynomial function ( $T_0(x) = 1$ ,  $T_1(x) = x$ ,  $T_2(x) = 2x^2 - 1$ ,  $T_3(x) = 4x^3 - 3x$ ),  $\Delta m$  is the difference between the central mass value of the  $K^{*\pm}$  and measured  $K^{*\pm}$  mass,  $a$ ,  $b$  and  $a_i$  are free parameters. The resulting uncertainties range from 2.6% up to 7.8% for different analysis bins.

### $K_S^0$ Decay Topology

As already discussed in section 7.1.3, a  $K_S^0$  has two different geometrical decay topologies, “sailor” and “seagull”. The uncertainty estimation of the  $K_S^0$  decay products invariant mass was performed by using the following ratio :

$$R = \frac{p}{t_1 + p + t_2}, \quad (8.10)$$

where  $p$  represents the number of  $K_S^0$  under the invariant mass peak ( $0.470 < M_{K_S^0} < 0.520 \text{ GeV}$ ),  $t_1$  and  $t_2$  are the numbers from the tails at the left and right side of the signal mass peak. The terms  $p$ ,  $t_1$  and  $t_2$  are indicated in Fig. 8.6. The ratio was studied separately for both decay topologies and the uncertainty directly translates into the cross section systematic error. The ratio  $R$  was checked for each decay topology and both data

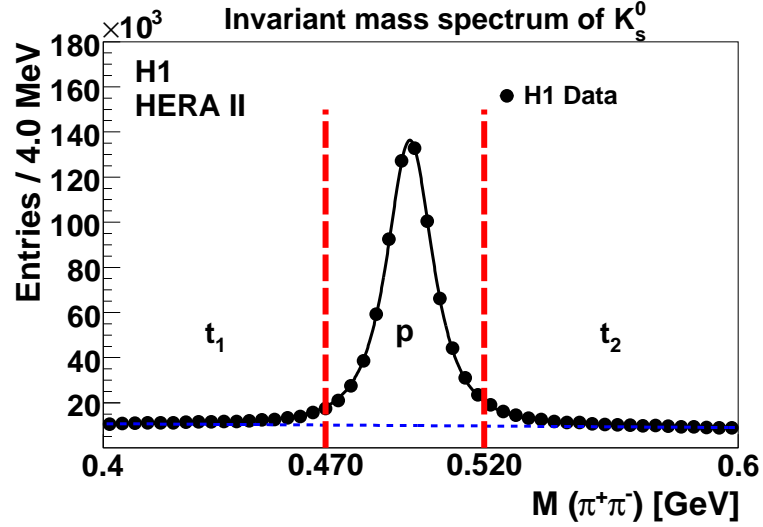


**Figure 8.6:** The terms which are used for the calculation of the ratio  $R = \frac{p}{t_1+p+t_2}$ .

and DJANGO MC simulation. Then the double ratio  $R_{double}^{topology}$  is calculated as following:

$$R_{double}^{topology} = \frac{R_{data}^{topology}}{R_{MC}^{topology}}, \quad (8.11)$$

where  $R_{data}^{topology}$  and  $R_{MC}^{topology}$  represent the ratio obtained for the data and the DJANGO MC simulation using Eq. 8.10, respectively. Here, *topology* stands for seagull or sailor decays. The obtained values are  $R_{double}^{seagull} = 0.962$  and  $R_{double}^{sailor} = 0.978$ . This leads to a systematic uncertainty of 3%.

### Model Dependence

The uncertainty attributed to the model dependence is derived by comparing acceptance corrections obtained with RAPGAP 3.1 and DJANGO 1.4, leading to a systematic error overall 3%, changing from bin to bin by up to 9%.

A summary of the different possible systematic sources and uncertainties in the visible cross section is listed in Table 8.2. The scattered electron energy, luminosity, and track efficiency are the dominant uncertainty sources. The total systematic error per bin is obtained by adding all different systematic errors in quadrature. The total systematic uncertainty sums up to 9%.

Possible Source	Variation	Uncertainty
Scattered electron Energy $E_{e'}$	$\pm 1\%$	3.4%
Scattered electron angle $\theta_{e'}$	$\pm 1$ mrad	2.0%
Luminosity		3.62%
Track efficiency	2% per track	6.0%
Trigger efficiency		1.0%
Signal extraction		1.0%
Photoproduction background		$\sim 0.15\%$
Primary vertex fit		2.5%
Background fit function	polynomial-Chebyshev function usage	2.5%
$K_S^0$ decay topology		3%
Model dependence	$0.5 \cdot \frac{\varepsilon_{rec}^{DJANGO} - \varepsilon_{rec}^{RPGAP}}{\varepsilon_{rec}^{DJANGO}}$	3%
<b>Total systematic uncertainty</b>		<b>9.0%</b>

**Table 8.2:** Summary of the systematic uncertainties.

# Chapter 9

## Results

The determination of the inclusive  $K^{*\pm}$  differential cross sections obtained from the analysis of the  $K^{*\pm} \rightarrow K_S^0 \pi^\pm$  decay chain has been explained in the preceding chapter. In this chapter the results of the inclusive  $K^{*\pm}$  meson cross section measured in neutral current DIS are presented. The total cross section is calculated according to Eq. 8.2 and the differential cross sections are obtained by using Eq. 8.3.

Inclusive cross sections  $\sigma(ep \rightarrow eK^{*\pm}X)$  are presented single and double differentially as a function of various kinematic variables in the laboratory and photon proton frames. The measured cross sections are compared to leading order Monte Carlo predictions obtained from the DJANGO and RAPGAP generators which are described in chapter 5. The results allow comparison of CDM model used by the DJANGO Monte Carlo program with MEPS model used by the RAPGAP. The various production mechanisms which contribute to the production of strange  $K^{*\pm}$  mesons are discussed.

### 9.1 Total Inclusive Cross Section

The total “visible” inclusive  $K^{*\pm}$  cross section  $\sigma_{total}^{vis}$  is measured in the kinematic range :

$$\begin{aligned} 5 < Q^2 < 100 \text{ GeV}^2, \\ 0.1 < y_{e\Sigma} < 0.6, \\ p_{T(K^*)} > 1 \text{ GeV}, \\ |\eta_{(K^*)}| < 1.5, \end{aligned} \tag{9.1}$$

and has the result

$$\sigma_{total}^{vis}(ep \rightarrow eK^{*\pm}X) = 7.36 \pm 0.087 \text{ (stat.)} \pm 0.88 \text{ (sys.) nb.}$$

Here the first error represents the statistical error and the second the systematic uncertainty. It can be seen that the precision of the measurement is dominated by the systematic uncertainty. The total cross section obtained with the DJANGO MC simulation amounts to  $\sigma_{total}^{vis} = 6.92 \text{ nb}$  and is in agreement with the measurement within

the errors. The RAPGAP MC simulation slightly underestimates the measurement and predicts  $\sigma_{total}^{vis} = 6.40$  nb. A summary of the total cross section measured and predicted by the leading order Monte Carlo DJANGO and RAPGAP can be found in Table 9.1.

total cross section [nb]	
Data	$7.36 \pm 0.087$ (stat.) $\pm 0.88$ (sys.)
DJANGO	6.92
RAPGAP	6.40

**Table 9.1:** Summary of the total inclusive  $K^{*\pm}$  cross sections in the visible range.

## 9.2 Differential Inclusive Cross Sections

The differential cross sections for inclusive  $K^{*\pm}$  in deep inelastic scattering are presented as a function of transverse momentum,  $p_T$ , pseudo-rapidity,  $\eta$ , four momentum squared of the virtual photon,  $Q^2$ , Feynman- $x$ ,  $x_F$ , the transverse momentum squared,  $P_T^{*2}$  and the centre-of-mass energy of the hadronic final state  $W_{\gamma p}$ . The quantities  $p_T$ ,  $\eta$  and  $Q^2$  are calculated in the laboratory frame while  $x_F$ ,  $P_T^{*2}$  and  $W_{\gamma p}$  in the  $\gamma^*p$  frame.

The measured inclusive differential cross sections are compared to leading order predictions given by DJANGO and RAPGAP. In order to have an easier comparison between the data and the MC simulations, the ratio  $R$  is calculated for all single differential cross section measurements as : for any measured quantity  $\xi$  is calculated as following :

$$R = \frac{d\sigma^{Data}}{d\xi} / \frac{d\sigma^{MC}}{d\xi}. \quad (9.2)$$

Here  $d\sigma^{Data}/d\xi$  and  $d\sigma^{MC}/d\xi$  are the differential cross sections of data and MC for any measured quantity  $\xi$ .

The results of measured single differential cross sections are tabulated in appendix A.

The measured inclusive cross section as a function of the transverse momentum of the  $K^{*\pm}$  meson in the laboratory frame,  $p_T$ , is shown in Fig. 9.1. A steep falling is observed with  $p_T$ . Reasonable good agreement is found with the leading order predictions DJANGO (CDM model implemented in) and RAPGAP (MEPS model implemented in). At low  $p_T$ , the measurement is underestimated by both predictions, at high  $p_T$  it is overestimated.

In Fig. 9.2 the measured differential cross section as a function of the pseudorapidity of the  $K^{*\pm}$ ,  $\eta$ , is presented. The distribution of  $\eta$  gradually falls down towards positive values of  $\eta$  and has a maximum in the bin of  $-0.750 < \eta < -0.375$ . DJANGO (CDM model) is in reasonable agreement with the measurement over the whole spectrum. The RAPGAP (MEPS model) simulation is not compatible with the data in the forward region  $\eta > 0.375$ . Since the influence of the hadronisation process is enlarged in the forward region ( $\eta > 0.375$ ) different suppression factor values can be tried. It can be seen

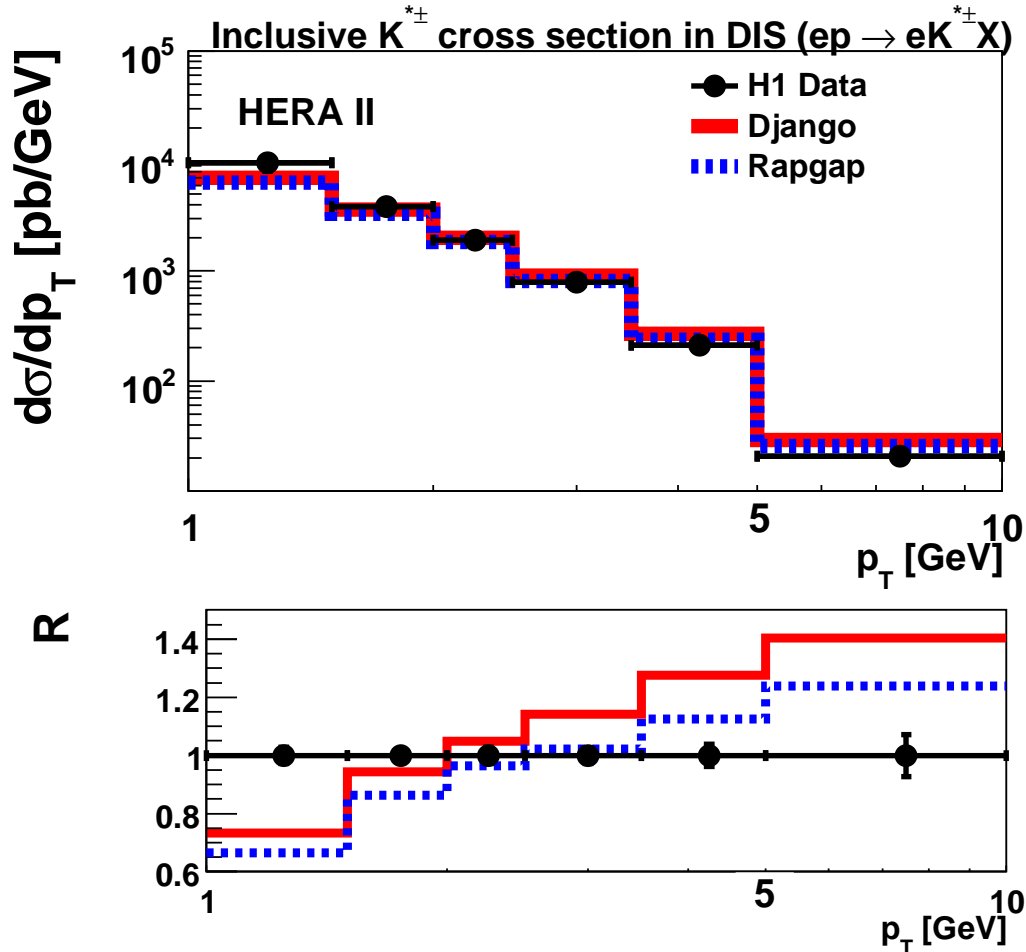


**Figure 9.1:** The measured inclusive differential cross section as a function of the transverse momentum  $p_T$ . The cross sections is measured in the visible range defined by  $p_{T(K^*)} > 1 \text{ GeV}$ ,  $|\eta_{(K^*)}| < 1.5$ ,  $5 < Q^2 < 100 \text{ GeV}^2$  and  $0.1 < y_{e\Sigma} < 0.6$ . The inner error in the figure represents the statistical error, while the outer is the statistical and the systematic errors added in quadrature. The measured cross section is compared to the DJANGO 1.4 (continuous red line) and RAPGAP 3.1 (dashed blue line) calculations. The corresponding ratios of the MC DJANGO and RAPGAP to the data,  $R$ , are shown at the bottom of the figure.

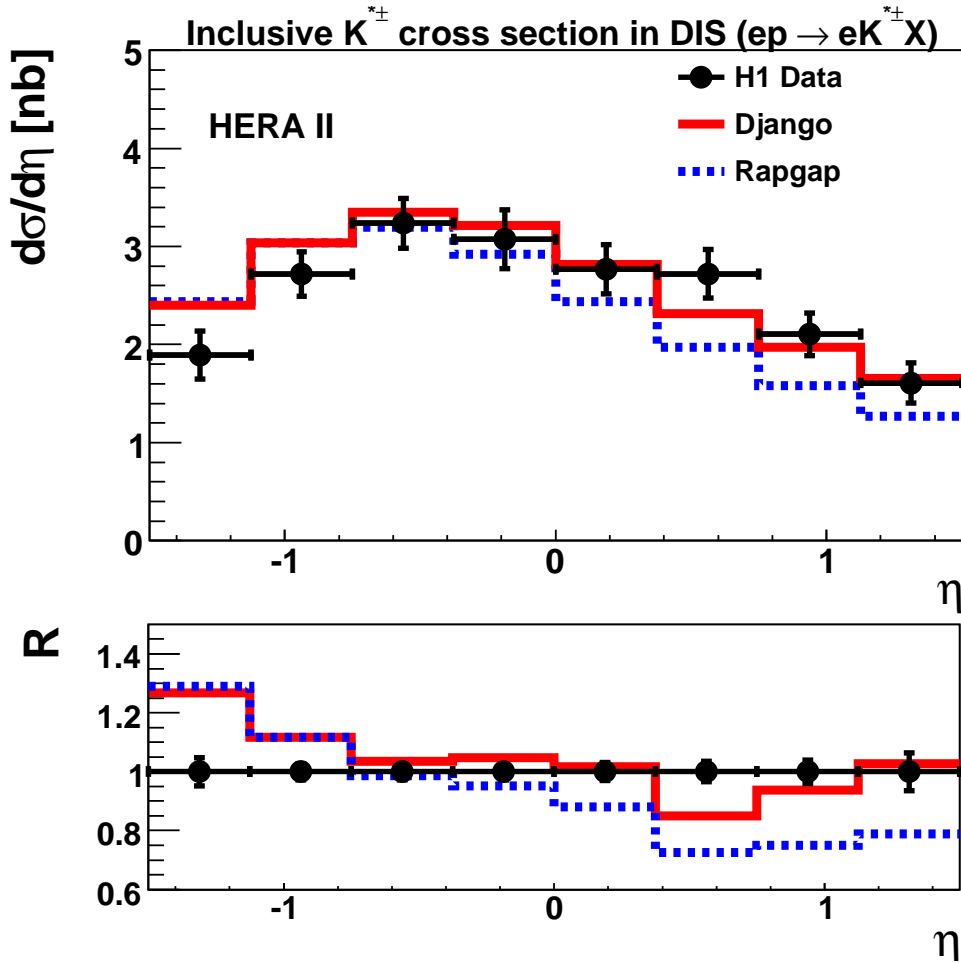


**Figure 9.2:** The measured inclusive differential cross section as a function of the pseudorapidity  $\eta$ . For details see the caption of Fig. 9.1.

that the RAPGAP (MEPS model) is not able to describe the  $\eta$  distribution. The similar observation has been seen by the recent measurement of the H1 experiment [101].

The differential cross section as a function of photon virtuality  $Q^2$  is displayed in Fig. 9.3. A good description of the shape is observed in overall distribution.

In this analysis the production of strange  $K^{*\pm}$  mesons is studied in the hadronic centre of mass system (CMS) which is the rest system of the beam proton and the exchanged boson. The hadronic CMS is defined by:

$$\vec{q} + \vec{P} = 0, \quad (9.3)$$

where  $\vec{q}$  is the momentum of the photon emitted by the electron and  $\vec{P}$  is the momentum of the incoming proton (see Fig. 9.4). Both particles collide in the hadronic CMS head on along the  $z$ -axis, giving rise (in the Quark Parton Model) to a scattered quark and a

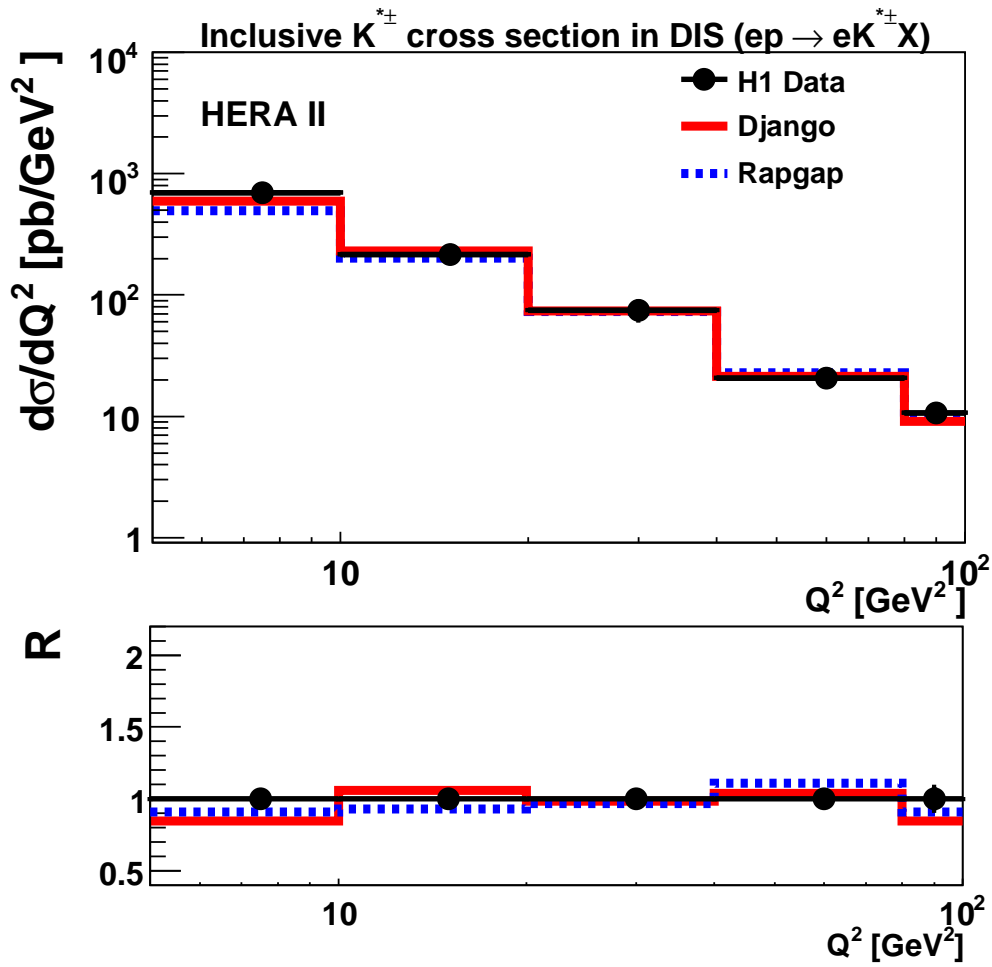


**Figure 9.3:** The measured inclusive differential cross section as a function of the four momentum squared  $Q^2$ . For details see the caption of Fig. 9.1.

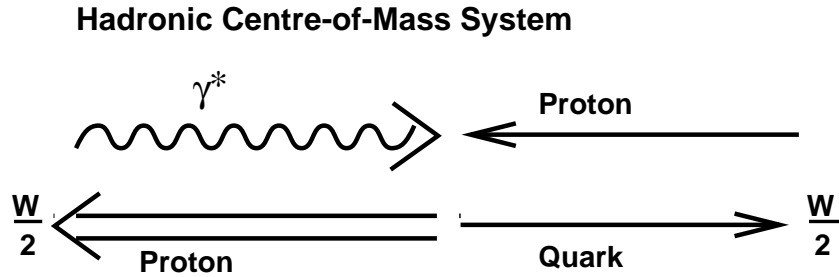


**Figure 9.4:** An illustration of the hadronic centre-of-mass system, i.e.  $\gamma^*p$  frame.

proton remnant flying apart in opposite directions. The positive  $z$ -axis is defined by the direction of the virtual photon  $\vec{q}$ . The incoming proton and photon each have energy  $W/2$ . Particles moving forward are said to belong to the current or photon hemisphere, while particles moving backwards are assigned to the target or proton remnant hemisphere. Each hemisphere has energy of  $W/2$ . In the centre-of-mass frame H1 data can be easily compared to other experiments and to theoretical models. In the current photon hemisphere the mechanism of particle production should in principle resemble that of collisions  $e^+e^-$  annihilation. The analogy with  $e^+e^-$  collisions can be performed by introducing a variable, the so called Feynman- $x$ ,

$$x_F = \frac{2 \cdot p_L}{W}, \quad (9.4)$$

where  $p_L$  is the momentum of  $K^{*\pm}$  along the photon direction and  $W$  is the centre of mass energy of the hadronic system. Fig. 9.5 shows the inclusive differential cross section as a function of Feynman- $x$ ,  $x_F$ . The DJANGO MC simulation which uses the CDM model provides a slightly better description of the shape than the RAPGAP MC in which the MEPS model is implemented.

In Fig. 9.6a, the inclusive differential cross section is depicted as a function of the centre-of-mass energy of the  $\gamma p$  system,  $W_{\gamma p}$ . The plot of ratio  $R$  is displayed at the bottom of figure and shows a good description of the shape by both LO MC models. The RAPGAP MC model gives a somewhat steeper slope than the data at values of  $W_{\gamma p} > 175$  GeV. The event kinematic quantity  $W_{\gamma p}$  is well described over the whole spectrum.

The cross section is also displayed as a function of the transverse momentum of the  $K^{*\pm}$  meson in the  $\gamma p$  system,  $P_T^{*2}$ , in Fig. 9.6b. The  $P_T^{*2}$  spectrum is not described by both LO MC models which show a tendency to overshoot the data starting from the low values of  $P_T^{*2}$ .

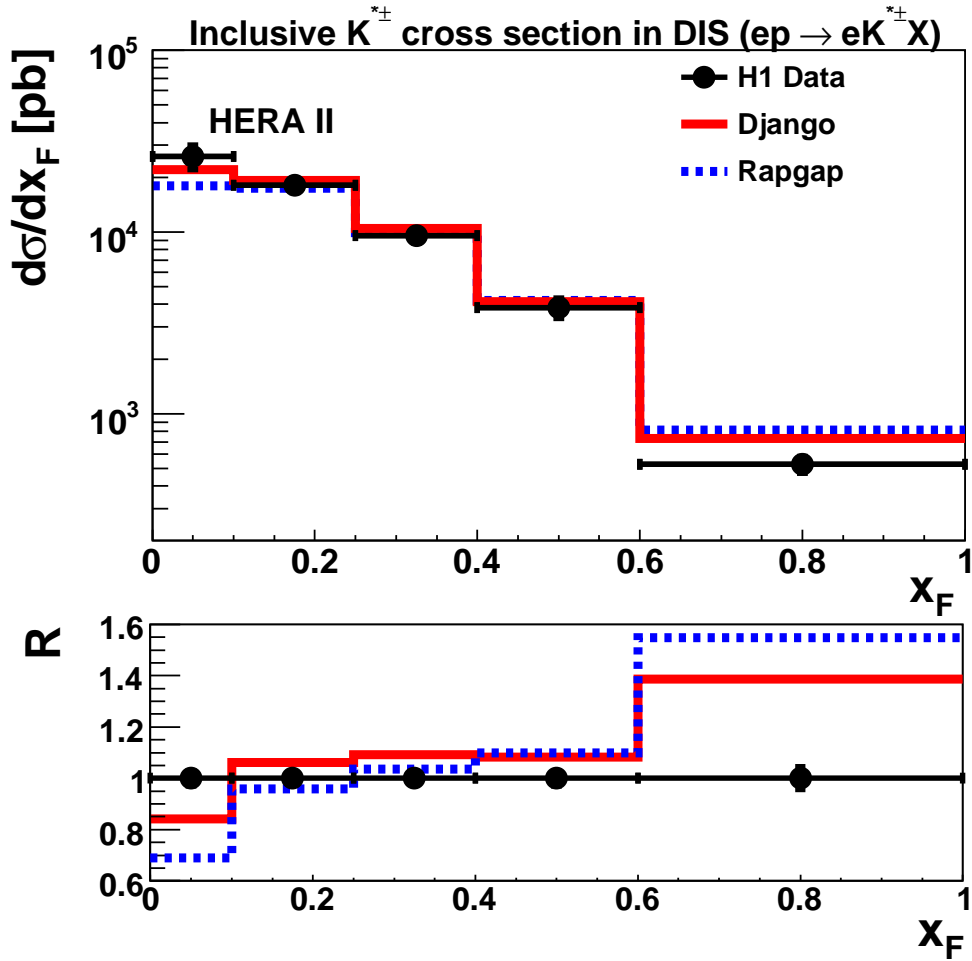


**Figure 9.5:** The measured inclusive differential cross section as a function of the Feynman- $x$ ,  $x_F$ . For details see the caption of Fig. 9.1.

### 9.3 Contribution of Different Production Mechanisms

As discussed earlier in section 3.3, strange particles can originate from various production mechanisms. In this section, contributions of such processes to the production of strange  $K^{*\pm}$  mesons are presented. In order to separate the different subprocesses, the flavour of the quark which participates in the hard interaction is labelled using the CDM Model implemented in the DJANGO MC generator. In Fig. 9.7, the relative fractions of the different quarks are shown as a function of the four momentum squared of the virtual photon  $Q^2$ , the pseudorapidity  $\eta$  and the transverse momentum of  $p_T$  and Feynman- $x$ ,  $x_F$ . The fraction of  $K^{*\pm}$  particles produced by a bottom quark is negligible in all distributions. The bottom quark is heavier than charm quark and its production threshold is effectively  $Q^2 = (2M_b)^2 \approx 100 \text{ GeV}^2$ . The bottom quark production is suppressed by a factor of  $(e_c/e_b)^2 = 4$  with respect to charm production at finite  $Q^2$ . The charm production is slightly enriched in the high  $Q^2$  region. At high  $p_T$  values the strange fraction is

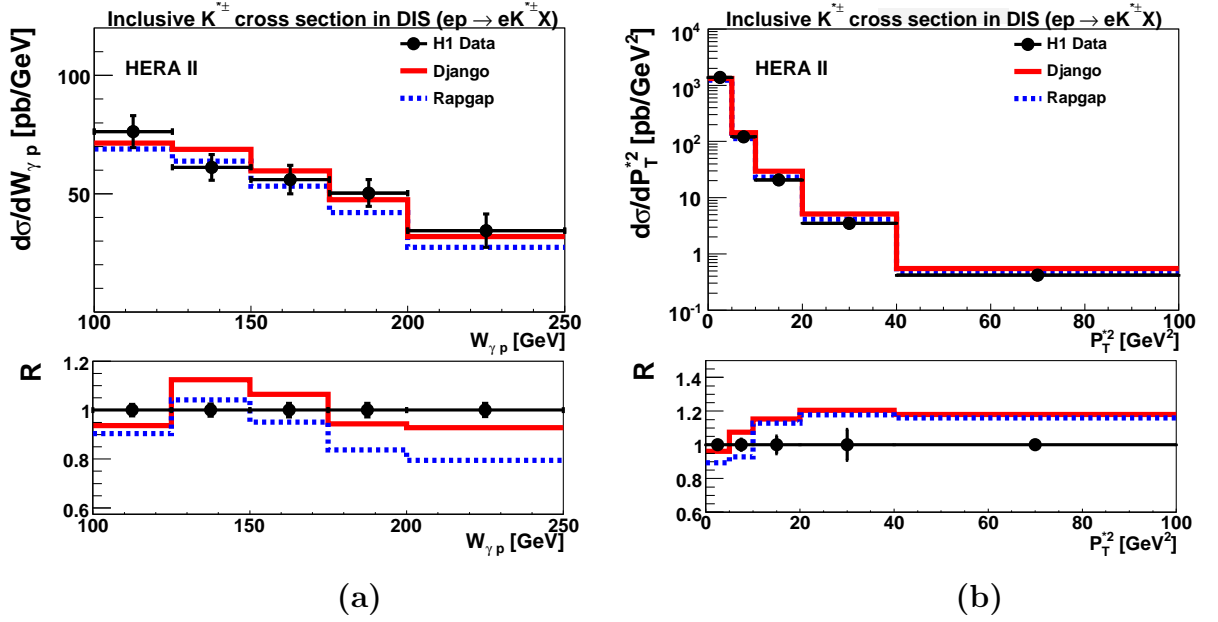


**Figure 9.6:** The measured inclusive differential cross sections as a function of: (a) the centre-of-mass energy of the hadronic final state  $W_{\gamma p}$ , and (b) the transverse momentum squared in the hadronic final state  $P_T^{*2}$ . For details see the caption of Fig. 9.1.

enhanced allowing to tag events where a strange quark participates in the hard interaction. Hence, the measurement of strange mesons with large  $p_T$  provides a possibility for the measurement of the structure function  $F_2^s$ . This is particularly interesting with respect to strange hadron physics at the large hadron collider (LHC). In the forward region the sensitivity to strange and charm quarks is reduced. In the high  $x_F$  region, the strange contribution becomes more prominent than charm.

The cross sections shown in Figs. 9.1 - 9.6 are shown again in Fig. 9.8 with the contribution of various quark flavors which are the primarily incoming particles of the hard subprocess from the proton side. In general  $u$  and  $d$  quarks give the largest contribution to the production of  $K^{*\pm}$ . The second largest contribution is from  $c$  and  $b$ . Only  $\approx 20\%$  of the contribution originates from  $s$  quarks. Dependence on  $x_F$  has been observed for the  $ud$  quark contribution. The  $x_F$  dependence of the  $ud$  quark contribution is less steep than the  $x_F$  dependence of the cross section. The contribution from  $c$  and  $b$  quarks are mainly from decays of heavy hadrons. At small  $x_F$  values, heavy quarks are exclusively produced via boson gluon fusion (BGF). The  $s$  quarks are also directly originating from the BGF. The fraction of  $s$  rises with  $x_F$ .

Since the measurement is dominated by fragmentation, it is a challenge to disentangle the strange content of the proton. However, in the bins of  $0.6 < x_F < 1$  and  $40 < P_T^{*2} < 100$  GeV<sup>2</sup> the contribution from  $s$  quarks to the  $K^{*\pm}$  cross section is enhanced. This region can be used for the double differential cross sections which will be discussed in the following section.

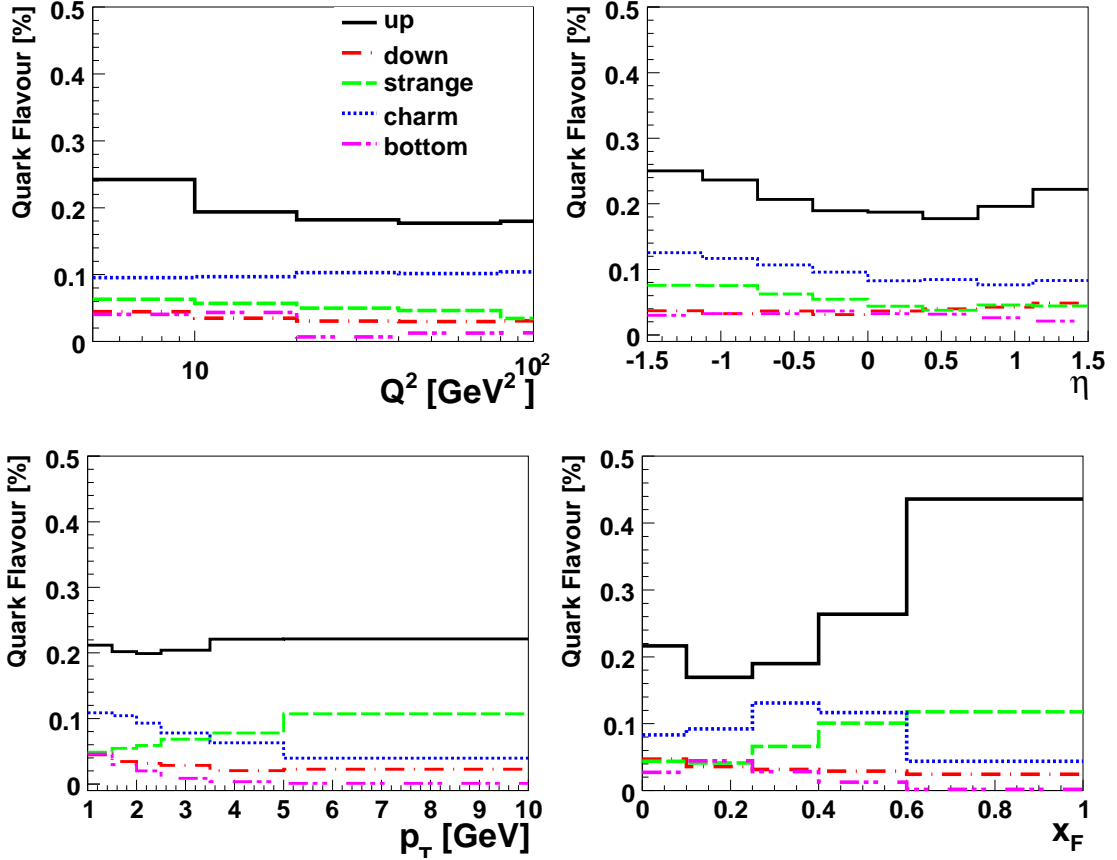


**Figure 9.7:** The relative fractions of the different quarks (up (full line), down (dash-dotted line), strange (dash line), charm (dotted line) and bottom (dash-double-dotted line)) are shown. contributing in the hard interaction to the production of  $K^{*\pm}$  in the visible range. The fractions are shown as a function of  $Q^2$ ,  $\eta$ ,  $p_T$  and  $x_F$ .

## 9.4 Double Differential Inclusive Cross Sections

In order to disentangle the quark contributions, the cross section measurements were performed double differentially as functions of  $P_T^{*2} - x_F$ ,  $Q^2 - x_F$ , and  $P_T^{*2} - Q^2$  with the following bin intervals:

$$\begin{aligned}
 x_F &: 0, 0.1, 0.25, 0.4, 0.6, 1 \text{ for } 0 < P_T^{*2} < 100 \text{ GeV}^2, \\
 x_F &: 0, 0.1, 0.25, 0.4, 0.6, 1 \text{ for } 5 < Q^2 < 100 \text{ GeV}^2, \\
 P_T^{*2} &: 0, 5, 10, 20, 40, 100 \text{ for } 5 < Q^2 < 100 \text{ GeV}^2.
 \end{aligned}$$

The double differential cross section,  $\frac{d\sigma}{dP_T^{*2}dx_F}$ , as a function of  $P_T^{*2}$  in bins of  $x_F$  is displayed in Fig. 9.9. The results are compared to the leading order DJANGO MC model. A strong rise of the  $s$  contribution and a strong decrease of the  $c$  and  $b$  contribution with increasing  $P_T^{*2}$  and  $x_F$  are observed. The contribution from  $u$  and  $d$  quarks has a minimum at medium values of  $x_F$  and small values of  $P_T^{*2}$ .

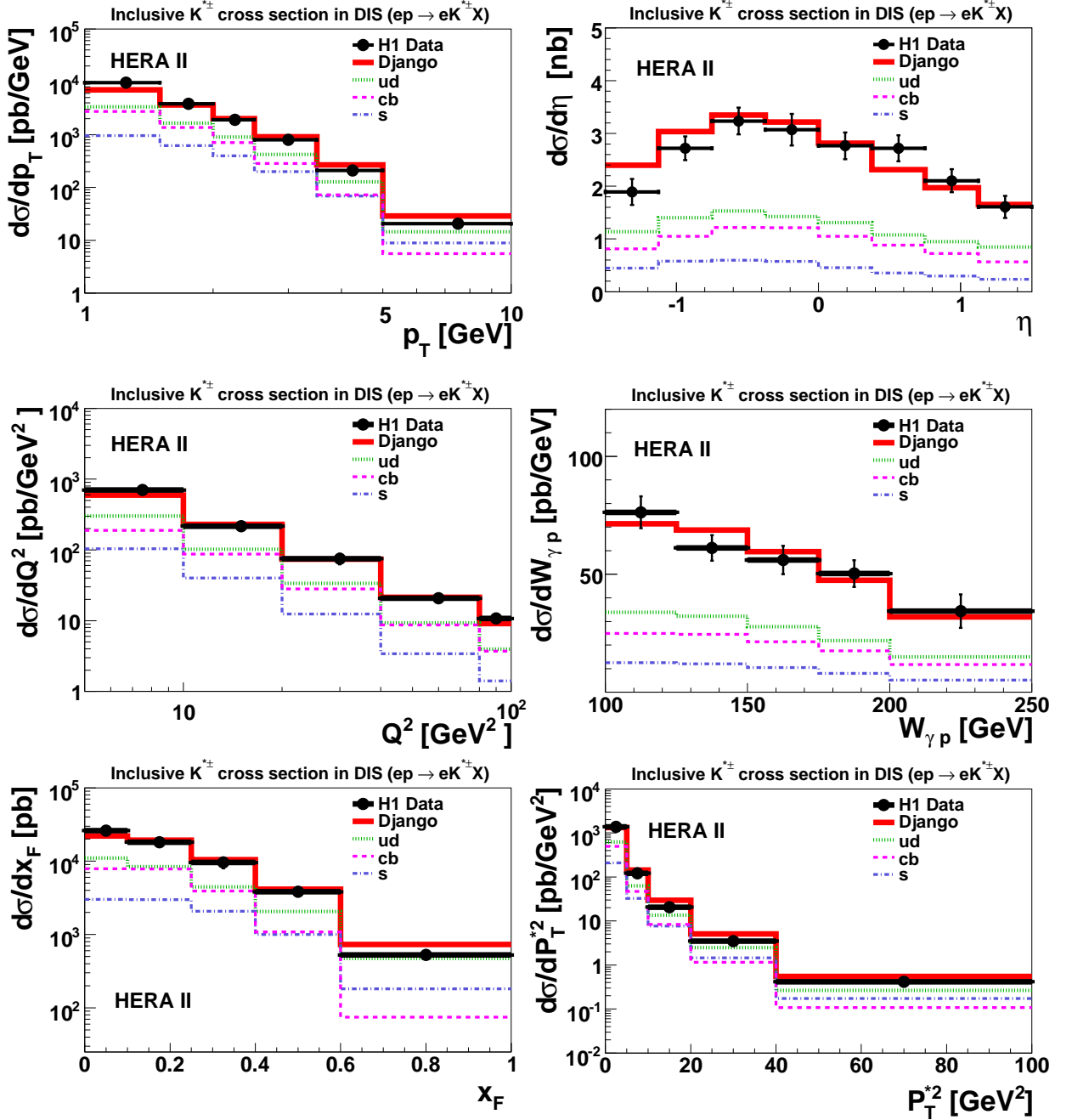


**Figure 9.8:** The measured inclusive differential cross sections as a function of the transverse momentum  $p_T$ ,  $\eta$ ,  $Q^2$ ,  $W_{\gamma p}$ ,  $x_F$  and  $P_T^{*2}$ . The cross sections are measured in visible range defined by  $p_{T(K^*)} > 1 \text{ GeV}$ ,  $|\eta_{(K^*)}| < 1.5$ ,  $5 < Q^2 < 100 \text{ GeV}^2$  and  $0.1 < y_{e\Sigma} < 0.6$ . The inner error in the figure represents the statistical error, while the outer is the statistical and the systematic errors added in quadrature. The quark contributions (ud (dotted lines), cb (dashed lines), and s (dash-dotted lines)) are shown.

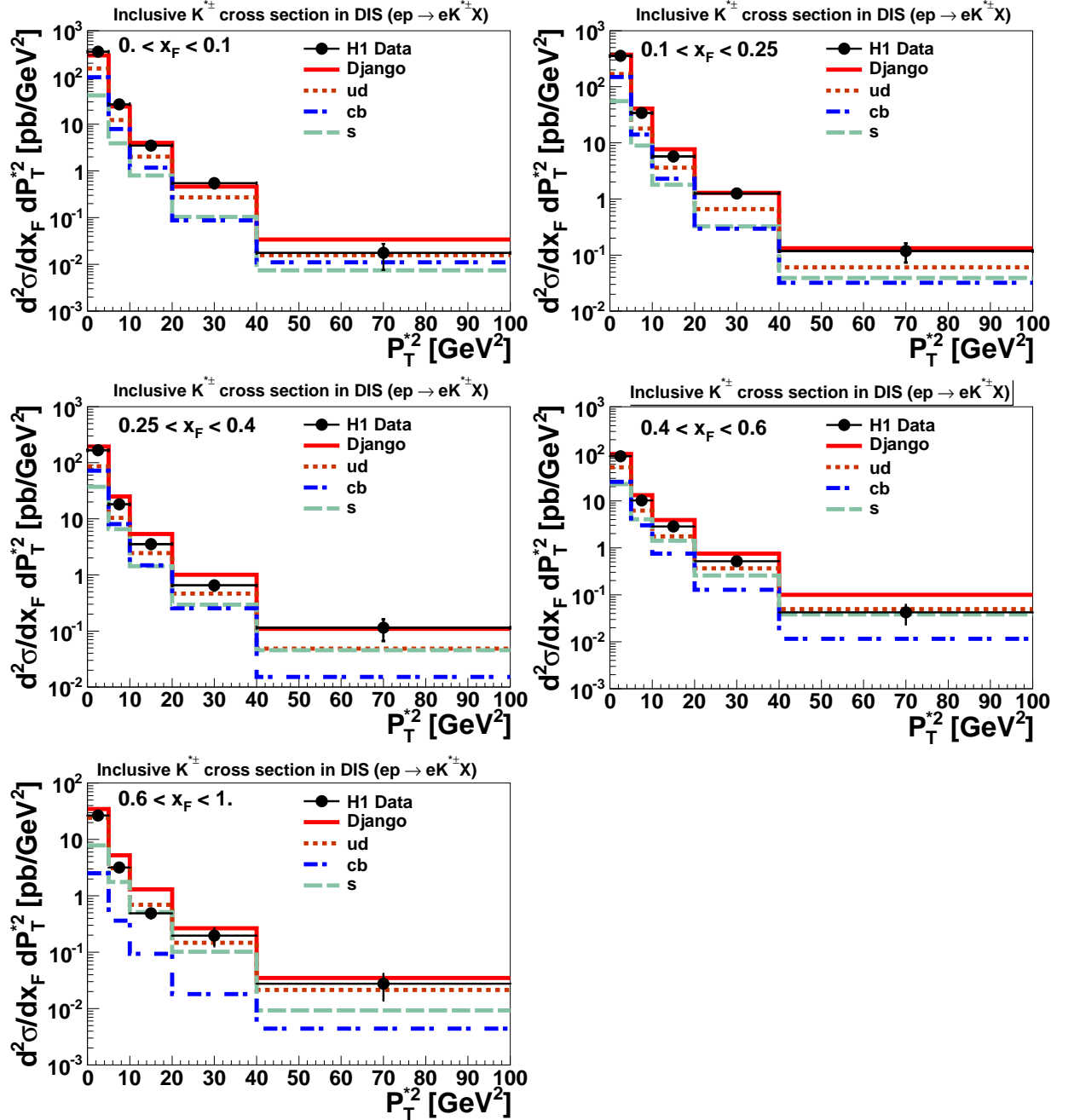


**Figure 9.9:** The double differential cross section of inclusive  $K^{\pm}$  mesons, presented as functions of  $P_T^{*2}$  in bins of  $x_F$ . The cross sections are measured in visible range defined by  $p_{T(K^*)} > 1$  GeV,  $|\eta_{(K^*)}| < 1.5$ ,  $5 < Q^2 < 100$  GeV<sup>2</sup> and  $0.1 < y_{e\Sigma} < 0.6$  and compared with the LO DJANGO MC predictions (solid line). The inner error in the figure represents the statistical error, while the outer is the statistical and the systematic errors added in quadrature. The quark contributions (ud (dotted lines), cb (dash-dotted lines), and s (dashed lines)) are shown.

In Fig. 9.10, the double differential cross section,  $\frac{d^2\sigma}{dQ^2 dx_F}$ , as a function of  $Q^2$  is presented in bins of  $x_F$ . The contribution of  $s$  quarks rises with  $Q^2$  in the highest  $x_F$  bin while the  $c$  and  $b$  contribution decreases with  $x_F$ . A similar behaviour is observed for the  $u$  and  $d$  quark contributions as for  $\frac{d^2\sigma}{dP_T^{*2} dx_F}$ . It has a minimum at medium  $x_F$  and  $Q^2$  values. The double differential cross section,  $\frac{d^2\sigma}{dP_T^{*2} dQ^2}$ , as a function of  $P_T^{*2}$  in bins of  $Q^2$  is shown in Fig. 9.11. The contribution of  $s$  quark is more prominent than the  $c$  and  $b$  contribution in all bins of  $Q^2$ .

If an  $u$  or a  $d$  quark participates in the hard interaction, the strange particle  $K^{*\pm}$  is produced by the hadronisation process. The influence of the hadronisation process is reduced in the hadronic centre-of-mass system and the fraction of  $c$  quark is enhanced. Strange particles from charm production can also originate with the fraction  $f$  from the following channels:

$$\begin{aligned} f(c \rightarrow D^0) &\approx 0.658, & f(D^0 \rightarrow K^{*\pm}\text{anything}) &= 0.185 \pm 0.09, \\ f(c \rightarrow D^\pm) &\approx 0.202, & f(D^\pm \rightarrow K^{*\pm}\text{anything}) &= 0.06 \pm 0.050, \\ f(c \rightarrow D_s) &\approx 0.10, & f(D_s \rightarrow K^{*\pm}\text{anything}) &= 0.123 \pm 0.034. \end{aligned}$$

The fraction  $f$  from charm quarks to  $D$  mesons is taken from the measurement of the H1 experiment [157] and from  $D$  mesons to  $K^{*\pm}$  is taken from [4]. The given contributions due to the  $c$  quark production possess a problem due to the large uncertainties ( $f(c \rightarrow K^{*\pm}\text{anything}) \approx 15 \pm 3.5\%$ ) in fractions to  $K^{*\pm}$ .

The results of the measured double differential cross sections are tabulated in appendix B.

## 9.5 $K^{*+}$ and $K^{*-}$ Production Asymmetry

As already mentioned in section 3.2, the proton consists of three valence quarks,  $uud$ , which are connected to each other via gluons. However, the quarks can radiate extra gluons which can split into two other gluons or quark-antiquark ( $q\bar{q}$ ) pairs. The result is a constant flux of gluon annihilation and creation usually known as “the sea”. Sea quarks are much less stable (i.e. exist only for a short time,  $\Delta\tau \approx \frac{\hbar}{m_q}$ , where  $m_q$  is the quark mass) than their valence counterparts. Despite this, sea quarks can hadronise into baryonic or mesonic particles.

It is very interesting to compare the cross sections for  $K^{*+}$  and  $K^{*-}$  production, as the difference between them can point to the charge asymmetry in the quark sea. The differential cross sections for  $K^{*+}$  and  $K^{*-}$  production as a function of the transverse momentum  $p_T$ , the pseudorapidity  $\eta$  and of the event variable  $Q^2$  are shown in Fig. 9.12. It can be clearly seen that there are no significant differences to the MC models with no intrinsic asymmetry included. The  $\eta$  discrepancy (see Fig. 9.2) can not be easily fixed by the inclusion of the effect. The total visible cross sections of  $K^{*-}$  and  $K^{*+}$  are measured as :

$$\sigma_{vis}(ep \rightarrow e'K^{*-}X) = 3.39 \pm 0.02 \text{ (stat.)} \pm 0.44 \text{ (sys.) nb,}$$

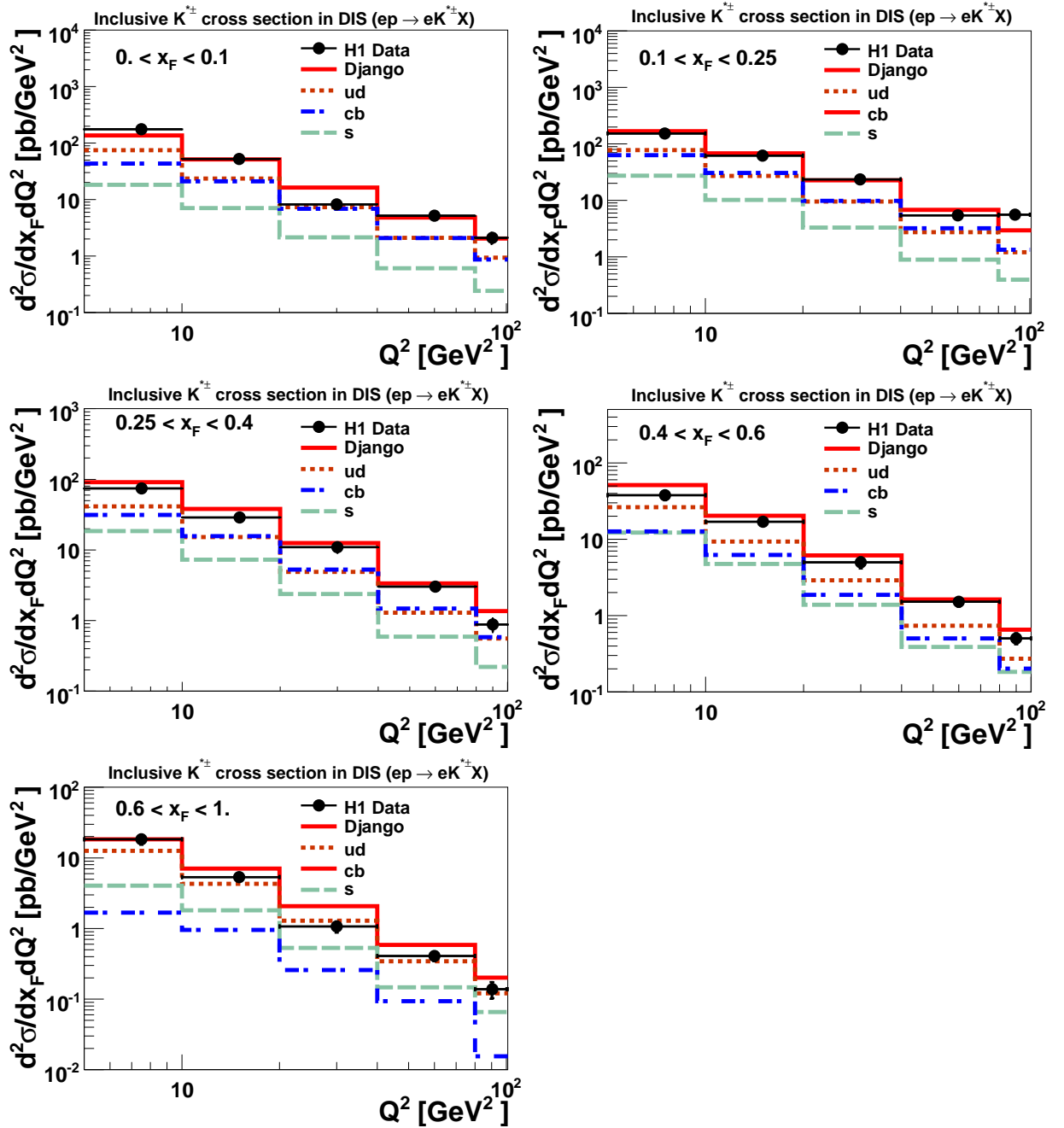


Figure 9.10: The double differential cross section of inclusive  $K^{*\pm}$  mesons, presented as functions of  $Q^2$  in bins of  $x_F$ . For details see the caption of Fig. 9.9.

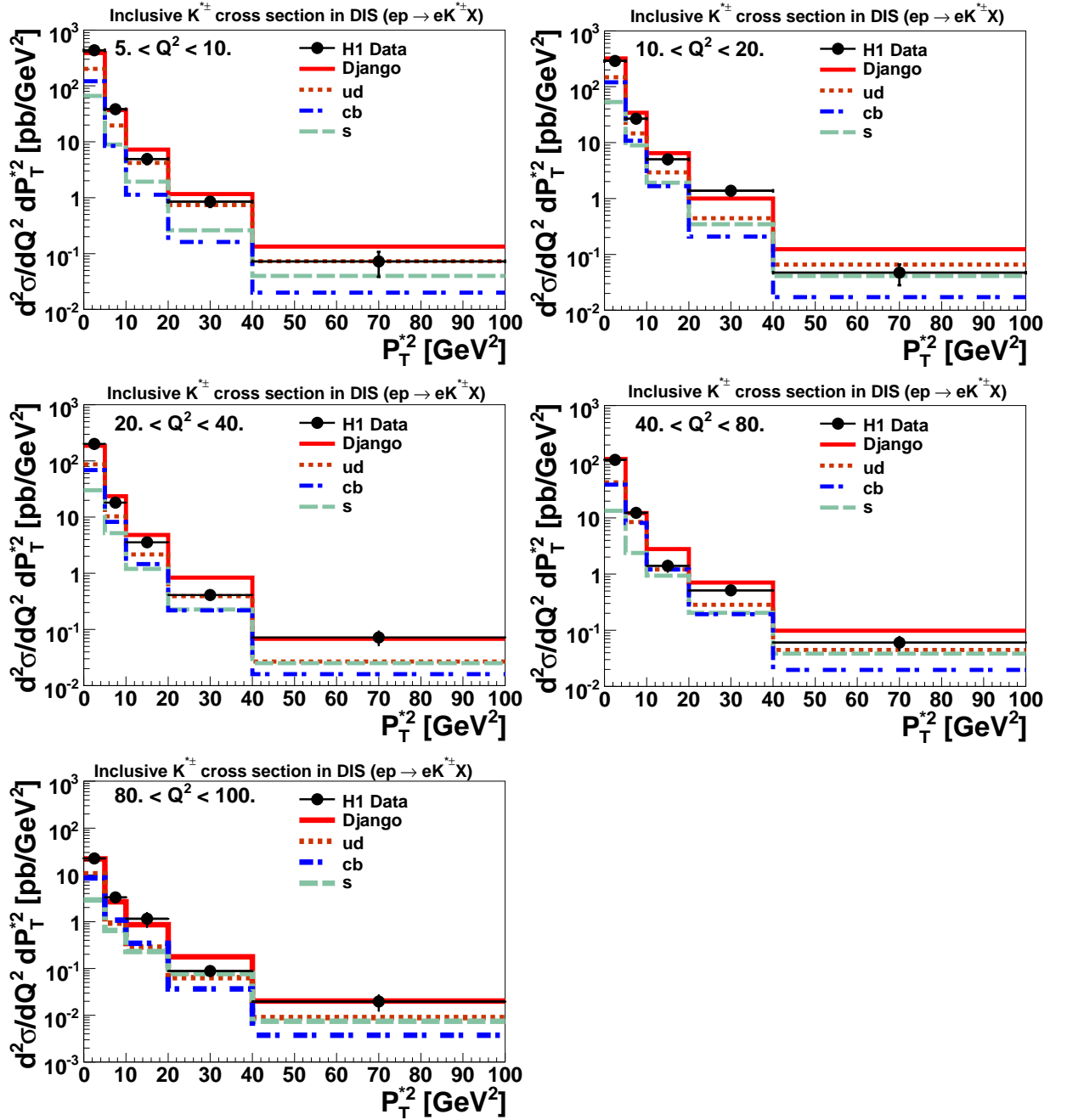
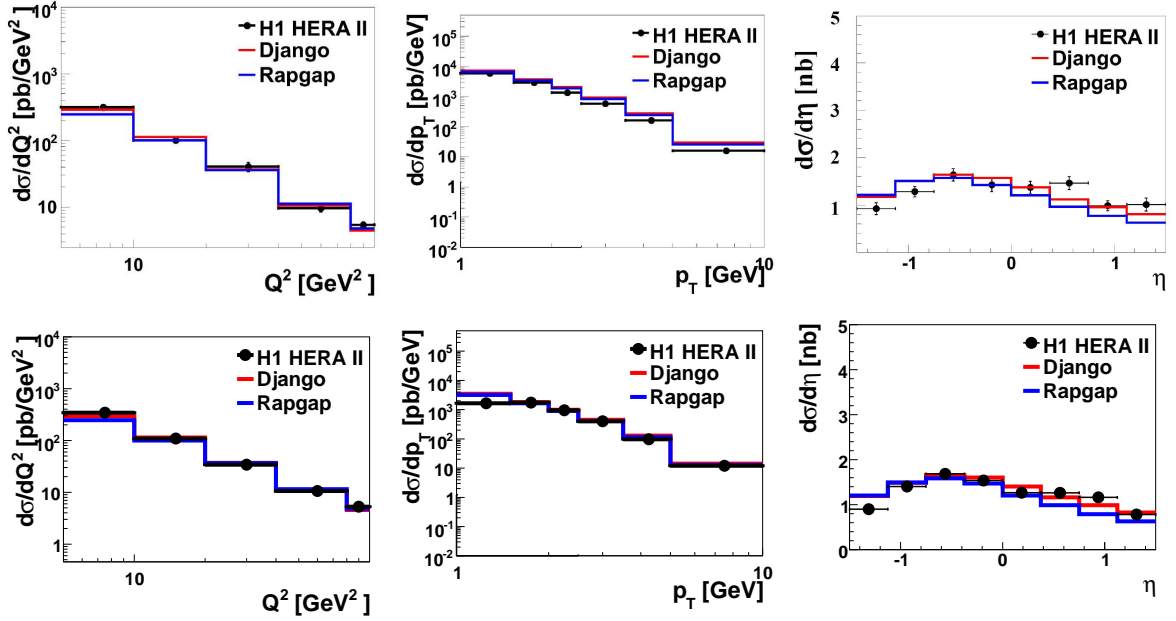


Figure 9.11: The double differential cross section of inclusive  $K^{*\pm}$  mesons, presented as functions of  $P_T^{*2}$  in bins of  $Q^2$ . For details see the caption of Fig. 9.9.



**Figure 9.12:** The differential cross section of inclusive  $K^{*+}$  mesons (upper plots) and  $K^{*-}$  mesons (lower plots) are presented as functions of  $Q^2$ ,  $p_T$  and  $\eta$ .

$$\sigma_{vis}(ep \rightarrow e'K^{*+}X) = 3.22 \pm 0.02 \text{ (stat.)} \pm 0.41 \text{ (sys.) nb.}$$

The asymmetry in the production of  $K^{*+}$  with respect to  $K^{*-}$  is measured by the variable,  $A_{K^*}$  :

$$A(K^*) = \frac{\sigma^{vis}(ep \rightarrow e'K^{*-}X) - \sigma^{vis}(ep \rightarrow e'K^{*+}X)}{\sigma^{vis}(ep \rightarrow e'K^{*-}X) + \sigma^{vis}(ep \rightarrow e'K^{*+}X)}.$$

In this analysis asymmetry is measured as  $A(K^*) = 0.0025 \pm 0.0043 \text{ (stat.)} \pm 0.090 \text{ (syst.)}$  and is found to be compatible with zero within the errors. Hence, it can be concluded that the present analysis finds no significant asymmetry between strange ( $K^{*-}$ ) and anti-strange ( $K^{*+}$ ) sea quark distributions.

## Summary

In this chapter the inclusive cross sections  $K^{*\pm}$  were presented as a function of various kinematic variables in the laboratory and photon proton rest frames. The measurements were compared with the leading order MC models, DJANGO and RAPGAP. However, the predictions found to not provide a satisfactory description of the measurements.

The results present an important test of our understanding of strange quark production. The main focus was put on the contribution to the production of  $K^{*\pm}$  of those quarks which primarily originate from the proton.

The measured  $K^{*\pm}$  cross sections can be utilised to derive the contribution of strangeness to the proton structure function,  $F_2^s(x, Q^2)$ .

The production of  $K^{*\pm}$  is not well described by the MC models. These, however, contain various parameters which control both the suppression of strange quarks relative to up and down quarks and the production of baryons relative to mesons and could be further tuned to the data.

The strange ( $s$ ) - antistrange ( $\bar{s}$ ) asymmetry  $A$  has been measured and no significant asymmetry was observed. This suggests that in the considered parts of the  $ep$  phase space, strange and antistrange particles are produced according to the same mechanism. This observation is consistent with previous measurements [104].

# Chapter 10

## Summary and Conclusion

The Standard Model (SM) is the experimentally well-tested theory of particle physics based on fundamental particles and their interactions. Within this model, fundamental particles can be classified according to three basic types: quarks, leptons and the gauge bosons. The description of electron-proton deep inelastic scattering (DIS) is formulated within the SM in terms of an exchanged boson resolving the proton and interacting with a quark ( $q$ ) or antiquark ( $\bar{q}$ ). The struck quark scatters, and together with the proton remnant, fragments, initiating a parton shower of gluon radiation and  $q\bar{q}$  pair production, which, through hadronisation, leads to observable final state particles.

Experiments carried out at the HERA ring, the world's first electron-proton collider located in Hamburg, have greatly improved our understanding of the quark and gluon structure of the proton. The H1 experiment is one of two all-purpose detectors observing electron-proton collisions and was used to collect the data for the present analysis.

In this analysis, the first measurement of strange  $K^{*\pm}$  meson production in DIS has been performed, using the data collected with the H1 detector at the HERA collider during the 2005-2007 running periods, corresponding to an integrated luminosity of  $302 \text{ pb}^{-1}$ . Approximately  $14.1 \times 10^6$  events are obtained after all the event selections.

The production of strange particles in high energy particle collisions provide an opportunity to study the strong interactions in the perturbative and non-perturbative regimes. In DIS, strange particles can be produced either in the hard sub-process or in the hadronisation of the colour field. Within the hard-subprocesses, strange quark  $s$  can be created either via boson gluon fusion (BGF) or originate directly from the sea quark  $s$  inside the proton. The production of  $s$  quarks in a BGF process, where a gluon emitted from the nucleon splits into a heavy quark antiquark pair (charm, bottom) with subsequent weak decay into  $s$  ( $\bar{s}$ ) quarks, is suppressed at low  $Q^2$  due to the large masses of the heavy quarks. The production mechanisms of strange quark are characterised by a hard scale allowing for a perturbative treatment. The relative rate of the BGF process to the direct production depends strongly on the Bjorken scaling variable  $x$  due to the strong rise of the gluon density at low  $x$ . In the kinematic region studied in this analysis (low  $Q^2$ ) the BGF contributions are expected to be significant. According to the Monte Carlo predictions from DJANGO and RAPGAP, about 20% of the strange hadrons originate from

strange quarks produced in the hard interaction either directly or through heavy quark production in BGF processes.

The measurements were done in the kinematic region defined by  $5 < Q^2 < 100 \text{ GeV}^2$  and  $0.1 < y < 0.6$ . The visible range of the  $K^{*\pm}$  meson is restricted in transverse momentum and pseudorapidity to  $p_T(K^{*\pm}) > 1 \text{ GeV}$  and  $-1.5 < \eta(K^{*\pm}) < 1.5$ . The events with  $K^{*\pm}$  mesons have been reconstructed via the decay

$$K^{*\pm} \rightarrow K_S^0 \pi^\pm,$$

with the  $K_S^0$  subsequently decaying into  $\pi^+ \pi^-$ . The signal yield is obtained by fits to the  $K_S^0 \pi^\pm$  invariant mass distribution. The  $K^{*\pm}$  signal is located on top of a large combinatorial background due to a large charged particles multiplicity. Therefore, a detailed study of the parametrisation of the signal and the background has been performed.

The reconstruction of event kinematics was carried out by using the  $e\Sigma$ -method. In  $e\Sigma$ -method the kinematic variables are determined by using both the electron and the hadronic final state variables. This method provides low systematic errors in the kinematic region probed by the measurement. The total  $K^{*\pm}$  production cross section in the visible region is measured as

$$\sigma_{total}^{vis}(ep \rightarrow eK^{*\pm}X) = 7.36 \pm 0.087 \text{ (stat.)} \pm 0.88 \text{ (sys.) nb.}$$

Differential cross sections are measured as a function of the photon virtuality  $Q^2$ , the transverse momentum of  $K^{*\pm}$ ,  $p_T$ , the pseudorapidity of  $K^{*\pm}$ ,  $\eta$ , the centre-of-mass energy of the hadronic final state,  $W_{\gamma p}$ , the Feynman variable  $x_F$  and the squared transverse momentum of the  $K^{*\pm}$  meson in the photon proton rest frame,  $P_T^{*2}$ . Since the majority of the  $K^{*\pm}$  mesons are produced during the fragmentation process, the results of the measurement have been compared to the predictions of leading order Monte Carlo generators, DJANGO and RAPGAP. In general, both the colour dipole model (CDM, implemented in DJANGO) and matrix element+parton shower (MEPS, implemented in RAPGAP) provide a reasonable description of the data. However, the CDM model is found to describe the data slightly better than the MEPS model.

Comparisons of leading order Monte Carlo predictions with the measurements demonstrate that a single strangeness suppression factor  $\lambda_s$  fails to adequately describe the data as significant disagreements are observed in various distributions. This conclusion is consistent with that found in  $K_S^0$  production measurements [101]. This is partly due to the fact that in various regions of phase space, the relative contributions of direct production of strange to other quarks differ; in particular at larger scales (e.g.  $Q^2$ ,  $p_T$ ) the charm contributions become substantial and need to be properly included into the description.

The measurement of the  $K^{*\pm}$  cross sections provide further insight in the fragmentation process and helps to disentangle the uncertainties related to the measurement of strangeness suppression. Different production mechanisms which contribute to the production of strange  $K^{*\pm}$  mesons were investigated. In order to separate the different subprocesses, the flavour of the quark which participates in the hard interaction was studied

using the CDM model. A small dependence on  $x_F$  has been observed for the  $u$ ,  $d$  quark contribution while the contribution from  $c$  and  $b$  quarks originates from decays of heavy hadrons. The production of heavy quarks via BGF was seen at small  $x_F$  values. The  $s$  and  $\bar{s}$  quarks can be directly produced from the hard subprocess. The fraction of  $s$  rises with  $x_F$ .

In general, both models CDM and MEPS provide an overall satisfactory description of the data although small differences between data and the model predictions have been observed, particularly for  $\eta(K^{*\pm})$  distribution. The CDM model tends to describe the data slightly better than the MEPS model. The contribution of different processes to the strange production was studied with DJANGO where the CDM model is implemented in. An important result has been found that only 20% of  $K^{*\pm}$  mesons can be traced back to strangeness inside the proton. No difference has been observed between  $K^{*+}$  and  $K^{*-}$  cross sections which, if observed, might indicate an asymmetry between  $s$  and  $\bar{s}$  distributions of the sea quarks in the proton.

## 10.1 Outlook

The measurement of the  $K^{*\pm}$  production presented in this dissertation is an attempt to a better understanding of strange quark production. The combination of the HERA I data and including the run period of 2004 at HERA II is not likely lead to a significant increase of the statistical precision of the measurement. However, there is still potential to reduce the systematic uncertainties.

The reconstruction efficiency of the  $K^{*\pm}$  daughter particles need to be investigated extensively in order to reduce the corresponding systematic uncertainty. Another important point is the Monte Carlo model description of kinematic quantities. In order to gain a better description, other Monte Carlo models, for instance the CASCADE model [158], could be further investigated.

Due to the large statistics of the data sample, it was shown that the double differential cross section measurement is possible. It has to be investigated whether the precision is sufficient to allow measurement of the strange quark structure function  $F_2^s$ , which depends on the double differential cross sections as a function of the scaling variable  $Q^2$  and Bjorken- $x$ . Further insight in the production of strange quark mechanisms may be gained by a comparison with next to leading order QCD predictions.

An investigation of the relative production rates of vector (in this case  $K^{*\pm}$ ) and pseudoscalar (for instance  $K_S^0$ ), i.e. ratio of vector meson to pseudoscalar meson ( $V/(V+P)$ ), mesons can also be performed. This study provides information about the relative probabilities for the corresponding spin states to be produced in the hadronisation.

Data on short-lived resonance particles, e.g.  $K^*$ , are useful probes of the collision dynamics and help to understand the characteristics of the hot and dense matter which is produced in heavy ion collisions. In this respect a study of resonance production will be important for the  $pp$  and  $AA$  collisions studied at the Large Hadron Collider (LHC) which will soon begin operations at CERN.

# Chapter 11

## Samenvatting en Besluit

Het Standaard Model (SM) is een goede experimenteel geteste theorie in de elementaire deeltjesfysica die de fundamentele deeltjes en hun interacties kan beschrijven. In dit model kunnen deze fundamentele deeltjes opgedeeld worden in 3 verschillende basis types: quarks, leptonen en ijkbosonen. De beschrijving van diepe inelastische elektron-proton verstrooiingen (DIS) is binnen het SM geformuleerd in termen van een uitgewisseld boson dat in het proton met een quark ( $q$ ) of anti-quark ( $\bar{q}$ ) interageert. De verstrooide quark gaat dan samen met de andere overgebleven delen van het opgebroken proton een parton shower van gluon straling en  $q\bar{q}$  paar productie initialiseren wat na hadronisatie leidt tot observeerbare deeltjes in de eindtoestand.

Experimenten uitgevoerd met de HERA versneller, 's werelds eerste elektron-proton versneller in Hamburg, hebben onze kennis van de quark en gluon structuur van het proton sterk vergroot. Het H1 experiment verbonden aan deze versneller is één van de twee algemene detectoren die de elektron-proton botsingen waarnemen en werd gebruikt voor het nemen van de data voor deze analyse.

In deze analyse werd een eerste meting van een vreemde  $K^{*\pm}$  meson productie in DIS uitgevoerd gebruikmakend van de verkregen data met de H1 detector bij de HERA versneller gedurende meetperiodes van 2005 tot 2007 wat overeenkomt met een totale geïntegreerde luminositeit van  $302 \text{ pb}^{-1}$ . Ongeveer  $14.1 \times 10^6$  gebeurtenissen bleven over na alle toegepaste selecties.

Dankzij de productie van vreemde deeltjes in hoog energetische interacties heeft men de mogelijkheid om de sterke interacties te bestuderen in de perturbatieve en niet-perturbatieve regimes. Zo kunnen in DIS de vreemde deeltjes geproduceerd worden in een hard subprocess of tijdens de hadronisatie van het kleurveld. Binnen de harde subprocessen kunnen ze dan geproduceerd worden via boson-gluon fusie (BGF) of direct vanuit de zee quarks in het proton komen. De productie van  $s$  quarks tijdens een BGF proces, waarbij een uitgezonden gluon van het nucleon in een quark antiquark paar (charm, bottom) splitst en vervolgens via een zwak verval naar  $s$  ( $\bar{s}$ ) quarks gaat, is onderdrukt bij lage  $Q^2$  door de grote massa van de zware quarks. De mechanismen voor de productie van vreemde quarks is verder ook gekarakteriseerd door een 'harde schaal' parameter die een perturbatieve behandeling toelaat. De relatieve verhouding tussen de BGF processen en de

directe producties hangt sterk af van de Bjorken schalings variabele  $x$  omdat de gluon dichtheden sterk stijgen naar lage  $x$  toe. In het bestudeerde kinematisch gebied (lage  $Q^2$ ) verwacht men dat de BGF bijdrage significant is. Volgens de Monte Carlo voorspellingen van DJANGO en RAPGAP zal ongeveer 20% van de vreemde hadronen afkomstig zijn van vreemde quarks geproduceerd in de harde interactie, zowel via directe processen of via zware quark productie in BGF processen.

De metingen werden uitgevoerd in een kinematisch gebied waarbij  $5 < Q^2 < 100 \text{ GeV}^2$  en  $0.1 < y < 0.6$ . Het zichtbare  $K^{*\pm}$  gebied is beperkt tot een transversale impuls van  $p_T(K^{*\pm}) > 1 \text{ GeV}$  en een pseudorapidity van  $-1.5 < \eta(K^{*\pm}) < 1.5$ . De gebeurtenissen met de  $K^{*\pm}$  mesonen zijn gereconstrueerd via het  $K^{*\pm} \rightarrow K_S^0 \pi^\pm$  verval waarbij het  $K_S^0$  vervolgens vervalt naar een  $\pi^+$  en  $\pi^-$ . Het signaal is verkregen door de  $K_S^0 \pi^\pm$  invariante massa distributie te fitten en bevindt zich bovenop een grote combinatorische achtergrond toe te schrijven aan een grote geladen deeltjesmultipliciteit. Daarom werd een gedetailleerde studie van de parametrisatie van het signaal en de achtergrond uitgevoerd.

De reconstructie van de botsingskinematica werd uitgevoerd met een  $e\Sigma$ -methode waarbij de kinematische variabelen bepaald werden uit de elektron en hadronische eindtoestanden. Deze methode zorgt voor lage systematische fouten in het gemeten kinematisch gebied. De bekomen totale werkzame doorsnede van de  $K^{*\pm}$  productie in het zichtbare gebied is:

$$\sigma_{total}^{vis}(ep \rightarrow eK^{*\pm}X) = 7.36 \pm 0.087 \text{ (stat.)} \pm 0.88 \text{ (sys.) nb.}$$

De differentiële werkzame doorsnedes zijn bepaald in functie van de foton virtualiteit  $Q^2$ , de transversale impuls  $p_T$  van  $K^{*\pm}$ , de pseudorapidity  $\eta$  van  $K^{*\pm}$ , de massamiddelpunts energie  $W_{\gamma p}$  van de hadronische eindtoestand, de Feynman variabele  $x_F$  en de kwadratische transversale impuls  $P_T^{*2}$  van het  $K^{*\pm}$  meson in het foton-proton ruststelsel. Aangezien de meerderheid van de  $K^{*\pm}$  mesonen geproduceerd wordt tijdens het fragmentatie proces zijn de resultaten van de metingen vergeleken met leading order Monte Carlo generators DJANGO en RAPGAP. Algemeen gezien geven het Colour Dipole Model (CDM, geïmplementeerd in DJANGO) en het matrix element + parton shower model (MEPS, geïmplementeerd in RAPGAP) beide een redelijke beschrijving van de data hoewel het CDM model de data toch net iets beter lijkt te beschrijven.

De goede statistiek van de data liet ook metingen van de dubbele differentiële werkzame doorsnedes toe in functie van  $P_T^{*2}$  in bins van  $x_F$ , van  $Q^2$  in bins van  $x_F$  en van  $P_T^{*2}$  in bins van  $Q^2$ . De DJANGO Monte Carlo generator beschrijft de vorm van de distributies goed voor alle gemeten resultaten. Het moet echter nog onderzocht worden of de precisie van de resultaten goed genoeg is om bij te dragen tot de meting van de vreemde quark structuurfunctie  $F_2^s$  die van de dubbele differentiële werkzame doorsnede afhangt als functie van  $Q^2$  en Bjorken- $x$ .

Het vergelijken van de resultaten met voorspellingen van leading order Monte Carlo modellen met parton showers toont consistentie aan met de conclusies van de  $K_S^0$  productie metingen. Samengevat blijkt dat één enkele vreemdheids onderdrukkingsfactor  $\lambda_s$  echter niet voldoende is voor een consistente gedetailleerde beschrijving van alle distributies. Dit is gedeeltelijk vanwege het feit dat in verschillende faseruimte gebieden de relatieve

bijdragen van de directe  $s$  productie tot de andere quarks verschilt, in het bijzonder bij hoge  $Q^2$  en  $p_T$  waarden zal de charm ( $c$ ) bijdrage aanzienlijk worden en moet deze dan ook correct aan de beschrijving toegevoegd worden.

De meting van de  $K^{*\pm}$  werkzame doorsnede geeft verder ook inzicht in het fragmentatieproces en helpt om de onzekerheden gerelateerd aan de vreemdheids onderdrukking te ontwarren. De verschillende mechanismen die bijdragen tot de  $K^{*\pm}$  productie werden onderzocht en om de verschillende subprocessen te scheiden werd de flavour van de quark die deelnam aan de harde interactie onderzocht met het CDM model. Een kleine afhankelijkheid van  $x_F$  werd waargenomen voor de  $u$  en  $d$  bijdragen terwijl de contributies van de  $c$  en  $b$  quarks afkomstig zijn van het verval van zware hadronen. De productie van zware quarks via BGF processen kwam voor bij kleine  $x_F$  waarden. De  $s$  en  $\bar{s}$  quarks kunnen direct geproduceerd worden vanuit een hard subprocess en de fractie van  $s$  quarks stijgt met  $x_F$ .

Algemeen gezien geven de CDM en MEPS modellen beide een goede beschrijving van de data alhoewel er (kleine) verschillen tussen de gegevens en de modellen waargenomen zijn, in het bijzonder voor de  $\eta(K^{*\pm})$  distributie. Verder lijkt het CDM model de gegevens lichtjes beter te beschrijven dan het MEPS model. De bijdrage van de verschillende processen tot de  $s$  productie is bestudeerd met DJANGO waarin het CDM model geïmplementeerd is en een belangrijk gevonden resultaat is dat slechts 20% van de  $K^{*\pm}$  mesonen gelinkt kan worden aan de vreemdheid binnenin het proton. Er werd geen verschil waargenomen tussen de  $K^{*+}$  en  $K^{*-}$  werkzame doorsnedes en indien wel zou dit kunnen wijzen op een asymmetrie tussen de  $s$  en  $\bar{s}$  distributies van de zee quarks in het proton.

## 11.1 Vooruitzichten

De meting van de  $K^{*\pm}$  productie uitgevoerd in deze thesis is een poging om de strange quark productie beter te begrijpen. De combinatie van de HERA I en HERA II (metingen uitgevoerd in 2004) data zou niet kunnen leiden tot een sterke verbetering van de statistische precisie maar heeft wel het potentieel om de systematische onzekerheden te

De huidige resultaten kunnen nu verbeterd worden door deze systematische onzekerheden te verkleinen en hiervoor is het nodig de reconstructie efficiëntie van de  $K^{*\pm}$  dochter deeltjes verder nauwkeurig te onderzoeken. Een ander belangrijk aspect is de beschrijving van de kinematische variabelen in Monte Carlo modellen: om een betere beschrijving van de data te bekomen kunnen eventueel andere modellen, zoals bijvoorbeeld CASCADE [158], gebruikt worden.

Dankzij de goede statistiek van de data was het mogelijk de dubbele differentiële werkzame doorsnede te bepalen maar er moet nog onderzocht worden of de precisie hiervan voldoende is om bij te dragen tot de meting van de strange quark structuurfunctie  $F_2^s$  die van de dubbele differentiële werkzame doorsnede afhangt als functie van de schalingsvariabele  $Q^2$  en Bjorken- $x$ . Meer inzicht in strange quark productiemechanismen kan bekomen worden door een vergelijking met *next to leading order* QCD voorspellingen.

Een studie van de relatieve productie van vector (in dit geval  $K^{*\pm}$ ) en pseudoscalaire (bv.

$K_S^0$ ) mesonen zoals bijvoorbeeld de verhouding van vector mesonen tot pseudoscalaire mesonen,  $(V/(V+P))$ , kan ook gedaan worden wat informatie levert over de relatieve probabiteit voor de overeenkomstige spin toestanden die geproduceerd worden tijdens de hadronisatie.

De beschikbare data van kort-levende resonantiedeeltjes zoals  $K^{*\pm}$  is ook bruikbaar voor het onderzoeken van de botsingsdynamica en helpt ons met het begrijpen van de kenmerken van hete en dichte materie die geproduceerd wordt in zware ion botsingen. In dit opzicht zal een studie van de resonantieproductie ook belangrijk zijn voor de pp en AA botsingen in de Large Hadron Collider (LHC) die binnenkort opstart te CERN.

# Appendix A

## Cross Section Tables

Interval [GeV]	$d\sigma/dp_T$ [nb/GeV]	$\delta^{stat}$ [%]	$\delta^{sys.}$ [%]
1.0 – 1.5	9597.79	2.01217	15.97
1.5 – 2.0	3841.21	1.48	10.11
2.0 – 2.5	1904.32	1.97	12.06
2.5 – 3.5	793.121	1.89	10.50
3.5 – 5.0	210.156	2.65	9.04
5.0 – 10.	20.5957	5.11	10.04

**Table A.1:** The single differential  $K^{*\pm}$  meson production cross section as a function of the transverse momentum,  $p_T$ .

Interval	$d\sigma/d\eta$ [nb]	$\delta^{stat}$ [%]	$\delta^{sys.}$ [%]
-1.500 – -1.125	1.89	3.42	12.97
-1.125 – -0.750	2.71	1.95	8.32
-0.750 – -0.375	3.23	1.95	7.84
-0.375 – 0.000	3.07	1.97	9.71
0.000 – 0.375	2.76	2.14	9.15
0.375 – 0.750	2.71	2.44	9.07
0.750 – 1.125	2.10	2.81	10.30
1.125 – 1.500	1.60	4.57	12.91

**Table A.2:** The single differential  $K^{*\pm}$  meson production cross section as a function of the pseudorapidity,  $\eta$ .

<b>Interval</b> [GeV <sup>2</sup> ]	$d\sigma/dQ^2$ [ pb/GeV <sup>2</sup> ]	$\delta^{stat}$ [%]	$\delta^{sys.}$ [%]
5. – 10.	699.64	2.17	10.91
10. – 20.	216.69	1.31	9.68
20. – 40.	75.12	1.53	16.60
40. – 80.	20.67	2.16	12.66
80. – 100.	10.72	5.55	10.86

**Table A.3:** The single differential  $K^{*\pm}$  meson production cross section as a function of the four momentum squared,  $Q^2$ .

<b>Interval</b> [GeV]	$d\sigma/dW_{\gamma p}$ [pb/GeV]	$\delta^{stat}$ [%]	$\delta^{sys.}$ [%]
100. – 125.	76.27	1.62	8.83
125. – 150.	61.20	1.74	8.87
150. – 175.	56.04	1.91	10.71
175. – 200.	50.29	1.99	11.26
200. – 250.	34.38	1.90	20.59

**Table A.4:** The single differential  $K^{*\pm}$  meson production cross section as a function of the centre-of-mass energy of the hadronic final state,  $W_{\gamma p}$ .

<b>Interval</b>	$d\sigma/dx_F$ [pb]	$\delta^{stat}$ [%]	$\delta^{sys.}$ [%]
0. – 0.1	26088.1	2.0713	15.4396
0.1 – 0.25	18141.6	1.45998	8.76
0.25 – 0.4	9573.56	1.61322	8.75
0.4 – 0.6	3825.29	2.04729	12.86
0.6 – 1.	526.259	3.1635	10.46

**Table A.5:** The single differential  $K^{*\pm}$  meson production cross section as a function of the Feynman variable,  $x_F$ .

<b>Interval</b> [GeV <sup>2</sup> ]	$d\sigma/dP_T^{*2}$ [pb/GeV <sup>2</sup> ]	$\delta^{stat}$ [%]	$\delta^{sys.}$ [%]
0. – 5.	1378.23	0.92	11.90
5. – 10.	121.63	2.32	7.58
10. – 20.	20.6116	3.72	10.63
20. – 40.	3.50264	6.52	15.69
40. – 100.	0.418268	0.23	10.07

**Table A.6:** The single differential  $K^{*\pm}$  meson production cross section as a function of the squared transverse momentum  $P_T^{*2}$  of the  $K^{*\pm}$  meson in the photon proton rest frame

# Appendix B

## Double Differential Cross-Section Tables

In this appendix the double differential cross sections of inclusive  $K^{*\pm}$  mesons are tabulated as a function of  $P_T^{*2}$  in interval of  $x_F$ , as a function of  $Q^2$  in interval of  $x_F$ , and as a function of  $P_T^{*2}$  in interval of  $Q^2$ .

<b>Interval</b> [GeV <sup>2</sup> ]	$d\sigma/dP_T^{*2}dx_F$ [pb/GeV <sup>2</sup> ]	$\delta^{stat}$ [%]	$\delta^{sys.}$ [%]
<b>0. &lt; x<sub>F</sub> &lt; 0.1</b>			
0. – 5.	352.85	2.44	10.97
5. – 10.	26.56	6.11	11.38
10. – 20.	3.47	10.95	9.83
20. – 40.	0.54	11.45	9.82
40. – 100.	0.01	16.49	7.26
<b>0.1 &lt; x<sub>F</sub> &lt; 0.25</b>			
0. – 5.	355.04	1.98	10.88
5. – 10.	34.05	4.14	10.45
10. – 20.	5.72	6.18	17.64
20. – 40.	1.25	11.43	16.92
40. – 100.	0.11	16.88	8.05
<b>0.25 &lt; x<sub>F</sub> &lt; 0.4</b>			
0. – 5.	166.27	2.18	10.92
5. – 10.	18.07	5.47	11.05
10. – 20.	3.55	8.40	8.54
20. – 40.	0.64	15.71	10.06
40. – 100.	0.11	11.51	12.54
<b>0.4 &lt; x<sub>F</sub> &lt; 0.6</b>			
0. – 5.	89.38	2.60	11.01
5. – 10.	10.23	6.36	11.51
10. – 20.	2.83	9.11	8.87
20. – 40.	0.52	15.03	9.53
40. – 100.	0.0012	7.30	7.35
<b>0.6 &lt; x<sub>F</sub> &lt; 1.</b>			
0. – 5.	26.67	3.99	11.42
5. – 10.	3.18	8.55	12.85
10. – 20.	0.48	18.89	10.10
20. – 40.	0.02	10.66	12.18
40. – 100.	0.027	19.59	10.46

**Table B.1:** The double differential cross section of inclusive  $K^{*\pm}$  mesons, presented as functions of  $P_T^{*2}$  in intervals of  $x_F$ .

<b>Interval</b> [GeV <sup>2</sup> ]	$d\sigma/dQ^2 dx_F$ [pb/GeV <sup>2</sup> ]	$\delta^{stat}$ [%]	$\delta^{sys.}$ [%]
<b>0. &lt; x<sub>F</sub> &lt; 0.1</b>			
5. – 10.	175.59	3.78	7.85
10. – 20.	52.63	3.55	10.23
20. – 40.	8.26	6.55	17.78
40. – 80.	5.16	7.83	14.73
80. – 100.	2.10	10.51	12.54
<b>0.1 &lt; x<sub>F</sub> &lt; 0.25</b>			
0. – 5.	153.75	4.47	11.59
5. – 10.	62.05	2.86	10.01
10. – 20.	23.50	2.97	9.79
20. – 40.	5.44	4.22	13.17
40. – 100.	5.60	10.26	13.87
<b>0.25 &lt; x<sub>F</sub> &lt; 0.4</b>			
0. – 5.	74.27	6.58	12.56
5. – 10.	28.85	2.98	10.05
10. – 20.	10.91	3.52	10.90
20. – 40.	3.02	4.17	9.15
40. – 100.	0.87	7.84	11.93
<b>0.4 &lt; x<sub>F</sub> &lt; 0.6</b>			
0. – 5.	37.67	9.19	14.11
5. – 10.	16.93	3.19	10.11
10. – 20.	4.97	4.53	7.14
20. – 40.	1.51	5.75	9.74
40. – 100.	0.50	13.91	10.75
<b>0.6 &lt; x<sub>F</sub> &lt; 1.</b>			
0. – 5.	18.34	12.85	10.72
5. – 10.	5.33	4.68	10.68
10. – 20.	1.068	8.10	10.40
20. – 40.	0.40	10.01	10.00
40. – 100.	0.137	15.40	10.06

**Table B.2:** The double differential cross section of inclusive  $K^{*\pm}$  mesons, presented as functions of  $Q^2$  in interval of  $x_F$ .

<b>Interval</b> [GeV <sup>2</sup> ]	$d\sigma/dQ^2 dx_F$ [pb/GeV <sup>2</sup> ]	$\delta^{stat}$ [%]	$\delta^{sys.}$ [%]
<b>0. &lt; x<sub>F</sub> &lt; 0.1</b>			
5. – 10.	431.54	3.01	11.11
10. – 20.	38.13	7.27	12.04
20. – 40.	4.94	11.63	10.21
40. – 80.	0.84	15.57	9.95
80. – 100.	0.072	16.77	10.70
<b>0.1 &lt; x<sub>F</sub> &lt; 0.25</b>			
0. – 5.	288.48	1.77	10.84
5. – 10.	26.62	3.99	10.39
10. – 20.	5.01	5.96	7.57
20. – 40.	1.37	14.60	9.21
40. – 100.	0.047	39.90	10.98
<b>0.25 &lt; x<sub>F</sub> &lt; 0.4</b>			
0. – 5.	174.22	2.26	10.93
5. – 10.	18.32	4.87	10.76
10. – 20.	3.48	7.77	8.26
20. – 40.	0.39	16.83	9.95
40. – 100.	0.31	45.60	9.54
<b>0.4 &lt; x<sub>F</sub> &lt; 0.6</b>			
0. – 5.	108.47	2.54	10.99
5. – 10.	12.35	7.70	12.30
10. – 20.	1.40	13.8	11.54
20. – 40.	0.51	13.2	8.20
40. – 100.	0.060	24.8	9.53
<b>0.6 &lt; x<sub>F</sub> &lt; 1.</b>			
0. – 5.	22.54	7.68	13.17
5. – 10.	3.30	18.03	10.43
10. – 20.	1.14	28.14	12.64
20. – 40.	0.087	10.29	10.04
40. – 100.	0.019	16.06	16.63

**Table B.3:** The double differential cross section of inclusive  $K^{*\pm}$  mesons, presented as functions of  $P_T^{*2}$  in interval of  $Q^2$ .

# References

- [1] D. Sunar, “Measurement of  $\mathbf{K}^{*\pm}$  Production in Deep Inelastic  $ep$  Scattering at HERA,” XVII International Workshop on Deep-Inelastic Scattering and Related Subjects DIS 2009, Madrid, 26-30 April 2009”. [23](#)
- [2] C. Grab, “Strangeness Production and Hadron Spectroscopy at HERA,” Contributed to 34th International Conference on High Energy Physics (ICHEP 2008), Philadelphia, Pennsylvania, 30 July-5 August 2008, [arXiv:hep-ex/0810.0404]. [23](#)
- [3] A. Kropivnitskaya, “Proceedings of the 38th International Symposium on Multiparticle Dynamics (ISMD08),” Hamburg, Germany, 15-20 September 2008, [arXiv:hep-ph/0902.0377]. [23](#)
- [4] C. Amsler *et al.*, “Review of Particle Physics,” *Phys. Lett.*, vol. B667, p. 1, 2008. [20](#), [26](#), [27](#), [43](#), [45](#), [46](#), [101](#), [104](#), [107](#), [108](#), [112](#), [118](#), [143](#)
- [5] A. I. Abazov *et al.*, “Search for Neutrinos from Sun Using the Reaction Ga-71 ( $\nu_e e^-$ ) Ge-71,” *Phys. Rev. Lett.*, vol. 67, pp. 3332–3335, 1991. [26](#)
- [6] P. Anselmann *et al.*, “Solar Neutrinos Observed by GALLEX at Gran Sasso,” *Phys. Lett.*, vol. B285, pp. 376–389, 1992. [26](#)
- [7] D. N. Abdurashitov *et al.*, “Results from SAGE,” *Phys. Lett.*, vol. B328, pp. 234–248, 1994. [26](#)
- [8] Y. Fukuda *et al.*, “Solar Neutrino Data Covering Solar Cycle 22,” *Phys. Rev. Lett.*, vol. 77, pp. 1683–1686, 1996. [26](#)
- [9] T. Araki *et al.*, “Measurement of Neutrino Oscillation with KamLAND: Evidence of Spectral Distortion,” *Phys. Rev. Lett.*, vol. 94, p. 081801, 2005. [26](#)
- [10] J. Hosaka *et al.*, “Solar Neutrino Measurements in Super-Kamiokande-I,” *Phys. Rev.*, vol. D73, p. 112001, 2006. [26](#)
- [11] S. L. Glashow, “Partial Symmetries of Weak Interactions,” *Nucl. Phys.*, vol. 22, pp. 579–588, 1961. [26](#)
- [12] S. Weinberg, “A Model of Leptons,” *Phys. Rev. Lett.*, vol. 19, pp. 1264–1266, 1967. [26](#)

- [13] A. Salam, “Weak and Electromagnetic Interactions,” Originally printed in *Svartholm: Elementary Particle Theory, Proceedings of the Nobel Symposium Held 1968 at Lerum, Sweden, Stockholm 1968*,. 26
- [14] F. Englert and R. Brout, “Broken Symmetry and the Mass of Gauge Vector Mesons,” *Phys. Rev. Lett.*, vol. 13, pp. 321–322, 1964. 27
- [15] P. W. Higgs, “Broken Symmetries and the Mass of Gauge Vector Mesons,” *Phys. Rev. Lett.*, vol. 13, pp. 508–509, 1964. 27
- [16] G. S. Guralnik, C. R. Hagen, and T. W. B. Kibble, “Global Conservation Laws and Massless Particles,” *Phys. Rev. Lett.*, vol. 13, pp. 585–587, 1964. 27
- [17] R. P. Feynman, “Very High-Energy Collisions of Hadrons,” *Phys. Rev. Lett.*, vol. 23, pp. 1415–1417, 1969. 30
- [18] J. D. Bjorken, “Asymptotic Sum Rules at Infinite Momentum,” *Phys. Rev.*, vol. 179, pp. 1547–1553, 1969. 30
- [19] M. Breidenbach *et al.*, “Observed Behavior of Highly Inelastic Electron-Proton Scattering,” *Phys. Rev. Lett.*, vol. 23, pp. 935–939, 1969. 30
- [20] E. D. Bloom *et al.*, “High-Energy Inelastic  $ep$  Scattering at 6-Degrees and 10-Degrees,” *Phys. Rev. Lett.*, vol. 23, pp. 930–934, 1969. 30
- [21] R. Brandelik *et al.*, “Evidence for Planar Events in  $e^+e^-$  Annihilation at High-Energies,” *Phys. Lett.*, vol. B86, p. 243, 1979. 30
- [22] F. Halzen and A. D. Martin, *Quarks and Leptons: An Introduction Course in Modern Particle Physics*. John Wiley & Sons, 1984. 31, 33
- [23] J. Callan, Curtis G. and D. J. Gross, “High-Energy Electroproduction and the Constitution of the Electric Current,” *Phys. Rev. Lett.*, vol. 22, pp. 156–159, 1969. 31
- [24] G. Ingelman *et al.*, “Deep Inelastic Physics and Simulation,” In Hamburg 1987, Proceedings, HERA Workshop, vol. 1 3-17. (see Conference Index). 31
- [25] C. Adloff *et al.*, “Measurement and QCD Analysis of Neutral and Charged Current Cross Sections at HERA,” *Eur. Phys. J.*, vol. C30, pp. 1–32, 2003. 13, 32, 41
- [26] H. D. Politzer, “Reliable Perturbative Results for Strong Interactions?,” *Phys. Rev. Lett.*, vol. 30, pp. 1346–1349, 1973. 33
- [27] D. J. Gross and F. Wilczek, “Ultraviolet Behavior of Non-Abelian Gauge Theories,” *Phys. Rev. Lett.*, vol. 30, pp. 1343–1346, 1973. 33
- [28] B. Andersson, *The Lund Model*. Hardback, 471 pages, ISBN 0521420946: Cambridge University Press, 1998. 33

- [29] F. D. Aaron *et al.*, “Jet Production in  $ep$  Collisions at High  $Q^2$  and Determination of  $\alpha_s$ ,” 2009, submitted to *Eur. Phys. J. C*, [arXiv:hep-ex/0904.3870]. 13, 34, 35
- [30] A. Aktas *et al.*, “Measurement of Inclusive Jet Production in Deep-Inelastic Scattering at High  $Q^2$  and Determination of the Strong Coupling,” *Phys. Lett.*, vol. B653, pp. 134–144, 2007. 34
- [31] S. Chekanov *et al.*, “Inclusive Jet Cross Sections in the Breit Frame in Neutral Current Deep Inelastic Scattering at HERA and Determination of  $\alpha_s$ ,” *Phys. Lett.*, vol. B547, pp. 164–180, 2002. 34
- [32] J. C. Collins, D. E. Soper, and G. Sterman, “Factorization of Hard Processes in QCD,” *Adv. Ser. Direct. High Energy Phys.*, vol. 5, pp. 1–91, 1988. 34
- [33] J. C. Collins, “Choosing the Factorization/Renormalization Scale in Perturbative QCD Calculations,” *High Energy Interactions edited by J. Tran Thanh, Gif-sur-Yvette:Editions Frontieres*, pp. 123–128, 1990. 35
- [34] V. N. Gribov and L. N. Lipatov, “Deep inelastic  $e p$  scattering in perturbation theory,” *Sov. J. Nucl. Phys.*, vol. 15, pp. 438–450, 1972. 37
- [35] V. N. Gribov and L. N. Lipatov, “ $e^+e^-$  Pair Annihilation and Deep Inelastic  $ep$  Scattering in Perturbation Theory,” *Sov. J. Nucl. Phys.*, vol. 15, pp. 675–684, 1972. 37
- [36] L. N. Lipatov, “The Parton Model and Perturbation Theory,” *Sov. J. Nucl. Phys.*, vol. 20, pp. 94–102, 1975. 37
- [37] G. Altarelli and G. Parisi, “Asymptotic Freedom in Parton Language,” *Nucl. Phys.*, vol. B126, p. 298, 1977. 37
- [38] Y. L. Dokshitzer, “Calculation of the Structure Functions for Deep Inelastic Scattering and  $e^+e^-$  Annihilation by Perturbation Theory in Quantum Chromodynamics. (In Russian),” *Sov. Phys. JETP*, vol. 46, pp. 641–653, 1977. 37
- [39] E. A. Kuraev, L. N. Lipatov, and V. S. Fadin, “The Pomernanchuk Singularity in Nonabelian Gauge Theories,” *Sov. Phys. JETP*, vol. 45, pp. 199–204, 1977. 38
- [40] I. I. Balitsky and L. N. Lipatov, “The Pomernanchuk Singularity in Quantum Chromodynamics,” *Sov. J. Nucl. Phys.*, vol. 28, pp. 822–829, 1978. 38
- [41] S. Catani, M. Ciafaloni, and F. Hautmann, “High-Energy Factorization and Small  $x$  Heavy Flavor Production,” *Nucl. Phys.*, vol. B366, pp. 135–188, 1991. 38
- [42] M. Ciafaloni, “Coherence Effects in Initial Jets at Small  $Q^2/s$ ,” *Nucl. Phys.*, vol. B296, p. 49, 1988. 39
- [43] S. Catani, F. Fiorani, and G. Marchesini, “QCD Coherence in Initial State Radiation,” *Phys. Lett.*, vol. B234, p. 339, 1990. 39

- [44] G. D. Rochester and C. C. Butler, “Evidence for the Existence of New Unstable Elementary Particles,” *Nature*, vol. 160, p. 855, 1947. [40](#)
- [45] A. Pais, “Some Remarks on the V-Particles,” *Phys. Rev.*, vol. 86, pp. 663–672, 1952. [40](#)
- [46] W. Cheston and H. Primakoff, “Nonmesonic” Bound V-Particle Decay,” *Phys. Rev.*, vol. 92, pp. 1537–1541, Dec 1953. [40](#)
- [47] M. Gell-Mann, “A Schematic Model of Baryons and Mesons,” *Phys. Lett.*, vol. 8, pp. 214–215, 1964. [40](#)
- [48] G. Zweig *Preprint CERN Rep. 8182/TH*, 1964 (unpublished). [40](#)
- [49] Combined ZEUS and H1 Plots for ElectroWeak Interactions and Unified Theories 2004. [http://www-zeus.desy.de/physics/sfew/PUBLIC/sfew\\_results/preliminary/mori13](http://www-zeus.desy.de/physics/sfew/PUBLIC/sfew_results/preliminary/mori13), [41](#)
- [50] K. Hagiwara *et al.*, “Review of Particle Physics,” *Phys. Rev.*, vol. D66, p. 010001, 2002. [41](#)
- [51] Y. Ne’eman, “Derivation of Strong Interactions from a Gauge Invariance,” *Nucl. Phys.*, vol. 26, pp. 222–229, 1961. [42](#)
- [52] M. Gell-Mann, “Symmetries of Baryons and Mesons,” *Phys. Rev.*, vol. 125, pp. 1067–1084, 1962. [42](#)
- [53] S. Aid *et al.*, “Strangeness Production in Deep-Inelastic Positron Proton Scattering at HERA,” *Nucl. Phys.*, vol. B480, pp. 3–34, 1996. [48](#), [55](#)
- [54] C. Adloff *et al.*, “Photoproduction of  $K^0$  and  $\Lambda$  at HERA and a Comparison with Deep Inelastic Scattering,” *Z. Phys.*, vol. C76, pp. 213–221, 1997. [48](#), [55](#)
- [55] J. Breitweg *et al.*, “Charged Particles and Neutral Kaons in Photoproduced Jets at HERA,” *Eur. Phys. J.*, vol. C2, pp. 77–93, 1998. [48](#)
- [56] P. D. Acton *et al.*, “Inclusive Neutral Vector Meson Production in Hadronic  $Z^0$  Decays,” *Z. Phys.*, vol. C56, pp. 521–536, 1992. [49](#), [50](#)
- [57] P. Abreu *et al.*, “Production Characteristics of  $K^0$  and Light Meson Resonances in Hadronic Decays of the  $Z^0$ ,” *Z. Phys.*, vol. C65, pp. 587–602, 1995. [49](#)
- [58] M. R. Adams *et al.*, “Production of Neutral Strange Particles in Muon - Nucleon Scattering at 490-GeV,” *Z. Phys.*, vol. C61, pp. 539–550, 1994. [49](#)
- [59] A. Breakstone *et al.*, “Production of Charged Pions at High Transverse Momentum in  $pp$  Collisions at  $\sqrt{s} = 45$  GeV and 62-GeV,” *Phys. Lett.*, vol. B135, p. 505, 1984. [49](#)
- [60] A. Bohrer, “Inclusive Particle Production in Hadronic Decays of the Z Boson at LEP I,” *CERN-OPEN/96-021 Physics Reports*, vol. 291, pp. 108–217, 1996. [49](#)

- [61] P. Abreu *et al.*, “Measurement of the Spin Density Matrix for the  $\rho^0$ ,  $K^*(892)^0$  and  $\Phi$  Produced in  $Z^0$  decays,” *Phys. Lett.*, vol. B406, pp. 271–286, 1997. 49
- [62] G. D. Lafferty, P. I. Reeves, and M. R. Whalley, “A Compilation of Inclusive Particle Production Data in  $e^+e^-$  Annihilation,” *J. Phys.*, vol. G21, pp. A1–A151, 1995. 49
- [63] P. Abreu *et al.*, “Production of Strange Particles in the Hadronic Decays of the  $Z^0$ ,” *Phys. Lett.*, vol. B275, pp. 231–242, 1992. 49, 50
- [64] P. D. Acton *et al.*, “A Measurement of  $K^*(892)^\pm$  Production in Hadronic  $Z^0$  decays,” *Phys. Lett.*, vol. B305, pp. 407–414, 1993. 49
- [65] M. Derrick *et al.*, “Neutral  $K^*(890)$  and  $\rho^0$  Meson Production in  $e^+e^-$  Annihilation at the  $\sqrt{s} = 29$  GeV,” *Phys. Lett.*, vol. B158, p. 519, 1985. 50
- [66] G. Alexander *et al.*, “A Study of  $K_s^0$  Production in  $Z^0$  Decays,” *Phys. Lett.*, vol. B264, pp. 467–475, 1991. 50
- [67] P. Abreu *et al.*, “Measurement of Inclusive Production of Light Meson Resonances in Hadronic Decays of the  $Z^0$ ,” *Phys. Lett.*, vol. B298, pp. 236–246, 1993. 50
- [68] P. D. Acton *et al.*, “A Measurement of Strange Baryon Production in Hadronic  $Z^0$  Decays,” *Phys. Lett.*, vol. B291, pp. 503–518, 1992. 50
- [69] H. J. Behrend *et al.*, “Inclusive Strange Particle Production in  $e^+e^-$  Annihilation,” *Z. Phys.*, vol. C46, pp. 397–404, 1990. 14, 51
- [70] W. Bartel *et al.*, “Charged Particle and Neutral Kaon Production in  $e^+e^-$  Annihilation at PETRA,” *Z. Phys.*, vol. C20, p. 187, 1983. 51
- [71] M. Althoff *et al.*, “A Detailed Study of Strange Particle Production in  $e^+e^-$  Annihilation at High-Energy,” *Z. Phys.*, vol. C27, p. 27, 1985. 51
- [72] W. Braunschweig *et al.*, “Strange Meson Production in  $e^+e^-$  Annihilation,” *Z. Phys.*, vol. C47, pp. 167–180, 1990. 51
- [73] W. Braunschweig *et al.*, “Strange Baryon Production in  $e^+e^-$  Annihilation,” *Z. Phys.*, vol. C45, p. 209, 1989. 51
- [74] R. Brandelik *et al.*, “ $\Lambda$ ,  $\bar{\Lambda}$  Production in  $e^+e^-$  Annihilation at 33-GeV Center of Mass Energy,” *Phys. Lett.*, vol. B105, p. 75, 1981. 51
- [75] G. Alexander *et al.*, “Strange Baryon Production in Hadronic  $Z^0$  Decays,” *Z. Phys.*, vol. C73, pp. 569–586, 1997. 51
- [76] G. Alexander *et al.*, “ $\Sigma^+$ ,  $\Sigma^0$  and  $\Sigma^-$  Hyperon Production in Hadronic  $Z^0$  Decays,” *Z. Phys.*, vol. C73, pp. 587–600, 1997. 51
- [77] P. Abreu *et al.*, “Strange Baryon Production in Z Hadronic Decays,” *Z. Phys.*, vol. C67, pp. 543–554, 1995. 51

- [78] P. Abreu *et al.*, “ $\pi^\pm$ ,  $K^\pm$ ,  $p$  and anti- $p$  Production in  $Z^0 \rightarrow q\bar{q}$ ,  $Z^0 \rightarrow b\bar{b}$ ,  $Z^0 \rightarrow u\bar{u}$ ,  $d\bar{d}$ ,  $s\bar{s}$ ,” *Eur. Phys. J.*, vol. C5, pp. 585–620, 1998. [51](#)
- [79] R. Barate *et al.*, “Studies of Quantum Chromodynamics with the ALEPH Detector,” *Phys. Rept.*, vol. 294, pp. 1–165, 1998. [51](#), [83](#)
- [80] G. Abbiendi *et al.*, “Leading Particle Production in Light Flavour Jets,” *Eur. Phys. J.*, vol. C16, pp. 407–421, 2000. [52](#)
- [81] V. Blobel and *et al.*, “Observation of Vector Meson Production in Inclusive  $pp$  Reactions,” *Phys. Lett.*, vol. B48, p. 73, 1974. [52](#)
- [82] K. Bockmann *et al.*, “Inclusive  $K^{*\pm}$  (892) Production in  $pp$  and  $\pi^+p$  Interactions,” *Nucl. Phys.*, vol. B166, p. 284, 1980. [52](#)
- [83] H. Kichimi *et al.*, “Observation of  $K^*(890)$  and  $K^*(1420)$  Production in 405 GeV/ $c$   $pp$  Interactions,” *Lett. Nuovo Cim.*, vol. 24, pp. 129–135, 1979. [52](#)
- [84] D. Brick *et al.*, “Inclusive Strange Resonance Production in  $pp$ ,  $\pi^+p$  and  $K^+p$  Interactions at 147-GeV/ $c$ ,” *Phys. Rev.*, vol. D25, pp. 2248–2258, 1982. [52](#)
- [85] T. Aziz *et al.*, “Inclusive  $K^*$  and  $\Sigma^*$  Production in 360-GeV/ $c$   $pp$  Interaction Using the European Hybrid Spectrometer,” *Z. Phys.*, vol. C30, p. 381, 1986. [52](#)
- [86] C. V. Eldik,  *$K^{*0}$  Production in Proton-Nucleus Collisions*. PhD thesis, Universitat Dortmund, 2004. [14](#), [52](#)
- [87] J. Adams *et al.*, “ $K^*(892)$  Resonance Production in Au + Au and p + p Collisions at  $\sqrt{s_{NN}} = 200$  GeV at STAR,” *Phys. Rev.*, vol. C71, p. 064902, 2005. [14](#), [53](#)
- [88] B. I. Abelev *et al.*, “Spin Alignment Measurements of the  $K^{*0}(892)$  and  $\phi(1020)$  Vector Mesons in Heavy Ion Collisions at  $\sqrt{s_{NN}} = 200$  GeV,” *Phys. Rev.*, vol. C77, p. 061902, 2008. [53](#)
- [89] H. Z. Huang and J. Rafelski, “Hadronization and Quark Probes of Deconfinement at RHIC,” *AIP Conf. Proc.*, vol. 756, pp. 210–227, 2005. [54](#)
- [90] E. J. Kim, “System and Rapidity Dependence of Baryon to Meson Ratios at RHIC,” *Nucl. Phys.*, vol. A774, pp. 493–496, 2006. [54](#)
- [91] P. Fachini, “Overview of Resonance Production,” *J. Phys.*, vol. G35, p. 044032, 2008. [54](#)
- [92] I. Abt *et al.*, “ $K^{*0}$  and  $\phi$  Meson Production in Proton-Nucleus Interactions at  $\sqrt{s} = 41.6$  GeV,” *Eur. Phys. J.*, vol. C50, pp. 315–328, 2007. [54](#)
- [93] I. Abt *et al.*, “V0 Production in p+A Collisions at  $\sqrt{s} = 41.6$  GeV,” *Eur. Phys. J.*, vol. C51, 2008. [54](#)

- [94] S. L. Belostotsky, “Strange Particle Production and Polarization of Lambda Hyperons in the HERMES Experiment,” *Nucl. Phys. Proc. Suppl.*, vol. 79, pp. 526–528, 1999. [54](#)
- [95] O. Grebenyuk, “Transverse Polarization of  $\Lambda$  and  $\bar{\Lambda}$  Produced Inclusively in e N scattering at HERMES,” *Acta Phys. Polon.*, vol. B33, pp. 3797–3801, 2002. [54](#)
- [96] S. Radomski, “CERES Measurement of Strangeness Production at Top SPS Energy,” *J. Phys.*, vol. G35, p. 044003, 2008. [54](#)
- [97] A. Andronic, P. Braun-Munzinger, and J. Stachel, “Hadron Production in Central Nucleus Nucleus Collisions at Chemical Freeze-out,” *Nucl. Phys.*, vol. A772, pp. 167–199, 2006. [54](#)
- [98] G. J. Alner *et al.*, “Kaon Production in  $\bar{p}p$  Reactions at a Center of Mass Energy of 540 GeV,” *Nucl. Phys.*, vol. B258, p. 505, 1985. [54](#)
- [99] R. E. Ansorge *et al.*, “Kaon Production in  $\bar{p}p$  Interactions at C.M. Energies From 200 GeV to 900 GeV,” *Z. Phys.*, vol. C41, pp. 179–190, 1988. [54](#)
- [100] R. E. Ansorge *et al.*, “Hyperon Production at 200 GeV and 900 GeV Center-of-Mass Energy,” *Nucl. Phys.*, vol. B328, p. 36, 1989. [54](#)
- [101] F. D. Aaron *et al.*, “Strangeness Production at low  $Q^2$  in Deep-Inelastic  $ep$  Scattering at HERA,” *Eur. Phys. J. C*, 2008. [14](#), [55](#), [135](#), [149](#)
- [102] F. D. Aaron *et al.*, “Inclusive Photoproduction of  $\rho^0$ ,  $K^{*0}$  and  $\phi$  Mesons at HERA,” *Phys. Lett.*, vol. B673, pp. 119–126, 2009. [14](#), [56](#)
- [103] M. Derrick *et al.*, “Neutral Strange Particle Production in Deep Inelastic Scattering at HERA,” *Z. Phys.*, vol. C68, pp. 29–42, 1995. [56](#)
- [104] S. Chekanov *et al.*, “Measurement of  $K_s^0$ ,  $\Lambda$ ,  $\bar{\Lambda}$  Production at HERA,” *Eur. Phys. J.*, vol. C51, pp. 1–23, 2007. [56](#), [147](#)
- [105] D. Naumov *et al.*, “A study of Strange Particles Produced in Neutrino Neutral Current Interactions in the NOMAD Experiment,” *Nucl. Phys.*, vol. B700, pp. 51–68, 2004. [57](#)
- [106] P. Astier *et al.*, “Measurement of the  $\Lambda$  Polarization in  $\nu_\mu$  Charged Current Interactions in the NOMAD Experiment,” *Nucl. Phys.*, vol. B588, pp. 3–36, 2000. [57](#)
- [107] P. Astier *et al.*, “Measurement of the  $\bar{\Lambda}$  Polarization in  $\nu_\mu$  Charged Current Interactions in the NOMAD Experiment,” *Nucl. Phys.*, vol. B605, pp. 3–14, 2001. [57](#)
- [108] P. Astier *et al.*, “Inclusive Production of  $\rho(770)^0$ ,  $f_0(980)$  and  $f_2(1270)$  Mesons in  $\nu_\mu$  Charged Current Interactions,” *Nucl. Phys.*, vol. B601, pp. 3–23, 2001. [57](#)

- [109] P. Astier *et al.*, “A Study of Strange Particle Production in  $\nu_\mu$  Charged Current Interactions in the NOMAD Experiment,” *Nucl. Phys.*, vol. B621, pp. 3–34, 2002. [57](#)
- [110] A. Chukanov *et al.*, “Production Properties of  $K^*(892)^\pm$  Vector Mesons and Their Spin Alignment as Measured in the NOMAD Experiment,” *Eur. Phys. J.*, vol. C46, pp. 69–79, 2006. [57](#)
- [111] P. Schmueser, “The Electron Proton Colliding Beam Facility HERA,” *Nucl. Instrum. Meth.*, vol. A235, pp. 201–208, 1985. [59](#)
- [112] U. Holm, “The ZEUS Detector,” *Status Report 1993*, 1993. [60](#)
- [113] T. Lohse *et al.*, “HERA-B: An Experiment to study CP Violation in the B system Using an Internal Target at the HERA Proton Ring Proposal,” 1994. DESY-PRC-94-02. [60](#)
- [114] HERMES Collaboration. Technical Design Report, DESY-PRC-93-06, 1993. [60](#)
- [115] H1 Collaboration. <https://www-h1.desy.de/h1/www/h1det/lumi/lplots/>. [14](#), [61](#)
- [116] I. Abt *et al.*, “The H1 Detector at HERA,” *Nucl. Instrum. Meth.*, vol. A386, pp. 310–347, 1997. [62](#), [75](#)
- [117] H1 Collaboration. [14](#), [64](#)
- [118] B. Heinemann, *Measurement of Charged Current and Neutral Current Cross Sections in Positron-Proton Collisions at  $\sqrt{s} = 300$  GeV*. Ph.D. Dissertation, Hamburg University, Germany, 1999. [71](#)
- [119] M. Peez *et al.*, “An Energy Flow Algorithm for Hadronic Reconstruction in OO: Hadroo2,” *H1-Internal Note*, vol. H1-01/05-616, DESY, 2005. [71](#)
- [120] T. Nicholls *et al.*, “Performance of an Electromagnetic Lead / Scintillating Fiber Calorimeter for the H1 Detector,” *Nucl. Instrum. Meth.*, vol. A374, pp. 149–156, 1996. [71](#)
- [121] H1 SPACAL Group, “H1 Backward Upgrade with a SPACAL Calorimeter: the Hadronic Section,” *DESY Report*, vol. DESY-96-013, DESY, 1996. [71](#)
- [122] R. D. Appuhn *et al.*, “Hadronic Response and  $e/\pi$  Separation with the H1 Lead/Fibre Calorimeter,” *Nucl. Instrum. Meth.*, vol. A 382, pp. 395–412, 1996. [71](#)
- [123] D. Reyna, “Modifications to SPACAL for H1 High Luminosity Operation and the Effect on Acceptance,” *H1-Internal Note*, vol. H1-11/98-555, 1998. [73](#)
- [124] H. Bethe and W. Heitler, “On the Stopping of Fast Particles and on the Creation of Positive Electrons,” *Proc. Roy. Soc. Lond.*, vol. A146, pp. 83–112, 1934. [73](#)

- [125] E. Elsen, “Aspects of the H1 Trigger and Data Acquisition System,” 1992. Prepared for 2nd Annual Conference on Electronics for Future Colliders, Chestnut Ridge, N.Y., 19-21 May 1992. 75
- [126] C. Beigbeder, “Level 2 Topological Trigger (L2TT) Hardware,” *H1-Internal Note*, vol. H1-07/98-547, 1998. 76
- [127] J. K. Kohne *et al.*, “Realization of a Second Level Neural Network Trigger for the H1 Experiment at HERA,” *Nucl. Instrum. Meth.*, vol. A389, pp. 128–133, 1997. 76
- [128] E. Barrelet *et al.*, “The Hardware Implementation of L3 Triggers in H1,” *H1-Internal Note*, vol. H1-09/88-100, 1988. 76
- [129] A. Baird *et al.*, “A Fast High Resolution Track Trigger for the H1 Experiment,” *IEEE Trans. Nucl. Sci.*, vol. 48, pp. 1276–1285, 2001. 76
- [130] G. Gustafson, “Dual Description of a Confined Color Field,” *Phys. Lett.*, vol. B175, p. 453, 1986. 15, 79, 80
- [131] G. A. Schuler and H. Spiesberger, “DJANGO: The Interface for the Event Generators HERACLES and LEPTO,” In Hamburg 1991, Proceedings, Physics at HERA, vol. 3 1419-1432. (see High Energy Physics Index 30 (1992) No. 12988). 79, 83
- [132] H. Jung, “Hard Diffractive Scattering in High-Energy  $ep$  Collisions and the Monte Carlo Generation RAPGAP,” *Comp. Phys. Commun.*, vol. 86, pp. 147–161, 1995. 79, 83
- [133] H. Jung, “The RAPGAP Monte Carlo, version 3.1,” <https://www.desy.de/%7Ejung/rapgap/welcome.html>. 80
- [134] L. Lonnblad, “ARIADNE Version 4: A Program for Simulation of QCD Cascades Implementing the Color Dipole Model,” *Comput. Phys. Commun.*, vol. 71, pp. 15–31, 1992. 80, 83
- [135] B. Andersson, G. Gustafson, and B. Soderberg, “A General Model for Jet Fragmentation,” *Z. Phys.*, vol. C20, p. 317, 1983. 81
- [136] T. Sjostrand, S. Mrenna, and P. Skands, “PYTHIA 6.4 Physics and Manual,” *JHEP*, vol. 05, p. 026, 2006. 81
- [137] G. Corcella *et al.*, “HERWIG 6.5 Release Note,” 2002. 83
- [138] H. L. Lai *et al.*, “Global QCD Analysis of Parton Structure of the Nucleon: CTEQ5 Parton Distributions,” *Eur. Phys. J.*, vol. C12, pp. 375–392, 2000. 83
- [139] M. Gluck, E. Reya, and A. Vogt, “Dynamical Parton Distributions of the Proton and Small  $x$  Physics,” *Z. Phys.*, vol. C67, pp. 433–448, 1995. 83
- [140] A. Mucke, R. Engel, J. P. Rachen, R. J. Protheroe, and T. Stanev, “Monte Carlo Simulations of Photohadronic Processes in Astrophysics,” *Comput. Phys. Commun.*, vol. 124, pp. 290–314, 2000. 83

- [141] T. Sjostrand, “High-Energy Physics Event Generation with PYTHIA 5.7 and JETSET 7.4,” *Comput. Phys. Commun.*, vol. 82, pp. 74–90, 1994. 84
- [142] A. Kwiatkowski, H. Spiesberger, and H. J. Mohring, “HERACLES: An Event Generator for  $ep$  Interactions at HERA Energies Including Radiative Processes: Version 1.0,” *Comp. Phys. Commun.*, vol. 69, pp. 155–172, 1992. 84
- [143] J. Meyer, “Guide for the H1 Simulation Program H1SIM,” *Internal Software-Note 03-11/89*, vol. DESY, 1989. 84
- [144] R. Brun *et al.*, “GEANT3 User’s Guide,” *CERN-DD/EE-84-1*, 1989. 84
- [145] 2005. H1REC documentation page, <https://www-h1.desy.de/icas/imanuals/h1rec/h1rec9> 85
- [146] V. Boudry *et al.*, “The Inclusive Electron Trigger for the SPACAL: Design and CERN-Test Results,” *H1 Internal Report H1-03/95-430*, 1995. 87
- [147] T. Wolff *et al.*, “A Drift Chamber Track Finder for the First Level Trigger of the H1 Experiment,” *Nucl. Instrum. Meth.*, vol. A323, pp. 537–541, 1992. 87
- [148] M. O. Boenig, “Messung des  $D^*$  Meson Produktionwirkungsquerschnittes in Tiefinelastischer Streuung mit dem H1-Experiment,” PhD Thesis, Universitat Dortmund, 2007. 93
- [149] K. Lohwasser, “Optimisation of the Selection Capability of the H1 Fast Track Trigger,” Diploma Thesis, Universitat Dortmund, 2006. 93
- [150] S. Bentvelsen, J. Engelen, and P. Kooijman, “Reconstruction of  $(x, Q^2)$  and Extraction of Structure Functions in Neutral Current Scattering at HERA,” NIKHEF-H-92-02. 93
- [151] A. Blondel and F. Jacquet, “Proceedings of the Study of an  $ep$  Facility for Europe,” *ed. U. Amaldi, DESY 79/48*, p. 391, 1979. 94
- [152] U. Bassler and G. Bernardi, “On the Kinematic Reconstruction of Deep Inelastic Scattering at HERA: The Sigma Method,” *Nucl. Instrum. Meth.*, vol. A361, pp. 197–208, 1995. 95
- [153] U. Bassler and G. Bernardi, “Structure Function Measurements and Kinematic Reconstruction at HERA,” *Nucl. Instrum. Meth.*, vol. A426, pp. 583–598, 1999. 95
- [154] L. West, “How to Use the Heavy Flavour Working Group Track, Muon and Electron Selection Code,” *H1 Internal Software Manual*, 1997. 96
- [155] J. Podolanski and R. Armenteros, “Analysis of V-events,” *Phil. Mag.*, p. 13, 1954. 102
- [156] C. Niebuhr, S. Schmitt, *et al.*, “Lumi-TF: Luminosity Status Report,” June 2008. [https://www-h1.desy.de/h1/iww/iminutes/agenda\\_physics\\_plenary.20080605.html](https://www-h1.desy.de/h1/iww/iminutes/agenda_physics_plenary.20080605.html). 128

- 
- [157] A. Aktas *et al.*, “Inclusive Production of  $D^+$ ,  $D^0$ ,  $D_s^+$  and  $D^{*+}$  Mesons in Deep Inelastic Scattering at HERA,” *Eur. Phys. J.*, vol. C38, pp. 447–459, 2005. [143](#)
- [158] H. Jung, “The CCFM Monte Carlo Generator CASCADE,” *Comput. Phys. Commun.*, vol. 143, pp. 100–111, 2002. [150](#), [153](#)

# Curriculum Vitae

## Personal Data

Name	Deniz Sunar
Date of birth	06 August 1978
Place of birth	Iskenderun (Turkey)
Nationality	Turkish

---

---

## Education

October 1991 - February 1994	Lyceum of Iskenderun, Iskenderun, Turkey Science & Mathematics area
October 1994 - June 1999	BSc. in Department of Physics, University of Çukurova, Adana, Turkey
October 1999 - August 2002	M.Sc in High Energy Particle Physics Institute of Basic and Applied Sciences, University of Çukurova, Adana, Turkey
December 2000 - January 2004	Research Assistant University of Çukurova, Adana, Turkey
January 2004 - December 2004	Graduate Research Programme Ecole Polytechnique Federale de Lausanne, Lausanne, Switzerland
March 2005 - June 2009	PhD student in Particle Physics Department of Physics, University of Antwerp Antwerp, Belgium